



Fakultät für Maschinenwesen  
Lehrstuhl für Carbon Composites

**Experimental Characterization and Numerical  
Modeling of the Mechanical Response for  
Biaxial Braided Composites**

Jörg A. Cichosz

Vollständiger Abdruck der von der Fakultät für Maschinenwesen der Technischen Universität München zur Erlangung des akademischen Grades eines

Doktor-Ingenieurs (Dr.-Ing.)

genehmigten Dissertation.

Vorsitzender: Univ.-Prof. Dr.-Ing. Harald Klein  
Prüfer der Dissertation: Univ.-Prof. Dr.-Ing. Klaus Drechsler  
Prof. Pedro P. Camanho, PhD  
(University of Porto, Portugal)

Die Dissertation wurde am 03.03.2015 bei der Technischen Universität München eingereicht und durch die Fakultät für Maschinenwesen am 13.01.2016 angenommen.

All things are difficult before they are  
easy.

---

Thomas Fuller (1608-1661)

# Abstract

The growing use of composite materials raises the need for automated manufacturing processes, which increase material throughput, cost-efficiency and part quality. The braiding process has considerable potential for cost-efficient high-volume production. It allows automated production of near net-shaped preforms for slender and hollow structures, and combines low material waste with a high flexibility in mechanical properties.

A number of challenges are given in the design of braided composite structures: the textile yarn architecture controls the material behavior and is likely to vary on a complex braided component, resulting in variable material properties. Currently, no established models are available for prediction of braided composites mechanical properties. Thus, the main goal of this thesis is to create a multi-scale modeling approach for the analysis of biaxial braided structural components. This requires efficient unit cell models, predicting mechanical properties for a multitude of yarn architectures, and macroscopic methods applicable for analyzing large braided components. Additionally, experimental work on yarn architecture and mechanical characterization, which is needed for model input and validation, respectively, has been carried out.

The yarn architecture parameters for ( $\pm 30^\circ$ ) and ( $\pm 45^\circ$ ) braided composites could be robustly measured using optical microscopy and image analysis of surface scans. Off-axis tensile and compressive experiments of ( $\pm 30^\circ$ ) biaxial braided composites showed that the material behavior was strongly nonlinear. Inelastic deformation and damage were identified as the underlying mechanisms, attributed to microscopic cracking at the fiber/matrix interface. The failure modes observed were dominated by yarn failure and transverse cracking, with the transverse yarn stress controlling the latter case.

A novel, generic, computationally efficient and parametric finite element unit cell modeling approach, using beam and continuum elements, was developed and applied to predict the mechanical properties. The stress fields obtained correlated well with classical continuum unit cell results. The predictions, employing a phenomenological plasticity model, in combination with a stress-based failure criterion, were in good correlation with the experiments. The input parameters of the macroscopic modeling were calculated from the unit cell results. The macroscopic analyses showed that it is crucial for the failure prediction to use an equivalent laminate model providing the stresses in the yarn directions. The equivalent laminate model in combination with Puck's 2D failure criterion correlated well with the experiments. Furthermore, the macroscopic model has been extended to non-linear predictions with a material subroutine in Abaqus/Explicit, improving the results considerably.

# Übersicht

Der wachsende Einsatz von Faserverbundwerkstoffen erhöht den Bedarf an automatisierten Fertigungsprozessen, mit dem Ziel, den Materialdurchsatz zu erhöhen sowie Kosteneffizienz und Bauteilqualität zu verbessern. Der Flechtprozess bietet ein großes Potential für kosteneffiziente Großserienproduktion und erlaubt eine automatisierte Herstellung von komplexen, endkonturnahen Preforms für Hohlbauteile. Der Materialverschnitt ist dabei sehr niedrig und die Materialeigenschaften sind flexibel einstellbar.

Die Auslegung von geflochtenen Strukturbauteilen beinhaltet jedoch einige Herausforderungen: Die komplexe Garnarchitektur beeinflusst das Materialverhalten, wobei die Garnarchitektur, und damit die Materialeigenschaften, auf komplexen Strukturbauteilen variieren. Aktuell existieren keine etablierten Methoden zur Materialmodellierung von geflochtenen Verbundwerkstoffen. Daher lag das Hauptziel dieser Arbeit in der Erstellung eines Multi-Skalen-Ansatzes zur Berechnung von biaxial geflochtenen Strukturbauteilen. Dies erforderte effiziente Einheitszellenmodelle zur Vorhersage der Materialeigenschaften für eine Vielzahl von Garnarchitekturen, sowie makroskopische Methoden, welche für die Strukturberechnung geflochtener Verbundstrukturen anwendbar sind. Zudem wurden die Garnarchitektur und das mechanische Verhalten experimentell charakterisiert und die Ergebnisse als Eingabeparameter und zur Validierung der Modelle verwendet.

Die Garnarchitekturparameter von ( $\pm 30^\circ$ ) und ( $\pm 45^\circ$ ) geflochtenen Verbundwerkstoffen konnten mit Hilfe von Mikroschliffen und Bildanalyse von Oberflächen-Scans robust gemessen werden. Off-Axis Versuche in Zug und Druck von ( $\pm 30^\circ$ ) geflochtenen Verbundwerkstoffen ergaben ein stark nichtlineares Materialverhalten. Inelastische Deformation und Schädigung, welche auf mikroskopische Risse an der Faser/Matrix-Grenzfläche zurückgeführt wurden, waren die dominanten Mechanismen für das nichtlineare Verhalten. Garnversagen und transversale Risse waren die dominanten Versagensmodi, wobei Letztere abhängig vom Querspannungszustand im Garn waren.

Ein neuer, generischer, parametrischer und effizienter Ansatz zur FEM Einheitszellenberechnung mit Balken- und Kontinuumselementen wurde entwickelt, und verwendet, um die mechanischen Eigenschaften vorherzusagen. Die berechneten Spannungsfelder korrelierten gut mit klassischen Kontinuums-Einheitszellen. Ein phänomenologisches Plastizitätsmodell, in Kombination mit einer spannungsbasierten Versagensvorhersage im Garn, lieferte gute Ergebnisse im Vergleich mit den Experimenten. Die Eingabeparameter der makroskopischen Modellierung wurden aus den Einheitszellen-Ergebnissen berechnet. Die makroskopischen Analysen zeigten, dass es für die Versagensvorhersage entscheidend ist, ein äquivalentes Laminatmodell und damit die Spannungen in den Garnrichtungen zu verwenden. Das äquivalente Laminatmodell ergab mit dem Puck 2D Versagenskriterium gute Übereinstimmung mit den Experimenten. Zudem wurde die makroskopische Modellierung mit einer Material-Subroutine in Abaqus/Explicit auf nichtlineare Vorhersagen erweitert, was die Ergebnisse deutlich verbesserte.

# Acknowledgements

I would like to thank my academic supervisor Prof. Dr.-Ing. Klaus Drechsler, head of the Institute for Carbon Composites, for giving me the opportunity to work on this thesis and for providing the research environment enabling this work. Further, I would like to express a great thank to my second supervisor Prof. Pedro Camanho for supporting the progress of this research work with numerous advises and fruitful discussions. I would also like to sincerely thank Dr. Roland Hinterhoelzl. You helped me a lot, encouraging me and guiding me through my research work.

The financial support from the Polymer Competence Center Leoben GmbH is gratefully acknowledged. Appreciation is expressed to the technical support of all the colleagues during the COMET-K1 research project, Dr. Markus Wolfahrt, Dr. Jakob Garger, and Dr. Martin Fleischmann, to name but a few.

Through the time at the Institute for Carbon Composites, I had the chance to work with many excellent colleagues; thank's for interesting conversations, inspiration and a lot of fun: Christoph Hahn, Petra Fröhlich, Michael Brand, Rhena Helmus, Daniel Leutz, Johannes Neumayer, Roland Lichtinger, and many more. I am also grateful to all my students, from which I learned a lot supervising their theses. I am especially thankful to Tobias Wehrkamp-Richter for the collaboration during my experimental and modeling work and the many fruitful discussion on my research. Furthermore, the support of Dr. Hannes Körber, during the experimental work, is gratefully acknowledged.

I would like to further express my thanks to the guys from Munich Composites GmbH, Felix Fröhlich and Olaf Rüger, for providing help and knowledge during the production of the braided preforms.

I am eternally grateful to my parents, Hans and Elly and my brother Thomas, for their never ending love, support, and encouragement. To my dear friends, Jonas, Simon, and Steffen: I am much obliged for a great friendship over many years!

Finally, my deepest thank goes to my wonderful wife Carolin. You have been the greatest support through all the ups and downs during this thesis. I cannot thank you enough!

# Contents

<b>Nomenclature</b>	<b>xiii</b>
<b>1. Introduction</b>	<b>1</b>
1.1. Thesis objective . . . . .	3
1.2. Structure of thesis . . . . .	4
<b>2. Literature review</b>	<b>7</b>
2.1. Types of textile composites . . . . .	9
2.2. Manufacturing of braided composites . . . . .	10
2.2.1. Braiding machines . . . . .	10
2.2.2. Types of braided reinforcements . . . . .	12
2.2.3. Basic equations for the braiding process . . . . .	14
2.2.4. Resin infusion . . . . .	16
2.3. Yarn architecture of braided composites . . . . .	16
2.3.1. Characterization of the yarn architecture . . . . .	21
2.3.2. Geometric modeling . . . . .	23
2.4. Mechanical testing of braided composites . . . . .	25
2.4.1. Elastic behavior . . . . .	25
2.4.2. Nonlinear and failure behavior . . . . .	25
2.5. Textile composites constitutive behavior prediction . . . . .	29
2.5.1. Analytical models . . . . .	30
2.5.2. Classical laminate theory methods . . . . .	31
2.5.3. Finite element unit cell modeling . . . . .	32
2.6. Multi-scale modeling and homogenization . . . . .	37
2.6.1. Averaging and effective properties . . . . .	37
2.6.2. Representative volume element / repeating unit cell . . . . .	38
2.6.3. Homogeneous boundary conditions . . . . .	38
2.6.4. Periodic boundary conditions . . . . .	38
2.7. Modeling of nonlinearities, failure and damage in composite materials . . . . .	41
2.7.1. Failure theories . . . . .	41
2.7.2. Damage modeling . . . . .	43
2.7.3. Inelastic deformation . . . . .	43
2.8. Conclusions . . . . .	44
<b>3. Experimental techniques</b>	<b>47</b>
3.1. Coordinate systems . . . . .	47
3.2. Manufacturing of biaxial braided composites . . . . .	48
3.2.1. Constituent materials . . . . .	48
3.2.2. Manufacturing of braided composite panels . . . . .	48

3.2.3.	Quality inspection and assurance . . . . .	51
3.3.	Yarn architecture characterization . . . . .	52
3.3.1.	Optical microscopy . . . . .	52
3.3.2.	Micro-CT . . . . .	53
3.3.3.	Analysis of surface images . . . . .	53
3.4.	Mechanical characterization . . . . .	57
3.4.1.	Manufacturing of specimen . . . . .	58
3.4.2.	Thickness measurement . . . . .	59
3.4.3.	Off-axis experiments . . . . .	60
3.4.4.	Test set-up and procedure . . . . .	62
3.4.5.	Strain measurement systems . . . . .	64
3.4.6.	Evaluation methods . . . . .	68
3.4.7.	Fiber volume fraction measurements . . . . .	72
<b>4.</b>	<b>Experimental testing and results</b>	<b>75</b>
4.1.	Yarn architecture of braided composites . . . . .	75
4.1.1.	Optical microscopy . . . . .	76
4.1.2.	Braiding angle measurements . . . . .	81
4.1.3.	Summary of measured yarn architecture properties . . . . .	84
4.1.4.	Micro-CT . . . . .	85
4.1.5.	Summary and strategy for yarn architecture measurements . . . . .	88
4.2.	Off-axis experiments of biaxial braided composites . . . . .	90
4.2.1.	Tensile experiments . . . . .	90
4.2.2.	Tensile loading/unloading experiments . . . . .	105
4.2.3.	Compression . . . . .	108
4.2.4.	Comparison of tension and compression off-axis experiments . . . . .	118
4.3.	Conclusion from experimental measurements . . . . .	121
4.3.1.	Yarn architecture characterization . . . . .	121
4.3.2.	Mechanical characterization with tensile and compressive off-axis experiments . . . . .	122
<b>5.</b>	<b>Geometric modeling and analytical predictions</b>	<b>125</b>
5.1.	Geometric model from WiseTex . . . . .	125
5.1.1.	Input parameters . . . . .	125
5.1.2.	Unit cell geometry . . . . .	126
5.1.3.	Comparison of unit cell geometry to micro-CT measurements . . . . .	127
5.2.	Elastic predictions . . . . .	128
5.2.1.	Comparison of predictions to experiments . . . . .	129
5.2.2.	Effects of yarn architecture variation on elastic results . . . . .	129
5.3.	Elastic predictions based on analytically calculated yarn architecture pa- rameters . . . . .	132
5.4.	Transfer of WiseTex geometry to finite element unit cell models . . . . .	133
5.5.	Conclusion on geometric modeling and analytical predictions . . . . .	134
<b>6.</b>	<b>Finite element unit cell modeling</b>	<b>135</b>
6.1.	Framework for unit cell modeling . . . . .	136

6.2.	Binary Beam Model: modeling and idealizations . . . . .	136
6.2.1.	Coupling of yarns and matrix . . . . .	139
6.3.	Constitutive laws . . . . .	139
6.3.1.	Volume fractions . . . . .	140
6.3.2.	Elastic properties . . . . .	140
6.3.3.	Strength properties . . . . .	142
6.3.4.	Plasticity model . . . . .	144
6.4.	Periodic boundary conditions . . . . .	146
6.4.1.	Coupling equations . . . . .	147
6.4.2.	Out-of-plane boundary conditions . . . . .	148
6.4.3.	Unit cell loading . . . . .	148
6.5.	Stress analysis: volume averaging . . . . .	149
6.5.1.	Averaging volume shape . . . . .	150
6.5.2.	Averaging volume size . . . . .	151
6.6.	Failure analysis . . . . .	151
6.6.1.	Yarn stresses in the BBM . . . . .	152
6.6.2.	Failure criterion . . . . .	152
6.7.	Comparison to continuum unit cell . . . . .	154
6.7.1.	Yarn stress profiles . . . . .	155
6.7.2.	Summary and conclusion of comparison . . . . .	159
6.8.	Elastic predictions . . . . .	159
6.9.	Parametric study: out-of-plane boundary conditions . . . . .	163
6.9.1.	Nonlinear deformation and failure . . . . .	166
6.9.2.	Summary out-of-plane boundary conditions . . . . .	168
6.10.	Prediction of failure and comparison to experiments . . . . .	168
6.10.1.	Parameter identification . . . . .	168
6.10.2.	Comparison to experiments . . . . .	170
6.11.	Conclusion on FE unit cell modeling . . . . .	176
<b>7.</b>	<b>Macroscopic modeling of biaxial braided composites</b>	<b>179</b>
7.1.	Analytical modeling approaches . . . . .	179
7.2.	Input property determination for SPA and APA method . . . . .	182
7.2.1.	Input for SPA . . . . .	182
7.2.2.	Input for APA . . . . .	182
7.3.	Analytical failure prediction with APA and SPA . . . . .	186
7.4.	Comparison of failure criteria for APA . . . . .	188
7.5.	APA application to test cases . . . . .	190
7.5.1.	Discussion and conclusion of linear predictions . . . . .	191
7.6.	Nonlinear constitutive law . . . . .	193
7.6.1.	Input properties . . . . .	193
7.6.2.	Braiding angle update . . . . .	193
7.6.3.	Strain increment transformation . . . . .	194
7.6.4.	Plasticity model . . . . .	195
7.6.5.	Damage model . . . . .	198
7.6.6.	Stress calculation . . . . .	199



7.6.7. Material point deletion . . . . .	200
7.6.8. Implementation . . . . .	200
7.7. BB_APA_NL model validation . . . . .	200
7.7.1. Nonlinear deformation . . . . .	201
7.7.2. Failure prediction . . . . .	204
7.8. Conclusion on macroscopic modeling . . . . .	206
<b>8. Conclusions and future work</b>	<b>209</b>
8.1. Discussions and conclusions . . . . .	209
8.2. Potential future work . . . . .	212
<b>A. Material properties</b>	<b>215</b>
<b>B. Orientation averaging for biaxial braided composites</b>	<b>217</b>
<b>C. Definition of RUC and RVE</b>	<b>219</b>
<b>D. Normalization of properties for braided composites</b>	<b>221</b>
<b>E. Software codes</b>	<b>223</b>
<b>F. Periodic boundary conditions</b>	<b>225</b>
<b>G. Supervised student theses</b>	<b>233</b>
<b>Bibliography</b>	<b>250</b>

# Nomenclature

## Symbols

### Lower case arabic letters

$c$	-	crimp ratio
$d_I$	-	damage variable for mode $I$
$d_1$	mm	yarn height
$d_2$	mm	yarn width
$d_{fil}$	mm	filament diameter
$d_m$	mm	mandrel diameter
$f$	MPa	value of the yield criterion
$f_E$	-	stress exposure
$f_{hg}$	1/s	horn gear frequency
$h$	mm	laminate thickness
$l_1$	mm	unit cell length
$l_2$	mm	unit cell width
$l_3$	mm	unit cell height
$m$	-	inverse hardening exponent
$p$	mm	yarn spacing
$\mathbf{p}^i$	mm	periodicity vector
$p_d$	%	packing density
$r$	MPa	hardening function
$t_{ply}$	mm	ply thickness
$\mathbf{u}$	mm	displacement vector
$v_m$	mm/s	mandrel take-up velocity

### Upper case arabic letters

$A_{fil}$	mm <sup>2</sup>	filament area
$A_{yarn}$	mm <sup>2</sup>	yarn cross-sectional area
$\mathbf{C}$	MPa	stiffness matrix
$E^0$	MPa	initial Young's modulus
$E^1$	MPa	unloading Young's modulus
$E_\psi$	MPa	Young's modulus in off-axis direction $\psi$
$E_{ii}$	MPa	Young's modulus in $ii$ direction

$E_{tan}$	MPa	tangent modulus
$\mathbf{F}$	mm	masternode/constraint driver force tensor
$FAW$	g/m <sup>2</sup>	area weight of preform
$G^I$	N/mm	fracture toughness for mode $I$
$G_{ij}$	MPa	shear modulus in $ij$ plane
$K$	MPa	hardening law parameter
$L_c$	mm	characteristic element length
$N_c$	-	number of yarn carriers
$N_{fil}$	-	filament number
$N_{hg}$	-	horn gear number
$\mathbf{P}$	mm	periodicity tensor
$\mathbf{Q}$	MPa	in-plane stiffness matrix (material coordinate system)
$\bar{\mathbf{Q}}$	MPa	in-plane stiffness matrix (global coordinate system)
$\mathbf{R}$	-	Reuter matrix
$\mathbf{S}$	MPa	in-plane compliance matrix (material coordinate system)
$\bar{\mathbf{S}}$	MPa	in-plane compliance matrix (global coordinate system)
$S_L$	MPa	in-plane shear strength
$T$	g/km	yarn linear density
$\mathbf{T}$	-	transformation matrix
$\mathbf{U}$	mm	masternode/constraint driver displacement tensor
$U_m$	mm	mandrel perimeter
$WR$	-	waviness ratio
$X_C$	MPa	longitudinal compressive strength
$X_T$	MPa	longitudinal tensile strength
$Y_C$	MPa	transverse compressive strength
$Y_T$	MPa	transverse tensile strength

### Greek letters

$\alpha$	-	accumulated plastic strain
$\beta$	°	fiber orientation (from optical sensor)
$\beta_{tol}$	°	tolerance for yarn orientation
$\gamma_{12}^{pl}$	-	plastic part of the in-plane shear strain
$\gamma_{ij}$	-	shear strain in $ij$ -plane
$\delta_{I,eq}$	mm	equivalent displacement for mode $I$
$\boldsymbol{\varepsilon}$	-	strain vector
$\langle \boldsymbol{\varepsilon} \rangle$	-	homogenized strain tensor
$\varepsilon^{UTS/UCS}$	-	failure strain tension / compression
$\varepsilon_{ie}$	-	inelastic strain
$\varepsilon_{ii}$	-	normal strain in $ii$ direction
$\zeta$	°	misalignment angle

$\eta$	-	nesting factor
$\theta$	°	braiding angle
$d\lambda$	-	plastic multiplier
$\nu_{ij}$	-	Poisson's ratio $ij$
$\rho_f$	kg/m <sup>3</sup>	fiber density
$\bar{\sigma}_{ii}^Y$	MPa	yarn normal stress in $ii$ -direction
$\bar{\sigma}_{ij}$	MPa	$\Omega^m$ volume averaged stress at beam node
$\boldsymbol{\sigma}$	MPa	stress vector
$\langle \boldsymbol{\sigma} \rangle$	MPa	homogenized stress tensor
$\sigma^{UTS/UCS}$	MPa	failure stress tension / compression
$\sigma_{I,eq}$	MPa	equivalent stress for mode $I$
$\sigma_{ii}$	MPa	normal stress in $ii$ -direction
$\tau_{ij}$	MPa	shear stress in $ij$ -plane
$\bar{\tau}_{ij}^Y$	MPa	yarn shear stress in $ij$ -plane
$\varphi_f$	%	fiber volume fraction
$\varphi_Y$	%	yarn volume fraction
$\chi$	°	oblique tab angle
$\psi$	°	off-axis angle
$\Omega^m$	mm <sup>3</sup>	averaging volume at beam node
$\omega_c$	rad/s	angular velocity of yarn carriers

### Superscripts and subscripts

$BB$	quantity in the biaxial braid coordinate system ( $12$ )
$el$	elastic
$eq$	equivalent yarn ply quantity
$F+/-$	quantity in the yarn (ply) coordinate system ( $1F$ )
$pl$	plastic

### Abbreviations

APA	angle ply approach
BB	biaxial braided composite
BBM	Binary Beam Model
BE	beam element
BM	Binary Model
CD	constraint driver
CLC	combined loading compression
CLT	classical laminate theory

CT	computer tomography
CUC	continuum unit cell
CV	coefficient of variation
DIC	digital image correlation
DOF	degrees of freedom
EM	effective medium
FE	finite element
FRP	fiber reinforced plastic
FVF	fiber volume fraction
IP	in-phase
OA	off-axis (angle)
OP	out-of-phase
PC	plain compressive
PT	plain tensile
ROI	region of interest
RTM	resin transfer molding
RUC	representative unit cell
RVE	representative volume element
SPA	smearred ply approach
STDV	standard deviation
UD	unidirectional
VAP	vacuum assisted process
WWFE	world wide failure exercise
XML	extensive markup language

# 1. Introduction

Reducing fuel consumption and CO<sub>2</sub> emissions for human transportation has become one of the major goals in the automotive and aerospace industry. Among many possible approaches, such as improving aerodynamics or developing more efficient engines, the reduction of structural weight yields a significant potential for economic and environmentally efficient transportation. Thus, lightweight design of structural components is one of the major challenges for future aircraft and automotive development. In the field of lightweight design, composite materials are outstanding, offering an excellent stiffness- and strength-to-weight ratio as well as great possibilities for integral design.

This has led to an increased usage of composite materials in automotive and aerospace industry: in 2013, BMW released the electric car *i3*, whose passenger compartment is completely built from composite materials (Fig. 1.1), with an anticipated production of 20,000 cars per year [1]. In the same period, Airbus and Boeing released their new aircraft generation, the A350 and the 787 *Dreamliner*, respectively, both having a ratio of over 50% composite materials in their structural weight. This increased usage of composite materials, e.g. 33 tons of composites per Boeing 787 aircraft, has accelerated research and development in the field of improved and automated manufacturing processes: traditional hand lay-up, which is too expensive and too slow for such a broad usage of composite materials, is being replaced by automated and accelerated production processes. However, when competing with traditional light-weight materials like aluminum, composites suffer from their high raw-material costs, which leads to the challenge of reducing the manufacturing costs, while increasing the material throughput.



Fig. 1.1: BMW i3 passenger compartment [2]

These requirements have led to a huge interest in textile composite materials: traditional textile processes like weaving or braiding are adapted to the high-strength and high-stiffness reinforcing fibers; these processes have been proven to be promising for cost-efficient production of high-volume composite components. Textile fiber preforms can be produced on well-developed textile machinery with high material throughput, and are



**Fig. 1.2:** Overbraiding process

capable of producing high-quality composite components, when combined with modern resin transfer molding injection technology.

From the textile processes used for composite materials, the braiding process outstands in terms of process automation, process flexibility, material efficiency and material throughput. Overbraiding (Fig. 1.2) allows production of highly-integrated composite structures, by forming the raw yarn material to a closed network of interwoven yarns shaped over a mandrel. Variable cross-sectional shape and dimensions along the length of the mandrel are possible; the choice of yarn angle and the number of yarn directions (uniaxial, biaxial, triaxial braid) allows adjusting the material properties to the structural needs. Furthermore, the overbraiding process significantly reduces the cut-waste, producing near-net-shaped preforms in a single process step from the raw yarn material.

Beside the production process itself, the predictability of mechanical properties of composite materials and structures is inevitable for their optimal usage. Analytical and numerical models for composite mechanical behavior prediction have to be available and applicable for structural analysis during the development process. However, from the perspective of a analysis engineer, braided composite materials still provide a number of challenges for structural simulation and sizing of components against material failure. For unidirectional (UD) composite materials, well-established predictive failure models are available. In the framework of the World Wide Failure Exercise (WWFE) [3], large efforts have been made to compare and judge the predictive capabilities of different theories. As most of the research in the previous decades was focused on UD composites, less knowledge exists on failure and damage prediction for braided composite materials. Additionally, various more challenges are present in the prediction: braided composites comprise a textile yarn architecture of undulating and crossing yarns, which crucially affects the mechanical properties of the material. Purely macroscopic modeling approaches, mostly used within the WWFE, are unlikely to be appropriate, as each yarn architecture configuration to be modeled requires a separate test campaign for input property definition.

Considering an example for a typical braided component, the yarn architecture and thus the mechanical properties are likely to change in dependence on the position on

the component: Fig. 1.3 shows the concept of an braided aircraft frame with integrated “mouseholes” for the crossing stringers. The cross-section not being cylindrical and the variation of cross-section height introduces a change of yarn architecture (e.g. braiding angle, preform thickness). The effort for an experimental material characterization would be largely increased, requiring many test series to cover the variation of yarn architecture and material properties on the component. Thus, a multi-scale modeling approach, predicting the influence of the yarn architecture on material properties, substituting experiments with numeric simulations, is much more efficient.

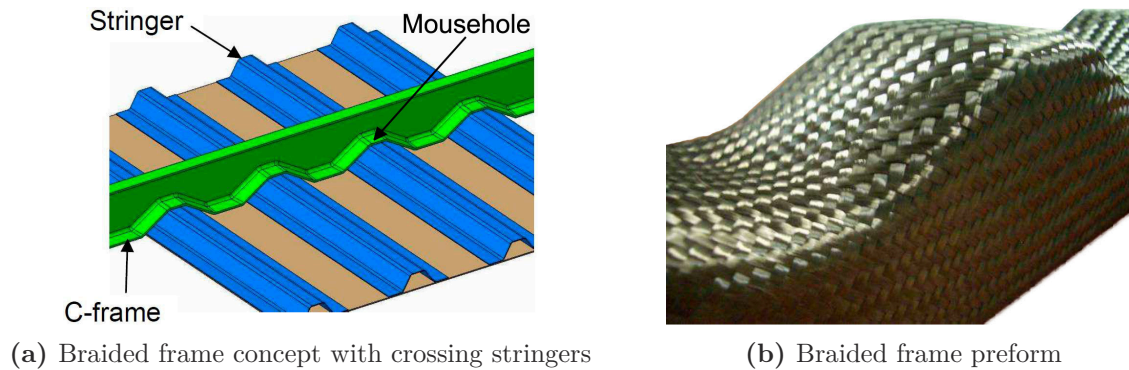


**Fig. 1.3:** Braided frame: concept with integrated mouseholes and braided preform [4]

## 1.1. Thesis objective

The main objective of the research work presented in this thesis was to develop a modeling framework for predicting the constitutive behavior of biaxial braided composites. The modeling was intended to incorporate details of yarn architecture and its impact on the mechanical properties, while being applicable for strength design of braided composite components. The core of the framework was multi-scale-modeling, including efficient unit cell models and macroscopic methods for structural simulation. Furthermore, experimental techniques for input property determination and model validation were required. The major goals of the thesis can be summarized as:

- Yarn architecture characterization: development of an experimental method for robust internal geometry measurements of braided composites.
- Mechanical characterization: experiments to determine the constitutive and failure behavior of biaxial braided composites under combined stress states.
- Unit cell modeling: development of an efficient and parametric finite element unit cell modeling approach, required to predict the mechanical behavior for a multitude of yarn architectures and load cases.
- Macroscopic modeling: formulation of a modeling approach, based on the unit cell simulation results, which is applicable for structural simulation of large braided composite components.



## 1.2. Structure of thesis

### **Chapter 2: *Literature review***

In Chapter 2, a literature review to previous published work in the field of experimental characterization and numerical modeling of braided composites is given: a short introduction is provided to manufacturing aspects of the braiding process and the basic equations for braiding process modeling are presented. Additionally, the work published on experimental characterization and available analytical and numerical models for textile and braided composites is reviewed. Finally, a short overview on modeling of failure, damage and inelastic behavior in composite materials is given and applications of the models to textile composite materials are described.

### **Chapter 3: *Experimental techniques***

Chapter 3 describes the experimental methods used for yarn architecture and mechanical characterization. A description of the manufacturing process used for the braided composites, characterized in this work, is provided. For yarn architecture characterization the different techniques are described, including sample preparation and results evaluation. Furthermore, specimen preparation, test set-up and evaluation methods for the mechanical characterization are given.

### **Chapter 4: *Experimental testing and results***

Chapter 4 includes the results of the experimental work conducted for yarn architecture characterization and mechanical testing. A strategy for yarn architecture measurement, based on optical microscopy, is introduced. This includes studies on the sample position dependence and the required number of the samples. Additionally, two braiding angle measurement techniques based on surface scanning are compared and three-dimensional effects based on micro computer tomography measurements are investigated. Off-axis tension and compression tests have been conducted to characterize the nonlinear and failure behavior of ( $\pm 30^\circ$ ) braided composites under combined stress states. Furthermore, the mechanics of failure in tension and compression are identified and damage and plasticity effects in the material are distinguished using loading/unloading experiments.

### **Chapter 5: *Geometric modeling and analytical predictions***

Chapter 5 describes the geometric unit cell modeling used in this thesis. Based on the geometric models, analytical predictions of the braided composite elastic behavior are given and parametric studies on yarn architecture variations are presented.

### **Chapter 6: *Finite element unit cell modeling***

The development of a novel finite element unit cell modeling approach based on beam and continuum elements is described in Chapter 6. The equations and implementation of the modeling approach, including constitutive modeling, periodic boundary conditions and a volume-averaging for stress calculation are presented. An assessment of the predicted

stress fields is obtained by comparison of the modeling results to a classical continuum unit cell approach. Furthermore, the influence of boundary conditions in thickness direction is studied, and the modeling results are finally validated by comparison to experimental results.

### **Chapter 7: *Macroscopic modeling of biaxial braided composites***

The approaches used for macroscopic modeling of braided composites are described in Chapter 7. Two analytical modeling approaches for failure prediction are compared and a method for input property definition, based on unit cell modeling results, is derived. In addition to the analytical modeling, a numerical modeling approach, considering plasticity and damage effects in the braided composites, is presented and the numerical results are compared to analytical modeling and experimental results.

### **Chapter 8: *Conclusions and future work***

Chapter 8 includes the overall conclusion on the experimental and numerical work conducted in this thesis. Topics, identified in experimental characterization and numerical modeling are discussed and possible solutions are given. Finally, possible points for future research work are discussed.

## 2. Literature review

Fiber reinforced plastics (FRPs) are composite materials typically consisting of two components: reinforcing fibers that are embedded into polymeric matrix [5]. The composite material utilizes the best properties of both components: the high stiffness and strength fibers take the task to carry the load and are the reinforcing constituent in the material, while the softer matrix introduces and distributes the load into the fibers, keeps the fibers in place and protects them against environmental effects. The usage of FRP materials in aerospace, automotive, and other industrial applications has a long history, spanning from the first half of the last century. In the 1930s and 1940s the first usages of FRPs for aircraft wings and fuselages have been reported. The World War II accelerated the development of composite components, mainly used as secondary structures in military airplanes. In Germany, the first usage of FRPs in highly-loaded structures was achieved by academic groups for gliding. In 1957 the glider airplane *Phönix*, which was the first aircraft built completely from glass fiber reinforced plastics, took off on his maiden flight [5]. Application of composite materials in commercial airplanes has been done piece by piece. At first, interior and secondary structures (e.g., leading edge skin vertical tail A300B) were built from composites and long-term behavior was studied before being used in primary structures [5].

The early applications of FRPs were focused on lightweight design and mass reduction. The components were typically produced using hand-layup of pre-impregnated unidirectional tapes, resulting in long and labor-intensive manufacturing processes. With the growing usage of composite materials in aerospace and with new applications within the automotive sector, the reduction of manufacturing costs and cycle times is of increasing interest. Due the increased interest in reduced costs and automation of manufacturing processes, textile reinforcements were established on the composite market [6].

Textile composites are fiber-reinforced plastics produced from a dry fiber textile reinforcement and a matrix (polymeric resin in most cases). The textile reinforcements are produced from yarns, typically consisting of several thousand fibers, on textile machinery specially adapted for high-performance fiber reinforcements [6]. The term textile composites describes a large range of materials, but in most cases, the reinforcements consist of two or more sets of tows, which are interwoven in a textile process. The dry fiber reinforcements are either produced directly in the desired shape (e.g. braiding) or produced in several preforming steps (e.g. woven fabrics). Commonly, the preforms produced are then impregnated by a liquid resin infusion process yielding the textile composites. A typical example for a textile process is given in Fig. 2.1.

The main reason for using textile composites is cost-efficiency [6]. Textile processes and textile machinery have been developed and automated over centuries, which serves as a good basis for automated and cost-efficient production processes. The classical textile processes have been adapted to enable manufacturing of fragile reinforcement fibers ren-

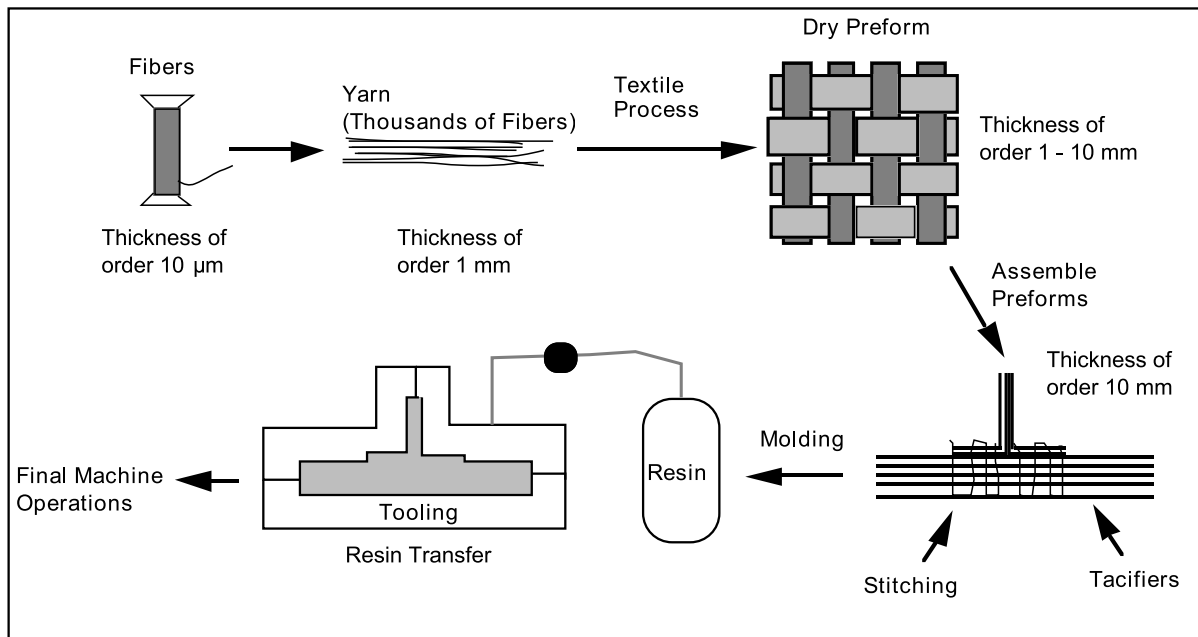


Fig. 2.1: Textile composite manufacturing process [7]

dering a high material throughput and low manufacturing costs. The variety of different textile preforms allows the designer to use a material specifically suited to the structural needs. Additionally, with direct textile preforming processes, such as braiding, it is possible to produce near-net-shaped preforms from the raw fiber material, which drastically decreases material waste and manual rework.

Applications for textile and braided composites can be found in all areas of the composite industry: a textile composite produced by 2D braiding in conjunction with a resin transfer molding (RTM) infused thermoset resin has been used by Dowty Propellers since 1987 [6]. The crash-box of the Mercedes-Benz McLaren SLR sports car was produced by braiding combined with other textile processes. The taper-shaped crash-box was overbraided with a triaxial braid and further reinforced with a tufting technique, yielding a very high specific energy absorption of 70 kJ/kg [8].

The recently developed Boeing 787 *Dreamliner* aircraft uses triaxial braided composites for the frames in the fuselage [9]. Additionally, General Electric used triaxial braided composites in their jet engine containment of the Boeing 787's engine for better damage tolerance. The braid provides 30% better containment properties along with approximately 160 kg weight savings per engine [10]. BMW AG also has used triaxial braided composites for the bumper beam of the BMW M6 sports car in a quantity of 6000 parts per year [11].

The following chapter gives an overview of the current state of research regarding braided composites. First, basic terms and definitions, the current state of braided composite manufacturing, and characterization methods for braided composites will be described. The second part will focus on the modeling of braided composites: an overview of existing models will be given and further points regarding unit-cell modeling, as well as modeling non-linear material behavior of composite materials will be dealt with.

## 2.1. Types of textile composites

Textile reinforcements comprise one or more sets of yarns, which are interlaced with each other or with additional stitching yarns. The yarns, which comprise several thousand filaments, are the raw product of the textile reinforcement. The most common classification of textile reinforcements refers to the directionality of the reinforcing fibers (Fig. 2.2): if the fibers in the preform alone (without a matrix) can continuously transport loads in the thickness direction, the reinforcements are termed “three-dimensional” [7].

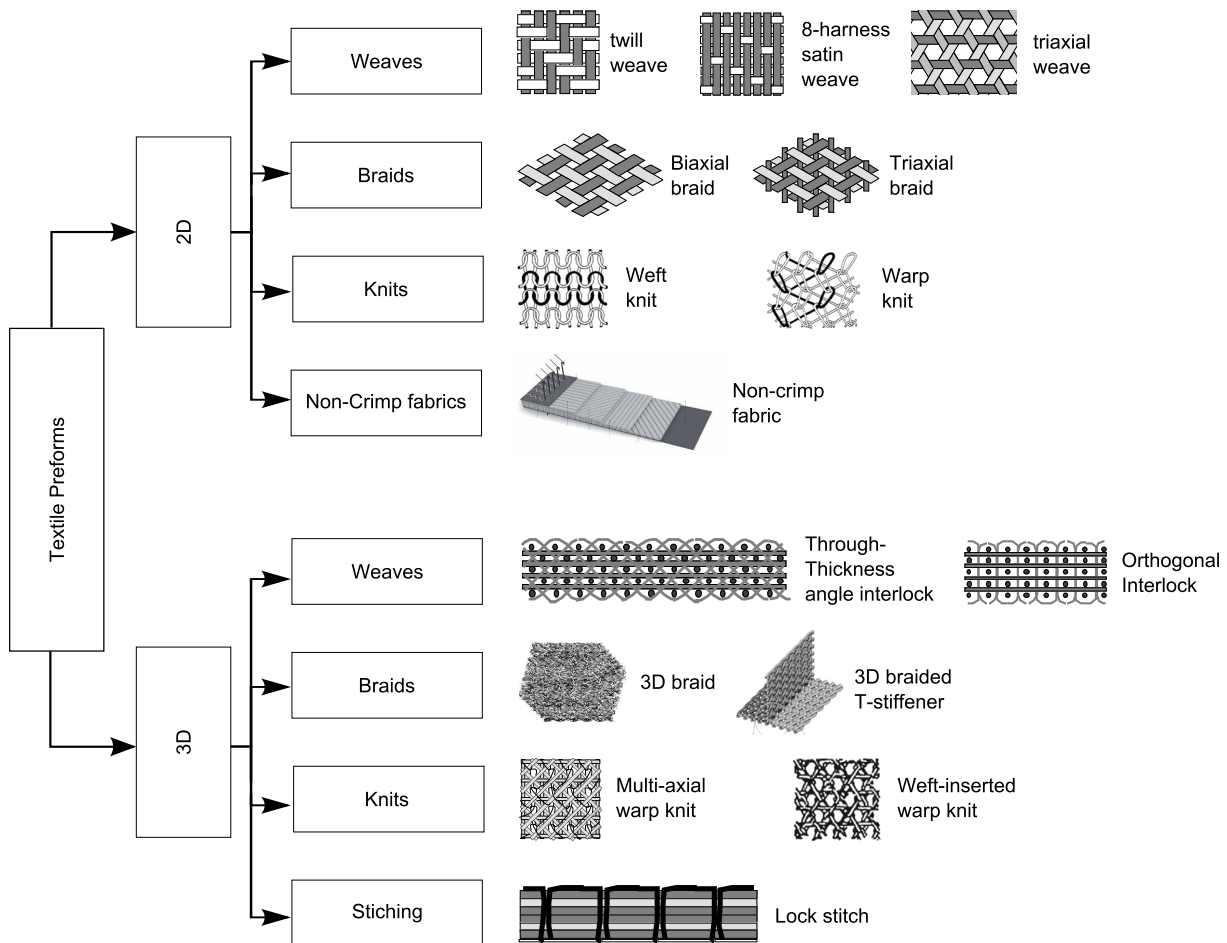


Fig. 2.2: Textile reinforcement classification adapted from [7, 12, 13]

Two-dimensional textile reinforcement are well suited for in-plane loads, but still offer a layered structure akin to conventional composite laminates. They can be produced in processes with high material throughput. The interwoven structure of 2D textile reinforcements creates an uneven ply interface, which helps to increase the resistance to delamination between the plies [14]. The in-plane properties are decreased due to the out-of-plane waviness caused by the yarn interlacements.

Three dimensional textile composites have a certain volume fraction of fibers running in the thickness direction. These 3D reinforcements offer great advantages in regions with three-dimensional stress states and in cases requiring great damage tolerance. Only a modest volume fraction of thickness fibers is needed to improve delamination resistance

[7], and with an increasing volume fraction of thickness fibers the in-plane properties suffer drastically due to the decreased in-plane volume fraction and additional fiber waviness. The mechanical properties and the complexity of textile machinery reducing the rate of production are the main reasons why the use of 3D textile composites is limited to special applications [15].

Cox [7] states that all 2D and most 3D textiles are quasi-laminar. They can be considered to function as laminates, as high fiber volume fractions in the thickness direction are seldom used as they lead to an unacceptable loss of in-plane properties [7]. If a higher volume fraction of the fibers is running in the thickness direction, the textiles are termed nonlaminar. This difference between quasi-laminar and nonlaminar textiles is particularly relevant when choosing an appropriate modeling approach for the textile composite.

Within the area of quasi-laminar textile composites, the braiding process stands out due to its high flexibility regarding material properties and the possibility to automate the production of near-net-shaped preforms. In the following section a brief review of the current state of research regarding manufacturing of braided composites will be given.

## 2.2. Manufacturing of braided composites

Braiding is a traditional textile manufacturing technique, comprising three or more yarns that are interlaced in a defined pattern. Classical applications for braided textiles are typically un-reinforced tows e.g., ropes or shoelaces. The first applications of the braiding process in composite materials were reported in the late 1970s by researchers at McDonnell Douglas Aircraft Company [16]. For composite materials, braiding combines the possibility of process automation, a high material throughput, low material waste and improved damage tolerance. This results in a high potential for high-volume production of composite structures [10, 15, 17, 18].

### 2.2.1. Braiding machines

Braiding machines can be separated regarding the directionality of the reinforcement produced into 2D and 3D braiding machines (see Fig. 2.2).

#### 2D braiding machines

Fig. 2.3 presents a state-of-the-art 2D braiding machine. The yarns spools are positioned on an outer ring and point towards the center of the braiding machine. The yarns are taken off the spools towards the center of the machine, where the braid is formed. The braids can be produced without a mandrel, resulting in braided sleeves [19], or with a mandrel in the overbraiding process. Commonly the mandrels have near-net-shaped geometry and are guided by a robot through the center of the braiding machine. The basic principle of 2D braiding is similar to the maypole dance: the yarns are stored in spools which are arranged around the center of the braiding machine. The spools are placed on two sets of yarn carriers; one rotating clockwise and the other counter-clockwise around the center of the braiding machine. The yarn carriers move on sinusoidal paths defined by horngears. Two adjacent horngears rotate alternately, passing the yarn spool from one horngear to

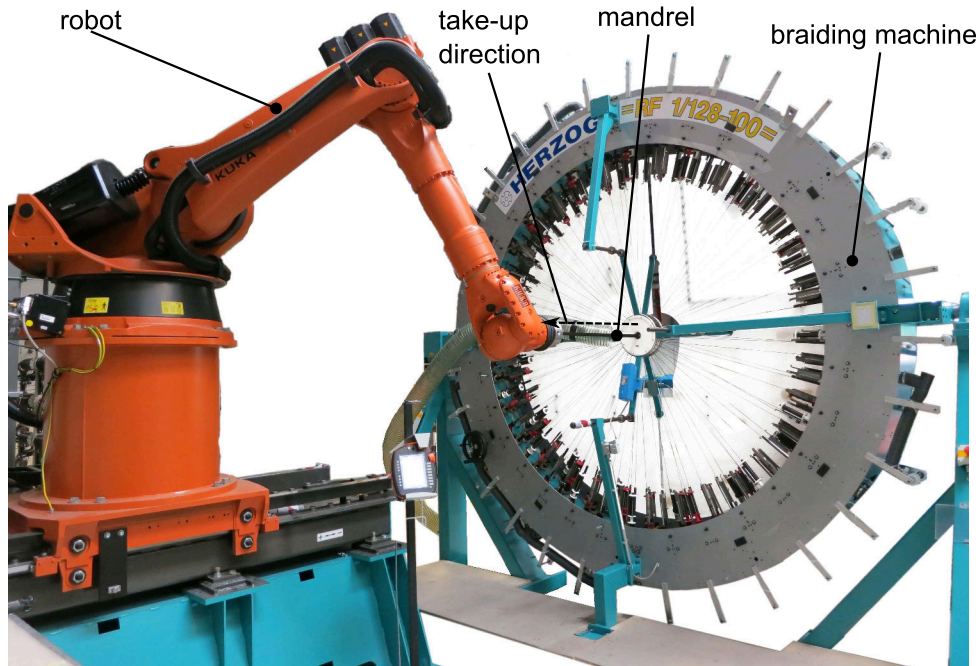


Fig. 2.3: 2D maypole braiding machine with 128 yarn carriers.

another, when opposing notches of two horngears meet (Fig. 2.4a). The pattern of yarn interlacement is thus controlled by the number and position of the spools with regard to the number of notches (most commonly: 4 notches) on each horngear: if all available yarn carriers are used on a four notch machine (“full configuration” see Fig. 2.4b), a  $2 \times 2$  braided fabric is formed. For triaxial braids, additional axial yarns can be introduced into the process through a tube in the center of the horngear. Special braiding machine configurations also allow the introduction of axial yarns between two braided plies of biaxial or triaxial braids [20, 21].

### 3D braiding machines

Through-thickness reinforced braids are manufactured on 3D braiding machines [15, 16, 22]. Two examples for 3D braiding processes, namely two-step and four-step braiding, are given in [22]. In two-step braiding, axial yarns, which are arranged in the cross-sectional shape of the desired preform, are interlaced by braider yarns. The braider yarns are then diagonally moved through an  $(n \times m)$  arrangement of axial yarns. In four-step braiding, the yarns are arranged rectangularly in the machine bed and interlacement is achieved by their relative displacement. One processing step involves four displacements of rows and columns that move alternately.

Industrial applications of 3D braiding are still rare and limited to special cases such as biomedical engineering [15]. In contrast, 2D braiding is a process used in several industrial applications in the automotive [8] and aerospace industry [6, 10, 17, 20, 21].

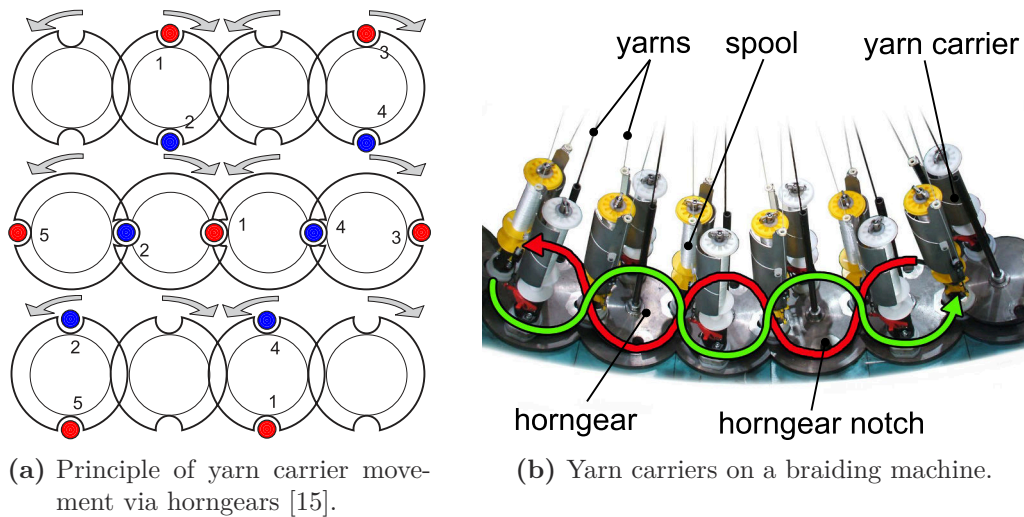


Fig. 2.4: Yarn carrier movement on maypole braiding machine.

### 2.2.2. Types of braided reinforcements

Depending on the configuration of the braiding machine, different types of reinforcements can be produced on 2D braiding machines. The type of reinforcement is primarily distinguished by the number of yarn directions, the braid interlacing pattern, and the type of preform [15]. The concept of repeating unit cells (RUC) is commonly used to describe the pattern of reinforcement, which can be done due to the periodicity of the interlacing pattern (see Appendix C). Three types of braided reinforcements can be distinguished according to the directionality of the reinforcement (Fig. 2.5):

**biaxial braid** Two sets of yarns directions are interlaced by the braiding machine with the braiding angle  $\theta$  defined relative to the take-up direction (see Fig. 2.5a).

**triaxial braid** A third set of yarns running in the axial direction is added (Fig. 2.5b).

**unidirectional braid** A UD braid is a special kind of biaxial braid, where one set of yarns is replaced by a thin thermoplastic binder yarn. A quasi-unidirectional reinforcement with reduced waviness is created [21].

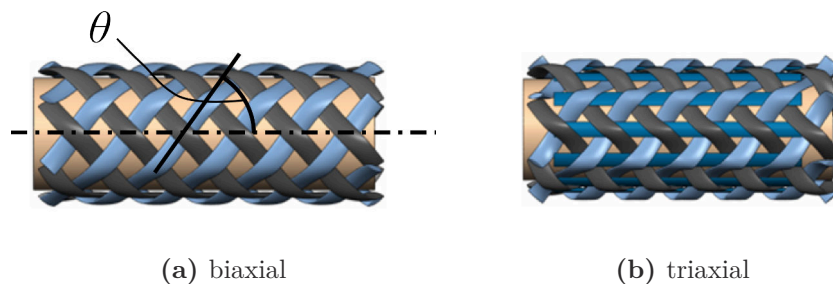


Fig. 2.5: Types of braid reinforcements [23].



### Braid patterns

The number of active yarn carriers defines the interlacing pattern of the braid (Fig. 2.6). Most common are the  $2 \times 2$  (regular braid) and  $1 \times 1$  (diamond braid) patterns, which are achieved by using all or half of the available yarn carriers on a regular 4-notch horngear braiding machine (*full configuration* on Fig. 2.4b). Furthermore,  $3 \times 3$  (hercules) and  $4 \times 4$  braids may be produced by braiding machines with six and eight notches per horngear, respectively, [24]. The waviness reduces with increasing length of the straight yarn region, yielding better in-plane material properties. On the other hand the stability of the braid decreases, which can be an issue for complex parts with large cross sectional changes. The choice of braid pattern is usually driven by the component dimensions, required mechanical properties and preform stability.

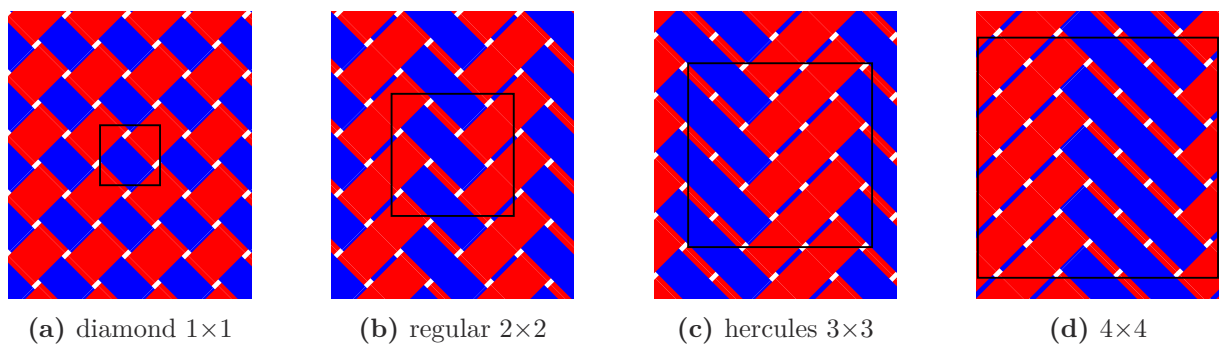


Fig. 2.6: Common of braid patterns with corresponding RUC.

### Braided preforms

Braided preforms can be produced in different types regarding the continuity of the yarns (Fig. 2.7). The most common is the overbraiding process, where a near net-shaped mandrel is used to define the contour of the final part. This is achieved by rotating the yarn carriers continuously around the braiding machine center through which the mandrel is

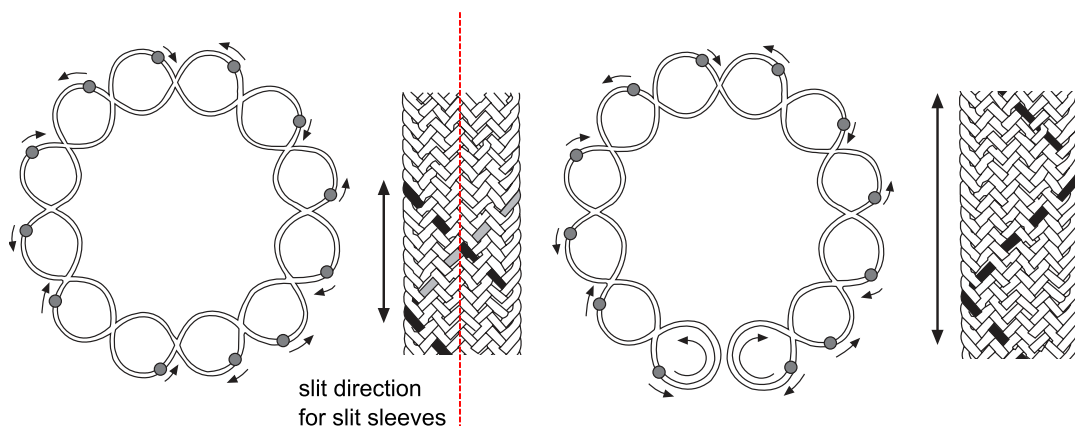


Fig. 2.7: Braided preforms: braided sleeves (left) and braided tapes (right) with the corresponding yarn carrier movement (adapted from [15])

moved. The overbraiding process produces closed braids (*braided sleeves* [19]): a yarn runs continuously from the starting point around the mandrel to the end of the component. Flat braided reinforcements (*braided slit tapes*) may be produced from braided sleeves by cutting the braid along the take-up direction [25] and subsequently draping it to a flat shape. Alternatively, flat reinforcements can be achieved by removing the mandrel from the braided sleeve and pressing the reinforcement flat [12, 26]. A special type of reinforcement are *braided tapes*, which are produced by introducing a yarn carrier turning point into the braiding machine (Fig. 2.7). In braided tapes the yarns are continuous, turning at the edge of the preform and running in the reverse direction.

### 2.2.3. Basic equations for the braiding process

The braiding process includes complex mechanical processes such as yarn tension, yarn deformation, yarn interaction, yarn mandrel interaction, and many more. Thus, the quality and uniformity of the resulting preform depends on many interacting parameters, such as yarn type, braiding machine size, and mandrel material. For a comprehensive description of the braiding process, including prediction of braiding angle distribution or possible defects, detailed models are needed. Finite element models [27, 28] provide a realistic model of the process including friction and yarn-yarn interaction, but suffer from the drawback of very high computational cost. Alternatively, improved kinematic models [29, 30] can be used. These models use complex kinematic equations and are typically based on the description of a single yarn, i.e. yarn-to-yarn contact is not considered. Besides these complex prediction models, some basic equations for the braiding process exist that can be used to estimate the process parameters of the overbraiding process.

#### Braiding angle

The braiding angle ( $\theta$ ) is the angle of the braid yarns relative to the braiding direction (Fig. 2.5) and is defined for a cylindrical mandrel guided through the center of the braiding machine [31]:

$$\theta = \tan^{-1} \left( \frac{U_m \omega_c}{2\pi v_m} \right) = \tan^{-1} \left( \frac{d_m \omega_c}{2v_m} \right), \quad (2.1)$$

where  $d_m$  and  $v_m$  are the mandrel diameter and the mandrel take-up speed, respectively, and  $\omega_c$  is the angular velocity of the yarn carriers around the take-up axis. This can be calculated from the horngear rotational speed:

$$\omega_c = \frac{4\pi f_{hg}}{N_{hg}}, \quad (2.2)$$

where  $f_{hg}$  and  $N_{hg}$  are the frequency and the number of the horngears, respectively. Although, strictly, Eq. 2.1 is only applicable to cylindrical cross sections, it can also be used to estimate the braiding angle of other cross sections by replacing the term  $U_m$  with the perimeter of the cross-section [15]. However, it should be noted that the braiding angle varies on a non-circular cross-section, i.e. the equation only provides an average value for the cross section.

## Coverage

The number of yarns in a braiding process is controlled by braiding machine size and the machine configuration. Commonly the braids are required to be *closed*<sup>1</sup> (see Fig. 2.8) with the active yarns in the process for the given mandrel size. This ensures a high fiber volume fraction and high mechanical properties of the braided composite. Thus, a certain number of yarns put a constraint on the mandrel perimeter and vice versa. The requirement of a *closed braid* can be checked by the spacing ( $p$ ) of two adjacent yarns [16]:

$$p = \frac{2\pi d_m}{N_c} \cos(\theta) \quad (2.3)$$

$N_c$  is the number of active yarn carriers, which is twice the number of horn gears for a full configuration on a 4-notch horn gear machine. As the width of a yarn in the braiding process can vary within certain boundaries, three different *braid states* shown in Fig. 2.8 are possible: a *closed* braid ensures a high fiber volume fraction without matrix-rich regions. But if the mandrel dimension changes drastically, the braid may be *open* (gaps between the yarns), or may not fit onto the mandrel (*jammed*) [27]. The status of the braid can be evaluated by comparing the calculated spacing with the maximum and minimum yarn width. The values for maximum and minimum yarn width are dependent on the specific manufacturing conditions and the yarn itself and should be determined experimentally.

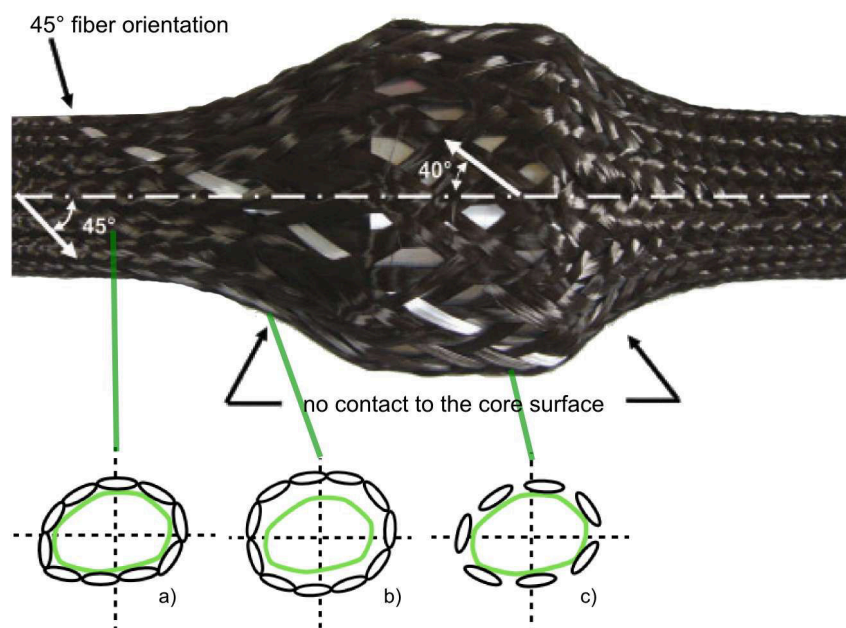


**Fig. 2.8:** Possible braid states on mandrel with changing cross-section: a) closed, b) jammed, and c) open (mandrel image from [27]).

<sup>1</sup>closed braid: the state of a braided preform, where all the yarns lie next to each other without a gap, the mandrel surface is no longer visible after the first ply is braided.

### Areal weight

The areal weight of a biaxial braided preform can be estimated by applying geometrical considerations. Potluri et al. [16] introduced a correction to account for the yarn crimp:

$$FAW = \frac{N_c T (1 + c)}{\pi d_m \cos(\theta)}, \quad (2.4)$$

where  $T$  is the linear density of one yarn and  $c$  is the crimp factor defined in Eq. 2.10. With  $c = 0$ , yarn crimp is neglected. If the thickness of the final part (such as in an RTM process) and the fiber density is known, the fiber volume fraction can be estimated using the fiber areal weight of the braid laminate

$$\varphi_f = \frac{FAW}{\rho_f h}. \quad (2.5)$$

### Preform mass produced per unit time

The preform mass produced within a certain time can be calculated from the fiber areal weight. The mass per unit time is defined as:

$$\dot{m}_{preform} = FAW \pi d_m v_m = \frac{N_c T v_m}{\cos(\theta)} = \frac{N_c T d_m \omega_c}{2 \sin(\theta)} \quad (2.6)$$

For a typical biaxial braid configuration ( $N_c = 176$  carrier braiding machine,  $T = 800$  tex with a  $d_m = 100$  mm mandrel and  $\theta = 30^\circ$  braiding angle) the theoretical fiber mass output is 14.5 kg/h.

#### 2.2.4. Resin infusion

Braided fabrics are either braided directly on a mandrel defining the shape of the part or produced to semi-finished products, which are subsequently draped into the final geometry. In most applications, a liquid composite molding process in conjunction with a polymeric resin is used for impregnation [6]. Both, closed mold RTM and single sided mold resin infusion with flexible tooling processes have been reported [25, 26, 32–34]. Compared to prepreg processes, considerable cost-savings can be achieved by using braided composites in conjunction with resin infusion processes [18, 35].

## 2.3. Yarn architecture of braided composites

Textile composites are hierarchical materials: the material definition has to be described on different length scales which are based on each other: the fibers in the yarns on the *micro-scale*, the internal geometry of yarns and fabric unit cells on the *meso-scale*, and the textile reinforcement on the *macro-scale*. Each scale has its characteristic length, 1-10  $\mu\text{m}$  for the fibers, 1-30 mm for the fabric the unit cell, and centimeters to several meters for the composite structures [15, 36].

It should be noted that the term *meso-scale* is not consistently used in literature. While Lomov et al., and others, [15, 37, 38] define the field of composite unit cell mechanics as *meso-mechanics*, the same type of models are defined as *micro-mechanical* in other publications [39–41]. Ladeveze et al. [42] define single (unidirectional) plies in composite laminates as *meso-scale*. Throughout this thesis, the definition of Lomov et al. [15] given in Table 2.1 will be used.

**Table 2.1.:** Definition for micro-, meso-, and macro-scale used.

<b>micro</b>	scale of fiber and matrix
<b>meso</b>	scale of yarns and fabric unit cells
<b>macro</b>	scale of textile composites and composite structures

The term “yarn architecture” refers to the internal geometry of a textile composite described on the meso-scale. The yarn architecture of a braided composite comprises three components, as shown in Fig. 2.9:

- Yarns, consisting of several thousand filaments impregnated with matrix.
- Matrix pockets, regions of pure matrix in-between the yarns.
- Voids: intra- or inter-yarn voids.

In the following section, an overview about previous works regarding the yarn architecture of textile composites with a focus on woven and braided composites will be given.

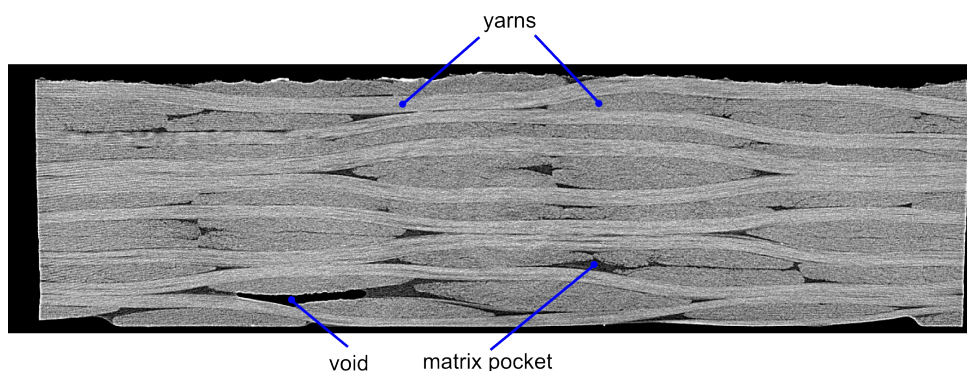


**Fig. 2.9:** Micro-CT scan of the internal geometry of a ( $\pm 45^\circ$ ) biaxial braided composite

### Volume fractions

Volume fractions can be defined according to the components in a textile composite [40]. The total fiber volume fraction ( $\varphi_f$ ) is the volume of fibers in the composites, while yarn volume fraction ( $\varphi_Y$ ) describes the volume of yarns in the composite and can be considered

as a measure of the tightness. Additionally, the packing density ( $p_d$ ) describes the fiber volume fraction inside the yarn. These can be described by the following:

$$\varphi_f = \frac{V_f}{V_{ges}}, \quad (2.7)$$

$$\varphi_Y = \frac{V_Y}{V_{ges}}, \quad (2.8)$$

$$p_d = \frac{V_{f,Yarn}}{V_Y} = \frac{\varphi_f}{\varphi_Y}. \quad (2.9)$$

The total fiber volume fraction can be measured directly from braided composites by using a variety of methods, such as digestion of the matrix [43]. The packing density can be calculated from the yarn area (measured, e.g. from micrographs) if the diameter and the number of filaments is known [33]. Typical values of the packing density have been reported to vary from 60% to 80% [33, 44, 45] for braided composite fiber volume fractions of 50-60%.

### Yarns cross section and yarn path

The shape of the yarns in a textile composite is usually described by using the yarn cross section, cross sectional orientation, and yarn path [46]. Commonly elliptical [40, 47] and lenticular [44, 48, 49] cross sections have been reported in literature. Birkefeld et al. [33] noted that both shapes of cross sections can be seen in micrographs of braided composites. While the braiding yarns typically manifest a mixture of both cross sections, elliptical cross sections dominate the axial yarns of triaxial braids. Byun [44] reports consistent and regular shapes for the axial yarns in a triaxial braid, while the shapes of the braiding yarns were irregular. Byun also described that the cross sections of the braiding yarns located on the surfaces of the specimens tended to flatten. This is in agreement with the observations from [33], where the flattening was considered to be due to the contact of the yarns with the solid mold or the vacuum bag. Ruijter et al. [50, 51] found that the average shape is close to lenticular, by applying an averaging routine to several cross section images obtained from micrographs of a woven fabric. Ruijter noted that the yarn geometry was variable (aspect ratio between 1:8 and 1:15) and that the automated image averaging of cross sections only quantifies the variation, but cannot provide information about the possible reasons (e.g. yarn crossover).

The yarn path can be divided into *crossover regions* (*straight regions, floats*: AB, CD, EF in Fig. 2.10), where the yarns run over/under the crossing yarns, and *undulation regions* (BC, DE in Fig. 2.10), where the yarn runs from the upper to the lower surface and vice versa [40].

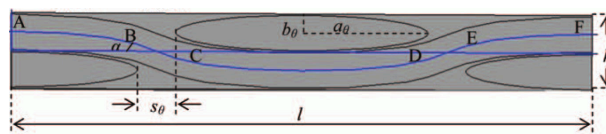


Fig. 2.10: Division of the yarn path [40].

Different parameters are used to characterize the magnitude of undulation: the crimp angle [7] is the maximum out-of-plane angle of the yarn path inside the undulation region; the yarn crimp ratio  $c$  given in Eq. 2.10 is most commonly defined by comparing the crimped yarn length to the length of the fabric [52] (cf. Fig. 2.11). It should be noted, that different definitions for the yarn crimp ratio have been described, e.g. by [53]. Owens et al. [54] use the waviness ratio WR, which is the thickness of the ply divided through the wavelength of the undulation.

$$c = l_{yarn}/l_{fabric} - 1 \quad (2.10)$$

$$WR = h_{ply}/l_{fabric} \quad (2.11)$$

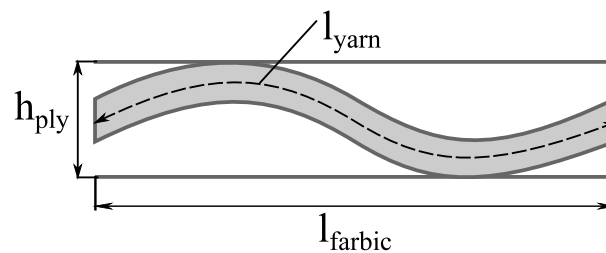


Fig. 2.11: Yarn crimp interval with parameters to calculate crimp measures.

Besides average descriptions of yarn shape and path, considerable effort has been undertaken to describe the variability of the yarn architecture. Vanaerschot et al. [55] presented a stochastic framework based on the period collation method for the analysis of variations in the yarn path and yarn cross sectional parameters based on micro-CT measurements. He defines two genres to calculate systematic and stochastic variations of the yarn path from the geometric properties measured. Dips in the *crossover region* of the yarn path shown in Fig. 2.12 are solely observed in inner plies, which he relates to the mold contact of the outer plies. Vanaerschot concludes that out-of-plane waviness and cross sectional parameters vary systematically, dependent on the relative positions on the yarn path,

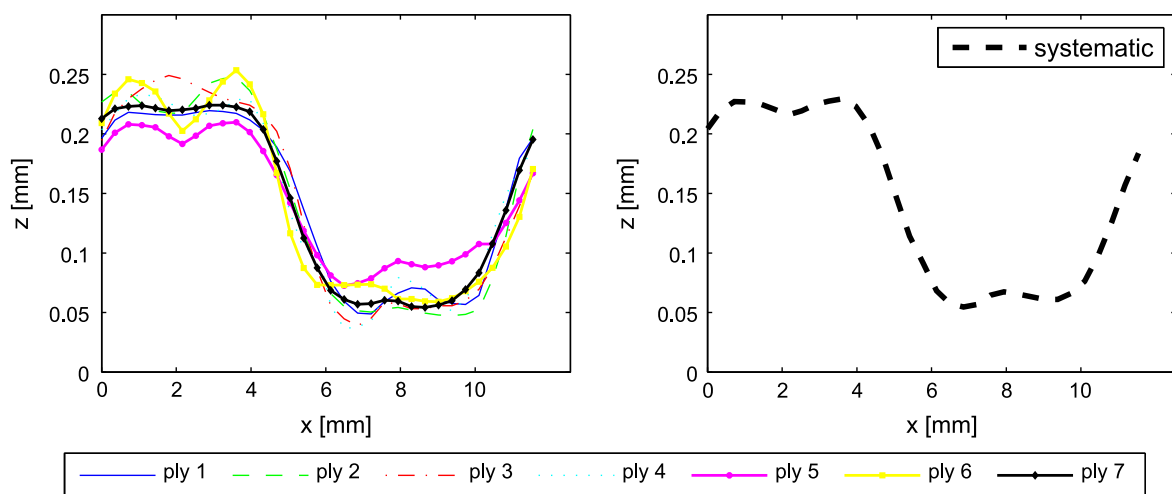


Fig. 2.12: Systematic yarn path representation from [55]

i.e. these values do not depend on the lateral and laminate position. However, this is different for the in-plane variation of the yarn path, but a reliable analysis of this would require a larger specimen. Matveev et al. [49] presented a similar evaluation method for variability of the yarn paths in a  $2 \times 2$  carbon-epoxy woven fabric. It was found that the variations in the out-of-plane coordinates of the yarn path were of the same magnitude as the resolution of the micro-CT images used for evaluation.

## Nesting

Nesting is a phenomenon typically described for textile composite laminates [33, 56–59]. When several plies of a textile are stacked on top of each other to build a laminate and compacted in a vacuum or RTM process, the thickness of the plies in the laminate decreases with increasing number of plies. This effect is described as *nesting* and leads to an increase of the laminate fiber volume fraction (compared to a single ply) and is mainly attributed to two mechanisms [58]:

1. If textile composite plies are stacked on top of each other, the discrete yarn architecture comprises regions with free volume within one ply, which is filled by the adjacent plies. Lomov et al. [56] presented a purely geometrical approach to model this.
2. The dry yarns themselves deform under the compressive force [60] applied to the preform during compaction. This may lead to yarn flattening or yarn cross section deformation (Fig. 2.13).

Main factors	Uncompressed	Compressed
Yarn cross-section deformation		
Yarn flattening		
Yarn bending deformation		
Void / gap condensation		
Nesting		

**Fig. 2.13:** Factors affecting fabric compression [59].

The degree of nesting is given by the nesting factor  $\eta$

$$\eta = \frac{N_{plies} t_{ply}}{h}, \quad (2.12)$$

where  $N_{plies}$  is the number of plies in the laminate, and  $t_{ply}$  and  $h$  are the thickness of a single ply and the laminate, respectively.



Chen [59] conducted compaction experiments with different textile reinforcements and found that the nesting of the laminate reached a stable state for more than 10 plies. The difference in ply thickness in laminates between 10 and 25 plies is negligible. Numerical studies regarding geometric nesting [56] show that closely packed fabrics are less prone to nesting. The tightness  $T$  can be defined as a measure for this

$$T = (d_1 + d_2)/(2p), \quad (2.13)$$

with  $d_1$ ,  $d_2$  being yarn height and width and  $p$  being the yarn spacing. It has also been shown that longer floats (i.e.  $2 \times 2$  compared to  $1 \times 1$ , cf. Fig. 2.7) and shear deformation (braiding angles  $\theta \neq 45^\circ$  for braids), reduce the nesting. This has also been measured experimentally for biaxial and triaxial braided composites with  $30$ - $60^\circ$  braiding angles [33]. In addition to the effects described above, Lomov et al. [56] noted that contradictory results were reported for fabric nesting: Pierce [61] found the ply thickness to increase with increasing number of plies in a plain glass woven fabric.

### 2.3.1. Characterization of the yarn architecture

Different methods can be used to characterize the internal geometry of textile composites, the most common methods are:

- Analytical equations.
- Optical analysis using photomicrographs.
- X-ray micro computer-tomography (micro-CT).
- Finite element process simulation.

Analytical equations can be used to calculate the width of the yarns in the overbraiding process if a closed braid is assumed [7]. The braiding angle can be calculated from the process parameters with Eq. 2.1. When assuming a closed braid, the spacing can be set equal to the yarn width and the yarn height can be calculated by estimating the packing density (Eq. 2.9). The applicability of this method for the prediction of the elastic properties of braided composites has been validated [33, 62].

Desplentere [63] presented a comparison of three methods, namely fabric scanning, optical microscopy and micro-CT for dry glass fabrics. Fabric scan images were acquired with a resolution of  $1200 \text{ dpi}^1$  from the fabric surface using a scanner and evaluated manually using image analysis software. For optical microscopy, small samples ( $15 \times 15 \text{ mm}$ ) were embedded in an epoxy matrix and analyzed under an optical microscope yielding a resolution of  $22 \mu\text{m}$  per pixel. Similar samples were used for the micro-CT scans yielding a comparable resolution ( $25 \mu\text{m}$  voxel<sup>2</sup> size). A rather large variation of yarn-architecture parameters was found for the fabrics investigated. The differences in results from the three methods were found to be not significant at a 95% confidence level.

---

<sup>1</sup>dpi: dots per inch

<sup>2</sup>voxel: three dimensional extension of pixel

Various researchers have used optical microscopy to determine the yarn architecture of textile composites [33, 44, 51]. Birkefeld et al. [33] characterized biaxial and triaxial braided composites with optical microscopy. They noted that an uncertainty was introduced as the measured values had to be transformed using the cut angle if the cut plane was not orthogonal to the yarn path. The cut angle is not known exactly due to uncertainties in the embedding process of the samples. Crookston [64] therefore recommends to section the samples perpendicular to the yarn path.

Ruijter [51] proposed a pixel-averaging technique to obtain the cross section from microsections of plain woven fabric composites. He averaged 80 polylines drawn around the yarn cross sections to calculate the average cross section, but the yarn geometry was rather variable with aspect ratios from 1:8 to 1:15 (Fig. 2.14). Ruijter furthermore notes that no correlation between yarn shape phenomena and the position of the cross section in the textile (e.g. flattened cross sections near the mold) has been done and that the proposed averaging technique suffers from the fact that the conformance of the yarn cross section with the longitudinal yarns may lead to an underestimation of yarn width.



**Fig. 2.14:** Yarn cross section obtained by pixel-averaging: distribution (left) and binary image with 0.5 threshold (right) [51].

Micro-CT measurements provide three-dimensional information about the yarn architecture. Changes in the yarn architecture can be correlated with the relative position and information on the variability can be obtained [63]. The main difficulty of an automated evaluation of the samples is segmentation of yarns and matrix pockets: the contrast between yarns and matrix is low, attributed to the low density difference of fibers and matrix in cured composite samples. Vanaerschot et al. [55] described the necessity of manual input for the image analysis of micro-CT scans to obtain reliable segmentation results. Djukic et al. [65] used different techniques to improve the contrast and found yarn coating prior to impregnation to be the most successful method for carbon/epoxy laminates. In particular, the issue of segmentation of neighboring yarns could be improved using coating.

Besides micrographs and micro-CT, which are both suitable for small samples of approximately 10-50 mm, image analysis techniques provide the possibility to investigate large areas. Recently, some approaches to image analysis of fabric scans have been published. Miene [66] presented an approach to automatically detect fiber angles and defects like gaps for dry fabrics. Thumfart and Tanner [67, 68] presented a sensor based on photometric stereo for similar purposes. As these approaches allow segmentation of the textile, yarn width and spacing can also be measured.

A fully predictive approach to the characterization of the yarn architecture of braided composites is FE braiding simulation [28, 69]. An explicit finite element simulation with truss elements modeling the yarns was conducted, which allows to include the yarn kinematics and friction during yarn contact. The results provide information about the yarn centerlines on the selected mandrel (Fig. 2.15). Pickett [69] introduced a special post-processing technique for the braiding simulation and calculated a full 3D continuum model of the yarns including yarn deformation and compaction. The main challenge for unit cell

simulations has been identified to be the meshing of the small matrix pockets, which was solved by using particle methods to represent the matrix.

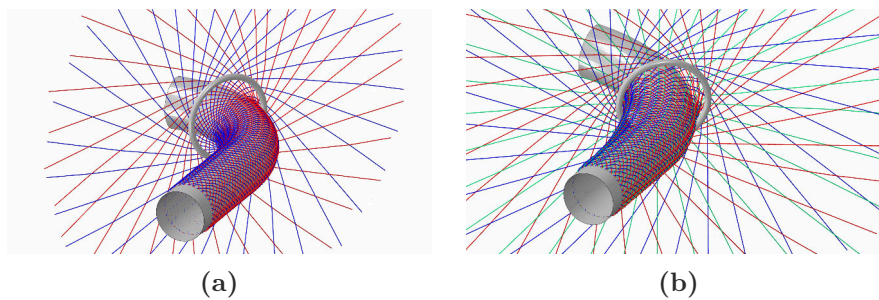


**Fig. 2.15:** Finite element braiding simulation for biaxial (a) and triaxial (b) braid.

### 2.3.2. Geometric modeling

Most geometric models of braided and woven composites use idealized descriptions for yarn paths and yarn cross sections [39, 48, 70, 71]. Several software packages such as WiseTex [46] and TexGen [71] have been developed for geometry modeling of textile composites and offer a general framework for idealized geometric modeling of the yarn architecture of various textile reinforcements.

WiseTex computes the internal geometry of the textile from user input, such as yarn properties and weave patterns, based on an energy minimization algorithm [36]. A combination of elliptical arcs and a 5th-order polynomial function represents the yarn path in the undulation interval. The cross section of the yarns can be chosen either circular, elliptical or lenticular. WiseTex serves various interfaces, to Mori-Tanaka micromechanics (TexComp [72]), permeability modeling (FlowTex [73]), and finite element (FETex) software. Recently, a command-line interface and an open XML-dataformat have been implemented in WiseTex [74]. This allows for straightforward integration of WiseTex geometry models into simulations realized with 3rd-party software.

TexGen [75] is an open-source software package for textile modeling, providing a Python scripting interface and various export options to Abaqus [76] FE software. TexGen uses spline interpolation for the yarn path in-between the user-defined master-nodes and provides several possible yarn cross sections including elliptical and lenticular [77]. The models from TexGen can be exported to third-party software as common geometric descriptions (*IGES*, *STEP*) or as a tetrahedral or voxel continuum element mesh to the FE-software Abaqus [38].

Idealized geometric models are rather simple to implement into generic software, however when a tight yarn architecture (high yarn volume fraction,  $\varphi_Y$ ) is modeled and used for finite element analysis, one faces the problem of yarn volume interpenetration as shown in Fig. 2.16 [24]. Finite element meshing with continuum elements requires the geometries to be consistent, which means that yarn volumes cannot overlap each other. Potluri et al. presented an analytical approach, which overcame this problem by using the same functions for yarn path and yarn cross section, but the geometry is limited to plain ( $1 \times 1$ ) fabrics [62].

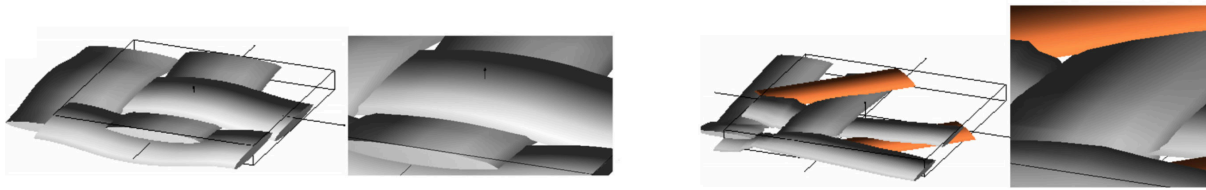


**Fig. 2.16:** Volume interpenetration for biaxial and triaxial braids [24]

Several researchers proposed improvements to overcome the problem of volume interpenetration by using analytical considerations or finite element contact analysis. Sherburn [77] used an idealized geometry of a 4-harness satin weave modeled with TexGen as a basis, refined the yarn path definition, and changed the cross sectional shape and orientation at the crossover points of the fabric. The improved geometry has been validated against micro-CT measurements and provided good correlation of yarn path, cross sectional shape, and rotation. In a second publication an automated algorithm for correction of volume penetration based on an FE contact analysis using plate elements was proposed [78]. The approach has been implemented in TexGen and led to good improvements regarding volume penetration for a 2D textile. On the other hand, the results for a 3D orthogonal weave were less accurate, still showing interpenetrations.

Lomov et al. [24] also presented an approach for interpenetration removal implemented into the MeshTex [79] software. The unit cell is divided into several sub-problems, each representing one contact pair, the yarn volumes are moved such that interpenetration is not occurring and beam elements are defined between the surfaces. The yarns are defined to be volume-constant ( $\nu = 0.5$ ) and pressed together to create tight, non-interpenetrating volumes. In the last step, the yarns are re-assembled into the complete unit cell.

In addition to idealized geometrical models with the option of volume-interpenetration correction as described above, analytical approaches for detailed geometric modeling of textile composites exist. Hivet and Boisse presented an analytical approach for consistent geometric modeling of fabric unit cells [80]. The model ensures a realistic contact surface without interpenetration of the yarns, which is achieved by changing the cross-section shape of the yarn along the yarn path. A CAD-preprocessor was used for the creation of the fabric unit cell geometry and export to a finite element code resulting in a high-quality regular mesh of the yarns. However, the model was applied to dry fabric unit cell simulations, which do not face the problem of matrix-meshing in the thin crossover regions.

Different methods using finite element analysis for modeling of compaction have been presented in the literature. Grail et al. presented a geometrical model with consistent surface meshes, which do not suffer from volume penetration or free volumes (voids) [81]. Meshes from a previous preforming simulation were used as an input and a subsequent compaction simulation with multi-layer unit cells yielded realistic yarn volume fractions within the unit cell. Hsu and Cheng presented an approach to geometry creation using multi-step FE-analysis [82]. The method included FE compaction simulation, re-construction of the geometry, and removal of geometric inconsistencies. Stig and Hallström recently presented a new FE-based approach for realistic geometric modeling of 3D woven textiles [83]. Based on a TexGen geometry, yarns were modeled as inflatable tubes

in an explicit FE analysis. The validation of the calculated yarn geometry with micro-CT scans shows good accordance. The model combines advantages of a few input parameters and is generic and extendable to other types of textiles.

## 2.4. Mechanical testing of braided composites

Mechanical characterization of braided composites is an important method for both understanding the complex and anisotropic material behavior and for creating a basis for the validation of predictions. Common standards for composite materials such as ASTM D3039 (plain tension, [84]) or ASTM D6641 (plain compression, [85]) were developed primarily for UD, angle-ply, or quasi-isotropic laminates. Special considerations regarding coupon geometry, measuring systems, and test procedures for textile composites are given in ASTM D6856 [85]. Among other points mentioned in [85], recommendations regarding specimen width and strain gauge size are given; the specimen width is recommended to be larger than two times the width of the representative unit cell marked in Fig. 2.6 to ensure a representative constitutive behavior. The strain gauge width and length are recommended to be, at minimum, equal to the unit cell dimensions – as the strain field on textile composites varies due to the textile architecture [86]. The recommendations are based on experimental campaigns on different triaxial braided composites that were carried out by Masters et al. [86–88].

### 2.4.1. Elastic behavior

Birkefeld et al. presented an experimental test campaign comprising biaxial and triaxial braided carbon/epoxy composites with  $\theta = 30^\circ, 45^\circ$ , and  $55^\circ$  braiding angles [33]. The triaxial braided composites exhibit a higher stiffness in both axial and transverse direction when compared to biaxial braids with the same braiding angle. The modulus in the axial direction was reported to decrease with the braiding angle. This is in accordance with the results presented by Charlebois et al. [25] based on tensile and compressive experiments of glass/epoxy biaxial braided composites with  $\theta = 35^\circ, 45^\circ$ , and  $50^\circ$  braiding angles. The shear behavior of the braided composites was also evaluated; the Iosipescu shear testing method used was found unsuitable due to the high stiffness and strength of the braided composites.

### 2.4.2. Nonlinear and failure behavior

Several publications have reported on the nonlinear and failure behavior of braided composites. During the early 90s, many experimental studies were published concerning triaxial braided composites [87–91]. Minguet and Gunther [92] compared the response of triaxial braided composites to tape laminates with equivalent material and layup. It was found that transverse tensional strength and shear strength was lower for the braids, which was attributed to the braid yarn undulation. Open-hole and filled-hole tensile strength can be increased with the braids, but all compressive properties were higher for the equivalent tape laminates.

A study on the mechanical behavior of biaxial braided composites was conducted by Tsai et al. [32]. They used pressurized cylinders with a braiding angle of  $45^\circ$  with biaxial and triaxial braided reinforcements of graphite and glass fibers. The hoop strength of the cylinders increased by 25% for graphite compared to glass fibers and triaxial braids were reported to have a lower hoop strength, which was attributed to the lower volume fraction of circumferential (braid) fibers in the triaxial braid.

An extensive study on glass/epoxy biaxial braids was conducted by Harte and Fleck, characterizing braided tubes with different braiding angles in tension, compression, and shear [93, 94]. The tensile and compressive strength increased with decreasing braiding angles, while shear strength decreased. This was attributed to the increased influence of the matrix material at higher braiding angles, where the angle between fibers and load direction is higher. The influence of the braiding angle was also observed in the stress-strain behavior, which was linear for small braiding angles and strongly nonlinear at higher angles (Fig. 2.17).

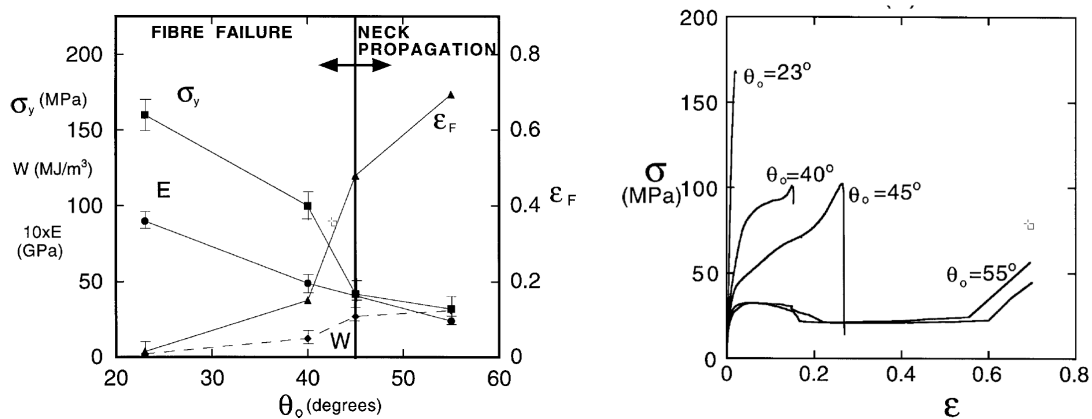


Fig. 2.17: Failure chart (left) and stress strain curves (right) measured from biaxial braided tubes [93].

Similar results have been obtained for glass/epoxy biaxial braids by using flat coupons [25]; a linear increase of strength with the braiding angle was reported in tension, while the compressive strength was lowest at a braiding angle of  $45^\circ$ . Further studies regarding strength at low braiding angles have been carried out by Huang and Ramakrishna [48]: a specimen with continuous yarns was studied (braided sleeves Section 2.2.2) and showed that the longitudinal strength increases by 50% for a braiding angle of  $15^\circ$  compared to  $25^\circ$ . While the stress-strain response was linear for small braiding angles, major nonlinearities before final failure were observed for braiding angles higher than  $25^\circ$ .

### Failure modes

The failure modes described for biaxial braided composites follow the same mechanics as those occurring in UD composites [95]. However, the internal structure of the braided composite triggers different failure modes than the ones observed in UD composites.

The micromechanical events during failure in yarns and matrix of textile composites are described by Cox et al. [7, 91]: for tensile loads, micro-cracking in the transverse oriented tows (if present) is the first failure event, followed by fiber (tow) rupture, which is the dominant failure mechanism. Fiber strength is reduced compared to UD materials

due to the uneven load-distribution within an undulated tow. If the load is not aligned with one of the fiber directions, shear failure or transverse cracking can become dominant. Compressive failure may involve several mechanisms such as shear micro-cracking, inter-ply and intra-ply delamination, and kink-band formation within the tows (Fig. 2.18). Shear failure within the tows starts with arrays of microcracks involving considerable micro-plasticity and propagates to larger matrix cracks with the damaged material broken into pieces.

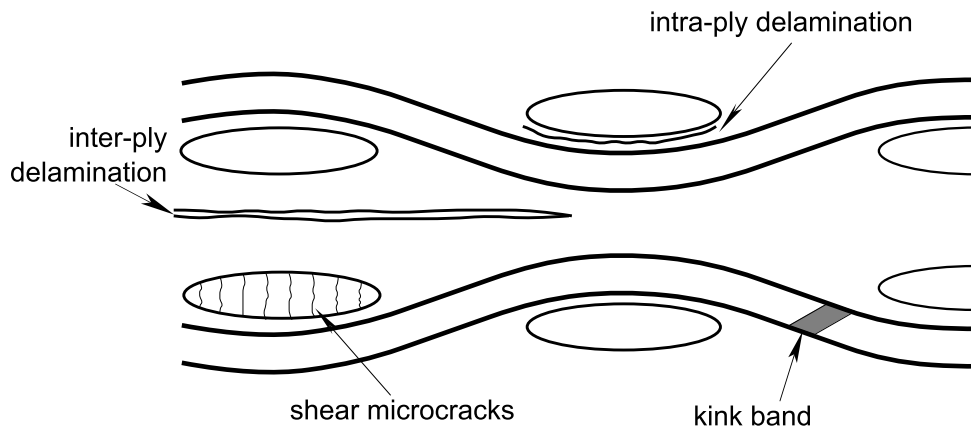


Fig. 2.18: Failure mechanisms in compression [7]

Harte and Fleck [93, 94] identified four failure modes for glass/epoxy braided tubes: fiber failure and neck propagation in tension, fiber microbuckling and diamond shaped buckling in compression and shear. There was a strong dependence of the failure mode on load and braiding angle. The results are summarized in a multi-axial failure mechanism map, presented in Fig. 2.19.

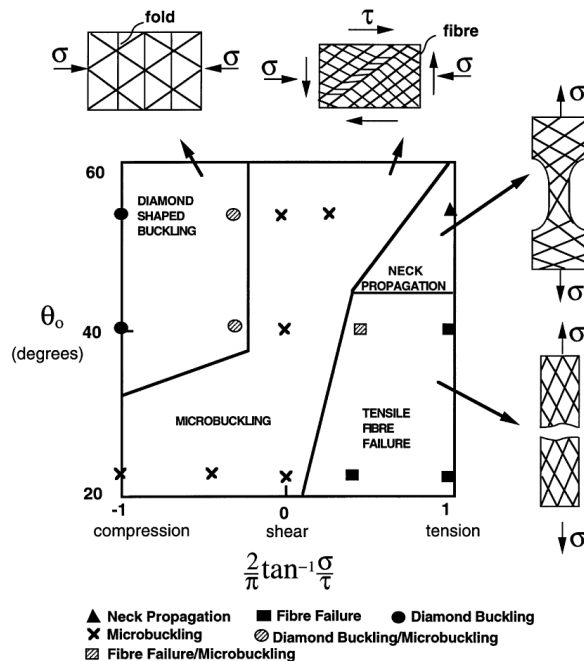


Fig. 2.19: Failure map for biaxial braided tubes under combined loads [94].

Fouinneteau [12] further stated that fiber failure in tension and compression and shear induced fiber/matrix debonding occurs as in-plane failure modes of biaxial braided composites. In addition, inter- or intra-laminar delamination, as shown in Fig. 2.18, may occur due to tow-straightening.

### Cutting of the specimen and coupon geometry

The internal structure of most braided composites is of similar length scales as common coupon dimensions for mechanical characterization [84, 85], which draws attention to the influence of coupon size [96]. In addition, the overbraiding process yields a continuous fiber network on the mandrel, i.e. a fiber (yarn) runs continuously from the beginning to the end of the mandrel. This is not the case, if braided coupons are cut from composite panels. The influence of coupon dimension and the effect of continuous yarns has been investigated by various researchers.

While the elastic properties of braids are not influenced by the continuity of the fibers, the strength of *uncut* coupons may exceed that of *cut* configuration coupons (see Fig. 2.20). The effect becomes particularly dominant for small braiding angles: more than 100% strength increase was reported by [70] for ( $\pm 17^\circ$ ) and ( $\pm 15^\circ$ ) biaxial braids, while moderate strength increase of 27.5% and 13.3% is measured by [34] for ( $\pm 25^\circ$ ) and ( $\pm 45^\circ$ ) biaxial braids, respectively.

Additionally, the failure mode of the specimen can change between cut and uncut configuration: while cracks are forming in the center of the specimen in the uncut configuration, edge cracks initiate the failure in the cut configuration [97].

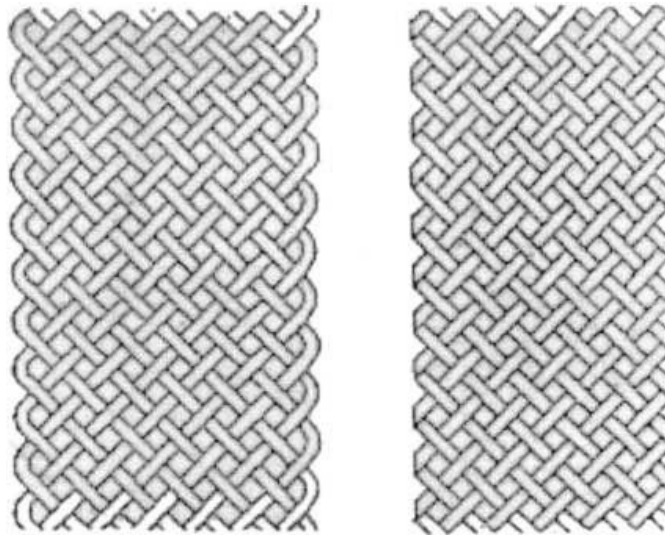


**Fig. 2.20:** Uncut (left) and cut (right) edge configuration of braided composites [70].

Kelkar and Whitcomb [26] characterized flattened braided sleeves and reported strong braiding angle variability to be a consequence of process inaccuracy during the flattening of braided tubes. It was possible to improve the braid angle variation by using “*slit tapes*”, which are braided on a circular mandrel and slit along the braiding direction.

Van den Berg [96] investigated the influence of the coupon width on the mechanical properties of biaxial carbon/epoxy braids. He found the Young’s modulus to be insen-



sitive, but the yield and ultimate stress were smaller, if the width of the coupon was decreased to less than twice the unit cell width. He attributed this fact to the failure mode, which was purely matrix-dominated in the case the coupon width was smaller the width of one unit cell. In contrast, the failure mode was fiber-dominated for larger coupon widths.

### **Damage initiation and progression**

A general methodology for the experimental characterization of damage initiation and progression in textile composites was published by Lomov et al. [98]. Different techniques such as acoustic emission, full-field strain measurement via digital image correlation (DIC), and postmortem micrograph investigation were proposed to study the occurrence and pattern of micro-cracking within different loading stages.

Littell et al. [99] used DIC techniques to obtain information about local deformation and failure mechanisms of triaxial braided composites. It was stated that DIC provides information about local failure initiation mechanisms in different yarn orientations and in-situ yarn properties could be measured by local evaluation of the strain field.

## **2.5. Textile composites constitutive behavior prediction**

A variety of analytical and numerical models exist to predict the constitutive behavior of textile composites. The models can be divided into three major groups:

1. Analytical methods, e.g., Iso-Strain/Stress, Mori-Tanaka, and methods of cells.
2. CLT-Methods: classical laminate theory is adapted to model the textile reinforcement.
3. Finite element unit cell models: the yarn architecture is modeled in a unit cell.

The models require different depth of input and numerical effort and offer different levels of detail regarding the predicted information: analytical models can include detailed geometric information about the yarn-architecture and provide a very efficient solution. However, such models often suffer problems in correctly representing the stress and strain fields in yarns and matrix, which is important for failure and damage modeling [100]. FE unit cell models provide detailed stress and strain fields and can include various constitutive models for plasticity and damage in matrix and yarns. However, these models require a considerable number of input properties, can be very complex to implement and require high computational cost [101]. Computational efficiency is the biggest advantage of the CLT-models, which enable ad-hoc implementation into most FE packages and can be used to analyze structural problems with existing FE methods [12]. The following section gives an overview of models for textile composite constitutive behavior prediction, with a focus on models for braided composites.

### 2.5.1. Analytical models

The first analytical models for woven composites were presented by Ishikawa and Chou in the early 1980s [102–105]. Three methods, namely the *Mosaic Model*, *Fiber Undulation Model*, and *Bridging Model* (Fig. 2.21) were developed. The mosaic model neglected undulation, and used cross-ply laminates assembled under the assumption of iso-strain and iso-stress to model woven fabrics. The *fiber undulation model* [105] calculates the stiffness knockdown due to yarn crimp in a woven fabric by modeling the out-of-plane waviness of the yarn as an assemblage of various slices of stacked matrix and UD off-axis laminates. The local stiffness of the yarn is transformed into the global coordinate system, one slice of yarn and matrix is assembled using iso-strain condition and the slices are assembled by applying the iso-stress condition. The *bridging model* can be described as a combination of mosaic and fiber undulation models: a woven fabric is sub-divided into regions of straight and undulating yarns and assembled by a combination of iso-stress and iso-strain conditions [102].

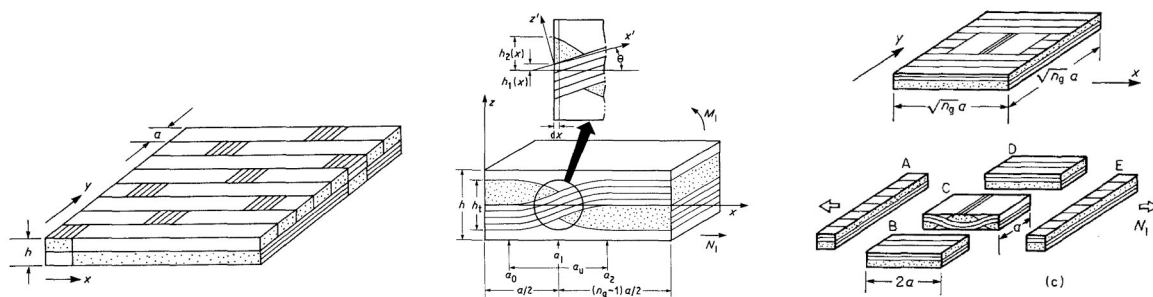


Fig. 2.21: Mosaic, fiber undulation and bridging model [102]

Many extensions and enhancements of Ishikawa’s and Chou’s models have subsequently been developed. Naik and Shembekar [106] extended the fiber undulation model to 2D using the Parallel-Series or Series-Parallel models. An iso-stress condition is used along the loading direction, while iso-strain is used in the transverse direction: the models are distinguished by the order of the homogenization. The Parallel-Series model has been noted to give better results for the elastic constants of woven fabrics.

A general model, namely the “orientation averaging” model, was proposed in [107–109]. The model treats the textile composite as an assembly of small volumes of unidirectional composites, weighted by their volume fraction and assembled under iso-stress or iso-strain assumption. Cox and Dadkhah [91, 110] used this method including a correction for stiffness knockdown due to fiber undulation and obtained good results for 3D woven and triaxial braided composites.

Various extensions of iso-strain / iso-stress methods have been applied to braided composites. Most models include a more detailed geometric description [44], and some are also extended to failure prediction [70]. An extensive overview and comparison of these models has recently been given by Hallal et al. [111].

Another approach to homogenization of textile composites using a Mori-Tanaka method has been proposed by Huysman et al. [72, 112]. The yarns in a fabric unit cell were subdivided into smaller segments, with the segments characterized by fiber volume fraction, orientation, cross section, and local curvature. The segments are then replaced with

ellipsoids of identical cross sectional shape and the length correlated to the curvature. Eshelby's equivalent inclusion principle and the Mori-Tanka scheme are used for the homogenization. The method was implemented into the TexComp software, which is part of the WiseTex package [46]. Good predictions for the elastic constants of woven and braided composites have been obtained with the method [33, 63, 112].

Recently, the *Methods of Cells* [113] has been applied to textile composites. Prodromou et al. presented an approach using the geometric description of WiseTex and *Methods of Cells* for the prediction of stiffness and strength [100]. It was outlined that the model is computationally very efficient and general. The results were compared to conventional methods and experiments and a promising correlation was achieved.

### 2.5.2. Classical laminate theory methods

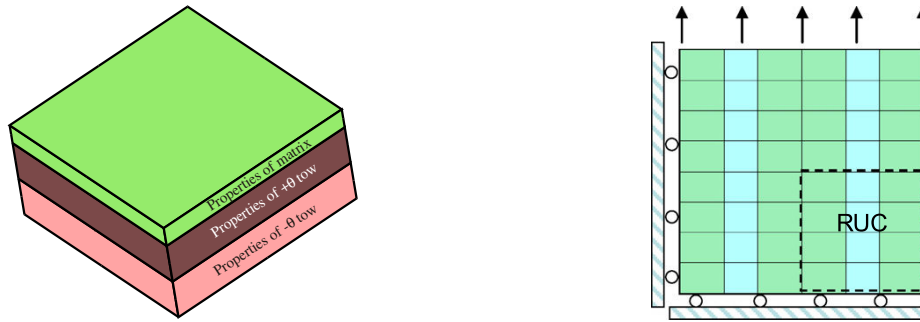
Classical laminate theory (CLT) was primarily designed for UD composites but can be applied to laminar textile composites [7] using equivalent tape laminates to represent the directionality of the reinforcement.

Smith and Swanson used the strain in the axial and braid fiber direction for failure prediction of triaxial braided composites [90, 114–116]. The global strain was transformed into the fiber directions and a maximum strain criterion in the yarn direction was used to predict the failure under various loads. The criterion was in good correlation with experimental data when the failure strain values for axial and braid yarns were obtained by correlation to selected test results.

Johnson et al. [117] presented a constitutive model for the prediction of nonlinearities and damage in woven composites. A continuum damage mechanics approach is used in conjunction with a one-dimensional plasticity law under shear. The approach was implemented in the explicit FE code PAM-Crash. Later, a similar model for braided composites was implemented into PAM-Crash and extended in order to account for tow-straightening and delamination [12]. Comparison to experimental results on coupon tests and sub-structures showed promising correlation, but the coupling between inter- and intra-ply damage was not considered due to the lack of experimental data [12].

Goyal et al. [118] presented an equivalent tape laminate model for biaxial braided composites. The laminate comprises one ply for every yarn direction and an additional matrix ply (Fig. 2.22a). Hill's yield criterion is used in yarn and matrix plies to predict nonlinearities prior to final failure. Comparison of the equivalent tape laminate to 3D continuum unit cell results show only minor deviations; this shows the potential of the equivalent tape laminate modeling approach. The correlation to experiments was good for both methods, but the equivalent tape laminates were stiffer than the unit cells as fiber undulation was not considered.

Zebdi et al. [119] presented an inverse modeling approach based on CLT. Equations were given to calculate the equivalent properties of the single plies within a virtual  $(\pm\theta)_s$  laminate based on the experimental results of biaxial braided composites. The calculated properties of the virtual plies differ significantly from those obtained for UD plies. The applicability of the approach to braids of various braiding angles and woven fabrics is successfully demonstrated.



(a) Equivalent tape laminate including matrix layer [118]. (b) Sub-cell approach for triaxial braided composites [120].

Another approach to modeling braided composites using CLT are the so-called sub-cell models [120–122]. These represent the textile architecture macroscopically using sub-cells with different layups in FE calculations (Fig. 2.22b). Usually, two types of sub-cells, comprising and not comprising axial yarns, are distinguished for triaxial braided composites.

### 2.5.3. Finite element unit cell modeling

FE unit cell modeling is commonly used for prediction of the elastic and nonlinear behavior of textile composites. The basis for FE unit cell modeling is a suitable geometric description of the yarn architecture of a representative unit cell (RUC). The geometry of yarn and matrix pockets is imported into FE software, meshed, and solved using periodic boundary conditions. The models typically require high effort for model generation and increased computational cost [101], which makes these models unattractive for macroscopic modeling. However, FE unit cell models provide a high level of detail in stress and strain fields inside yarns and matrix, making them suitable for the prediction of failure and damage inside textile composites. Lomov et al. [123] highlighted their potential by comparing the strain field calculated by FE unit cell models to experimental results obtained by shearography. The FE unit cell solution could represent the features of the measured strain field such as tension-bending coupling of single ply woven fabrics when loaded along one yarn. The calculated strain values have been reported very close to the measured values.

In an earlier publication, Lomov et al. [24] summarized the relevant modeling stages to be considered for meso-FE unit cell modeling:

1. Build a model of the yarn architecture.
2. Transfer the geometry to a volume representation .
3. Correction of volume interpenetration before meshing.
4. Meshing yarns and matrix.
5. Assignment of local material properties.

6. Definition of the smallest possible unit cell size and application of periodic boundary conditions.
7. Homogenization procedure.
8. Damage initiation modeling.
9. Damage propagation modeling.

The modeling stages described in [24] mainly refer to full 3D continuum element unit cells. Depending on the FE unit cell modeling technique used and on the aim of modeling, some points may be added or skipped; e.g. some of the models do not require a correction of volume interpenetration [124, 125] and others use a failure criterion for prediction of the bearable stress, which does not include damage propagation [47, 62]. A classification of the different FE unit cell modeling techniques may be given by the meshing technique (i.e. the type of finite elements) used. The following section gives a short overview of the available approaches to FE unit cell modeling.

The most common technique for finite element unit cell modeling is 3D continuum element modeling. Both yarns and matrix pockets are meshed with tetrahedral or hexahedral volume elements. As the yarn and the matrix domain have to be meshed with opposing nodes, a consistent geometry description is needed for continuum unit cells. As idealized geometric models are likely to provide penetrating volume descriptions for the yarns, several methods for interpenetration correction have been proposed [24, 77, 78]. For high fiber volume fractions resulting in high yarn volume fractions  $\varphi_Y$ , the matrix pockets in the RUCs become very small, which requires small and often distorted elements of coarse quality [37, 101]. To overcome this problem, models with decreased yarn volume fractions and adapted packing density are sometimes used to achieve a realistic total fiber volume fraction [45]. Alternative techniques including compaction simulation have been proposed to obtain models with realistic yarn volume fraction [81, 82], but these require an additional independent simulation step, which highly increases the computational cost.

Despite the complex mesh generation, continuum element unit cells have the advantage that common constitutive models can be used to describe damage initiation and damage progression in the yarns. Early unit cell computations [79, 126] used simple damage models, instantly reducing the stiffness to a value near zero after damage initiation. Zako et al. [79] compared the results of unit cell simulations of a single ply woven fabric to experiments and found that the transverse cracking within the yarns could be predicted in good correlation to the experimental results.

Ivanov et al. [45] used the physically-based Puck criterion [127] to predict damage initiation in the yarns and a continuum damage mechanics approach for damage progression. The local damage mechanics – i.e. relating the progression of damage to local values – can result in physically unrealistic predictions of damage progression. Thus, a non-local one-parameter damage evolution law based on the average shear stress in the yarn was proposed. The unit cell calculations were compared to experimental results and damage initiation as well as stiffness degradation were in good agreement.

Carvalho et al. [47] recently presented a study on the nonlinear behavior of woven fabrics, including a yarn failure criterion for failure onset, debonding between tows and matrix, and a plasticity criterion in the matrix. The predicted compressive strength

was highly dependent on the out-of-plane boundary conditions used. Considering matrix plasticity and tow/matrix debonding prior to final failure could improve the accuracy of the numerical results.

For biaxial braids, severe nonlinearity prior to final failure was described by Goyal [39]. An anisotropic Hill plasticity criterion was used to model the nonlinear behavior of the yarns, and hardening was defined by using a single master curve. The parameters for the yield criterion and hardening were obtained by fiber/matrix unit cell simulations under distinct load cases. Non-linearity of the braids prior to failure was predicted by full 3D unit cell simulations and compared to experiments for different braiding angles. The predictions were in excellent agreement for glass/epoxy braids, while reasonable agreement was obtained for the carbon/epoxy braids [118].

An alternative technique using 3D continuum elements is voxel meshing. Equivalent to micro-CT scans, the volume of the unit cell is sub-divided into cuboids of equal size, which are labeled **volumetric pixels**. The volume mesh is not consistent to the geometry, i.e. yarn and matrix volumes are solely defined by the material properties assigned to an element (cf. Fig. 2.23). Kim and Swan [128, 129] presented techniques for textile composite unit cell voxel meshing and proposed a refinement technique based on the virtual strain energy to improve the accuracy of the voxel meshes along material boundaries. Voxel meshing was found to be able to rapidly and automatically generate unit cell models maintaining excellent shape and aspect ratio of the elements under mesh refinement, which is not the case for tetrahedral meshes. It was concluded that for voxel-based meshing, a tradeoff exists between a higher computational expense of the models and the reduced time spend on manual mesh generation [128]. Crookston compared conformal tetrahedral and voxel meshing techniques for woven fabrics [38]. The conformal technique was found to converge faster in terms of fiber volume fraction and stiffness; however tight textiles with touching yarn boundaries are unlikely to be successfully meshed by conformal techniques. Thus, voxel meshing may be an appropriate technique for such tight textiles. Recently, Potter [37] presented a new voxel meshing algorithm including surface smoothing, which makes it possible to model tow/matrix debonding in the unit cell simulations.

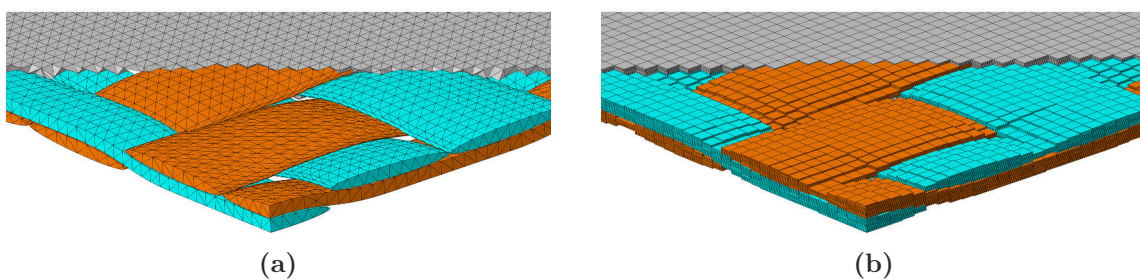


**Fig. 2.23:** Comparison of continuum (a) and voxel (b) mesh for ( $\pm 45^\circ$ ) biaxial braids [130].

The Binary Model, a reduced approach for textile composites finite element modeling, was presented by Cox et al. [125]. The model uses truss elements for the yarns, which are embedded in continuum elements: this represents a separation of the material properties into the two types of elements. While the longitudinal properties of the yarns are represented by the truss elements, the transverse and shear properties of the yarns, as well as the isotropic properties of the matrix, are smeared in the *effective medium* continuum

elements. Elastic and failure models related to the binary model representation and the implementation of the model in Abaqus for 2D and 3D woven composites were presented. In a subsequent publication, an improved constitutive model was proposed [131], which takes into account the effect of volume doubling and allows to calibrate the constitutive model on the basis of UD experiments. The Binary Model predictions were reported to give excellent correlation for the elastic constants of 3D woven composites. Further models for tensile or compressive fiber failure were provided, including the effect of tow misalignment and uneven load distribution.

Yang and Cox [132, 133] presented a further extension of the model by introducing a multi-point-constraint coupling between truss and continuum elements and an averaging technique for the strains in the effective medium. The strain field inside the effective medium is mesh dependent, as the mesh size introduces an averaging of the theoretically divergent strain at the point where the truss is embedded into the effective medium. Yang and Cox presented a strain averaging technique and demonstrated that the strains are mesh-independent when averaged over volumes with dimensions greater than half the width of a tow. It was also noted that these averaged strains were favorable for failure analysis, as the failure events inside a composite are connected to stresses or strains averaged over a distinct length scale [134, 135]. In a later publication, the applicability of the strain averaging approach for failure predictions was shown, including the comparison with experiments [133]. The material parameters used for the two failure modes were obtained from calibration of uniaxial experiments, and the strength of a triaxial braided composite could, in most load cases, be predicted within 10% of the experimental value.

Flores et al. [136] included a plasticity law into the Binary Model to account for matrix nonlinearity prior to final failure. A Drucker-Prager plasticity criterion with fully associated flow rule and perfectly plastic deformation was used in the effective medium. The material parameters were obtained by calibration of the model to uniaxial tests. Comparison of the model predictions to open-hole tension experiments (see Fig. 2.24) show that the Drucker-Prager criterion is able to accurately model the matrix nonlinearity and that gauge-averaged stresses are suitable for predicting the failure stress measured in the experiments.

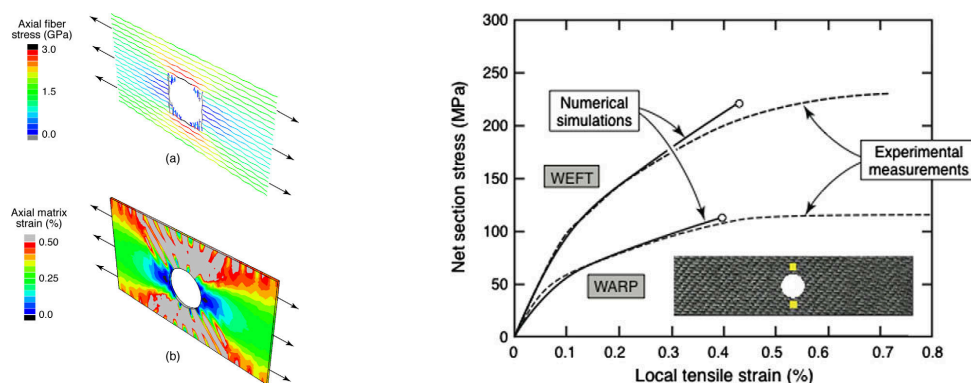
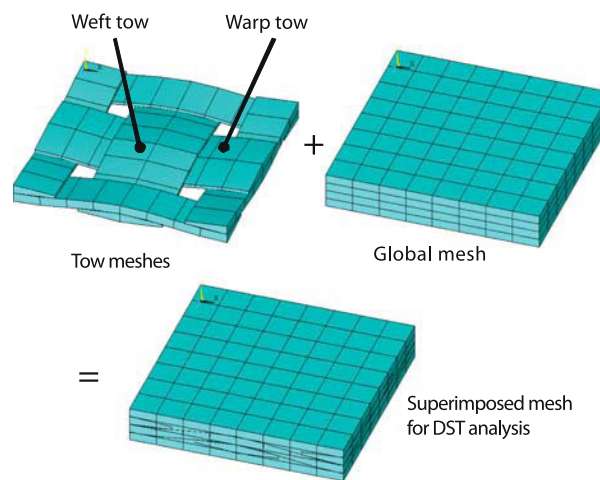


Fig. 2.24: Open-hole tension simulations using the Binary Model [136].

Blacklock [137] presented an approach for the generation of virtual textile specimens, using statistical data from micro-computed tomography and used the binary model to create a virtual specimen.

Jiang et al. [124] proposed a domain-superposition technique (DST), which can be considered as an extension to the binary model. But in contrast to the binary model, the DST embeds continuum yarns in the continuum matrix elements (Fig. 2.25). The coupling uses multi-point-constraints that relate the displacements of the yarn nodes to the displacement of the matrix *host* element. This is similar to the *embedded elements* function described by Yang and Cox [132]. The stiffness of the tow was adjusted by Jiang et al. by subtracting the matrix stiffness, which is required due to the doubling of volume. The error in stiffness and stress fields between DST and conventional FE analysis was reported to be less than 5%, while a significant reduction of model DOF can be achieved using DST. This was confirmed by Tabatabaei et al. [138], who performed a study on the DST and found the stress fields in good accordance with traditional continuum meshes.



**Fig. 2.25:** Domain superposition technique: overlay of meshes from tow and matrix [124].

An alternative reduced FE unit cell modeling technique for 2D woven and braided composites was proposed by Gager et al. [101, 139, 140]. The technique uses shell elements to model yarns and matrix within the unit cell (Fig. 2.26). The shell elements are connected with multi-point-constraints and nonlinear material models including damage and plastic deformation [141] are used for matrix pockets and yarns. The model comprises far fewer DOF compared to a conventional continuum model and thus allows a significant reduction of computational cost [140].

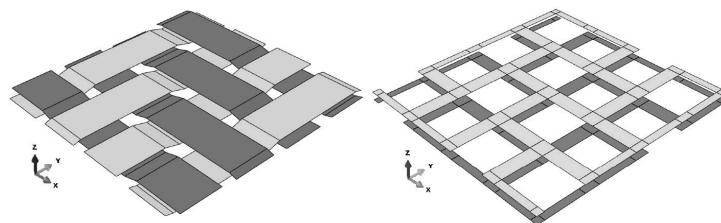


**Fig. 2.26:** Shell element unit cell [101].



## 2.6. Multi-scale modeling and homogenization

Multi-scale modeling is based on the principle of homogenization of properties from a smaller (commonly *micro*) scale to a larger (commonly *macro*) scale [142]. If a material has heterogeneous material properties  $\mathbf{C}(\mathbf{x})$  on the microscopic scale, the microscopic stress and strain fields  $\boldsymbol{\sigma}(\mathbf{x})$  and  $\boldsymbol{\varepsilon}(\mathbf{x})$  are also heterogeneous under a given boundary condition. For a macroscopic problem the microscopic variations of the strain field are not of interest and thus stress and strain are homogenized to macroscopic properties  $(\langle \boldsymbol{\sigma} \rangle, \langle \boldsymbol{\varepsilon} \rangle)$ . The effect of the changing microstructure can therefore be described by a change of the macroscopic material constitutive tensor  $\mathbf{C}^*$  (Fig. 2.27).

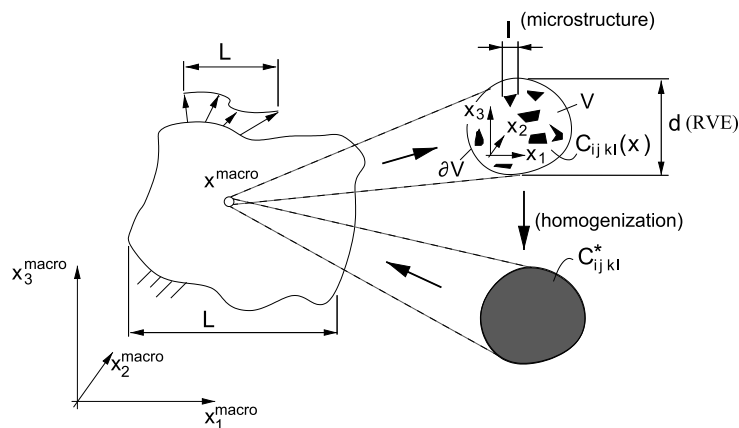


Fig. 2.27: Homogenization and characteristic length [142].

In this section, a short overview of homogenization and boundary conditions will be given.

### 2.6.1. Averaging and effective properties

A macroscopic material point is related to a microscopic volume with fluctuating stress and strain fields. The mechanical state of the macroscopic point is related to the microscopic field through volume averaging:

$$\langle \boldsymbol{\sigma} \rangle = \frac{1}{V} \int_V \boldsymbol{\sigma}(\mathbf{x}) dV \quad \langle \boldsymbol{\varepsilon} \rangle = \frac{1}{V} \int_V \boldsymbol{\varepsilon}(\mathbf{x}) dV. \quad (2.14)$$

The macroscopic constitutive equation,

$$\langle \boldsymbol{\sigma} \rangle = \mathbf{C}^* \cdot \langle \boldsymbol{\varepsilon} \rangle \quad (2.15)$$

can be used to calculate the effective macroscopic constitutive tensor  $\mathbf{C}^*$ , if macroscopic stress and strain are known [142]. For the calculation of a full constitutive tensor, six independent load cases in an FE unit cell are required [40].

### 2.6.2. Representative volume element / repeating unit cell

The difference in terminology between RVE and RUC is discussed in further detail in Appendix C, only a short description will be provided here. For a material with a statistically distributed microstructure, the concept of representative volume elements (RVE) is used: the subvolume investigated needs to be large enough that the volume fractions and the statistical distribution from the complete material can be reproduced. The repeating unit cell (RUC) concept describes a material whose microstructure is periodic. The RUC is the smallest volume that can reproduce the microstructure through repetition.

As braided composites have a periodic microstructure introduced through the interlacing yarn pattern (see Fig. 2.6), the RUC concept is commonly used for unit cell modeling [39, 40, 45, 62]. The RUCs used in literature are not always the smallest possible volume to describe the microstructure (cf. [40, 62]); this is primarily due to practical reasons such as simplicity of the boundary conditions implemented.

### 2.6.3. Homogeneous boundary conditions

Homogenous boundary conditions prescribe either the traction or the displacement on the boundary of the investigated volume. Fig. 2.28 presents a 2D example for a uniaxial stress and a uniaxial strain boundary condition. For homogenous materials, homogenous boundary conditions can be used to evaluate the material properties, but for heterogeneous materials, the response is dependent on the size of the investigated volume and on whether displacement or traction boundary conditions are used [143]. Applying these simplified boundary conditions to finite element unit cell calculations may be valid for some purposes, but should be handled with care as they can lead to artificial stress concentrations, as reported by [64], for an FE unit cell of a woven fabric.

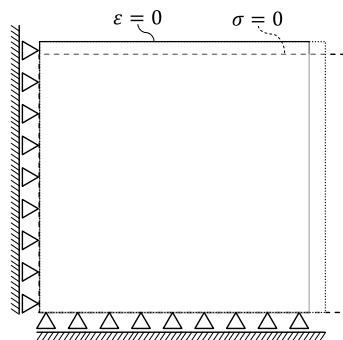


Fig. 2.28: Homogeneous boundary conditions

### 2.6.4. Periodic boundary conditions

The equations and theory of the periodic boundary conditions presented in this section are based on the publications of Pahr [144] and Anthoine [145]. A short review of the equations will be given here. The complete equations and numerical implementation for the unit cells used in this thesis can be found in Section 6.4.

Each periodic medium is defined by the so-called periodicity vectors  $\mathbf{p}^i$ , which are the vectors along the edges of a cuboid unit cell. Two periodicity vectors  $i = A, B$  are defined for plane (two-dimensional) periodic and three periodicity vectors  $i = A, B, C$  are defined for spatial (3D) periodic media. Periodicity implies that mechanical and geometrical properties  $\mathcal{F}$  are invariant for positions which differ by a linear combination of the periodicity vectors:

$$\mathcal{F}(\mathbf{x} + \mathbf{m}) = \mathcal{F}(\mathbf{x}), \quad (2.16)$$

$$\mathbf{m} = m^A \mathbf{p}^A + m^B \mathbf{p}^B + m^C \mathbf{p}^C, \quad (2.17)$$

where  $m^{A,B,C}$  are integers. A graphical interpretation of periodicity is given in Fig. 2.29.

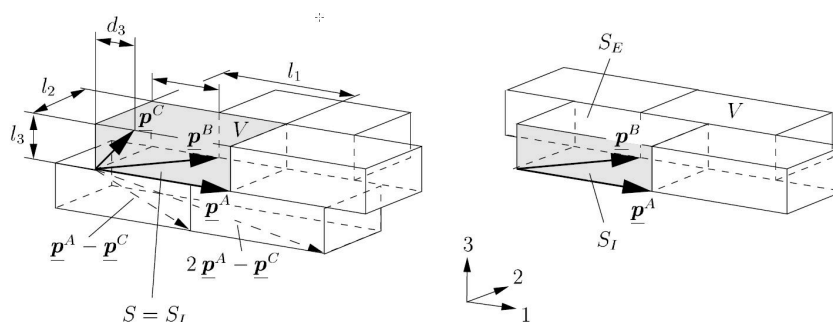


**Fig. 2.29:** Description of spatial and plane periodic medium [144].

Periodic boundary conditions are applied in cases in which a macroscopic homogeneous stress state is modeled. A homogenous macroscopic stress state in this case implies that all unit cells are subjected to the same stress and deform in the same way: two initially adjacent unit cells must still fit together in any deformed state. In mechanical terms, this enforces the following requirements when passing over a unit cell boundary to the adjacent unit cell:

1. stress vectors  $\boldsymbol{\sigma}$  are identical (tractions  $\mathbf{t} = \boldsymbol{\sigma} \cdot \mathbf{n}$  are opposite)
2. strains  $\boldsymbol{\varepsilon}$  are continuous (neither separation nor overlapping of the cell boundary)

To ensure the conditions described above, it is necessary that two opposing sides of the unit cell have identical displacements except for the macroscopic strain introduced into the unit cell. Such a displacement field is termed a periodic displacement field and can, in the absence of rigid body translation and rotation, be written as [144–146]:

$$\mathbf{u}(\mathbf{x}) = \langle \boldsymbol{\varepsilon} \rangle \mathbf{x} + \mathbf{u}^P(\mathbf{x}). \quad (2.18)$$

The total displacement,  $\mathbf{u}(\mathbf{x})$ , is given by the sum of the macroscopic strain tensor,  $\langle \boldsymbol{\varepsilon} \rangle$ , which is constant in the unit cell, multiplied by the position,  $\mathbf{x}$ , and the periodic part of the displacement field,  $\mathbf{u}^P(\mathbf{x})$ , which is zero when averaged over the unit cell volume (cf. Fig. 2.30).

The macroscopic strain can be calculated by volume-averaging the microscopic strain field, but in some cases of FE unit cell calculations this is not possible. In this case, an alternative averaging technique based on the displacement of special nodes can be used

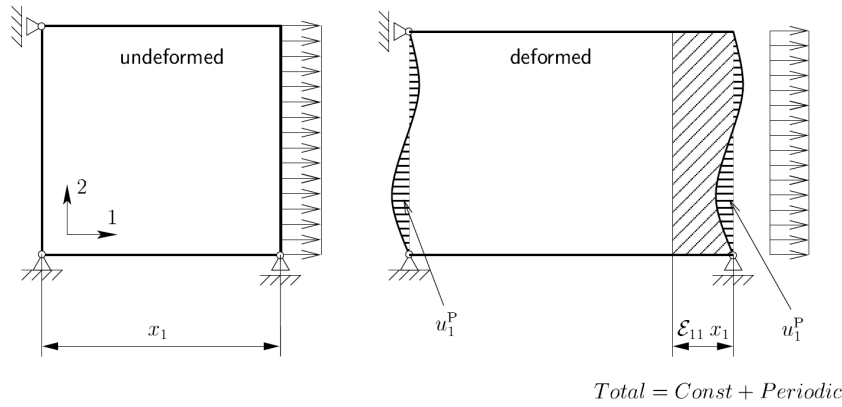


**Fig. 2.30:** Graphical interpretation of constant and periodic part of the displacement field [144].

[144, 145]. If Eq. 2.18 is evaluated at two adjacent points,  $\mathbf{x}$  and  $\mathbf{x} + \mathbf{p}^i$ , of the unit cell, where the periodic part of the displacement is equal (cf. Fig. 2.29), on yields

$$\mathbf{u}(\mathbf{x} + \mathbf{p}^i) - \mathbf{u}(\mathbf{x}) = \langle \boldsymbol{\varepsilon} \rangle \mathbf{p}^i. \quad (2.19)$$

If  $\mathbf{x}$  is set to zero and the origin of the unit cell is defined as fixed ( $\mathbf{u}(\mathbf{0}) = \mathbf{0}$ ), this leads to

$$\mathbf{U} = \langle \boldsymbol{\varepsilon} \rangle \cdot \mathbf{P}, \quad (2.20)$$

or

$$\begin{bmatrix} u_1^A & u_1^B & u_1^C \\ u_2^A & u_2^B & u_2^C \\ u_3^A & u_3^B & u_3^C \end{bmatrix} = \begin{bmatrix} \langle \varepsilon_{11} \rangle & \langle \varepsilon_{12} \rangle & \langle \varepsilon_{13} \rangle \\ \langle \varepsilon_{21} \rangle & \langle \varepsilon_{22} \rangle & \langle \varepsilon_{23} \rangle \\ \langle \varepsilon_{31} \rangle & \langle \varepsilon_{32} \rangle & \langle \varepsilon_{33} \rangle \end{bmatrix} \cdot \begin{bmatrix} p_1^1 & p_1^2 & p_1^3 \\ p_2^1 & p_2^2 & p_2^3 \\ p_3^1 & p_3^2 & p_3^3 \end{bmatrix}, \quad (2.21)$$

i.e. the homogenized strains are controlled by the displacements of the nodes at the end of the periodicity vectors (see Fig. 2.31).

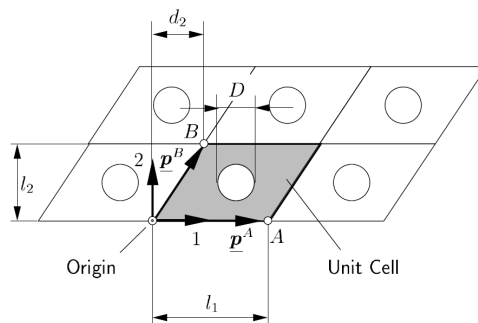


**Fig. 2.31:** Description of spatial and plane periodic medium according to [144].

Thus, the displacements to be introduced into the unit cell can be calculated from the macroscopic strain tensor and the periodicity tensor. The strain tensor as a function of the masternode displacements can be calculated by multiplying the inverse periodicity tensor:

$$\langle \boldsymbol{\varepsilon} \rangle = \mathbf{U} \cdot \mathbf{P}^{-1}. \quad (2.22)$$

Pahr [144] noted that Eq. 2.22 may lead to a non-symmetric strain tensor and suggests an alternative to calculate a symmetric strain tensor:

$$\langle \boldsymbol{\varepsilon} \rangle = \frac{1}{2} (\mathbf{U} \cdot \mathbf{P}^{-1} + (\mathbf{P}^{-1})^T \cdot \mathbf{U}^T). \quad (2.23)$$

In the case that a stress vector is given, considerations including the anti-periodicity of the traction on the faces of the unit cell [144] lead to:

$$\langle \boldsymbol{\sigma} \rangle = \frac{1}{2V} (\mathbf{F} \cdot \mathbf{P}^T + \mathbf{P} \cdot \mathbf{F}^T), \quad (2.24)$$

where  $V$  is the volume of the unit cell and  $\mathbf{F}$  is the master node force tensor defined similarly to  $\mathbf{U}$ .

$$\mathbf{F} = \begin{bmatrix} F_1^A & F_1^B & F_1^C \\ F_2^A & F_2^B & F_2^C \\ F_3^A & F_3^B & F_3^C \end{bmatrix}. \quad (2.25)$$

From this it is possible to obtain the master node forces from the macroscopic stress tensor.

$$\mathbf{F} = V \langle \boldsymbol{\sigma} \rangle \cdot (\mathbf{P}^T)^{-1}. \quad (2.26)$$

With the equations given above, the loading of the unit cell can be stress- or strain-controlled: either forces or displacements are prescribed, and the unknown quantity is obtained as the result of the FE analysis. Six independent load cases are required to calculate all entries of the effective stiffness tensor  $\mathbf{C}^*$  with the macroscopic constitutive Eq. 2.15. The numerical implementation of the periodic boundary conditions into the FE unit cell calculations conducted in this project will be given in Section 6.4.

## 2.7. Modeling of nonlinearities, failure and damage in composite materials

The analysis of large composite structures usually involves complex geometries and a large number of load cases. Due to computational efficiency, this restricts the analysis methods to macroscopic approaches. Thus, for use in structural problems, failure and damage modeling of braided composite materials on a macroscopic scale is favorable [12]. As few failure or damage models with a focus on braided composites are available in literature, a short overview of existing models for UD composites and applications to braided composites will be given in this section.

### 2.7.1. Failure theories

Numerous different failure theories are available in literature. Most of the commonly used models are macroscopic in a way that they are based on the homogenized stress values in the material coordinate system, which equates to the fiber and transverse direction for UD composites. This allows for a straightforward usage of these theories within structural simulations conducted with the use of FE codes.

In the World-Wide Failure Exercise (WWFE) Hinton, Soden, and Kaddour compared the predictive capabilities of different failure theories [3, 147–149]. The investigation included independent (e.g. maximum stress or maximum strain [150, 151]), fully interactive (e.g. Tsai-Wu [152]), and partly-interactive (e.g. Hashin [153], Puck [127]) failure theories. The predictions made by the participants were compared to experimental results and used to judge the predictive capabilities of the different theories.

No clear recommendation for one failure criterion could be made as the quality of predictions differed from the material configuration and the load cases. Among the five criteria that were ranked highest by the authors, the two physically-based failure criteria from Puck [127] and Cuntze [154] were highlighted as they gave the best predictions and captured more general features than the other criteria [3].

Further efforts have been made by the authors to benchmark existing 3D failure criteria in WWFE-II [155, 156] and predictive failure models including damage in the WWFE-III [157].

The considerations published in the framework of Puck's action-plane failure criterion [127] were used by several researchers to formulate improved failure criteria for UD composites. Davila et al. [158] presented the LaRC03 criterion which uses a Mohr-Coulomb approach to calculate the fracture angle under transverse compression and includes a criterion for fiber kinking as well as the usage of *in-situ* strength (cf. [159]) for transverse tensile cracking. The criterion was further developed to account for three-dimensional stress states and named LaRC04 [160]. Recently, Catalanotti et al. [161] presented an improved failure criterion that has been developed to account for *in-situ* effects under transverse tension, transverse compression, and in-plane shear.

### Application of failure theories to braided composites

Physically based failure criteria have been used to predict failure within the yarns of a woven or braided composite FE unit cell model [41, 45, 47, 101]. The yarns comprise several thousand filaments running in the yarn direction and thus can be considered to behave locally similar to unidirectional composites. Puck states that UD failure theories should be applicable to textile composites with low waviness, but questions the applicability for higher waviness as different failure mechanisms may become dominant [95]. Regardless of the waviness, it was concluded that the same failure and damage processes are occurring inside the yarns, but it was assumed that the *in-situ* effect (described in detail by Camanho et al. [159]) may be more prominent, as the yarn area is much smaller than a common UD ply.

Within macroscopic woven fabric and braided fabric laminate models, usage of independent failure criteria such as maximum strain [116] or maximum stress [12, 117] was reported. Charlebois et al. [25] used the Tsai-Wu criterion for the prediction of biaxial braided strength. They reported good correlation to experiments in tension, but higher deviations from the experiments in compression were attributed to the effect of fiber undulation.

### 2.7.2. Damage modeling

A general framework for the description of damage in materials has been developed by Kachanov [162]. The amount of damage on a specific plane of the material is described by an internal damage variable. The concept has been integrated by Lemaitre into a thermodynamic framework for solid mechanics of isotropic materials [163].

Kachanov's principle was used by several researchers to model damage in composite materials [12, 42, 117, 126, 164–168]. Common failure criteria as presented in the previous section are used to determine the stress state at which damage initiates. The main difference between the approaches lies in the type of failure criteria used and how damage progression is calculated. Early models, such as [79, 126], used independent or fully-interactive failure criteria for damage initiation, and the stiffness in the direction that the damage was predicted was suddenly reduced to a small fraction (typically 1-20%) of the initial value, by using a *discount factor*. A comprehensive overview of different stiffness degradation models was given by Goyal [39]. He found that the models, although showing differences in the way how properties are degraded, produce similar results, when the *discount factors* were equalized. A gradual decrease in stiffness after damage initiation can be modeled by continuum damage mechanics models [159, 164]. While Matzenmiller [164] proposed a damage evolution law based on strains, Maimí, Camanho and co-workers [166, 167] presented an improved damage model, based on Bažant's crack band model, including regularization of the dissipated energy with respect to the size of the finite element mesh. Fracture toughness values of the material were incorporated into exponential damage evolution laws and a mesh-independent solution was achieved, which is not the case for strain-controlled damage variables. Similar approaches exist, comprising different failure criteria and linear as well as exponential damage growth [141, 165, 168].

#### Application of damage to braided composites

Similar to the failure theories, damage modeling is often used within the yarns of woven or braided composite FE unit cells [41, 45, 79, 101, 126]. The application of damage mechanics to the macroscopic modeling of braided composites are rather rare. Fourneteau [12] used the ply damage model from Ladeveze [42] for biaxial braided composites. He added a phenomenological treatment for stiffness reduction due to delamination under fiber tension and assumed that transverse damage under normal stresses is negligible. Furthermore, the shear damage evolution model was improved to account for large strains observed experimentally. The model was implemented in the FE code PAM-Crash and validated with experiments.

### 2.7.3. Inelastic deformation

Ladeveze [42] states that damage within composite materials is highly complex and can include micromechanical mechanisms such as sliding and friction, which leads to inelastic deformation. Thus, the phenomenon of damage in composite materials may be coupled with plasticity or viscoplasticity.

This is in accordance with the experimental observations of Varna et al. [169], who measured a decrease in modulus in ( $\pm 25^\circ$  and  $\pm 40^\circ$ ) angle-ply laminates, but did not observe

any macroscopic cracking. The underlying mechanism for this behavior was believed to be caused by fiber/matrix microcracking induced by in-plane shearing. Puck also describes this phenomenon and terms it *micro-damage*: very small cracks (approximately the size of the fiber diameter) in the matrix and the interface. Puck described experimental evidence of the existence of micro-damage from opaqueness of GFPR laminates [170].

The inelastic deformation of composites is typically modeled using conventional or adapted plasticity models known from metals [12, 42, 117, 141, 171–173]. Early models assumed a transverse normal  $\sigma_{22}$  and in-plane shear  $\tau_{12}$  stress, or a combination of both, to cause the inelastic deformation. Flatscher [141] presented a multi-surface plasticity model describing plastic deformation under transverse compression and in-plane shear. A new plasticity model recently presented by Vyas et al. [168, 172] accounts for hydrostatic pressure, non-associated flow, and kinematic hardening. Vogler, Camanho, and co-workers [173, 174] presented an invariant-based plasticity criterion combined with a smeared crack model with the use of a structural tensor defining the fiber direction and accounting for hydrostatic pressure as well as non-associated flow. Vogler et al. [173] noted that hardening in polymer matrix composites was believed to be a mixture of isotropic and kinematic hardening, but used an isotropic hardening law due to a lack of experimental data for calibration of a mixed hardening law.

### **Application of inelastic deformation models to braided composites**

One-dimensional in-plane shear plasticity [12, 117] based on Ladeveze’s ply model [42] has been applied to biaxial braided and woven fabric composites. Fouinneteau [12] compared the predictions of inelastic strains to experiments and found a good correlation for the biaxial braided composites investigated. Goyal et al. [39, 118] used an anisotropic Hill-plasticity criterion in an equivalent laminate model and could successfully model the nonlinearities of biaxial braided composites loaded in tension in the take-up direction. The model required additional input-parameters to describe the anisotropy of the yield surface, which were calculated using a fiber-matrix unit cell model.

## **2.8. Conclusions**

The published literature regarding the braiding process, yarn architecture of braided composites, characterization methods for braided composites, and mechanical modeling approaches including FE unit cell modeling and macroscopic approaches has been reviewed.

Braiding offers significant possibilities for process automation, high-volume production, and cost reduction during the manufacturing process. High flexibility is available, as the type of reinforcement can be adapted to the mechanical needs and the overbraiding process allows for curved mandrels with changing cross sections. This makes the usage of braiding favorable for a multitude of lengthy structures.

From the designers viewpoint, the flexibility of the process creates the challenge of a highly variable yarn architecture and thus changing material properties of the braid. Different possibilities to characterize the yarn architecture and approaches to geometric modeling of the yarns have been reviewed. Different methods have been used to provide input for geometric models. However, to date there is no evidence, which of the charac-



terization methods and models provides a suitable balance between effort, level of detail, and robustness.

The mechanical behavior of braided composites was reviewed, with many publications describing the elastic, nonlinear, and failure behavior of braided composites under uniaxial loads. Failure mechanisms and modes were described for both textile composites and general and braided composites in particular. The mechanisms driving the failure and damage are similar to those of unidirectional composites, but influenced by the textile architecture.

Different approaches for the prediction of textile composite constitutive behavior have been evaluated with a focus on: simple and analytical models for stiffness prediction; FE unit cell models for the detailed modeling of the nonlinear effects and failure within a braided composite; and macroscopic CLT based methods favorable for structural simulation. Besides the analytical models, which are only suitable for stiffness prediction, FE unit cell methods can be used to provide detailed predictions of different damage and failure events inside the textile. Structural simulations typically use macroscopic approaches with high computational efficiency and good possibilities for implementation into conventional FE analysis. It should be noted that simple failure and damage models are mostly used for braided composites on a macroscopic scale and to date no validation of these models exists regarding the applicability on multi-axial stress states.

The literature review has emphasized the need for an integrated approach to the characterization and simulation of biaxial braided composites on different length scales. Furthermore, failure and damage models must to be validated under various combined load cases. Chapter 5 and 6 address this point, comparing FE unit cell simulations to various in-plane load cases under tension and compression. The experimental methods and results for mechanical and yarn architecture characterization are described in Chapter 3 and Chapter 4. Additionally, a focus is the transfer of the unit cell results to macroscopic modeling using CLT. Different failure theories and the effects of inelastic deformation and damage are investigated in Chapter 7.

### 3. Experimental techniques

Experimental investigations were carried out in this thesis to gain a knowledge about the material behavior and the internal structure of biaxial braided composites. Besides the goal of providing a phenomenological understanding, the experimental results can be used to provide both input data for simulation models and an experimental basis to validate the predictions made by the models.

Flat ( $\pm 30^\circ$ ) biaxial braided composite panels were produced from overbraiding and coupons cut from the panels were used in tension and compression off-axis tests. The goal was to characterize the elastic, nonlinear and failure behavior under combined load states. The manufacturing process of the braided panels, including preforming and infiltration, and the preparation of the specimen for coupon testing is described in this chapter. Furthermore, the test set-up including techniques for strain measurement and evaluation procedures for the nonlinear and fracture behavior are presented. Additionally, equations to normalize the mechanical properties of biaxial braided composite to a common fiber volume fraction are given.

Besides the mechanical experiments, different techniques to characterize the yarn architecture of braided composites, namely optical microscopy, micro-CT and image analysis, are explained. The machinery, machine configuration and processes for data acquisition are given. Furthermore, two evaluation techniques for braiding angle measurements based on surface images are described.

#### 3.1. Coordinate systems

Different coordinate systems and designations for distinct orientations (e.g. fiber orientation) are used for braided composites [40, 45, 62]. As no common definition is available for both meso- and macro-scale, the coordinate systems used are defined in Fig. 3.1 and Table 3.1.

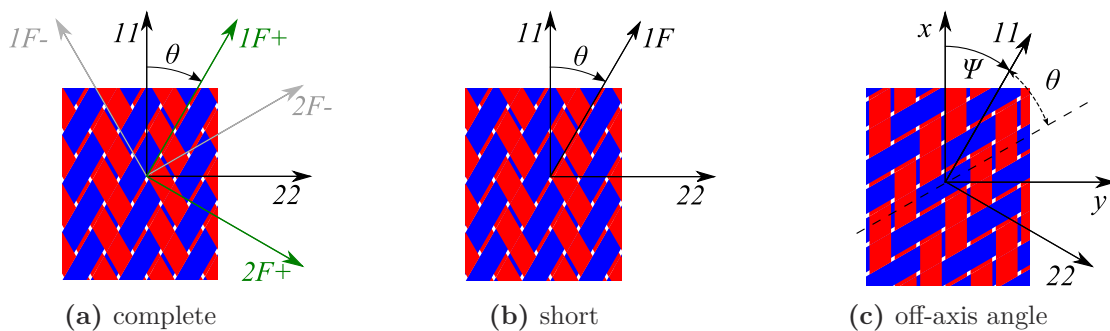


Fig. 3.1: Coordinate systems for braided composites (a,b) and definition of the off-axis angle (c)

Biaxial braided composites behave macroscopically orthotropic, thus the general orthotropic coordinate system [175] is used. For braided composites, the 11-axis is equal to the take-up direction with the yarns oriented at an angle  $\theta$  to the 11-axis. The longitudinal yarn direction and direction transverse to the yarn are labeled with by  $1F+$ / $1F-$  and  $2F+$ / $2F-$ , respectively. Furthermore, the off-axis angle  $\psi$  defines the angle between the global (e.g. load) direction and the braid 11-direction.

**Table 3.1.:** Coordinate systems for braided composites (Ivanov’s designation [45] given for comparison)

designation	orientation	material-CS	Ivanov [45]
take-up direction	$0^\circ$	11	MD
transverse direction	$90^\circ$	22	CD
fiber (yarn) direction 1	$+\theta$	1F+	BD
fiber (yarn) direction 2	$-\theta$	1F-	BD

The braided **composites** used within this thesis were produced from high-strength carbon fibers and epoxy matrix. Both constituent materials chosen are aerospace certified and the manufacturing processes were configured to provide with minimized waviness and fiber volume fraction of 60%, yielding optimal mechanical properties.

## 3.2. Manufacturing of biaxial braided composites

### 3.2.1. Constituent materials

#### Fiber material

Toho Tenax E HTS40 F13 12K (800 tex) 0z [176] yarn were used for the braiding process. The yarns consist of 12,000 high-tenacity carbon filaments with a polyurethane sizing. Untwisted yarns were used to yield optimal mechanical properties. Prior to the braiding, the yarns were rewound from the 2 kg spools delivered to the braiding spools used on the braiding machine (cf. Fig. 2.4b). A low yarn tension of 2 N during rewinding was used to minimize yarn damage. An overview of the yarn properties is given in Table 3.3a.

#### Matrix material

The matrix system used for the impregnation was a Hexcel HexFlow RTM6 monocomponent epoxy resin [177]. RTM6 has a high viscosity at room temperature, must be heated to  $80^\circ\text{C}$  prior to infusion and is cured at  $180^\circ\text{C}$ . Before the infusion, the resin was degassed for 15 minutes at a temperature of  $80^\circ\text{C}$ . An overview of the RTM6 properties is given in Table 3.3b.

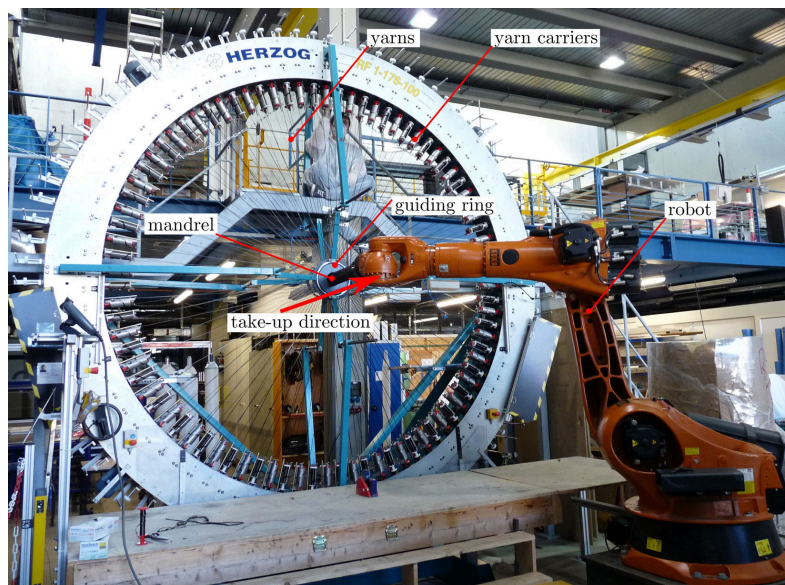
### 3.2.2. Manufacturing of braided composite panels

The preforms were braided on a *Herzog RF 1-176-100* maypole braiding machine at the Institute for Aircraft Design in Stuttgart. The braiding machine consists of 88 horn gears

**Fig. 3.2:** Manufacturer data sheet values for yarn and matrix system used

(a) Toho Tenax HTS40 12K yarn		(b) RTM6 monocomponent epoxy matrix	
yarn linear density [tex]	800	density [ $\text{g}/\text{cm}^3$ ]	1.14
filament count	12000	strength [MPa]	75
filament diameter [ $\mu\text{m}$ ]	7	Young's modulus [MPa]	2890
density [ $\text{g}/\text{cm}^3$ ]	1.77	fracture strain [%]	3.4
tensile strength [MPa]	4300		
Young's modulus [GPa]	240		
failure strain [%]	1.8		

and 176 yarn carriers. All yarn carriers at the machine were used, yielding a 2x2 braid pattern on a circular mandrel with 100 mm diameter and a length of 1500 mm. The diameter of the mandrel was found by a preliminary study to be an optimal choice between maximum yarn width (minimal waviness), and a complete coverage of the mandrel. The mandrel used was specially designed for braiding of flat plies and has two cutting channels: one around the cross section at the beginning and end, which is used to cut the ply to the desired length and one additional channel along its length to cut a flat preform from the mandrel. The braid guiding ring diameter was chosen circular with a diameter of 110 mm, which ensures a good deposit of the braided preform. The mandrel was guided by a robot (see Fig. 3.4) and the take-up velocity was constant and calculated by Eq. 2.1 to achieve a braiding angle of  $\theta = 30^\circ$ .

**Fig. 3.4:** Maypole braider *Herzog RF 1-176-100* with 176 yarn carriers

Some of the braided plies yielded quality issues due to an increased tension in the yarns, attributed to lubrication problems within the yarn carriers. The yarn tension and thus yarn-to-yarn friction was increased and defects (uneven braiding angle, locally open braid, etc. Fig. 3.5) arising from broken filaments were visible on some of the braided preforms.

All braided preforms were therefore visually inspected and only defect-free plies were used further.

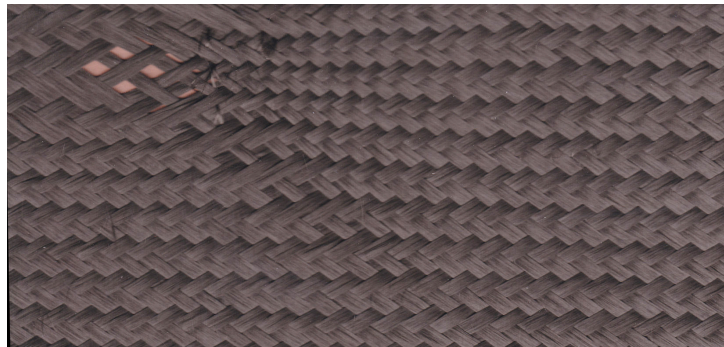


**Fig. 3.5:** Defect in the preform: uneven braiding angle and open braid

The manufacturing process of one braided ply can be summarized with the following steps:

1. Braiding of one ply with the length of 1500 mm on a cylindrical mandrel (Fig. 3.4).
2. Cut the ply to the desired length, place the mandrel on the cutting table, cut along the mandrel length and unroll the braided preform to the table (Fig. 3.6).
3. Cut two rectangular preforms of  $650 \times 314 \text{ mm}^2$  from the braided ply (Fig. 3.6)

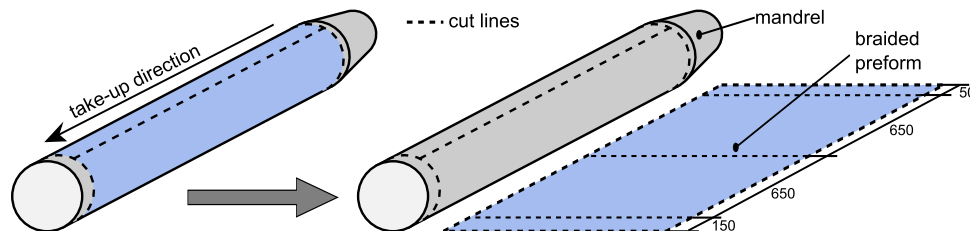


**Fig. 3.6:** Manufacturing process for flat preforms: braiding on circular mandrel (left) and cutting and unrolling of the ply (right).

All cutting lines were taped before the cutting with a 2 cm wide 180°C temperature-resistant tape<sup>1</sup> to avoid distortion of the preform during cutting. The first 150 mm and the last 50 mm of the braided plies (cf. Fig. 3.6) were not used, as local effects like e.g. yarn slippage at the beginning and end of the braiding process can lead to an uneven yarn architecture in these regions.

The described manufacturing process produces panels for coupons of the so-called *cut* configuration without continuous fibers at the edge (cf. Section 2.4.2). The process was chosen, as it is able to produce specimens with even quality and small deviations in the yarn architecture. Producing *uncut* specimen either requires a special braiding machine with a yarn carrier turning point (cf. Fig. 2.7) for braided tapes or it introduces an additional preforming step, which includes taking-off the braided sleeve from the mandrel and draping it flat. For the latter, the additional manual work introduces a high uncertainty

<sup>1</sup>To prevent a dissolving of the tape during infusion and curing, a 180°C resistant tape was used.

regarding the distortion of the preform and can result in an increased braiding angle variation as reported in [26].

Five and eight plies of the preforms were stacked on a flat glass tooling for the tension- and compression-test panels, respectively. For the compression tests, eight-ply laminates were chosen to prevent specimen buckling during the test. No considerations were given to create a distinct nesting configuration during the stacking. The laminates had a nominal thickness of 2.5 mm respectively 4 mm with a desired fiber volume fraction of 60% as calculated from Eq. 2.4 and Eq. 2.5. The braid laminates were vacuum-bagged for injection as shown in Fig. 3.7 and infiltrated and cured in a convection oven by using the vacuum assisted process (VAP) [178]. The infiltration process and cure cycle was chosen according to the resin manufacturers recommendation [177]. First, the resin was preheated to 80°C and the tool was heated over 120 minutes to 120°C, then the resin was injected and cured for 120 minutes at 180°C. After curing, the panels were cooled within 90 minutes to room temperature. The pressure loss at the vacuum bagging was checked prior to infusion to prevent leakage.

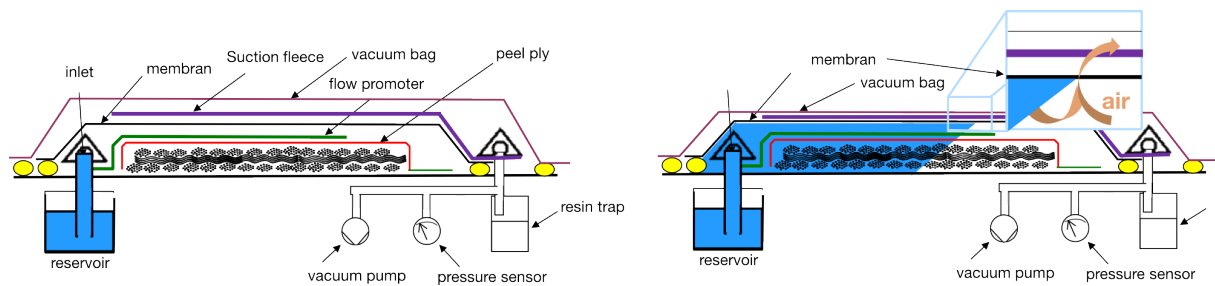


Fig. 3.7: VAP-process uncompact and during infiltration

After curing, the panels were demolded and inspected visually to check for areas on the surface with incomplete impregnation. The thickness of the panels was measured using a force triggered thickness gauge with a spherical anvil at 12 evenly distributed points. Additionally, the fiber volume fraction was measured by chemical digestion [43] from three specimen of each panel.

### 3.2.3. Quality inspection and assurance

The manufacturing process steps for the braided composite panels may introduce irregularities into the specimen, which could influence the material properties. Additionally, the braiding process introduces some inherent variability into the produced material. Therefore, several quality inspection steps during the production have been conducted to ensure a high and constant quality of the panels.

- The dry preforms were visually inspected and the braiding angle was measured at three points of every ply.
- Every preform was weighted prior to consolidation.
- The vacuum bagging was checked for leakage prior to infusion.
- Cured panels were visually checked for non-impregnated areas.

- Thickness of the panels was measured at 12 points over each panel.
- Fiber volume fraction was measured from 3 specimen per panel.
- Selected coupons were measured using an optical sensor to check the fiber orientation.

### 3.3. Yarn architecture characterization

The characterization of the yarn architecture of braided composites provides an inside view to the material: characteristics of the yarn architecture can be investigated and the results can be used for qualitative (e.g. occurrence of voids, yarn architecture compactness) and quantitative (e.g. yarn shape, dimensions) assessment.

This thesis compares different methods for the characterization of braided composites yarn architecture. The baseline process is optical microscopy, which is simple and robust and can be conducted with standard laboratory equipment. Additionally, the information obtained from X-ray micro-computed tomography (micro-CT) and surface image analysis is compared to the results obtained from micrographs. All investigations are based on cured samples to include possible effects of compaction and resin infusion. The different methods comprise advantages and disadvantages regarding resolution and dimensionality of the gathered information. In the following section the methodologies and the equipment used for yarn architecture characterization are described.

#### 3.3.1. Optical microscopy

For optical microscopy, small samples were cut from the cured laminates, embedded into a mounting resin and investigated under a reflecting-light microscope.

##### Sample preparation

Samples of 30-40 mm width are cut from the cured panels using a water-cooled diamond saw. In most cases cut-waste of the panels from mechanical specimen manufacturing was used. Due to the low depth of field of the microscope, the samples need to be embedded into epoxy resin, ground and polished to give a flat surface for microscopy. A cold-setting and transparent epoxy resin (*EpoFix* [179]) was used for embedding of the samples.

The grinding process was done using a *Struers TegraForce-5* grinding and polishing system [179]. Several grinding steps with decreasing grain size of the grinding plates were conducted. A four-step process using subsequent grinding with 180, 220 and 1200 grit SiC<sup>1</sup> grinding paper and an additional polishing step with a *MD-Largo<sup>TM</sup>* [179] disc and a corresponding diamond suspension was used. The process provided a constant quality of the samples for yarn architecture measurements.

---

<sup>1</sup>SiC: silicon carbide

### Microscopy measurements

The reflecting-light microscopy *Olympus BX41M-LED* was used for the measurements of the samples. The samples were pressed on the object slide to ensure a flat plane of measurements. A  $5\times$  amplification of the specimen was found to be adequate for measurements of yarn cross sections and yarns paths, whereas  $20\times$  amplification was used to investigate single filaments in a yarn. The software *Olympus Stream Motion* [180] was used for the measurements. In combination with an electronic-adjustable microscope table it provides the possibility to automatically align and assembly combined images out of several single pictures. Thus a complete sample, which does not fit on a single  $5\times$  amplification picture can be recorded in one step with a high resolution of approximately  $1\ \mu\text{m}$  per pixel.

#### 3.3.2. Micro-CT

Micro-CT images are based on the principle of X-ray absorption in solid materials. The sample is subjected to X-rays and the absorption is measured by a detector behind the specimen. A complete micro-CT scan comprises, depending on the sample size and resolution, several thousand images with the sample being rotated to obtain different projection angles. The complete set of images is reconstructed to a three-dimensional data set of voxels (3D pixels) representing the amount of absorption at a point of the sample. The contrast between different phases is based on the density of the material, which can be difficult for carbon/epoxy composites as yarns and matrix have similar densities [65].

The micro-CT scans used in this thesis were taken from small samples of cured braided material. The measurements were conducted on a GE phönix|x-ray Nanotom 180 NF with a flat  $2300\times 2300$  pixel detector an the *Fachhochschule Oberösterreich* in Wels (Austria). The samples were scanned at voxel sizes of  $11\ \mu\text{m}$  and  $7\ \mu\text{m}$ , yielding a measurement area of  $20\times 20\times 4\ \text{mm}^3$  and  $15\times 15\times 4\ \text{mm}^3$ , respectively. With  $11\ \mu\text{m}$  voxel size shown in Fig. 3.8a, longitudinal and transverse yarns could not be distinguished clearly. The  $7\ \mu\text{m}$  resolution shown in Fig. 3.8b yielded improved results: the yarns can be clearly identified and the contrast between longitudinal and transverse yarns is sufficient. The micro-CT scans have been evaluated by hand using the image analysis software ImageJ [181].

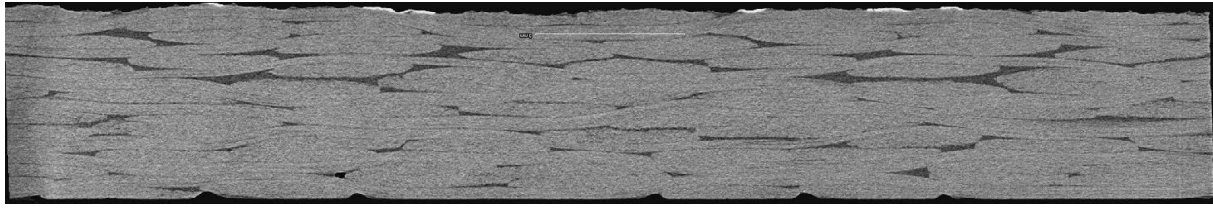
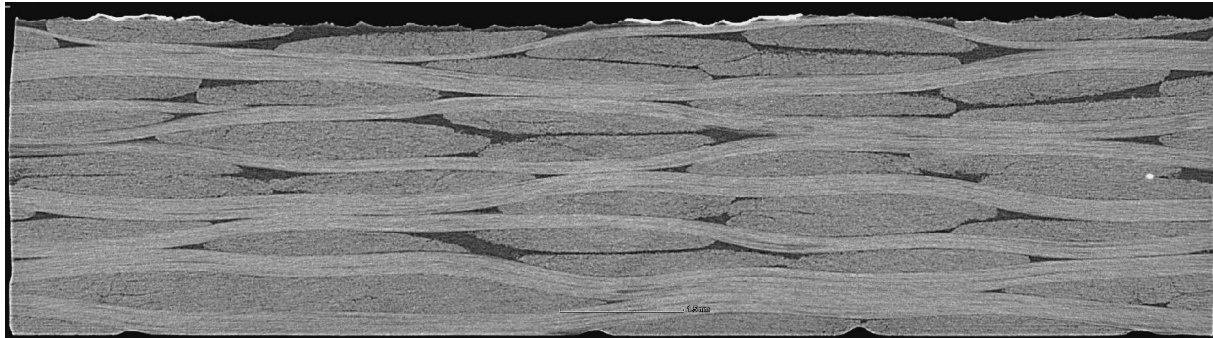
#### 3.3.3. Analysis of surface images

Two techniques were used for the measurement of the fiber orientation on the surface of the laminate:

- Manual evaluation of the fiber orientation based on images acquired on a regular scanner.
- Image analysis based on photometric stereo with an optical sensor developed by the Profactor GmbH [67].

Both techniques base on the assumption that the braiding angle of the surface ply is representative for the complete laminate. This is valid, as all plies are braided one after the other on the same mandrel. The compaction is believed to have minor effects on the



(a) 11  $\mu\text{m}$  voxel size micro-CT scan(b) 7  $\mu\text{m}$  voxel size micro-CT scan**Fig. 3.8:** Comparison of different resolutions from micro-CT scans

braiding angle, thus the surface ply is representative. If several plies are braided over each other on a mandrel, the braiding angle should be measured for every ply independently.

For the first technique, the braiding angle was obtained from scanned images of the cured braid laminates. The images were acquired on a regular scanner with 600 dpi resolutions and the angles between the two fiber directions were measured by using the image analysis software ImageJ. The method yields the advantages that a large area can be investigated including possible effect of local fiber angle deviations. No special equipment or software is needed for this method yielding information about average braiding angle and variability. The influence of the manual evaluation was checked by applying the technique to the same sample for several times and was found to be negligible. The braiding angle was calculated as half the angle between the two fiber directions, as the take-up direction is defined as the middle in-between the two fiber directions.

The second measurement technique used an optical sensor based on the principle of photometric stereo [67] to determine the yarn orientation. The optical sensor was used to measure the yarn orientations of selected coupons from the off-axis experiments. In contrast to the scanning technique, the sensor measures the yarn angles on an area of approximately  $60 \times 30 \text{ mm}^2$  and delivers a fiber orientation value for every pixel of the image recorded. The resolution of the recorded the images was  $1600 \times 950$  pixels. The optical scanner software enables an export of the results to MATLAB, where the results were analyzed by a user-written script. The analysis contains the following steps:

- Transform the results to a common coordinate system where  $0^\circ$  is equal to the given 11-direction of the braid.
- Remove artifacts from the data.
- Calculate misalignment of the sample.

- Calculate braiding angle for the evaluation windows given by the user.

The output from the sensor is a matrix containing the surface fiber azimuth angle  $\beta_{ij}$  (definition see Fig. 3.9) for every pixel in the image. The user input for the evaluation script contains the area of pixels of the image to be analyzed, the approximate value of the expected braiding angle  $\theta^0$ , the approximate orientation of the braid 11-direction in the image (off-axis angle)  $\psi^0$  and the number of horizontal and vertical evaluation windows  $N_h, N_w$ . Furthermore, a tolerance value  $\beta_{tol}$  has to be given to clean the results from artifacts.

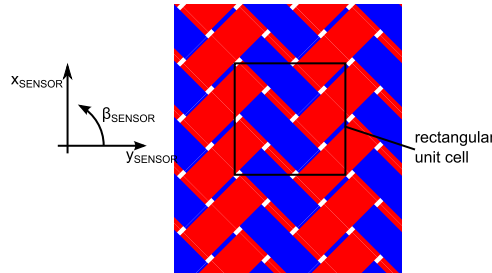


**Fig. 3.9:** Unit cell size for 2x2 biaxial braided composites and definition for fiber angle  $\beta$

First, the data set is reduced to the area given by the user to be evaluated. The azimuth angle provided by the sensor may be positive ( $\beta > 0$ ) or negative ( $\beta - 180^\circ < 0$ ) for the same physical fiber orientation (see Fig. 3.10a), which leads to an error when averaging the angles. This is corrected in the analysis by adding  $180^\circ$  to the negative angles.

$$\beta'_{ij} = \begin{cases} \beta_{ij} + \psi^0 - 90^\circ & \text{if } \beta_{ij} > 0 \\ \beta_{ij} + 180^\circ + \psi^0 - 90^\circ & \text{if } \beta_{ij} < 0 \end{cases}$$

The second term  $\psi^0 - 90^\circ$  added to all azimuth values rotates the coordinate system so that angles of  $0^\circ$  are equivalent with the braid 11-direction given by the user.

As the orientation of the 11-direction given by the user,  $\psi^0$  is only an approximate value and might differ from the actual one, the misalignment of the 11-axis is calculated. Therefore, every pixel is either allocated to one of the two fiber directions ( $f_k, k = 1, 2$ )

$$\begin{aligned} \beta^{f_1,0} &= -\theta^0 \\ \beta^{f_2,0} &= +\theta^0 \end{aligned} \quad (3.1)$$

or rejected as artifact, when lying outside the tolerance  $\beta_{tol}$  provided by the user. The allocation to the two fiber directions is given by the condition:

$$\beta^{f_k} = \left\{ \beta'_{ij} \mid \beta^{f_k,0} - \beta_{tol} < \beta'_{ij} < \beta^{f_k,0} + \beta_{tol}, k = 1, 2 \right\} \quad (3.2)$$

The removal of artifacts is necessary as the optical sensor serves unrealistic values for the azimuth angle in the regions with high out-of-plane orientation near the boundaries of the image (see Fig. 3.10b). All the azimuth angles  $\beta_{ij}$  lying outside the tolerance given by  $\beta_{tol}$  are not considered. Fig. 3.10c shows that this criterion removes the non-physical values at the edges of the samples (black areas on right image,  $\beta_{tol} = 10^\circ$ ).

With the pixels allocated to the two fiber directions, the average fiber orientations can be calculated. The misalignment angle is calculated from the average values  $\bar{\beta}^{fk}$  (calculated from all pixels satisfying Eq. 3.2) of the two fiber orientations:

$$\delta\beta = -\frac{1}{2}(\bar{\beta}^{f1} + \bar{\beta}^{f2}) \quad (3.3)$$

Subsequently, the misalignment angle is added all azimuth values:

$$\beta'_{ij} = \beta'_{ij} + \delta\beta. \quad (3.4)$$

As the rotation of the reference direction conducted in Eq. 3.4 changes the allocation, whether a azimuth value is an artifact or not (Eq. 3.2), the operations Eq. 3.2-Eq. 3.4 are conducted iteratively until the misalignment angle  $\Delta\beta = \sum \delta\beta$  converges. When the misalignment angle has converged, the 11-direction and the average fiber orientations ( $\bar{\beta}^{f1} = -\bar{\beta}^{f2}$ ) are known.

For the next steps, the image is subdivided into  $N_h \times N_w$  evaluation windows (see Fig. 3.10b), where one evaluation window is an averaging area for the braiding angle. The results from the optical scanner provide a fiber angle information for every pixel, which allows to calculate an overall average and standard deviation of the fiber angle. This information includes rather local misalignment effects, which are not representative for the braiding angle serving as an input for unit cell or structural simulations. Thus, it is meaningful to introduce a certain averaging. The size of the averaging area is arbitrary, but it is reasonable to choose the area of approximately the size of the repeating unit cell as given in Fig. 3.9. The braiding angle is calculated from

$$\theta = \frac{1}{2}(\bar{\beta}^{f1} - \bar{\beta}^{f2}). \quad (3.5)$$

The processing described was implemented into MATLAB. An example output, giving the average braiding angle for each evaluation window, of the image in Fig. 3.10 is:

```

1 Braiding angle (standard deviation of local fiber orientation) in the ...
   windows given by the user:
2 31.31° (3.25°)   31.46° (2.67°)
3 30.14° (2.70°)   30.56° (2.41°)
4 30.11° (2.57°)   30.34° (2.42°)
5 30.54° (2.51°)   30.48° (2.74°)
6
7 Average braiding angle and standard deviation evaluated from windows:
8 30.62° (0.51°)

```

A short description of *braiding\_angle\_analysis.m* is given in Appendix E.1.

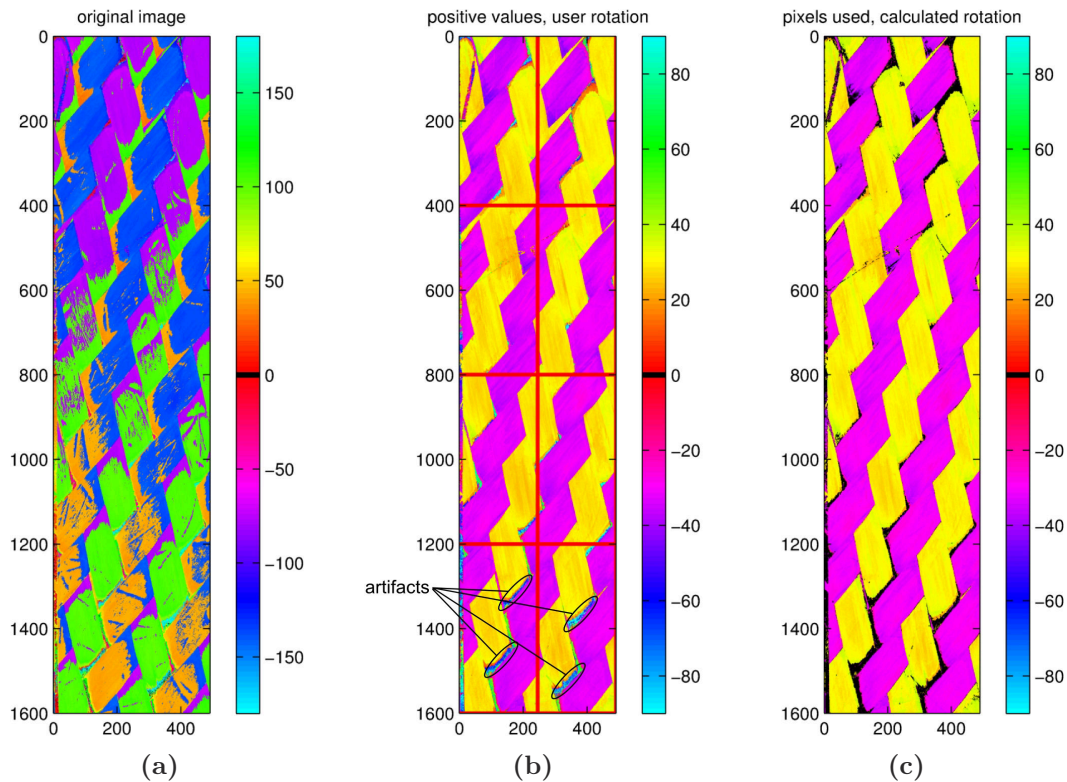


**Fig. 3.10:** Optical sensor analysis: raw azimuth distribution (a), evaluation windows (b) and artifact pixels marked black (c)

### 3.4. Mechanical characterization

In this thesis, the elastic, nonlinear and failure behavior of biaxial braided composites is characterized with off-axis<sup>2</sup> tension and compression tests of a ( $\pm 30^\circ$ ) braided composites. By using off-axis experiments, the material is subjected to loads in different load directions defined by the off-axis angle (see Fig. 3.1). This creates different combined stress states that are applied to the braid and thus triggers different failure and damage behavior.

The mechanical characterization of the ( $\pm 30^\circ$ ) biaxial braided composites was conducted according to the ASTM D3039 standard [84] for the tensile and ASTM D6641 standard [85] for the compressive tests. As the standards are intended for use with unidirectional or multi-directional laminates, additional requirements for textile reinforcements as given in ASTM D6856 [182] have been considered. Two requirements mainly influence the coupon manufacturing and testing: the required coupon width and the recommendations regarding strain gauge size. The coupon width shall be the minimum of twice the unit cell width (cf. Fig. 3.9) and the coupon width provided by the standard. The unit cell criterion yielded for the ( $\pm 30^\circ$ ) braid a minimum coupon width of approximately 13 mm, thus the width of 25 mm specified in the ASTM D3039 was used. The second requirement regarding the strain gauge size had no relevance for the tensile test as digi-

<sup>2</sup>Although, the experiments with off-axis angles of  $0^\circ$  and  $90^\circ$  are, strictly speaking, “in-axis” – the load is aligned with one of the orthotropy axes – the term off-axis (OA) will also be used for all experiments throughout this thesis.

tal image correlation (DIC) was used for deformation measurement. For the compression tests, the strain gauge size was limited by the free coupon length and the limited space for strain gauge bonding and wiring inside the combined loading compression (CLC) fixture [183]. The strain gauge was selected to have the maximum possible gauge length of 3 mm (8.8 mm backing length) fitting into the test fixture.

### 3.4.1. Manufacturing of specimen

The specimens were cut out by using a water-cooled diamond saw from the panels produced by overbraiding and VAP as described in Sec. 3.2.2. In a first step, so-called sub-plates were cut from the panels, where the size and orientation was chosen according to size, number and orientation of the coupons. The orientation of the off-axis coupons was measured from the edge of the panel, which was trimmed along the braid 11-direction. The dimensions of the specimens were chosen according to the standards [84, 85] and either rectangular or oblique tabs (see Sec. 3.4.3) were used. A 1 mm thick glass/epoxy fabric was used for the tabs and bonded onto the sub-plates at the desired position (see e.g. Fig. 3.11). While a water-cooled diamond saw was used to cut the rectangular tabs,

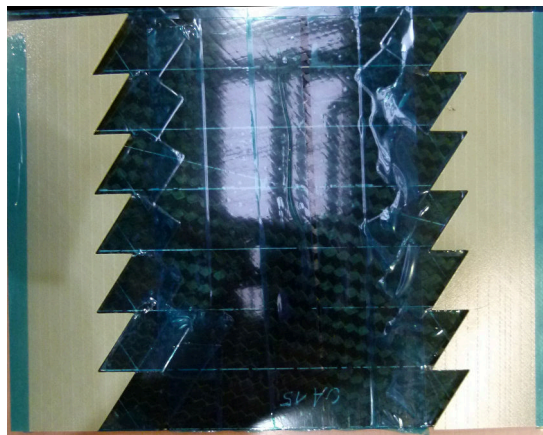


**Fig. 3.11:** Sub-plate for off-axis specimen ( $\psi = 15^\circ$ ) with waterjet-cut oblique tabs

waterjet-cutting was chosen for the oblique tabs to ensure high manufacturing precision regarding the tab angles. After tab-bonding, the specimens were cut in slices from the sub-plates. An overview about the coupon dimensions is given in Table 3.2.

After cutting from the sub-plates all coupon dimensions were measured as required in standard with a caliper. For the tensile coupons, a random speckle pattern required for the DIC measurements (see 3.4.5) was sprayed onto the front surface. The coupons were named according to the following system:

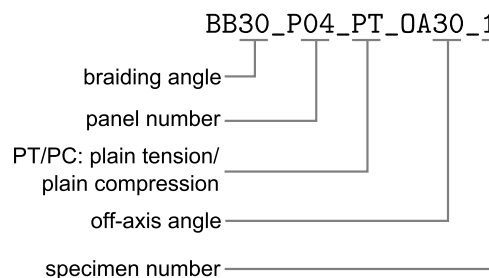


**Table 3.2.:** Coupon dimensions for material characterization

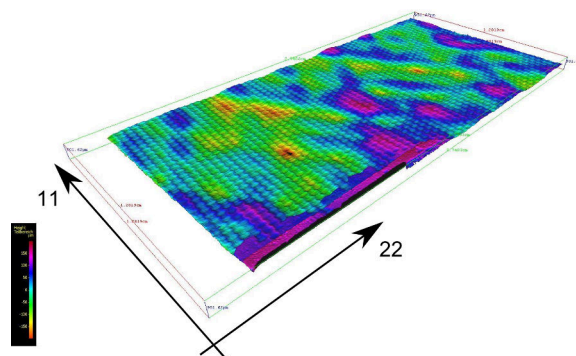
	tension	compression
standard	ASTM D3039	ASTM D6641
length [mm]	250	140
width [mm]	25	25
thickness [mm]	2.5	4
gauge length [mm]	150	13
tab shape	rectangular / oblique	rectangular
tab length [mm]	50	63.5
tab thickness [mm]	1	1

### 3.4.2. Thickness measurement

For braided composites produced in a vacuum infusion process, the interaction of the vacuum bag and the yarn architecture creates a wavy surface on the vacuum-bag side (c.f. Fig. 3.8b upper side). The waviness of the surface has to be considered for the thickness measurements: when using a common caliper, only the maxima of the wavy surfaces are considered leading to an overestimation of the thickness as reported in [33]. Overestimating the coupon thickness  $t$  leads to an underestimation of stress calculated from the load cell force  $F$ :

$$\sigma = F/(wt),$$

with  $w$  being the coupon width. The error introduced by this effect was investigated for the ( $\pm 30^\circ$ ) biaxial braid to provide a quantification of the overestimation. A first comparison with a caliper on a single coupon compared to thickness measurements using a micrometer screw showed that the caliper measurements provide as assumed an upper bound for the thickness values. To quantify the difference between the average thickness and the one obtained by caliper-measurements, focus-variation measurements of selected specimen (cf. Fig. 3.12) have been conducted [184]. The focus-variation measurements obtain the variation of thickness, with a vertical resolution of  $0.4 \mu\text{m}$ , by using the sharpness of recorded images.

**Fig. 3.12:** Two-dimensional thickness profile for a 0A00 specimen (shorter edge is 11-direction)

The error of a caliper measurement was estimated from a height profile in 22-direction (which represents the direction of the caliper for a thickness measurement) as

$$\text{error} = t^{max} - t^{mean}$$

Four measurements with two specimen (BB30\_OA00 and BB30\_OA90) revealed an error between 2% and 9% for the measurement of the thickness using the maximum value. For three out of the four specimen the error was around 2% while the bigger deviation was measured for one specimen that had a thickness gradient across the specimen width shown in Fig. 3.13. The investigations proofed that the error of the caliper thickness

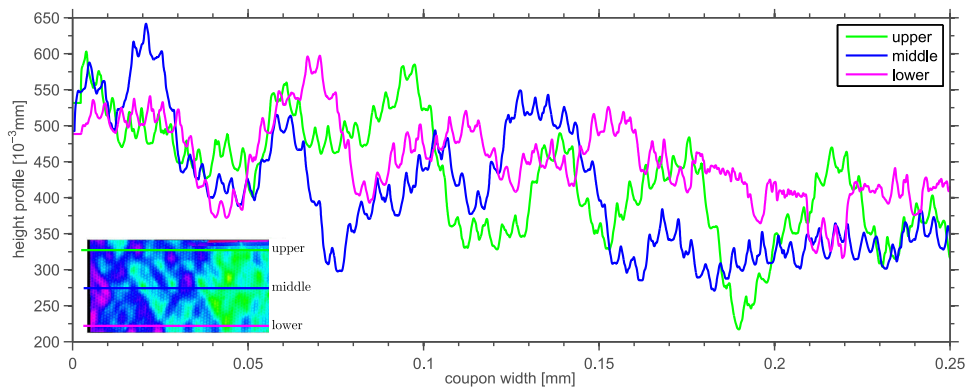


**Fig. 3.13:** Height profile with thickness gradient (height values are relative do not reflect actual specimen thickness)

measurement is comparable small for specimen without a thickness gradient. The presence of a thickness gradient shall be checked with caliper measurements from both sides of the coupon. Based on the results, caliper measurements were used for all specimens, which are much more efficient and can be performed with conventional equipment. Beside this, focus-variation measurements were shown to be useful for characterizing the thickness variation.

### 3.4.3. Off-axis experiments

When orthotropic materials are loaded off-axis, i.e. not in one of the orthotropic axes, a coupling exists between the longitudinal normal deformation and the in-plane shear deformation (shear-extension coupling, see e.g. [175]). This is the case in an off-axis experiments under uniaxial load. As the in-plane shear deformation is suppressed by the machine gripping system, additional shear stresses may be introduced in the proximity of the tabs, resulting in stress peaks and an undesirable non-uniform stress state on the coupon.

Sun and Chung [185] addressed this problem and proposed a new *oblique* tab design for off-axis experiments, which was shown to improve the homogeneity of the strain field for off-axis coupons. The main points of the theory are reviewed here and modifications for the application to braided composites are given.

The theory was originally developed for UD composites under off-axis load, but is applicable to any orthotropic material. The strains in an orthotropic material under uniaxial stress  $\sigma_{xx}$  can be calculated from

$$\begin{aligned}\varepsilon_{xx} &= \bar{S}_{11} \cdot \sigma_{xx} \\ \varepsilon_{yy} &= \bar{S}_{21} \cdot \sigma_{xx} \\ \gamma_{xy} &= \bar{S}_{61} \cdot \sigma_{xx}\end{aligned}\tag{3.6}$$

$\bar{S}_{ij}$  are the components of the compliance matrix  $\bar{\mathbf{S}}$  in the global xy-coordinate system that can be obtained from the orthotropic compliance matrix  $\mathbf{S}$  in the material coordinate system by transformation. Calculation of the compliance matrix  $S_{ij}$  requires the engineering constants  $E_{11}$ ,  $E_{22}$ ,  $G_{12}$ ,  $\nu_{12}$  to be known a priori, which was not the case for the ( $\pm 30^\circ$ ) braid. Due to this, an general approach using an equivalent laminate model is used. The biaxial braided composite is idealized as an ( $\pm 30^\circ$ ) angle-ply laminate with the orientations of the plies given by the braiding angle. In this case, the compliance matrix in the global xy-coordinate system for biaxial braided composite  $\bar{\mathbf{S}}^{BB}$  can be calculated from:

$$\bar{\mathbf{S}} = \bar{\mathbf{S}}^{BB} = \mathbf{T}^T(\psi) \cdot \mathbf{S}^{BB} \cdot \mathbf{T}(\psi)\tag{3.7}$$

$$\mathbf{S}^{BB} = [\mathbf{Q}^{BB}]^{-1} = \left[ \frac{1}{2} (\bar{\mathbf{Q}}^{UD+\theta} + \bar{\mathbf{Q}}^{UD-\theta}) \right]^{-1}\tag{3.8}$$

$$\bar{\mathbf{Q}}^{UD\pm\theta} = \mathbf{T}^{-1}(\pm\theta) \cdot \mathbf{Q} \cdot \mathbf{T}^{-T}(\pm\theta)\tag{3.9}$$

Where  $\bar{\mathbf{Q}}^{UD}$  is the global (xy) stiffness matrix of an UD material comprising the same fiber/matrix combination as the braided composites and  $\mathbf{T}$  is a transformation matrix given in Eq. D.9. Under the assumption of a linear displacement field and the stress strain relations from Eq. 3.6, Sun and Chung [185] showed that the displacement is uniform along a straight line at the angle  $\phi$  (Eq. 3.10) to the loading direction.

The definition of the oblique tab angle  $\phi$  given in [185] is shown in Fig. 3.14. The definition yields the drawback that  $90^\circ$  and  $-90^\circ$  describe the same (rectangular) shape of the tab, which leads to a discontinuity in the value of the oblique angle over the off-axis angle for biaxial braided composites as shown in Fig. 3.14. To overcome this, the angle between y-axis and oblique tab edge is defined as the oblique angle  $\chi$ . The derivation according to [185] yields:

$$\cot(\phi) = \tan(\chi) = -\frac{\bar{S}_{16}}{\bar{S}_{11}}.\tag{3.10}$$

The oblique angles for the coupons tested in this thesis have been calculated using material parameters from [186]:  $E_{11} = 143000$  MPa,  $E_{22} = 9400$  MPa,  $G_{12} = 5100$  MPa and  $\nu_{12} = 0.3$ . The oblique angles obtained are given in Table 3.3. Due to the small oblique tab angle calculated for the OA30 ( $\psi = 30^\circ$ ) case, rectangular tabs were used. Linear FE calculations were conducted for all off-axis load cases to check the influence of the oblique tabs to the homogeneity of the strain field. A stress concentration reduction was found in all cases, when oblique tabs were used. Furthermore, it was found by a parametric



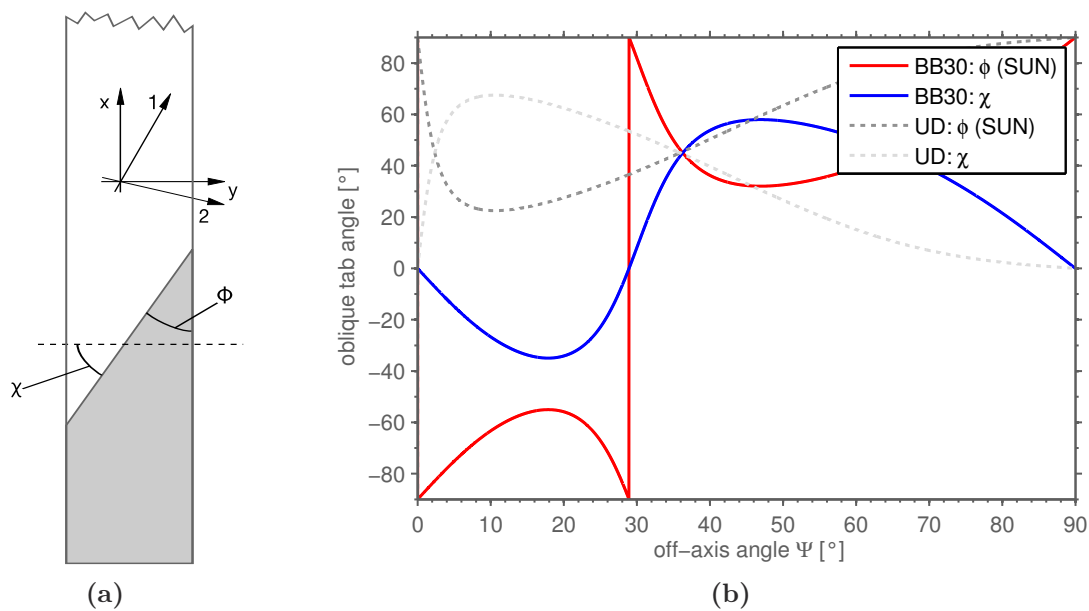


**Fig. 3.14:** Comparison of oblique-tab angle definition  $\chi$  and the original one from [185] for UD and biaxial braid  $\pm 30^\circ$  (BB30)

**Table 3.3.:** Calculated oblique angles for the ( $\pm 30^\circ$ ) biaxial braid

$\psi [^\circ]$	15	30	45	60
$\chi [^\circ]$	-33.7	8.1	57.7	50.9

study that small changes of the off-axis angle (e.g. due to manufacturing tolerances) do not significantly change this tendency.

#### 3.4.4. Test set-up and procedure

All tensile test series with exception of the BB30\_OA30 tests have been conducted on a *Hegewald & Peschke Inspekt 250* (HP250) universal testing machine with 250 kN maximum force. The BB30\_OA30 tensile test series and the compression test have been done on a *Hegewald & Peschke Inspekt table 100* (HP100) universal testing machine with 100 kN maximum force. The load was introduced into the specimen with a servo-hydraulic gripping system at the HP250 (Fig. 3.15), and with mechanical wedge type grips for tension tests and spherical hinge mounted steel platens for the compression tests (Fig. 3.16a) at the HP100. Load cell force and machine head displacement were recorded from the testing machines with a frequency of 50 Hz during the experiments. The machine head speed was chosen according to the standards [84, 85] to 2 mm/min and 1.3 mm/min for the tension respectively the compression tests.

At least five experiments with monotonic loading up till specimen failure were conducted for each configuration in tension and compression. In addition to the monotonic experiments, two tensile loading/unloading experiments have been conducted for each off-axis angle. The goal was to obtain information about modulus change and inelastic

deformation. In the loading/unloading experiments, the specimen were loaded in four load cycles incrementally to approximately 25%, 50%, 80% and 100% maximum force. For each cycle, the specimen were loaded to the designated load, unloaded completely to a small force (approximately 10 N) and reloaded to the next load level. The machine head speed for both, loading and unloading was identical to the monotonic experiments. The maximum force for the first three load cycles was estimated from the previous monotonic experiments, while the specimen were loaded up till failure in the fourth load cycle.

During the tensile tests, a *Photron FASTCAM SA5* high-speed video camera (Fig. 3.15) was used to record the final failure process of the specimen. Due to the limited memory in the camera, the choice of image resolution, duration of the recording and camera frame rate requires a compromise. A resolution of  $384 \times 1008$  pixels<sup>2</sup> gave an image acquisition rate of 17,500 frames per second and a total recording time of approximately 1.3 seconds was chosen. The chosen frame rate provided enough pictures to observe the final failure process and the resolution was fine enough to observe the formation of cracks on the specimen surface. A 400 watt flood light was used to provide an adequate lightening for the high-speed video camera. Due to the coverage of the end of the specimen by the gripping system, the area filmed by the high-speed camera was around  $80 \times 30$  mm<sup>2</sup> (height  $\times$  width) and positioned in the middle of the specimen's gauge section. The camera was triggered manually directly after final failure with the last 1.3 seconds recorded being stored on the memory.

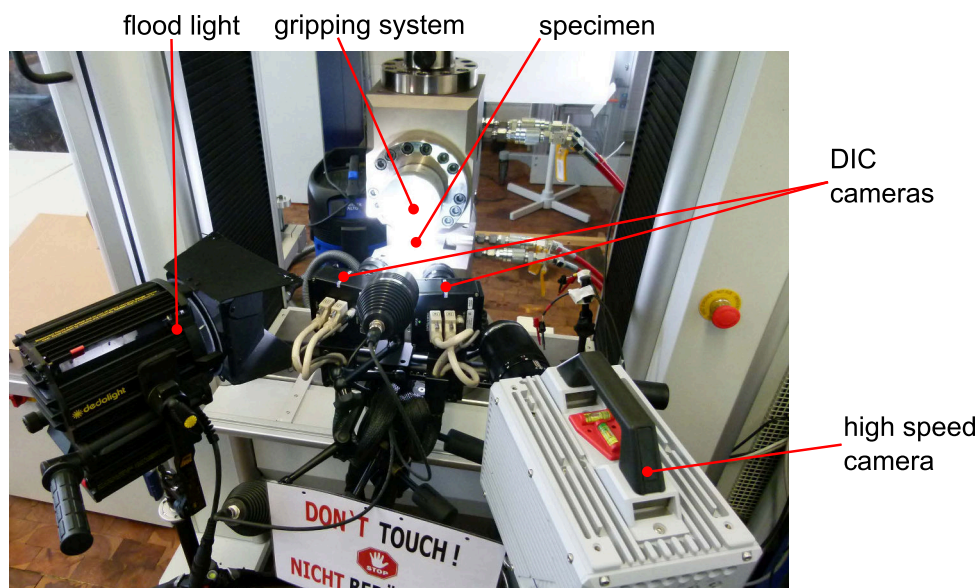


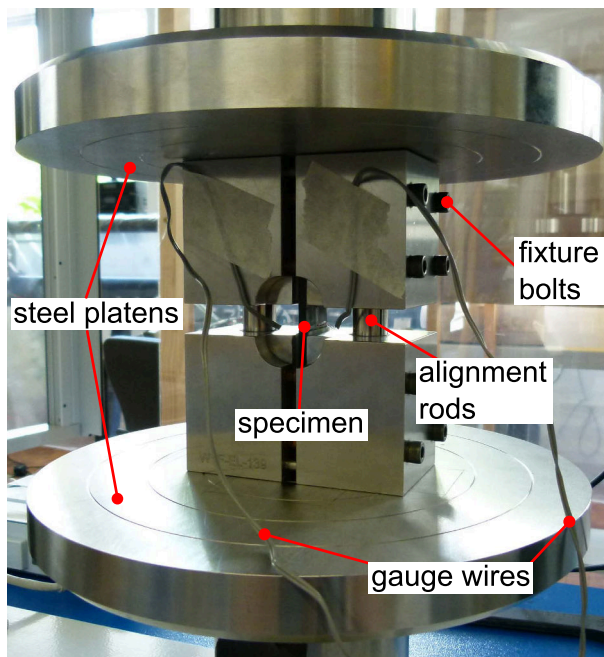
Fig. 3.15: Set-up for the tensile experiments (HP250)

The compression test used the combined loading compression (CLC) test fixture according to ASTM D6641 [85, 183]. The CLC is shown in shown in Fig. 3.16a and consists of four steel blocks, aligned with vertical rods and eight bolts to fixate the specimen. The load is introduced via shear and end-loading into the specimen, with the bolt torque controlling the shear to end-load ratio.

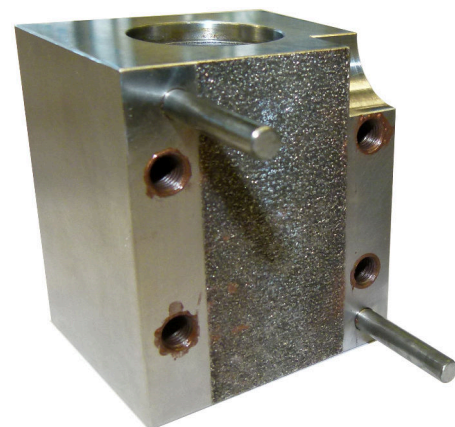
The specimens were installed into the fixture according to the procedure given in the standard. The torque of the fixture bolts chosen was 3 Nm in all experiments except for the OA30 test series, where 10 Nm were used. The torque for the OA30 series was increased,

as recommended in the standard, to prevent end-crushing. End-crushing can occur for specimen with a high amount of fibers in the loading direction. Wegner and Adams [183] investigated the effect of the clamping and showed that torques up till 10 Nm have only minor effect on the measured strength.

After the first test series OA90, which was conducted without tabs, preliminary failure in the gripping area resulting in low strength values was observed for the OA00 test series without tabs. The lowered strength is believed to be to the introduction of stress concentration through the interaction of the wavy specimen surface (Sec. 3.4.2) with the rough clamping area of the CLC (see Fig. 3.16b). As a consequence, tabs (dimensions given in Table 3.2) were bonded for all further compression test series (OA00, OA15, OA30, OA45, OA60). The tabbed specimen provided approximately 20% higher strength values for the OA00 test series. For the OA90 test series, the influence of the rough clamping area to the strength could be neglected, as failure occurred within the gauge section and no cracking was observed in the clamping area. The high-speed camera was not used for the compression tests as it was not possible to capture and illuminate the coupon sufficient in the test fixture.



(a) CLC test fixture placed in the test machine



(b) Carbide particle-coated gripping surface

**Fig. 3.16:** Combined loading compression (CLC): four blocks of the test fixture assembled (left) and single steel block with gripping surface (right)

### 3.4.5. Strain measurement systems

Strain on mechanical specimen is commonly measured with foil strain gauges bonded to the surface of the specimen. The conventional strain gauge measurement technique can be applied to braided composites, but attention has to be paid regarding interpretation of the measured values, as the surface strain field of textile composites normally is inho-

mogeneous [86, 99, 123]. The strain gauge selected should be sufficient big compared to the yarn architecture, to ensure that the measured strain is representative for the average specimen strain: the length of the strain gauge should be bigger than the unit cell size in load direction [88]. Additionally, the applicability of strain gauges is normally limited to relative small strains (5% maximum strain according the manufacturers specification [187]) and surface cracking can lead to preliminary failure of the strain gauge [12].

An alternative to strain gauges is digital image correlation, which is a contact-free measurement technique for spatial or 3D deformation measurement. The deformation on the specimen is calculated by correlation of several images of the specimen surface taken during the experiment. DIC provides a full-field strain information, thus all in-plane strain components can be investigated in the measurement area. This enables correlation of local effects such as strain peaks with the geometry of the local reinforcement. DIC was successfully used to measure local and average strain fields of biaxial braided composites up to high strains of 20% [12]. Furthermore, DIC results can be used to determine information about the damage initiation [123] and damage mechanisms, i.e. crack location and orientation, of braided composites [99]. The present section gives an overview about the strain measuring methods used in this thesis.

### Digital image correlation

The commercial DIC system GOM ARAMIS 4M with 4 megapixel resolution cameras was used to measure the deformation of the coupon during the tensile tests. The system was used in the three-dimensional measuring mode, comprising two cameras aligned to the surface of the specimen at a defined angle as shown in Fig. 3.15. Three-dimensional deformation measurement allows to obtain both, in-plane and out-of-plane deformation. The flood light of the high-speed camera was used as a light source for the DIC.

The choice of the region of interest (ROI) of the DIC measurement requires a compromise between size and resolution. For textile composites, a high resolution is required to capture the quantity of local strain variations, but also low resolutions allow to determine quantitative effects [123]. The ROI was chosen  $65 \times 48 \text{ mm}^2$  (height  $\times$  width) at the center of the specimen, which was found to be appropriate to resolve the local variations of the strain field induced by the discrete yarn architecture.

The DIC system was calibrated prior to the measurements using a calibration panel. The calibration is necessary for the system to recognize the exact position and orientation of the cameras relative to each other and to the specimen. A precise calibration is necessary as the system calculates the 3D-deformation of the specimen from the 2D images from the two cameras. The frequency of image recording was in most cases set to 2 Hz, which provided appropriate frame rate and storage size of the images recorded during one measurement.

In advance to the experiments, the plain tool-surface of the specimen was painted white and subsequently sprayed with a black random speckle pattern. The speckle pattern is required for the DIC system to recognize the points on the coupon surface. The principle of DIC measurements is described e.g. by [188]: the ROI is divided into an evenly spaced grid comprising so-called *facets*, with the center of a facet representing one *result point* for the displacement (Fig. 3.17). The deformation of the facets is tracked by the DIC system with the use of the gray value distribution inside the facet. Several criteria for

the correlation of the facets are provided by Pan et al. [188]. The choice of the facet size is a compromise between local resolution of deformation and noise, which is increased with smaller facets, as the averaging area for the deformation is decreased. A facet size of  $17 \times 17$  pixels with a 2 pixel overlap of the facets (Fig. 3.17) was chosen for the experiments. The resolution yielded 50 facets over the width of a coupon, which was equivalent to approximate 7 facets per yarn width.

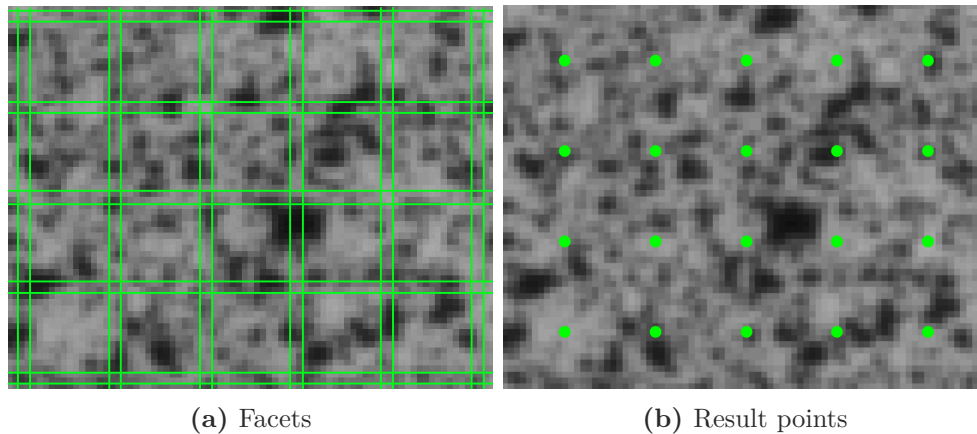


**Fig. 3.17:** Speckle pattern including facets and corresponding result points for  $17 \times 17$  pixel facets with 15 pixel facet distance (2 pixel overlap)

With the deformed position of the facets known, the displacement and deformation gradient for every result point can be calculated. The deformation gradient at the result points is commonly calculated by a least square fit over a square window (strain calculation window) of a minimum of  $3 \times 3$  result points. This is equivalent to assuming the deformation field in the strain calculation window to be a linear function of the coordinates. The fitting process helps to largely remove the noise from the strain signal [188], thus a large fitting strain calculation window is desirable for homogenous strain fields. But in the case of inhomogeneous strain fields, a small strain calculation window is required, thus the minimum  $3 \times 3$  strain calculation window was used.

### DIC: average strain calculation

Digital image correlation provides a strain tensor for every result point on the specimen surface. Different methods can be used to calculate the average specimen strain from the strain field:

1. Averaging the strain from of all result points (facets) of the strain field
2. Definition of a certain averaging region (virtual strain gauge) on the specimen
3. Calculation of the average strain from discrete points (virtual extensometer)

Every method yields advantages and disadvantages: Averaging of all result points is simple to use, but it may overestimate the average strain, when small cracks are forming

on the specimen surface which are not recognized as cracks by the DIC system<sup>1</sup> (marked at the coupon edges in Fig. 3.18). The definition of a virtual strain gauge omits this issue at least for edge cracks which were observed in some of the experiments, but a large part of the deformation field is neglected by the averaging and size and position of the virtual strain gauge are somehow arbitrary. A virtual extensometer defined between two points provides a simple averaging for longitudinal strains but is more complex to be used for transverse and shear strain e.g. in the case of a non-rectangular facet field.

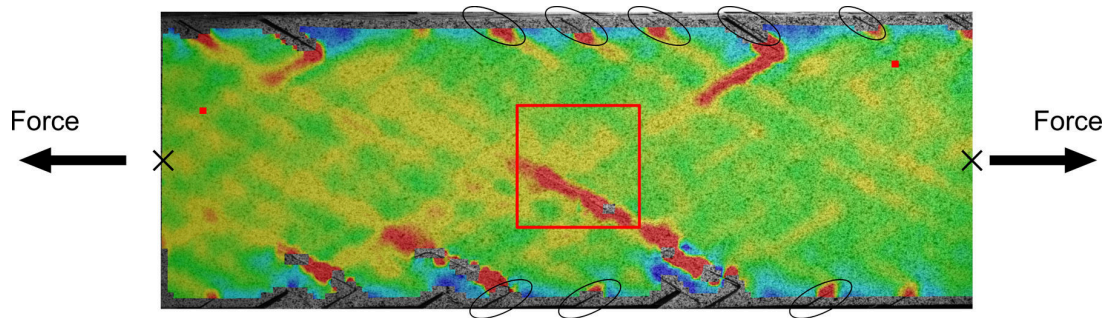


**Fig. 3.18:** DIC measurement of a BB30\_PP02\_PT\_0A00\_3 specimen with surface cracks at the edges and in the center, the red area refers to the virtual strain gauge, the black crosses mark the points used for the virtual extensometer

The different methods were compared for several measurements, with the results summarized in Fig. 3.19. The virtual strain gauge was chosen in the middle of the gauge section with a size of  $10 \times 10 \text{ mm}^2$  and the virtual extensometer used the two points marked with crosses in Fig. 3.18. In many cases the results from the three methods are similar as shown in Fig. 3.19a, where the DIC measurements were additionally compared to the measurements from a foil strain gauge placed on the backside of the coupon. The strain measured from the foil strain gauge is slightly higher as the DIC strain prior to final failure, which is due to surface cracking in the area, where the strain gauge is bonded. Furthermore, it should be noted that the strain obtained by the virtual extensometer can vary depending on the position of the points picked. The virtual strain gauge is problematic, if the crack localization on the specimen is in the area of the virtual strain gauge, as shown in Fig. 3.18. The average specimen strain is in these cases overestimated by the virtual gauge method (Fig. 3.19b). Due to the dependence of the average strain on the position of the chosen strain averaging region for the virtual gauge and the virtual extensometer, the average over all facets was chosen for all specimen to calculate the average strain.

### Strain gauge measurements

The alignment rods of the CLC compression test fixture (Fig. 3.16a) inhibit a proper view to the surface of the specimen. These geometric constraints prohibit an adequate illumination and image acquisition as required for the DIC system. Additionally, the

<sup>1</sup>If the DIC-system does not recognize the cracks, a strain value is calculated over the crack, which is artificially high due to the crack opening and has to be judged as non-physical, as no continuum exists in the position of the crack.

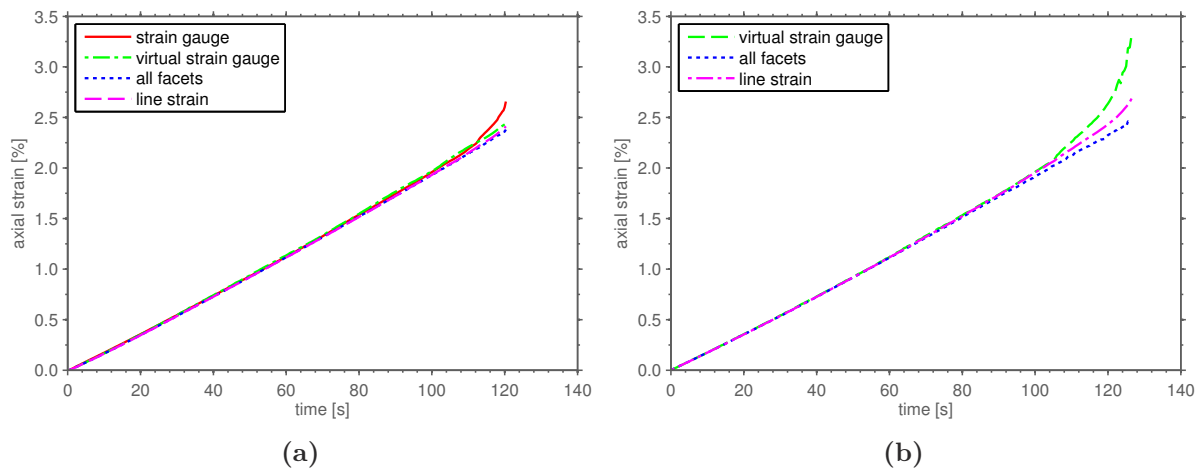


**Fig. 3.19:** Comparison of strain averaging methods for specimens BB30\_PP02\_PT\_OA00\_2 (a) and BB30\_PP02\_PT\_OA00\_3 (b)

ASTM D6641 standard requires a validation of the coupon test with the bending of the specimen to ensure that the specimen failed due to material fracture rather than stability failure. The bending is calculated from the strains on two sides of the specimen, which would require a two-sided DIC measurement.

Linear foil strain gauges were therefore chosen for the compression experiments in a back-to-back arrangement. *Tokyo Sokki Kenkyujo FLA-3-11* strain gauges with a gauge size of  $3 \times 1.7 \text{ mm}^2$  and a backing size of  $8.8 \times 3.5 \text{ mm}^2$  were bonded on both sides of the specimen. The strain gauges were the maximum size fitting onto the free gauge length of the specimen, as additional space is needed for the gauge wires. The gauge signals were recorded with a *HBM MX840A* universal data recorder at a frequency of 50 Hz. Bending of the specimens was calculated over the complete experiment according to

$$B = \frac{\varepsilon^1 - \varepsilon^2}{\varepsilon^1 + \varepsilon^2}, \quad (3.11)$$

where  $\varepsilon^1$  and  $\varepsilon^2$  are the strain signals of the two strain gauges.

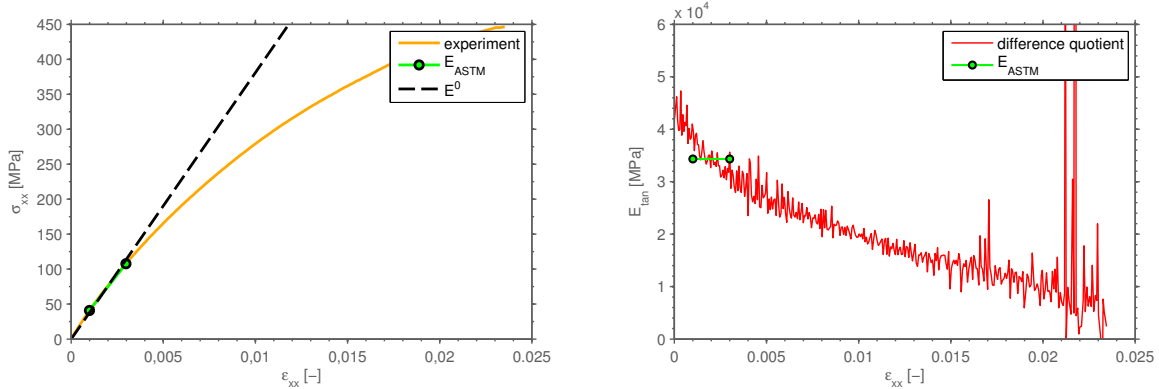
### 3.4.6. Evaluation methods

Besides the evaluation procedure given in the standard, advanced methods were used to characterize the nonlinear behavior of the ( $\pm 30^\circ$ ) braided composite in the off-axis experiments. The tangent modulus was calculated for each specimen to determine the degree of nonlinearity of the stress-strain curve. Furthermore, the loading / unloading experiments were evaluated to determine the degree of inelastic deformation. The following section describes the evaluation methods used.

#### Tangent modulus

For both, tension and compression experiments the elastic modulus shall according to the standards be evaluated within a range of 0.1%-0.3% axial strain. This is appropriate for

materials behaving linear within this strain range, but leads to an overestimation of the modulus for biaxial braided composites, when considering the complete strain range (cf. Fig. 3.20a).



(a) Modulus according to ASTM D3039 and initial modulus

(b) Progression of the tangent modulus

**Fig. 3.20:** Stress-strain curve and tangent modulus for specimen BB30\_PP02\_PT\_0A00\_2

The tangent modulus evaluated from the stress-strain curve can provide both, the initial modulus and information about the degree of nonlinearity of the stress-strain curve:

$$E_{tan} = \frac{d\sigma}{d\varepsilon} = \frac{\Delta\sigma}{\Delta\varepsilon} = \frac{\sigma_{i+1} - \sigma_i}{\varepsilon_{i+1} - \varepsilon_i} \quad (3.12)$$

Fig. 3.20b shows that the tangent modulus evaluated with the finite difference quotient given in Eq. 3.12 is rather noisy and the initial modulus obtained by the finite difference quotient will be strongly influenced by the noise. To compensate the issues regarding noise in the tangent modulus, a regression analysis of the stress-strain curve is used. A 2nd degree polynomial function given in Eq. 3.13 is fitted to the stress strain curve, which allows to directly obtain the modulus.

$$\sigma = a_0 + a_1\varepsilon + a_2\varepsilon^2 \quad (3.13)$$

Fitting the stress strain curve instead of the tangent modulus is beneficial, as the goodness of the fit can be judged more accurately as in the case of the noisy tangent modulus. The regression analysis was done within MATLAB by using the *polyfit* function, which uses the least square method to calculate the unknown coefficients  $a_i$  in Eq. 3.13. The goodness of fit of the regression was checked by using the R squared ( $\mathbf{R}^2$ ) coefficient of determination. A minimum of three data points is required to determine the unknown coefficients, while a certain smoothing is introduced when more points are used.

The data point intervals for the regression were chosen overlapping as shown in Fig. 3.21. The interval is shifted by one data point to the next interval: the regression for the point  $m = 1/2 \cdot (N_P + 2i - 1)$  is calculated over the strain points  $n = i \dots i + (N_P - 1)$ .



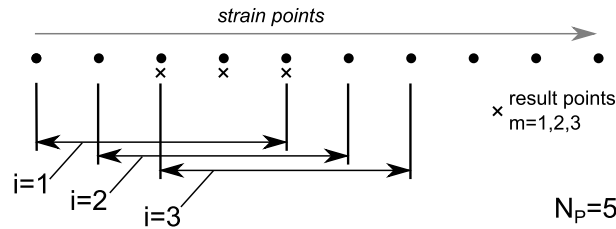


**Fig. 3.21:** Data point intervals used for data regression

The regression yields the unknown coefficients in Eq. 3.13, i.e. the stress-strain behavior is known in the regression interval. From the stress strain behavior, the tangent modulus can be calculated directly as

$$E_{tan} = \frac{d\sigma}{d\varepsilon} = a_1 + 2a_2\varepsilon. \quad (3.14)$$

The initial modulus can be obtained from the first interval ( $i = 1$ ):

$$E^0 = E_{tan}(\varepsilon = 0) = a_1^{i=1} \quad (3.15)$$

For the experiments in this thesis, a window size of  $N_P = 10$  was chosen for 2 Hz measurements respectively linearly scaled for other frequencies. The progress of the tangent modulus calculated as described above is shown in Fig. 3.22 and compared to the tangent modulus obtained by finite differences. The tangent modulus calculation was used to determine the initial modulus and the progression of the modulus for both, monotonic and loading/unloading experiments.

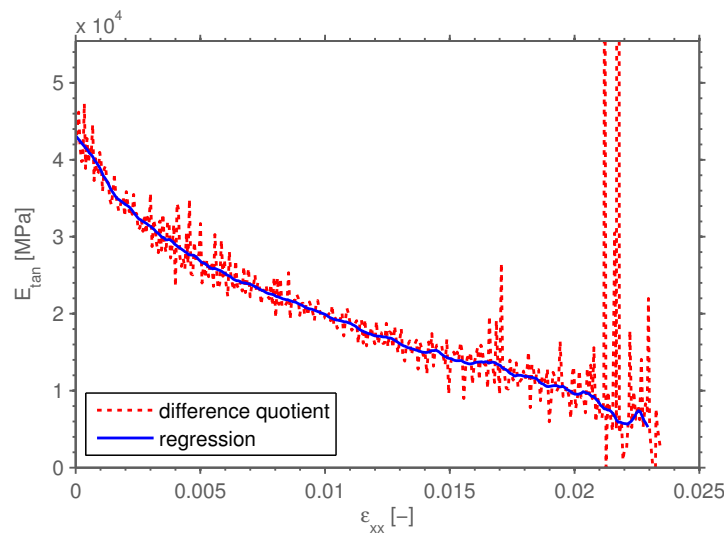


**Fig. 3.22:** Comparison of tangent modulus for BB30\_PP02\_PT\_0A00\_2 obtained by finite difference and regression

### Evaluation of loading/unloading experiments

During the loading/unloading experiments a significant hysteresis, i.e. loading and unloading on different paths, was observed within the stress-strain curves, as schematically shown in Fig. 3.23. The hysteresis effect is commonly observed in composite materials and attributed to residual stresses at the fiber-matrix interface [189] or fiber-matrix interface friction, as well as plastic and viscoelastic effects in the matrix [190]. Fouinneteau [12] reported hysteresis for biaxial braided composites and also attributed it to friction between fiber and matrix.

For the evaluation of the experiments, the basic theory of elastic and inelastic material nonlinearities is used [191]. The principle is shown in Fig. 3.23: the unloading modulus is obtained from the unloading (1) and reloading (2) point and compared to the cases of *ideal inelastic* and *ideal elastic* deformation.

$$E^1 = \frac{\sigma^{(1)} - \sigma^{(2)}}{\varepsilon^{(1)} - \varepsilon^{(2)}} \quad (3.16)$$

With the superscripts in brackets referring to the points given in Fig. 3.23. Ideal inelastic

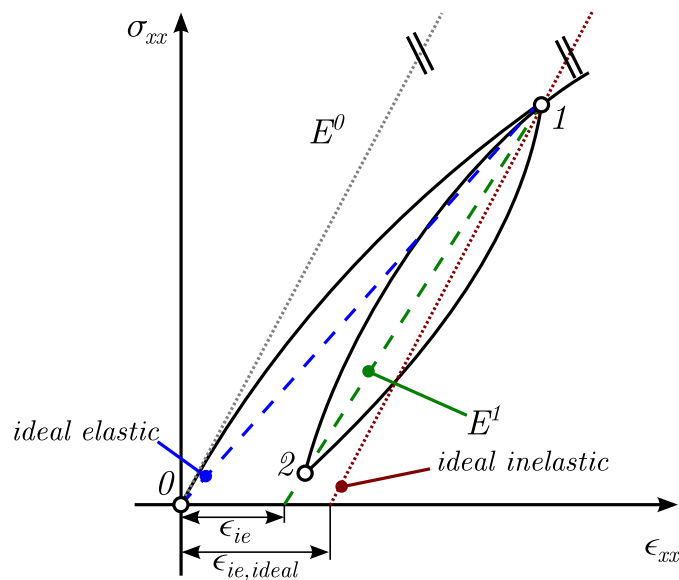


**Fig. 3.23:** Principle for evaluation of the loading/unloading experiments

deformation is calculated under the assumption that the initial modulus does not change, while ideal elastic deformation, i.e. all the nonlinearity of the stress-strain curve is due to material damage [163], is calculated under the assumption of zero residual inelastic deformation. The residual inelastic (ie) deformations yield as

$$\varepsilon_{ie} = \varepsilon^{(1)} - \sigma^{(1)}/E^1 \quad (3.17)$$

$$\varepsilon_{ie,ideal} = \varepsilon^{(1)} - \sigma^{(1)}/E^0, \quad (3.18)$$

where Eq. 3.17 extrapolates the residual inelastic deformation from the unloading curve as shown in Fig. 3.23. The amount of inelastic deformation  $\eta_{ie}$  is determined by comparing the measured inelastic residual strain with the inelastic strain for the ideal inelastic case:

$$\eta_{ie} = \frac{\varepsilon_{ie}}{\varepsilon_{ie,ideal}} \quad (3.19)$$

Additionally, the damage variable at the unloading point (1) can be evaluated according to Lemaitre [163]:

$$d = 1 - \frac{E^1}{E^0} \quad (3.20)$$

The two quantities, the inelastic strain  $\varepsilon_{ie}$  and the damage variable  $d$  can be used to determine the mechanics of the nonlinearity in the stress-strain curve, i.e. if dominated by elastic or inelastic effects.

For the low forces and strains at the beginning of the experiment, some inherent errors may influence the loading/unloading evaluation: noise in the force signal, misalignment of the specimen, setting effects of the gripping or noise in the DIC strain signal. These measurement errors can lead to two cases that require an idealization for the evaluation, namely a progressive stress strain curve (Fig. 3.24a) or a progressive elastic modulus (Fig. 3.24b). For these cases, the following approximations are introduced:

For the first case, the secant modulus of the first cycle is used as the initial modulus:

$$E^0 = E^{sec,cycle1} = \frac{\sigma^{(1)}}{\varepsilon^{(1)}} \quad (3.21)$$

For the second case, the first unloading modulus is assumed to be the initial modulus.

$$E^0 = E^{1,cycle1} \quad (3.22)$$

As the elastic modulus of the material can be assumed to not increase, the lower tangent modulus at the start of the test is attributed to setting effects. In this case, the unloading modulus is set equal to the initial modulus. The errors reported mainly occurred during the first load cycle with small stresses and strain, i.e. high influence of measurement errors, while the second and third cycle were not influenced.

### 3.4.7. Fiber volume fraction measurements

Fiber volume fraction (FVF) strongly influences the material properties of composite materials and thus is determined during material characterization to ensure comparability of the results. The FVF of the panels used in the mechanical characterization was measured according to the procedure described as *Method I* in ASTM D3171 [43]. The weight of the fibers was obtained after chemical digestion of the matrix, which allows to measure values for fiber volume fraction as well as void volume fraction.

At least three specimen evenly distributed over the panel were used. The specimen size was squared with an edge length of 20–25 mm, which included approximately 10 rectangular unit cells (Fig. 3.9) of the braided reinforcement.

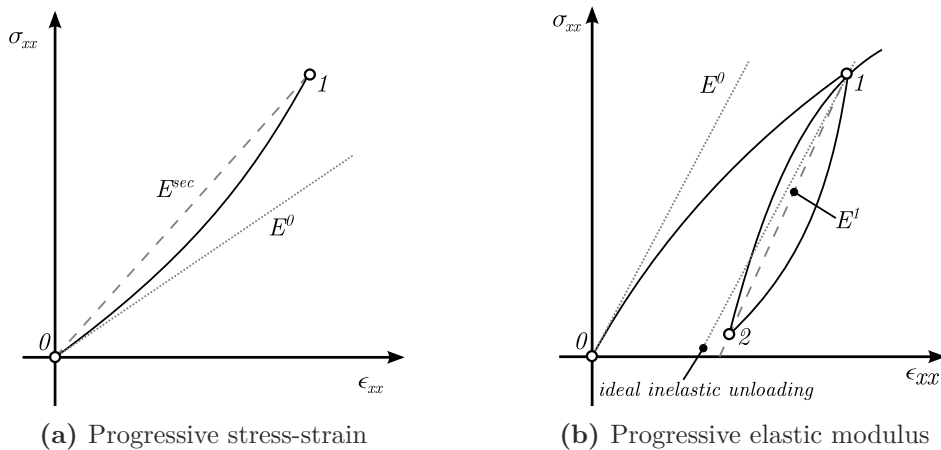


Fig. 3.24: Idealizations during evaluation of the loading/unloading experiments

### Normalization of the test results

When comparing mechanical properties from different test series, the results should be reported for equal FVF. As the measured FVF from different panels normally varies, a data normalization procedure needs to be applied. The method commonly reported for composite materials is linear normalization of properties to the desired FVF [192]:

$$NP = EP \cdot \frac{\varphi_f^{norm}}{\varphi_f^{exp}} \quad (3.23)$$

Where  $EP$ ,  $NP$  are the property determined experimentally and normalized, respectively.  $\varphi_f^{exp}$  and  $\varphi_f^{norm}$  are the FVF of the experiment and the normalization FVF. The normalization procedure is commonly applied to fiber-dominated values as recommended in [192], but for matrix-dominated properties, such as e.g. in-plane shear, no normalization procedure is commonly accepted. As the mechanical behavior of biaxial braided composites is matrix-dominated for various load cases, a normalization procedure applicable for matrix-dominated values is needed.

Within this thesis the experimental results are normalized based on an alternative approach published by Zebdi et al. [119] comprising micromechanics and classical laminate theory. The approach bases on the assumption that the change of a property due to FVF difference in a biaxial braided composite is equal to the change of a property in an analogous laminate due to the same FVF difference. Zebdi et al. [119] proposed the following equation for normalization of elastic properties:

$$NP = EP - (PP^{exp} - PP^{norm}) \quad (3.24)$$

Where  $PP^i$  is the predicted property of the equivalent laminate at the FVF  $\varphi_i$  obtained by micromechanics and CLT and  $EP^{exp}$  respectively  $NP^{norm}$  are the measured and normalized value. Furthermore, the strength is assumed to follow the same trend as the stiffness.

$$\frac{X^{norm}}{X^{exp}} = \frac{NP^{norm}}{EP^{exp}} \quad (3.25)$$

The approach is used within this thesis with minor modifications to the formulation given in [119]. The applied procedure can be summarized as:

1. Calculate UD properties of the plies in the equivalent laminate at FVF of  $\varphi_f^{exp}$  and  $\varphi_f^{norm}$ . The rule of mixtures is used in the fiber direction and Chamis' micromechanics formulae are used for matrix dominated values.
2. Calculate the elastic properties of the  $(\pm\theta)_s$  equivalent laminate from classical laminate theory.
3. Calculate the equivalent laminate's Young's modulus ( $E_\psi$ ) in the off-axis direction.
4. Normalize stiffness and strength with the Young's moduli calculated according to Eq. 3.24 and Eq. 3.25.

More details and equations for the normalization are given in Appendix D. The fiber and matrix mechanical properties used for the micromechanical equations are given in Table A.1 and Table A.2. A comparison of the applied normalization procedure to linear normalization given in Fig. 3.25 shows, that the error of linear normalization can be considerable also for small changes of volume fraction.

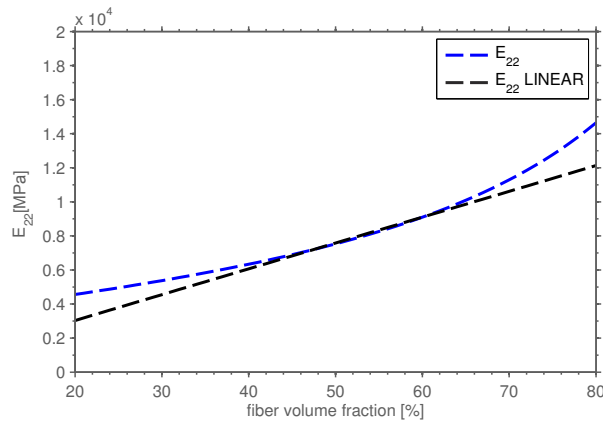


**Fig. 3.25:** Comparison of linear and improved normalization for  $E_{22}$  of a  $(\pm 30^\circ)$  braided composite

## 4. Experimental testing and results

Experimental characterization of biaxial braided composites was carried out for two main purposes within this thesis:

- Get information about the yarn architecture (internal geometry) of biaxial braided composites.
- Characterize the constitutive behavior, with focus to the elastic, nonlinear and failure behavior of biaxial braided composites under combined stress states.

For the yarn architecture, the main goal was to define a strategy for characterization to obtain reliable and robust input parameters for unit cell modeling. The investigation focuses on methods, which on the one hand serve all relevant information for unit cell modeling, and on the other hand can be scaled up to capture yarn architecture changes on braided components. Therefore, ( $\pm 30^\circ$ ) and ( $\pm 45^\circ$ ) biaxial braided composites were investigated to define the measurement procedures, sample sizes and sample positions for the characterization. Optical microscopy and image analysis of surface scans were used as baseline methods. In addition, micro-CT measurements were conducted to gain information about 3D effects in the yarn architecture. The results obtained from the investigations are given in Section 4.1.

The main goal of the mechanical characterization was to measure the elastic, non-linear and failure behavior of carbon/epoxy 2×2 biaxial braided composites under combined stress states. Most of the experimental work found in literature investigates braided composites with different constituent materials and yarn architectures under uniaxial load in one of the orthotropic directions (e.g. [12, 26, 33, 96, 193]). Only little information is available on the mechanical behavior under combined loads (e.g. [32, 93, 94]), which is essential to judge the quality of predictions from different failure criteria. Off-axis experiments of ( $\pm 30^\circ$ ) biaxial braided composites have been used for this purpose, as they offer the possibility to introduce combined stress states into a material with a uniaxially loaded coupon. Universal testing machines and established standard testing procedures could be used to conduct the experiments. Six different off-axis angles were tested in tension and compression, with the failure behavior being evaluated with DIC, high-speed camera recordings and postmortem specimen inspection. The results from the off-axis test series are given in Section 4.2.

### 4.1. Yarn architecture of braided composites

The yarn architecture of braided composites represents the internal geometry of the material, such as yarn angles, yarn paths and yarn shapes. These geometric characteristics are crucial for the material properties on the macroscopic scale: e.g. increased out-of-plane

waviness of yarns will lead to decreased stiffness and strength properties. Thus, the yarn architecture is an important input parameter for modeling the mechanical behavior of braided composites and needs to be robustly characterized. The method used should be both, capable to capture details of the yarn architecture with a high resolution and applicable to measure the yarn architecture on big components.

The methods, commonly reported in literature, for yarn architecture characterization are analytical equations, optical microscopy, micro-CT and image analysis [33, 44, 51, 55, 62–67]. The measured values have been successfully used to predict textile composite mechanical behavior [33, 44] and a comparative study using dry fabric materials proved that the different methods yield comparable results [63]. From the work published on yarn architecture characterization, so far no information on the reliability of these methods to braided composites with high fiber volume fractions is available. Furthermore, no information exists on the dependence of the results on the specimen positions and on the number of required specimen. The goal of the presented study was to provide a robust and efficient strategy for yarn architecture measurement of braided composites. Optical microscopy was chosen as the baseline method for characterization, as its use is successfully reported in literature for braided composites [33, 44].

Measurement techniques for the required geometric parameters were proposed and applied to micrographs. A study with a panel from a ( $\pm 45^\circ$ ) braided composite has been conducted to gather information about the number of the required sections and to investigate the effect of the micrograph position. In addition, to optical microscopy, two techniques, based on surface images were investigated: manual measurements of the braiding angle from scanned images of the panels and automated evaluation of the fiber angles on the surface with an optical sensor [67].

Furthermore, micro-CT measurements were used to capture 3D effects within the yarn architecture. Qualitative considerations are given to the dependence of yarn shape and dimensions to the position along the yarn path. Furthermore, nesting behavior of the plies and yarn shape changes near the surface were investigated.

Finally, the measured properties are summarized and recommendations for the characterization of the yarn architecture of braided composites are given. The results are compared to analytical predictions to illustrate the potential of such predictions, which can be used if no measurements of the yarn architecture are available.

#### 4.1.1. Optical microscopy

Optical microscopy was used to measure the yarn architecture of the braided composites. The method yields several advantages compared to other characterization techniques:

- Optical microscopy can be done with standard laboratory equipment, only machinery for grinding and a microscope are needed.
- Microscopy serves high quality images of infused and cured samples, thus effects of compaction and infusion are included in the measured values.
- It is applicable to both, small materials samples (high resolutions) and also to samples cut out of bigger components.

Two materials, namely a ( $\pm 30^\circ$ ) and a ( $\pm 45^\circ$ ) biaxial braided composite, were investigated. Both braids were manufactured by using similar process conditions for braiding and infusion as described in Section 3.2, with the ( $\pm 45^\circ$ ) braid comprising eight plies in the laminate. For the ( $\pm 45^\circ$ ) braid, a complete panel was available for the characterization and 16 specimen were taken distributed along the length and width of the panel. The measurements from the complete panel were used to determine whether there is a dependence of the results on the position of the micrograph. For the ( $\pm 30^\circ$ ) braid, the specimen were extracted out of cut-waste from the mechanical specimen production. The specimen were embedded and polished as described in Section 3.3.1. The nominal braiding and infusion properties of the materials used are given in Table 4.1.

**Table 4.1.:** Nominal properties of braided composites used for yarn architecture characterization

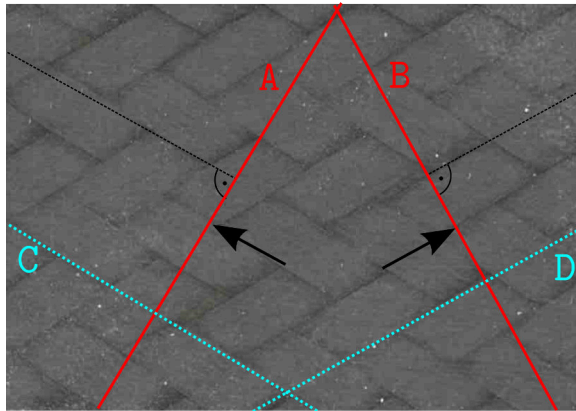
	( $\pm 30^\circ$ )	( $\pm 45^\circ$ )
braiding angle [ $^\circ$ ]	30	45
braid mandrel diameter [mm]	100	125
pattern	2x2	2x2
plies in laminate	5	8
areal weight (per ply) [ $\text{g}/\text{m}^2$ ]	520	540
laminate thickness [mm]	2.5	4
fiber volume fraction [%]	60	60
source of specimen	cut-waste from mechanical coupons	panel not used for specimen production

### Orientation of cuts and parameters measured

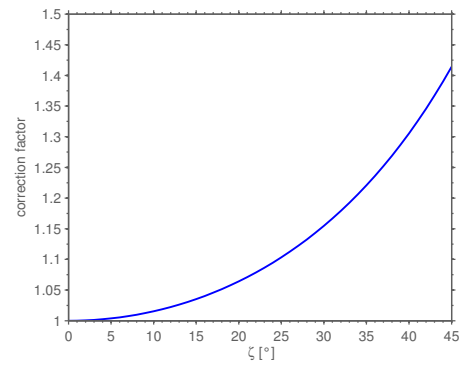
The parameters required to characterize the yarn architecture normally depend on the type of geometric model used for the yarn architecture. While simple models get along with one or two yarn path parameters like amplitude and wavelength of the yarn undulation, more detailed models require additional input about yarn shape, yarn dimension and yarn cross section parameters. In this thesis, the geometric models of the braided composites were built with the academic software package WiseTex [46]. WiseTex requires yarn shape (elliptical, lenticular), yarn width, yarn height, spacing of yarns and the braiding angle to built up a geometric model of a biaxial braid. Additionally, the braid laminate thickness is required if nesting of adjacent plies in a laminate shall be considered. The required properties are summarized in Table 4.2

All parameters, except the braiding angle, can be measured from an out-of-plane micrograph of a braided composite. The required sections A,B to measure the parameters for both yarn directions  $F + / F -$  are shown in Fig. 4.1a: For a measurement of the yarn cross section dimensions, the section should always be perpendicular to the yarns. Additional measurements along the yarn direction (C,D) can be used to get the yarn path coordinates, but have a high uncertainty for yarn dimension measurements. When dimensions are not yarn are not measured perpendicular to the yarn direction, they need





(a) Required micrographs for yarn architecture measurement in a braided composite ( $\pm 30^\circ$ )



(b) Correction factor  $1/(\cos \zeta)$  for misalignment

**Fig. 4.1:** Sectioning for biaxial braided composites: required sections and misalignment error

to be corrected. With the misalignment angle  $\zeta$ , which is the angle between the actual cut and the plane orthogonal to the yarn direction investigated, the correction is e.g. for the yarn width ( $d_2$ ) conducted by:

$$d_2 = d_2^{measured} \cos \zeta \quad (4.1)$$

The misalignment angle is normally not known exactly due to tolerances in the embedding and grinding process. As shown in Fig. 4.1b, the slope of the correction factor, i.e. the potential error due to a wrongly estimated misalignment angle increases with the misalignment angle. Thus, the most robust choice are perpendicular sections  $\zeta = 0$ , where a small misalignment has a negligible effects.

### Measure yarn dimensions

The dimensions measured from the micrographs together with the methods used for the measurement are given in Table 4.2. The yarn cross sections in the geometrical model can be chosen as elliptical or lenticular, which makes it reasonable to use a similar approximation for the yarn dimension measurements. An elliptical cross section was found to be appropriate for the investigated braids. The main advantage of this idealization is that it enables the operator of the measurement to determine both dimensions, yarn height and width within one measurement. Especially yarns with a certain rotation can be measured more precisely.

The operator of the measurement chooses, whether the yarn cross sections in the micrograph can be idealized as ellipses. To validate the manual choice of the operator, the manual judgment was compared to the percentage of areal overlapping from ellipse idealization and real yarn cross section for the ( $\pm 45^\circ$ ) braid. The overlapping area was measured by using a polygon measurement for every cross section. It was found that the manual choice of the operator could be used as a criterion, with the cross sections judged as *good* having an average of 88%-96% areal overlap. For the ( $\pm 45^\circ$ ) braid 88% of the yarn cross section were judged as *good*, giving a sufficient number of measurements. Most

**Table 4.2.:** Parameters describing the yarn architecture of biaxial braids

dimension	variable	measurement method
yarn height	$d_1$	minor axis of ellipse
yarn width	$d_2$	major axis of ellipse
spacing	$p$	distance between two ellipse centers
laminate height	$h$	perpendicular distance between upper and lower surface
braiding angle	$\theta$	angle between yarns at crossover or optical sensor measurements

cases of rejecting the ellipse idealization were two adjacent yarns that were *grown together* (e.g. regions marked blue in Fig. 4.2) and could not be distinguished.

With the yarns defined as ellipses, the spacing can be measured as the distance between two adjacent yarns in the same ply. To avoid the influence of vertical difference between the yarns (see e.g. yarns (28) and (29) in Fig. 4.2), the distance was projected to a horizontal line defined by the mold side (lower edge in Fig. 4.2). The thickness of the laminate was measured perpendicular to the horizontal mold side of the laminate.

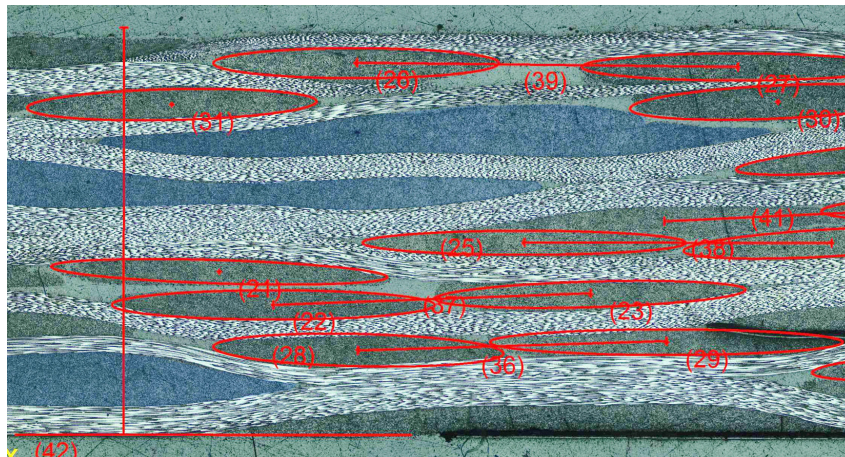


**Fig. 4.2:** Yarn architecture measurements: idealization of yarn cross section as ellipse and grown-together yarns marked blue

### Dependence on position on the panel

As the yarn architecture has an inherent variability, the question arises whether there is a dependence of the measured properties on the position on the panel. This was investigated for the ( $\pm 45^\circ$ ) braid by taking a total of 16 micrographs from positions evenly distributed over a panel. The positions of the samples on the panel are shown in Fig. 4.3. At every position, one micrograph in  $F+$  and one in  $F-$  direction was taken and at least 15 measurements per property have been conducted at each section. The following dependencies were evaluated:

- micrographs taken in length (11) or width (22) direction

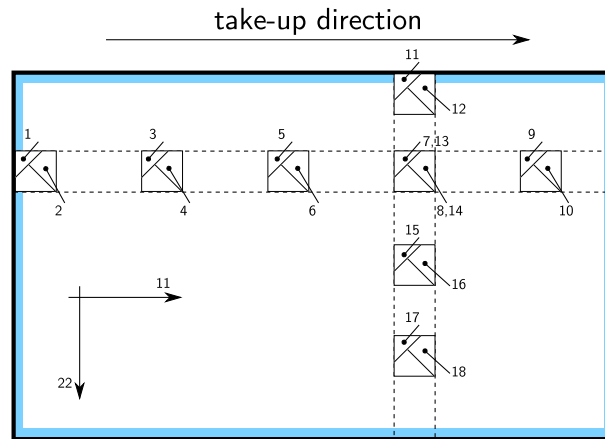


**Fig. 4.3:** Positions of the micrographs on the ( $\pm 45^\circ$ ) panel

- micrographs taken from F+ or F- yarn direction
- micrographs taken from the border or from the middle of the panel

The statistical significance of difference was checked by using a two-sample t-test at 95% significance level. With exception of the yarn height, the differences for all properties did not significantly change depending on the criteria defined above. For the yarn height, a significant difference was found for the values at the edge, when compared to the values in the inner region of the plate (Fig. 4.4). This is due to the the tape present at

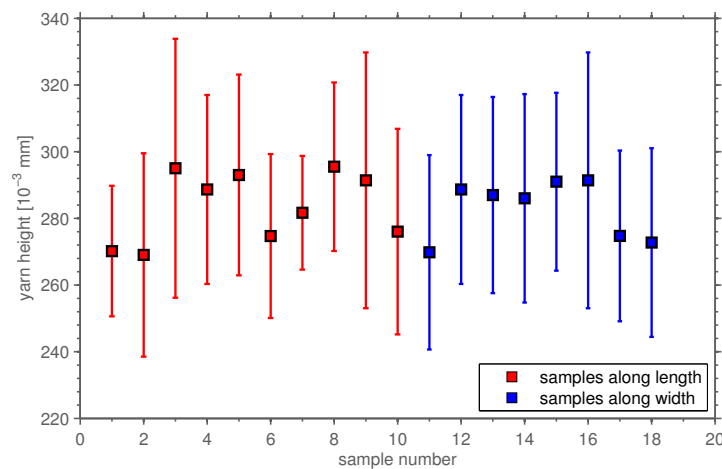


**Fig. 4.4:** Yarn height in dependence of the position on the panel (sample numbers refer to Fig. 4.3)

this position, which is used during the braiding process for stabilization of the plies (cf. Section 3.2). As it can be seen in Fig. 4.4 the values for the yarn height are less in this region (samples 1, 2, 10, 11, 17, 18), which is attributed to the increased compaction during infusion.

### Number of required measurements

Besides the dependence on the position, an important question is how many measurements have to be conducted to achieve a certain accuracy. The number of required samples

was calculated by using a two-sided t-test with a significance level of  $\alpha = 0.05$  and the results are given for a power of 0.8 and 0.95. To determine the required sample size, a technical relevant difference in average values needs to be defined, which was chosen half the standard deviation (cf. Table 4.5) for yarn height and width, 0.05 mm for the thickness, which is equivalent to 1% fiber volume fraction change and  $1^\circ$  for the braiding angle. The calculation furthermore requires the standard deviation of the properties to be known, which was taken from the ( $\pm 45^\circ$ ) measurements. The results for required sample

**Table 4.3.:** Required sample sizes for the geometric parameters

value	average	standard deviation	difference of technical relevance	required samples (power=0.8)	required samples (power=0.95)
$d_1$	282.3 $\mu\text{m}$	29.5 $\mu\text{m}$	15 $\mu\text{m}$	62	102
$d_2$	3091.5 $\mu\text{m}$	260.7 $\mu\text{m}$	130 $\mu\text{m}$	65	106
$p$	3048.1 $\mu\text{m}$	246.1 $\mu\text{m}$	130 $\mu\text{m}$	58	95
$h$	3886.9 $\mu\text{m}$	43.1 $\mu\text{m}$	50 $\mu\text{m}$	13	21
$\theta$	45.6°	1.3°	1°	28	45

sizes are summarized in Table 4.3.

- Yarn width and height need over 100 measurements to be representative with a power of 0.95. With 15-20 measurements per micrograph, which was the case for most micrographs investigated, six to eight different sections need to be investigated.
- The spacing needs the same number of measurements, which is more difficult as less measurements are possible on each section. When not enough measurements are available, the approximation of spacing being equal to the yarn width is reasonable.
- For the braiding angle approximately 50 measurements are needed. It should be noted the standard deviation measured is representative for a complete panel, where effects like s-shape dominate the variance.

It can be summarized that a high effort is needed to obtain precise results for the yarn architecture. However, the position of samples for the sections does not have a significant effect on the results and the approximation of yarn shape as an ellipse is reasonable. The described procedures for measurements and requirements regarding the number of samples were used for the further investigations.

#### 4.1.2. Braiding angle measurements

The braiding angle was not measured from the micrographs, as the samples are limited in size and the braiding angle is known to vary due to the s-shape of the yarns on a panel [33]. The braiding angle was measured as described in Section 3.3.3 from scanned images of the ( $\pm 30^\circ$ ) and ( $\pm 45^\circ$ ) panel. For both panels 70 points evenly distributed over the panel were measured. A repetition of the measurements showed no significant difference, i.e. the influence of the manual measurements is negligible.

The results of the braiding angle measurements are shown in Fig. 4.5. The braiding

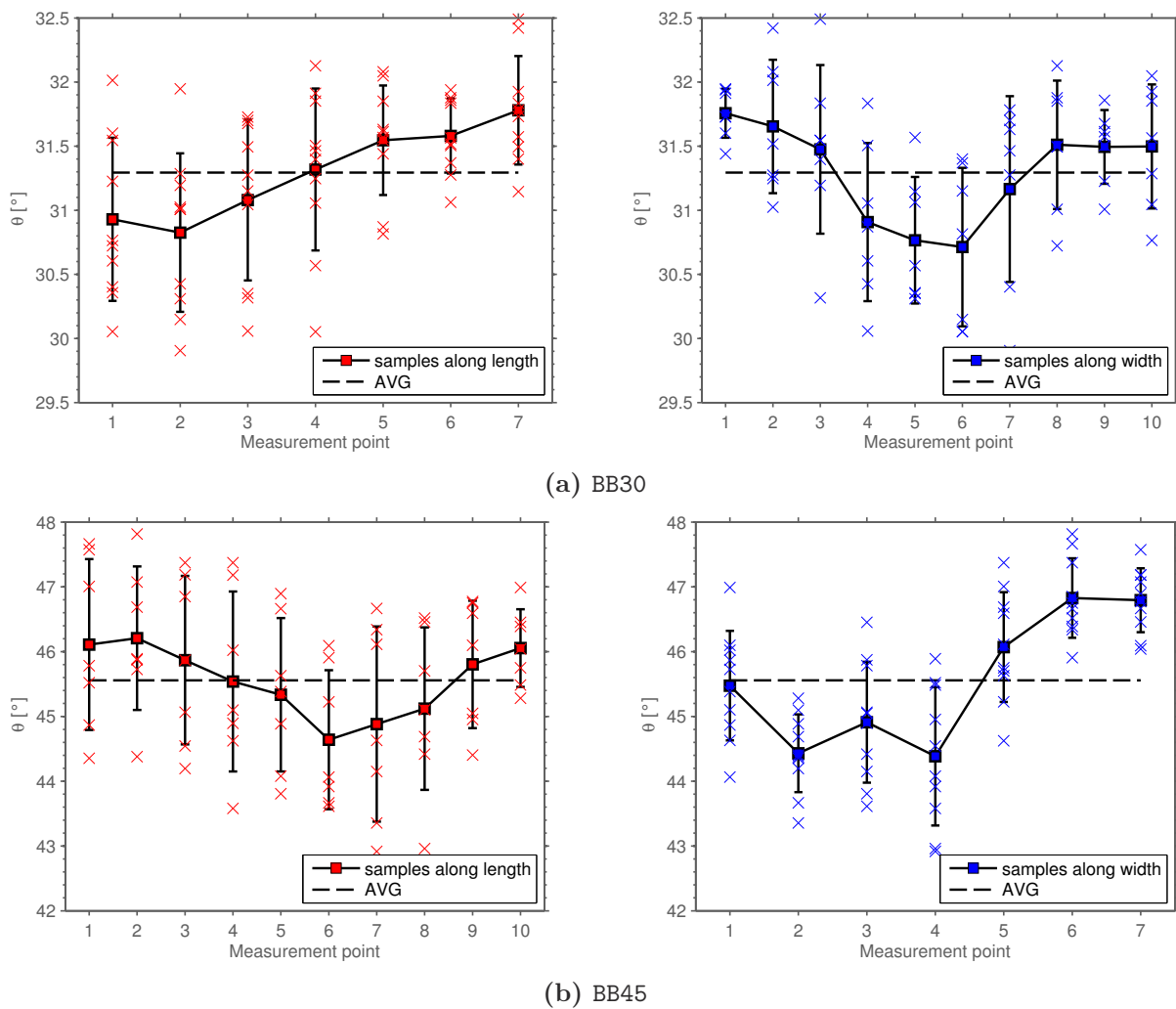


**Fig. 4.5:** Braiding angle over the width and length of the panels (crosses mark the measurements)

angle varies for both braids along the length (equivalent with the take-up direction) and the width of the panel. While the variation in the length direction is different for the two configurations and is attributed to manufacturing tolerances during braiding and ply handling, a clear trend is visible for the braiding angles measured over the width direction: the braiding angle increases in both cases at the edges of the panel. A difference of  $1^\circ$  for the  $(\pm 30^\circ)$  respectively  $1.7^\circ$  for the  $(\pm 45^\circ)$  is measured between center and edge of the panel. The difference is attributed to the so-called s-shape effect of the yarns (cf. [33]), which is believed to be introduced into the braiding process through the effect of gravity.

The average values of the braiding angle, including the standard deviation, for both panels is given in Table 4.4. The braiding angle of  $(\pm 30^\circ)$  is  $1.3^\circ$  higher as desired, which is believed to be due to tolerances in the control system of the braiding machine (cf. Section 3.2). The coefficients of variation are small compared to the other yarn architecture parameters, but an inherent dependence of the braiding angle on the position on the panel is observed, which is important for further considerations, as this dependence can be believed to be also present on braided components.

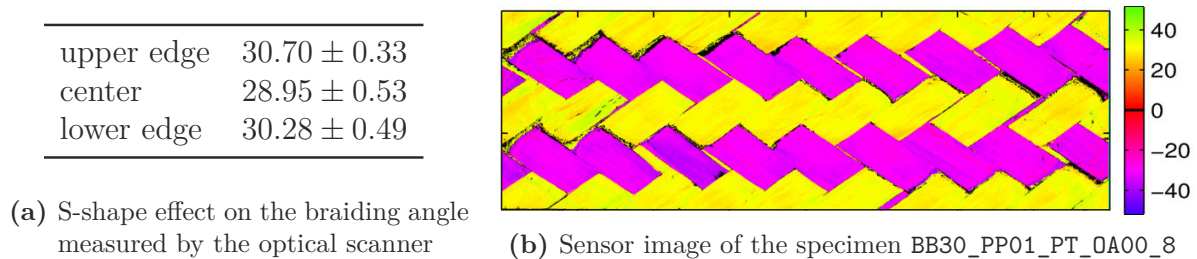
**Table 4.4.:** Results from braiding angle measurements

braid	average braiding angle [°]	standard deviation [°]	CV [%]	number of measurements
BB30	31.29	0.61	1.9	70
BB45	45.56	1.23	2.7	70

### Image analysis

In addition to the manual measurements, an optical sensor [67] was used to measure the braiding angle on selected specimen from the off-axis experiments. The sensor reduces the effort for the measurements of the braiding angle, as the data of the fiber angles can be acquired very quickly and the evaluation is automated using the user-written script described in Section 3.3.3.

The analysis of images from different positions over the panel width, shows that the sensor reproduces the same results regarding the s-shape of the yarns: The braiding angle is lower in the center of the panel and gets bigger towards the edges as shown in Fig. 4.6a.

**Fig. 4.6:** Sensor measurements with OA00 specimen

The results of the sensor were compared to the manual measurements for three specimens oriented in the take-up (11) direction of the ( $\pm 30^\circ$ ). The specimens were measured manually at 42 positions, two images per specimen were taken with the optical sensor, as one image could not capture the complete specimen. One of the images evaluated by the sensor is shown in Fig. 4.6b. An overview to the comparison of manual and sensor measurements is given in Fig. 4.7.

The results from both measurements methods show similar trends, with the average values of the hand-measurements being between  $0.3^\circ$  and  $1.5^\circ$  higher. The main reason for the deviation is believed to be the difference of point-wise hand measurements of yarn edges at crossovers in comparison to complete areal measurements by the sensor. The bigger values from hand-evaluation indicate that the fiber angles are bigger at the crossover points of the yarns. Summarizing the comparison, it can be concluded that both methods can be used for braiding angle measurements, but the sensor yields a higher precision of results, as the measurement is spatial and the hand-evaluation tends to overestimate the braiding angle.

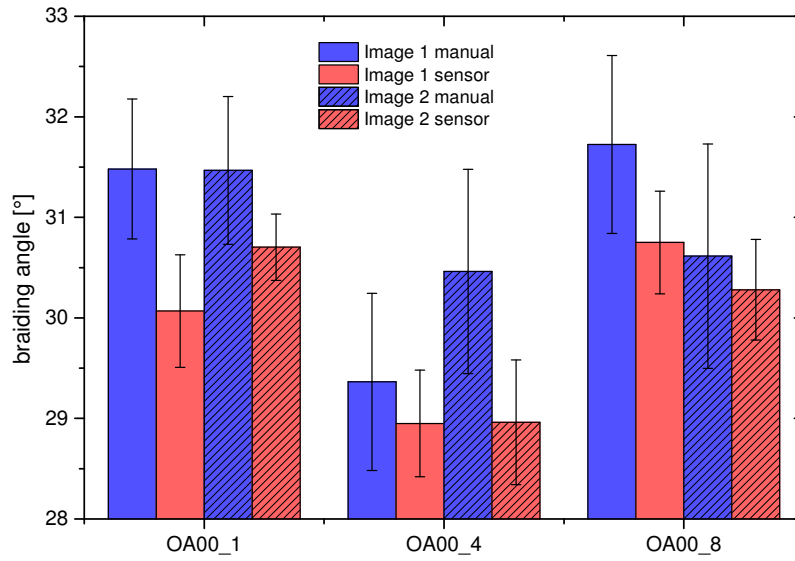


Fig. 4.7: Comparison of values from sensor measurements and manual measurements

### 4.1.3. Summary of measured yarn architecture properties

An overview to the properties measured is given in Table 4.5. From the dimensions of the yarn cross-section the average packing density inside the yarns can be calculated by dividing the area of the filaments in the yarn  $A_{fil}$  by the area of the yarn  $A_{yarn}$ .

$$p_d = \frac{A_{fil}}{A_{yarn}} = \frac{N_{fil} \cdot \pi/4 \cdot d_{fil}^2}{\pi/4 \cdot d_1 \cdot d_2} = \frac{N_{fil} \cdot d_{fil}^2}{d_1 \cdot d_2} \quad (4.2)$$

Where  $N_{fil}$  is the number of filaments in the yarn and  $d_{fil}$  is the filament diameter. The nominal filament diameter  $d_{fil} = 7 \mu\text{m}$  given in Table 3.3a was used and the values for the packing density are given in Table 4.5. The nesting factor  $\eta$  was calculated from

$$\eta = (N_{plies} \cdot 2 \cdot d_1)/h \quad (4.3)$$

Table 4.5.: Average values and standard deviation of the measured yarn architecture parameters; the coefficient of variation is given in brackets

	BB30			BB45		
$d_1$ [ $\mu\text{m}$ ]	276	$\pm 29$	(10.4%)	282	$\pm 30$	(10.6%)
$d_2$ [ $\mu\text{m}$ ]	3080	$\pm 251$	(8.1%)	3092	$\pm 261$	(8.4%)
$p$ [ $\mu\text{m}$ ]	3189	$\pm 284$	(8.9%)	3048	$\pm 246$	(8.1%)
$h$ [ $\mu\text{m}$ ]	2339	$\pm 79$	(3.4%)	3887	$\pm 43$	(1.1%)
$\theta$ [ $^\circ$ ]	31.3	$\pm 0.6$	(1.9%)	45.6	$\pm 1.2$	(2.7%)
$N_{plies}$	5			8		
$p_d$ [%]	69.2			67.4		
$\eta$	1.18			1.16		

### Comparison of results to analytical predictions

Besides measurements, the analytical formulae given in Section 2.2.3 can provide an approximation of the yarn architecture if no measurements are available. For the two braiding angles, the yarn architecture parameters were calculated based on the equations Eq. 2.1-Eq. 2.5. The spacing of the yarns was assumed to be equal to the yarn width and the yarn height was approximated as half of the ply thickness. Both, braiding angle and fiber volume fraction are assumed to have the nominal values and serve as input parameters for the calculations.

An overview of the results is given in Table 4.6. All values except of the yarn height lie within 5% of the measured values. The yarn height is underestimated by 12% and 18%, which shows that the approximation of half the ply thickness, used to calculate the yarn height, is rather rough. In the braid laminates investigated, the yarns locally spread into adjacent plies, which leads to a higher yarn height in total. An alternative to the described procedure could be to calculate the yarn height by assuming the packing density in the yarns as proposed in [33]. But the value of the packing density is commonly not known a priori and the values reported in literature vary largely between 60% and 80% [33, 44], which puts a high uncertainty to the prediction.

**Table 4.6.:** Analytical predictions and comparison to the measured values of the yarn architecture

	BB30		BB45	
	calculated	deviation	calculated	deviation
$d_1$ [ $\mu\text{m}$ ]	244	-11.6%	238	-17.6%
$d_2$ [ $\mu\text{m}$ ]	3092	0.4%	3155	2.0%
$p$ [ $\mu\text{m}$ ]	3092	-3.0%	3155	3.5%
$h$ [ $\mu\text{m}$ ]	2437	4.2%	3820	-1.7%
input values				
$\theta$ [ $^\circ$ ]	30		45	
$\varphi_f$ [%]	60		60	

In conclusion, it can be said that a reasonable prediction of the biaxial braided yarn architecture can be obtained by simple analytical formulae. But the yarn height showing the biggest deviation, should be taken with caution, as it has a big impact on the waviness and thus mechanical properties. Finally, it should be noted that the braiding process for the investigated braids was configured to provide minimal waviness. Thus, yarn architectures observed here were rather regular, with maximum yarn width and the mandrel being of constant shape and perimeter. In the case of abrupt mandrel diameter changes, the deviations can be bigger [27].

#### 4.1.4. Micro-CT

In addition to the optical microscopy, micro-CT was used to determine a 3D information about the yarn architecture. The main goals of the investigations were to provide



an estimate for the quality of information obtained from a 2D micrograph of the yarn architecture and to assess the possibilities of micro-CT measurements on cured braided composite samples. Publications regarding yarn architecture in textile composites (e.g. [51, 55]) report that the yarn dimensions change along the yarn path. Thus, the question arises if a 2D sample provides representative results for the yarn architecture. Therefore, the ( $\pm 45^\circ$ ) braid was measured with micro-CT as described in Section 3.3.2. Only a qualitative evaluation of the data will be given as the resolution of the micro-CT scans ( $7\ \mu\text{m}$ ) is coarse compared to the ones of the micrographs leading to a big inherent error of the measurement. Additionally, a comprehensive evaluation of the CT-data requires an automated procedure for thresholding and shape detection, which was out of the scope of this study.

The complete micro-CT scan on the ( $\pm 45^\circ$ ) braid is shown in Fig. 4.8. The yarn architecture of the braid can be seen, but the contrast is less compared to the micrographs. For the following investigations, only slices of the complete data will be shown. The focus of the investigations is put on yarn cross section deviations from the idealized elliptical shape and on the effect of nesting.

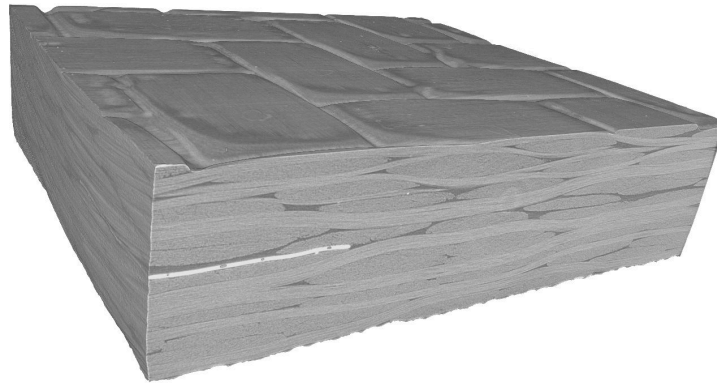


**Fig. 4.8:** 3D view of the ( $\pm 45^\circ$ ) sample used for micro-CT investigation

### **Dependence on the yarn shape and rotation on the position**

Different yarn shapes were observed on the micrographs. The micro-CT investigations were used to evaluate the variation of shape, dimensions and orientation of the yarn cross section along the yarn path. Fig. 4.9 shows a representative yarn cross section variation: the yarn shapes align with the transverse yarns near the crossing point (1), merge when the yarns run parallel (2) and split again when the next transverse yarn crosses (3). Thus, the yarn shape aligns with the transverse yarns inside the ply, but also with the yarns in adjacent plies (4,5). The cross section rotates according to the path of the transverse yarns (1,3), with a rotation angle of approximately  $\pm 3^\circ$  measured for the ( $\pm 45^\circ$ ). Yarn cross section shape and rotation are dependent on both, the position along the yarn path and on the relative position of the plies above and below the investigated ply. Thus, a comprehensive parametric description of yarn path and cross sections requires additional information on the relative position of the plies.

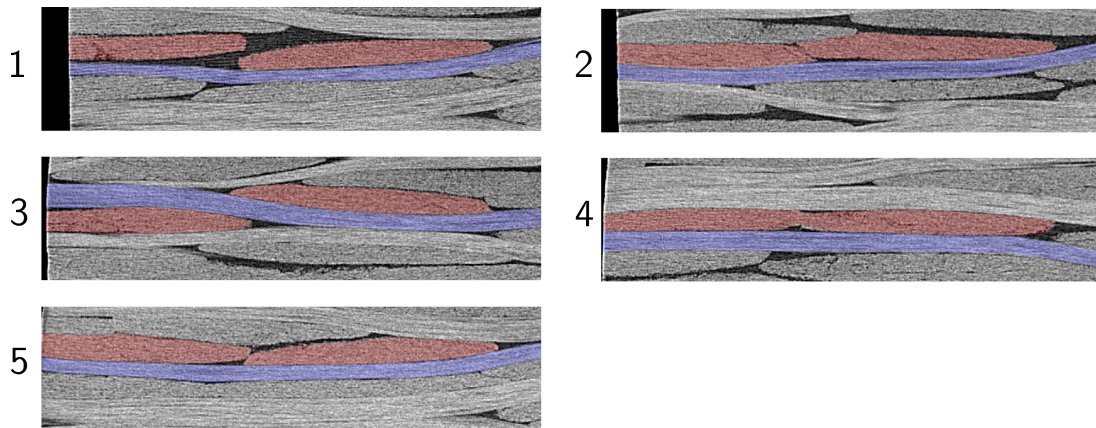


Fig. 4.9: Yarn cross section shape and orientation at different positions along the yarn path

### Influence of the ply position

The yarn shapes in the sample were found to be changing on mold side and vacuum bag side (Fig. 4.10): regular elliptical shapes are present on the vacuum-bag side, while the yarns are flattened on the other side due to the contact with the rigid mold. This also reflects in the yarn path, as an additional *dip* (cf. [55]) can be seen near the mold, whereas an additional waviness is present in the nominal straight part of the yarn on the side of the flexible vacuum bag. Changes of yarn architecture near the surfaces are especially

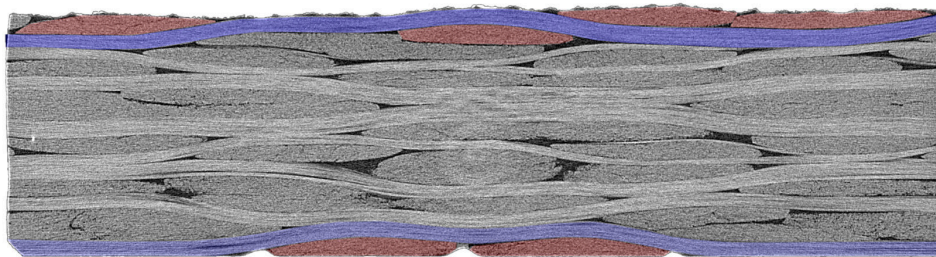


Fig. 4.10: Differences in the yarn architecture on tool-side (lower) and vacuum bag side (upper) of the sample

important, when considering surface measurements for yarn dimensions. The values of yarn width and spacing obtained from a surface scan can only serve as a rough estimate, as the architecture is different inside the braid laminate.

### Nesting

Nesting of adjacent plies can be either of *global* or *local* nature: *global* nesting describes the geometric effect due to the positioning of the plies relative to each other [56]. Empty volume in one ply is filled by the adjacent ply, i.e. the complete ply is evenly nested. *Local* nesting in contrast is mainly influenced by local boundary conditions and the deformation of yarns in a dry fabric and thus is a rather local effect.

The tendency for nesting in the ( $\pm 45^\circ$ ) braid laminate is shown in Fig. 4.11, where the green lines mark the nominal thickness of one ply (1/8th of the laminate thickness). The braid laminate shows only minor *global* nesting, which is in accordance with the results

of Lomov et al. [56], which describe geometric nesting to decrease with the tightness of the fabric. As the investigated fabrics are rather tight, there is almost no free volume to fill, thus less global nesting is present. It can be concluded that *global* nesting only has a minor effect for tight braid laminates. A nesting of the plies can only be observed locally, e.g. at the positions marked red in Fig. 4.11.

The stacking of the plies (i.e. the relative lateral position) does not follow a regular trend. Both, plies placed identically on each other (*In-Phase: IP*, plies 6,7) and plies shifted by twice the yarn width (*Out-of-Phase: OP*, plies 3,4) are present.

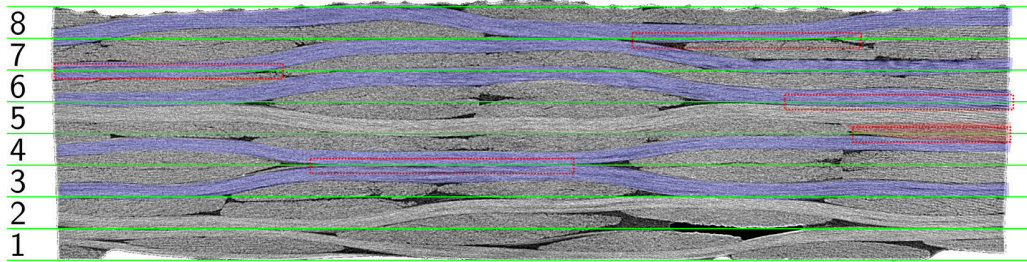


Fig. 4.11: Nesting effects in the ( $\pm 45^\circ$ ) braid laminate

### Assessment of micro-CT investigations

Summarizing the results of the measurements, the micro-CT method provides a good possibility to obtain qualitative information about the yarn architecture. The qualitative results can yield information for improved geometric models of the yarn architecture. On the other hand, optical microscopy offers a resolution seven times better compared to micro-CT data. Automatic evaluation of the complete CT-data may be possible, but simple thresholding for segmentation of yarns and matrix did not work for the samples, as the contrast between yarns and matrix was too low. Thus, improved image analysis techniques for post-processing or contrast enhancement techniques like given in [65] are required to gather qualitative results.

#### 4.1.5. Summary and strategy for yarn architecture measurements

The investigations conducted on the characterization of yarn architecture of biaxial braided composites can be summarized to a strategy for further measurements. Two sections perpendicular to the yarn path of the two yarn directions in a biaxial braided composites need to be extracted. If yarn cross section dimensions shall be measured, the investigated section must be orthogonal to the yarn direction investigated, as this minimizes the error introduced by a possible misalignment of the sample. An approximation of the yarn cross sectional shape as an ellipse was shown to be reasonable: it eases the measuring procedure, as it provides both, yarn width and height, from a single measurement. An ellipse shape was the best approximation of the yarn shapes in the investigated braids, but as other yarn shapes are reported in literature (cf. Section 2.3), the idealization of shape needs to be reviewed if different braids are investigated. The position of the extracted samples had no significant effect on the results, except for the yarn height, which changed near the panel edges. It is therefore recommended to avoid taking samples in the proximity of the

panel edges. Six to eight sections for microscopy are required to obtain reliable results within the margins defined above. For the braiding angle, measurements from an optical sensor are recommended, as they take into account the yarn orientation from the complete area scanned. If such measuring techniques are not available, hand-measurements as described above can be used. But it is noted that the hand measurements were shown to slightly overestimate the braiding angle and the accuracy suffers from the reduced number of measurement points. The results from optical microscopy and optical sensor measurements could provide all the information needed to create a geometrical model of the biaxial braided composite within WiseTex [46]. If additional details of the yarn architecture are required, a micro-CT analysis can provide useful results regarding 3D-effects on yarn shape and path and for the creation of improved geometric models.

## 4.2. Off-axis experiments of biaxial braided composites

The elastic, nonlinear and failure behavior of a ( $\pm 30^\circ$ ) braided composite has been studied by using off-axis specimen tested under uniaxial load. The different off-axis angles allow to introduce different combinations of combined stress states into the specimens. A total of six off-axis angles, namely  $\psi = 0^\circ, 15^\circ, 30^\circ, 45^\circ, 60^\circ, 90^\circ$  (see Fig. 4.12), were tested in tension and compression.

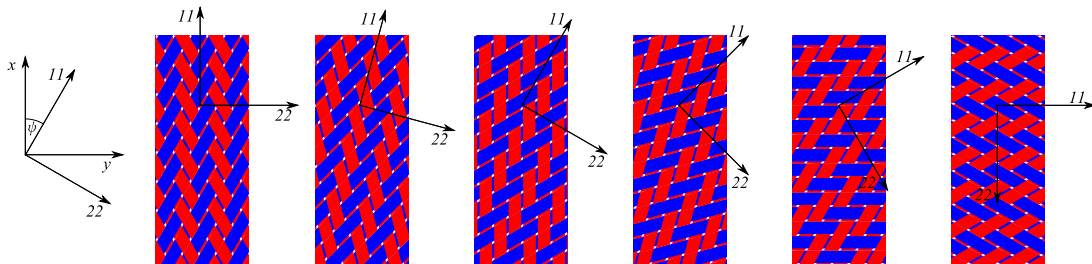


Fig. 4.12: Overview of ( $\pm 30^\circ$ ) off-axis experiments:  $\psi = 0^\circ, 15^\circ, 30^\circ, 45^\circ, 60^\circ, 90^\circ$

The off-axis angles were chosen from preliminary analytical considerations with an equivalent laminate model. The  $\psi = 75^\circ$  experiments were skipped as the test results were expected to be very similar to the  $\psi = 90^\circ$  results. All experiments were conducted according to the procedures described in Section 3.4. The experiments and designation of the test series are summarized in Table 4.7. In the following sections, the results from monotonic tensile, tensile loading/unloading and compressive experiments are described. Furthermore, a comparison between the tensile and compressive material behavior of the biaxial braided composites is given and conclusions for the formulation of predictive models are drawn.

Table 4.7.: Off-axis experiments with ( $\pm 30^\circ$ ) braided composite

	$\psi = 0^\circ$	$\psi = 15^\circ$	$\psi = 30^\circ$	$\psi = 45^\circ$	$\psi = 60^\circ$	$\psi = 90^\circ$
tension	PT_OA00	PT_OA15	PT_OA30	PT_OA45	PT_OA60	PT_OA90
compression	PC_OA00	PC_OA15	PC_OA30	PC_OA45	PC_OA60	PC_OA90

### 4.2.1. Tensile experiments

#### OA00

For the OA00 test series, five monotonic and two loading/unloading experiments were conducted. The test results are summarized in Table 4.8. The elastic moduli vary significantly between the coupons with the stiffest specimen having a modulus around 20% higher than the lowest one. This effect is attributed to the s-shape of the braid yarns, as described in Section 4.1.2: the braiding angle in the middle of the panel is higher (cf. Table 4.6a), which explains the increases of stiffness. As the specimen were cut over the width of a braided panel with the OA00\_1 coupon located close to the panel edge, the coupons 01 and 08 are the softest.

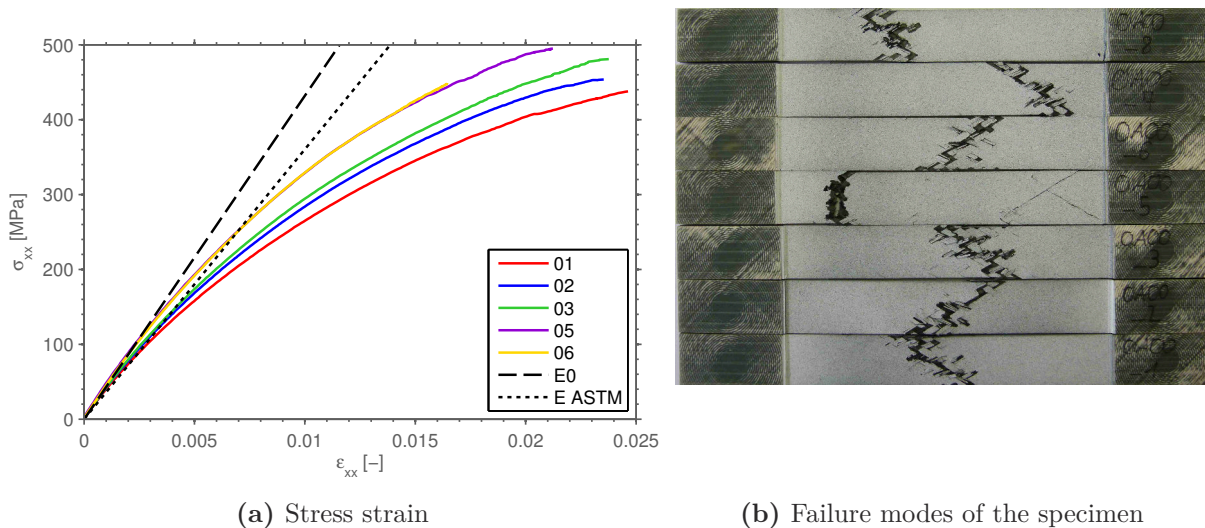
**Table 4.8.:** Test results from the BB30\_PT\_OA00 test series

Test	Modulus ASTM <sup>1</sup> $E_x$ [MPa]	Modulus initial $E_x^0$ [MPa]	Poisson's ratio $\nu_{xy}$ [-]	Failure strain $\varepsilon_{OA00}^{UTS}$ [-]	Strength $\sigma_{OA00}^{UTS}$ [MPa]
PT_OA00_01	32148	41641	1.50	0.0246	437.9
PT_OA00_02	34326	43148	1.49	0.0235	453.7
PT_OA00_03	35606	44249	1.51	0.0238	480.9
PT_OA00_05	38843	47024	1.51	0.0212	495.1
PT_OA00_06	39116	43461	1.50	0.0206	498.7
PT_OA00_07 <sup>2</sup>	35245	42637	1.48	0.0235	462.5
PT_OA00_08 <sup>2</sup>	32854	40252	1.50	0.0243	451.2
MEAN	35448	43202	1.50	0.0231	468.6
STDV	2505	1972	0.01	0.0014	21.6
CV (%)	7.1	4.6	0.7	6.2	4.6

<sup>1</sup>: evaluated within  $\varepsilon_{xx} = 0.001 - 0.003$     <sup>2</sup>: loading/unloading experiment

The same trend can be observed for the initial stiffness, failure strain and strength: the lower braiding angle in the center of the panel results in higher initial moduli, lower failure strains and higher strength. Thus, the increased standard deviation of the values can be believed to be systematic and inherent for biaxial braided composites. Only small influence of the braiding angle variation on the Poisson's ratio was observed.

The effect of varying braiding angle is also visible in the stress-strain curves in Fig. 4.13a: the curves from all coupons are quite similar in shape, but have different initial slopes and end points. Small drops in the stress-strain curves are seen for strains over 1.5%, which were found to be due to edge-cracking of the specimen as e.g. shown in Fig. 4.14b.

**Fig. 4.13:** Stress strain curves and failure modes from the BB30\_PT\_OA00 test series

### Failure mode

The failure mode was similar for all coupons: the major crack<sup>1</sup> included a broad area of damage oriented along one of the yarn directions, with exception of the coupon 05 that had a macro crack orthogonal to the load direction. The occurrence of two failure modes for BB30\_OA00 specimens was also observed in a preliminary study [194], but the failure mode had no influence on the strength observed.

The failed specimen show a broad band of damage oriented around 30° to the load direction. Several intra-yarn cracks are seen on the yarns in the damaged area. In addition to the in-plane failure, a large delamination of the plies is present in the damaged area (Fig. 4.14a). The recordings from the high-speed camera are shown for a representative specimen in Fig. 4.14b. The left image shows the coupon ultimately before the final failure and the other two images display the final failure process. Edge cracks are present on the coupon surface, which was also observed in the DIC-measurements. They start to develop at approximately 80% of the failure load. The cracks localize in the region, where the coupon finally fails: several transverse cracks spread over the coupon width along the F+ direction and the yarns oriented in the F- direction cannot resist the shear force and break as shown in the middle picture. The failure of the yarns can be summarized to be introduced by shearing with many intra-yarn cracks distributed over the width of the yarns after final failure.

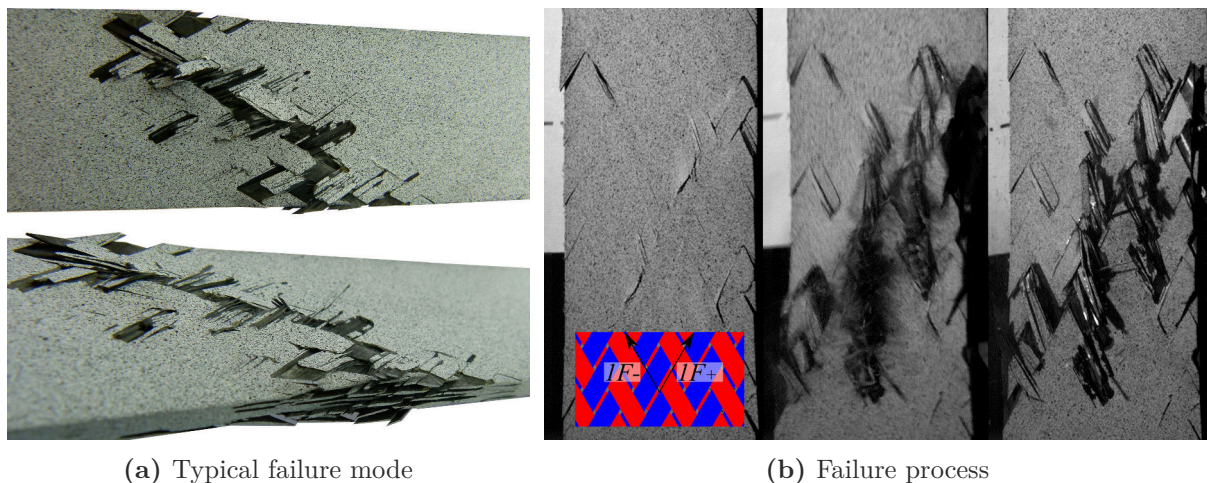


Fig. 4.14: Failure modes of the BB30\_PT\_OA00 test series

### OA15

Six specimen were in total tested for the OA15 test series. Four specimen were loaded monotonic up till failure and two loading/unloading experiments were conducted. An overview of the results in given in Table 4.9.

<sup>1</sup>major crack / macro crack: denotes the visible major crack of final failure, spreading over the complete width of the coupon. In contrast, micro-cracks or micro-cracking describes smaller cracks (size of a yarn width or unit cell) which develop on the coupon.

**Table 4.9.:** Test results from series BB30\_PT\_OA15

Test	Modulus ASTM <sup>1</sup> $E_x$ [MPa]	Modulus initial $E_x^0$ [MPa]	Poisson's ratio $\nu_{xy}$ [-]	Failure strain $\varepsilon_{OA15}^{UTS}$ [-]	Strength $\sigma_{OA15}^{UTS}$ [MPa]
PT_OA15_01	41079	46618	1.28	0.0184	520.3
PT_OA15_02	41053	46895	1.30	0.0193	530.8
PT_OA15_03	47663	53062	1.31	0.0169	589.8
PT_OA15_04 <sup>2</sup>	48990	54315	1.28	0.0156	602.0
PT_OA15_05 <sup>2</sup>	47295	52692	1.30	0.0151	552.5
PT_OA15_06	45446	53598	1.30	0.0174	564.4
MEAN	45254	51197	1.29	0.0171	560.0
STDV	3137	3180	0.01	0.0015	29.3
CV [%]	6.9	6.2	0.9	8.7	5.2

<sup>1</sup>: evaluated within  $\varepsilon_{xx} = 0.001 - 0.003$     <sup>2</sup>: loading/unloading experiment

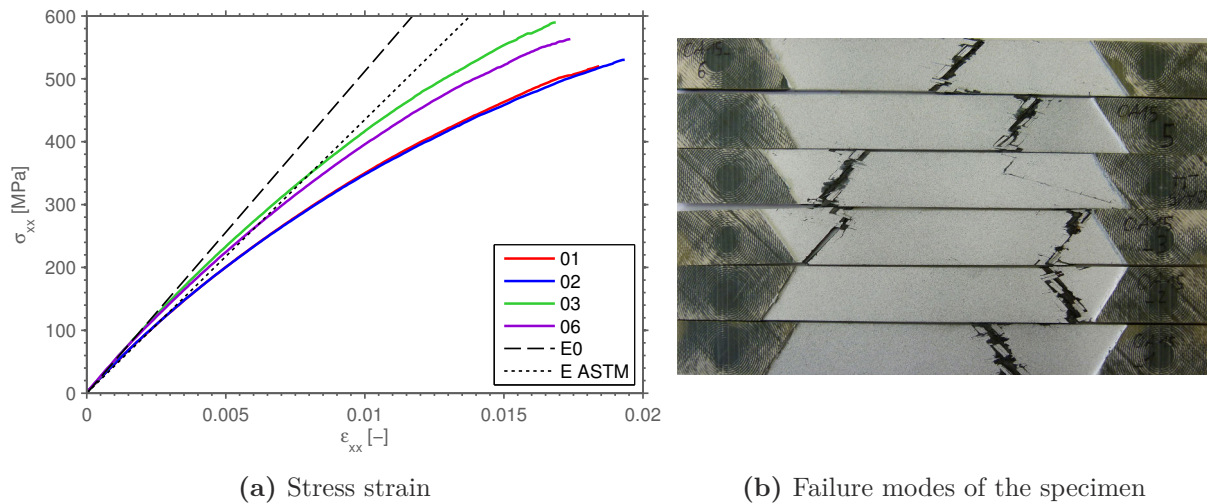
Similar to the OA00 series, some variation can be seen within the moduli  $E_x$  and  $E_x^0$  of the OA15 series. This is as for the OA00 series assumed to be related to variations of the braiding angle. The variation reflects in modulus, strength and failure strain. The specimen 01 and 02 have approximately 13% lower moduli compared to the other specimen. This correlates with the optical sensor measurements made on the specimen, which exhibited an average braiding angle of approximately  $1.5^\circ$  higher for these specimen (cf. Fig. 4.26a).

Fig. 4.15a shows the stress-strain behavior of the monotonically loaded specimen. The stress strain curves smoothly degrade from the start of the experiment up till final failure. This is in accordance with the observations made from DIC and high-speed camera during the experiments: they showed, besides a small number of edge cracks, no further cracking on the coupons before final failure.

### Failure mode

The same failure mode was observed for all specimen tested, with the failure patterns shown in Fig. 4.15b. A detailed view to a failed specimen given in Fig. 4.16a, shows the major crack is running along the 1F+ direction, which is oriented  $45^\circ$  to the load axis. Intra-yarn cracking in the 1F+ direction and yarn rupture in the 1F- direction were observed on the failed specimen. Furthermore, delamination of the plies in the laminate is present in the area of final failure. The high-speed camera videos show that transverse cracking localized at the specimen edge is initiating the final failure (Fig. 4.16b). The transverse cracking is limited to the edges, no cracks were observed over the complete coupon width. The specimen fails rather abrupt by yarn rupture in the 1F- direction, with the major crack oriented along the 1F+ direction. The failure is believed to be dominated by the yarn rupture in the 1F- direction, but the crack orientation along the





**Fig. 4.15:** Stress strain curves and failure modes from the BB30\_PT\_OA15 test series

1F+ yarns indicated influence from the transverse cracking in the 1F+ directions, as reported by e.g. [122] for triaxial braids.

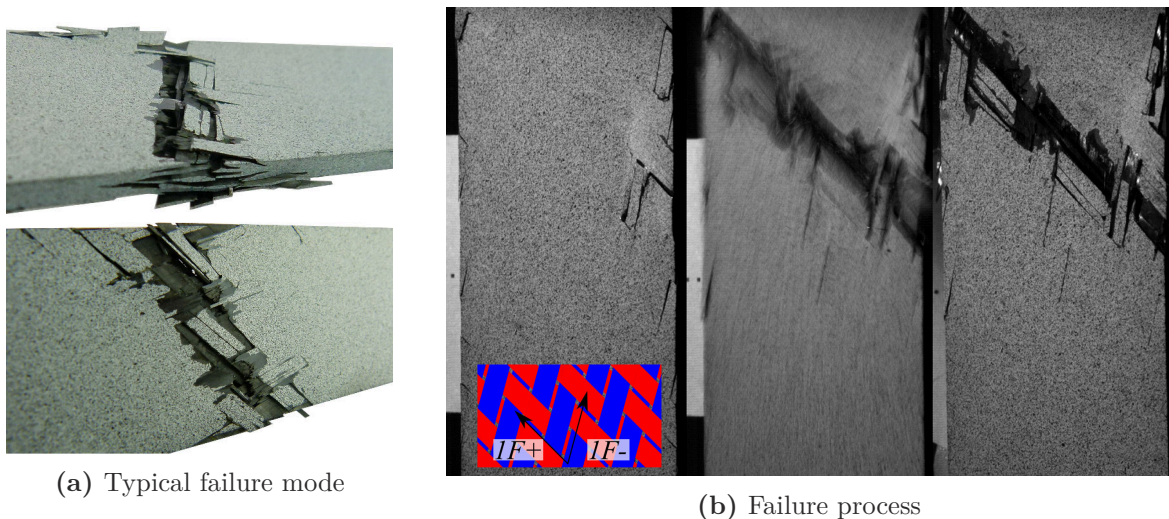


**Fig. 4.16:** Failure modes of the BB30\_PT\_OA15 test series

### OA30

Monotonic experiments with six specimen were conducted for the OA30 series. Loading/unloading experiments were omitted for this test series, as preliminary experiments showed only minor non-linear effects in the stress-strain behavior. For the OA30 test series, the strain on the specimen surface was measured with the DIC-system in 2D mode. The 2D mode was found to introduce an error in the strain measurement: due to an out-of-plane movement of the testing machine gripping device, the 2D strain measurement gave an artificial strain gradient on the coupon, which resulted in a non-physical s-shape of the stress-strain curve in the strain interval from  $\varepsilon_{xx} = 0 \dots 0.3\%$  shown in Fig. 4.17. As

this non-linearity was judged unphysical, the stress-strain curves were linearized in this region.

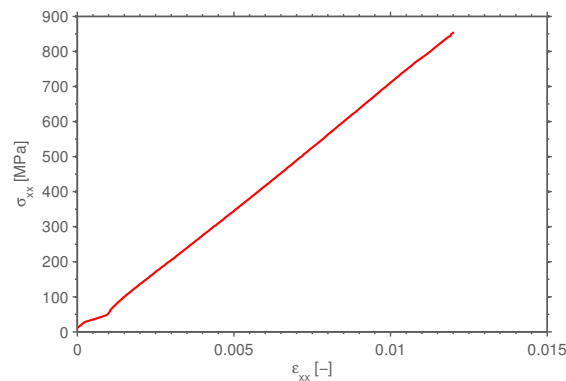


**Fig. 4.17:** S-shape of the BB30\_PT\_OA30 curves due to the DIC error

An overview to the test series results is given in Table 4.10. The initial modulus is not given in the table, as it was identical to the ASTM modulus  $E_x$ . Modulus, strength and failure strain all vary within approximately 5%, while the variation of the Poisson's ratio is higher around 20%. The increased variation is attributed to the fact that the Poisson's ratio for OA30 is very sensitive to small deviations of the off-axis angle (cf. Fig. 4.26b).

**Table 4.10.:** Test results from series BB30\_PT\_OA30

Test	Modulus ASTM <sup>1</sup> $E_x$ [MPa]	Poisson's ratio $\nu_{xy}$ [-]	Failure strain $\varepsilon_{OA30}^{UTS}$ [-]	Strength $\sigma_{OA30}^{UTS}$ [MPa]
PT_OA30_01	67151	0.28	0.0121	856.9
PT_OA30_02	68899	0.37	0.0113	798.9
PT_OA30_03	68266	0.42	0.0116	877.6
PT_OA30_04	64625	0.48	0.0116	754.5
PT_OA30_05	66360	0.52	0.0115	755.9
PT_OA30_06	64902	0.48	0.0126	813.9
MEAN	66701	0.42	0.0118	809.6
STDV	1589	0.08	0.0005	46.4
CV [%]	2.4	18.7	3.9	5.7

<sup>1</sup>: evaluated within  $\varepsilon_{xx} = 0.001 - 0.003$

Fig. 4.18a shows the stress-strain curves, which are linear up till final failure. Some of the specimens exhibit a slight stiffening, which is attributed to spatial alignment of the yarns to the load and to yarn stretching (reduction of waviness). However, the increase in stiffness was not significant and not observed on all of the specimen, as some specimen had a constant stiffness up till final failure.

## Failure mode

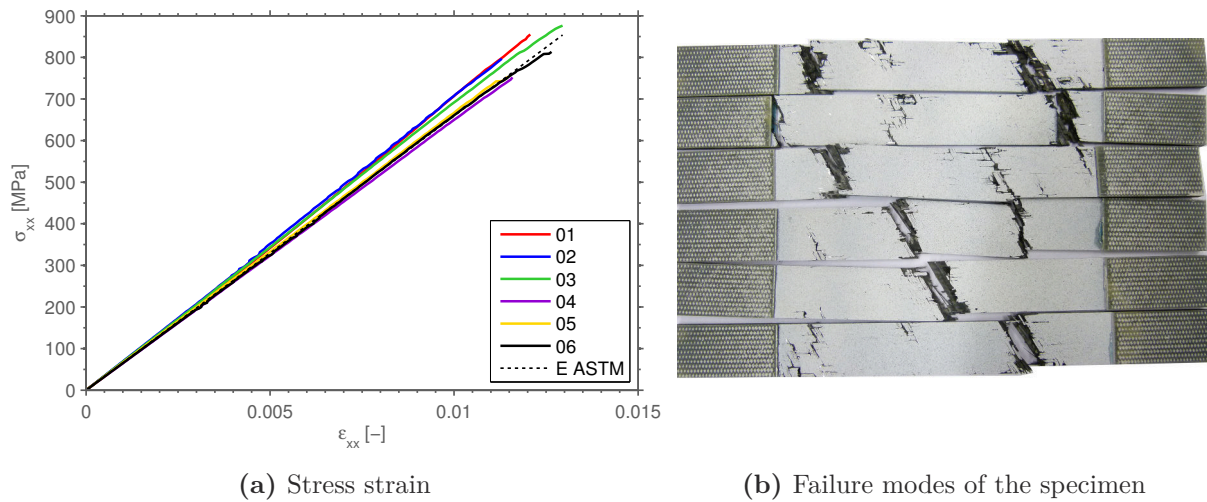


**Fig. 4.18:** Stress strain curves and failure modes from the BB30\_PT\_OA30 test series

The failure mode of the OA30 coupons was similar to the OA15 test series: the major failure location is a narrow fracture band along the F+ direction (Fig. 4.19a). Intra-yarn cracking in the F+ direction and yarn rupture in the F- direction are visible from postmortem inspection. For most of the specimen two major crack locations along the specimen were present, as shown in Fig. 4.18a. The high speed videos revealed that one of the two is the location of specimen final failure, while the other one is initiated by an elastic snap-back of the specimen after the first failure. Thus, the second failure is compressive, which explains kink-band failure of the yarns observed by optical microscopy of the tested specimen. The high-speed videos shown in Fig. 4.19b furthermore show that final failure initiates at the position of a transverse edge crack in the F+ direction. The main failure is yarn rupture of the yarns in F- direction. The orientation of the major crack along the F+ direction furthermore implies that yarn rupture is influenced by strain concentrations in the 1F+ direction.

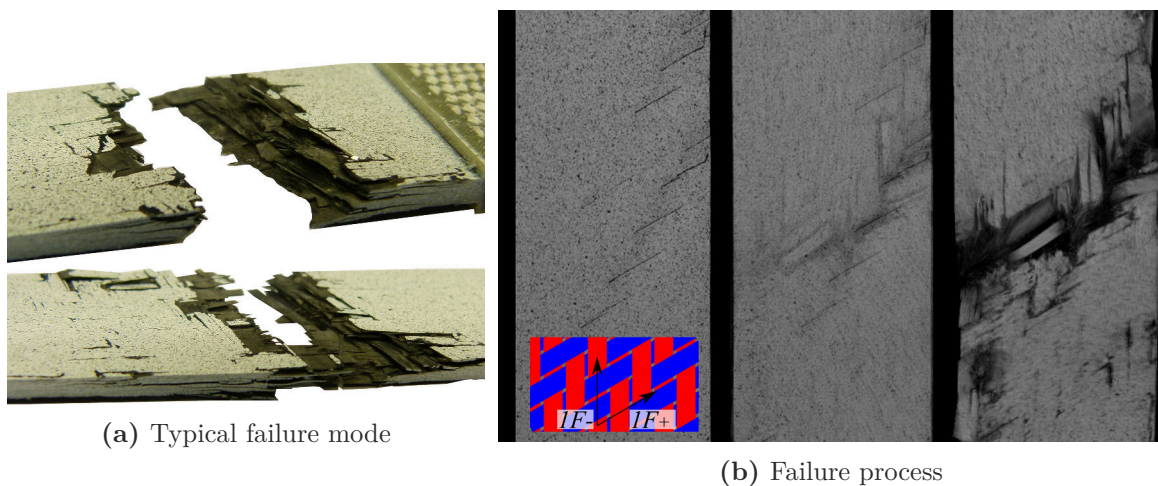


**Fig. 4.19:** Failure modes of the BB30\_PT\_OA30 test series

## OA45

Five monotonic and two loading/unloading experiments have been conducted for the OA45 test series. The test results are summarized in Table 4.11.

**Table 4.11.:** Test results from series BB30\_PT\_OA45

Test	Modulus ASTM <sup>1</sup> $E_x$ [MPa]	Modulus initial $E_x^0$ [MPa]	Poisson's ratio $\nu_{xy}$ [-]	Failure strain $\varepsilon_{OA45}^{UTS}$ [-]	Strength $\sigma_{OA45}^{UTS}$ [MPa]
PT_OA45_02	34766	35990	-0.20	0.0060	197.5
PT_OA45_03	34900	36012	-0.23	0.0057	193.0
PT_OA45_04	34924	36758	-0.23	0.0058	193.2
PT_OA45_05	35762	40136	-0.24	0.0058	197.3
PT_OA45_06 <sup>2</sup>	31670	38017	-0.13	0.0058	179.1
PT_OA45_07	38491	43897	-0.26	0.0053	198.4
PT_OA45_08 <sup>2</sup>	35654	36281	-0.21	0.0053	178.0
AVG	35167	38156	-0.21	0.0057	190.9
STDV	1858	2717	0.04	0.0002	8.1
CV [%]	5.3	7.1	18.6	4.1	4.2

<sup>1</sup>: evaluated within  $\varepsilon_{xx} = 0.001 - 0.003$     <sup>2</sup>: loading/unloading experiment

The average ASTM modulus  $E_x$ , evaluated between 0.1% and 0.3% strain, is similar to the one from OA00 test series, but Poisson's ratio, strength and failure strain differ significantly between OA00 and OA45. Additionally, the initial modulus is smaller compared to the OA00 test series, which means that the behavior of OA45 deviates less from linear at the beginning of the test. A negative Poisson's ratio was observed for the OA45 series, thus the coupons extended in transverse direction under axial tensile load. The high coefficient of variation is mainly due to the outlying value measured from specimen 06.

The stress-strain curves shown in Fig. 4.20a are slightly nonlinear up till final failure for all specimen. After the maximum load, which concedes with the first intra-yarn cracking on the coupon, the load does not drop completely to zero. Some further cracking at a slightly decreased load is observed, which results in the major crack seen on all of the coupons. The failure mode, being dominated by transverse tensile cracking, coincides with the average strength, which is much lower than for the off-axis angles  $\psi = 0 \dots 30^\circ$ .

### Failure mode

The failure pattern observed on all specimen by postmortem inspection was a single crack running along the 1F- direction (Fig. 4.20b). The cracking on the specimen is very localized, with the intra-yarn cracks spreading over a single yarn width (cf. Fig. 4.21a). No further intra-yarn cracking or delamination is observed on the specimen by postmortem inspection.

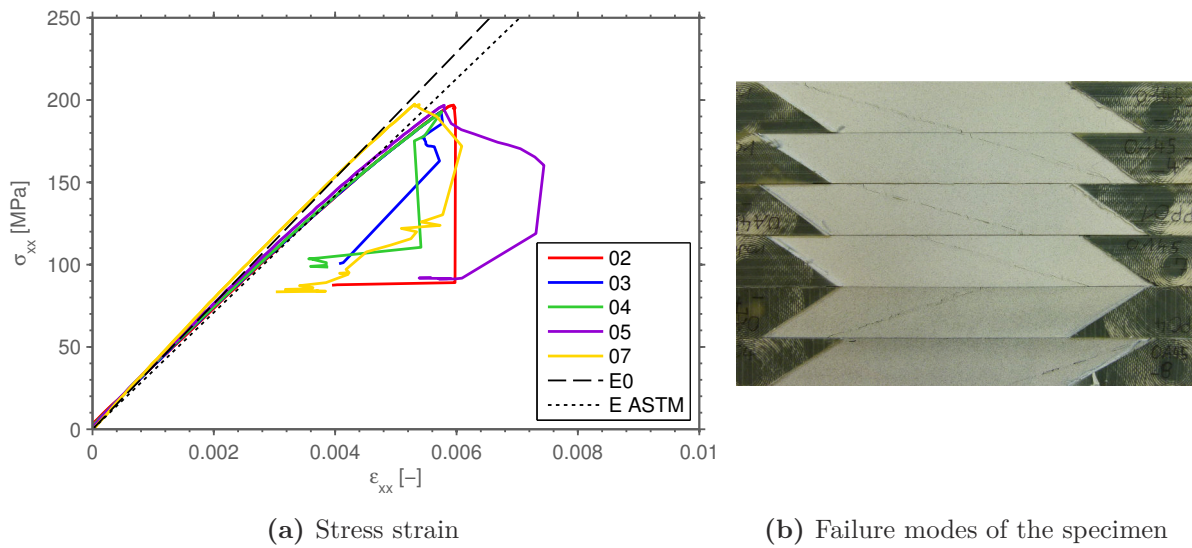


**Fig. 4.20:** Stress strain curves and failure modes from the BB30\_PT\_OA45 test series

The recordings from the high-speed camera show that final failure starts with intra-yarn cracks in the 1F+ direction at different positions on the coupon (Fig. 4.21b). With the first cracks in 1F+ direction appearing, the load slightly drops and further cracking in the 1F+ direction is introduced. The cracking then localizes into one macroscopic crack running along the 1F- direction, which is related with the final load drop at the end of the tests. The OA45 test series was the only series, where first cracking observed did not coincide with the final load drop. However, the complete failure process observed was very short, and no characteristic stress-strain behavior after first crack initiation was measured.

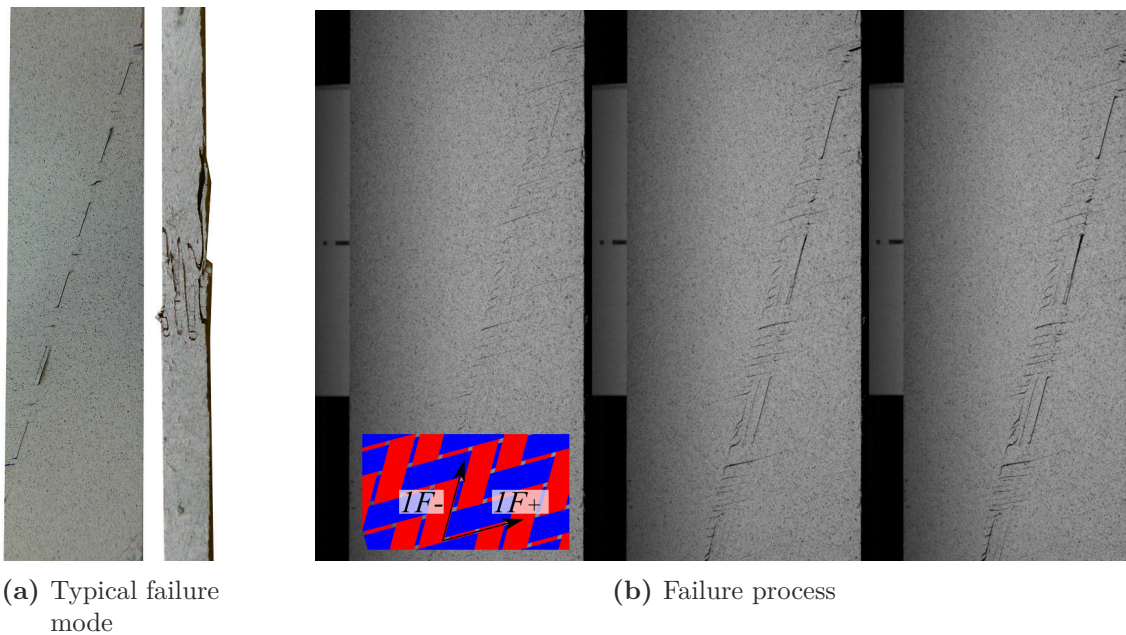


**Fig. 4.21:** Failure modes of the BB30\_PT\_OA45 test series

## OA60

For the OA60 test series, six specimen were tested in total. Four of the specimen were loaded monotonically and two specimen were used for loading/unloading experiments. The results of the test series are summarized in Table 4.12. The initial modulus is only slightly higher compared to the ASTM modulus, which shows that the behavior is nearly linear at the beginning of the test. All values except the Poisson's ratio show small variations less than 5%. The increased variability in the Poisson's ratio is attributed to the small amount of transverse deformation, which leads to an increased effect of noise present in the strain signal.

**Table 4.12.:** Test results from series BB30\_PT\_OA60

Test	Modulus ASTM <sup>1</sup> $E_x$ [MPa]	Modulus initial $E_x^0$ [MPa]	Poisson's ratio $\nu_{xy}$ [-]	Failure strain $\varepsilon_{OA60}^{UTS}$ [-]	Strength $\sigma_{OA60}^{UTS}$ [MPa]
PT_OA60_01 <sup>2</sup>	16574	17158	0.06	0.0076	105.8
PT_OA60_02 <sup>2</sup>	16829	17303	0.08	0.0074	105.1
PT_OA60_03	16302	17336	0.07	0.0083	116.6
PT_OA60_04	16231	18378	0.08	0.0075	108.6
PT_OA60_05	15814	15629	0.08	0.0079	110.0
PT_OA60_06	16034	16349	0.08	0.0077	109.6
AVG	16297	17025	0.07	0.0077	109.3
STDV	333	859	0.01	0.0003	3.7
CV [%]	2.0	5.0	11.6	3.8	3.4

<sup>1</sup>: evaluated within  $\varepsilon_{xx} = 0.001 - 0.003$     <sup>2</sup>: loading/unloading experiment

Fig. 4.22a shows the stress-strain behavior of the specimen: the stress strain curve is nearly linear until an axial strain of  $\varepsilon_{xx} = 0.4\%$  and progresses in a smooth degradation up till final failure. The stress-strain behavior is similar for all tested coupons and no influence from the different failure modes (cracking along 1F+ or 1F- cf. Fig. 4.22b) to the stress-strain behavior was observed.

## Failure mode

Two different failure modes were observed on the specimen after the experiments: the main crack was either running along 1F+ or along 1F- direction (Fig. 4.22a). In both cases, the yarns in the direction transverse to the final crack showed several intra-yarn cracks over the width. The high-speed videos, shown exemplarily in Fig. 4.23b, revealed that the failure in both cases starts with intra-yarn cracking in one of the yarn directions and localizes to a main crack oriented along 1F- or 1F+, which is spread over the complete coupon width. The failure of the specimen is rather brittle, as the first observation of intra-yarn cracks on the specimen surface coincides with the major load drop.

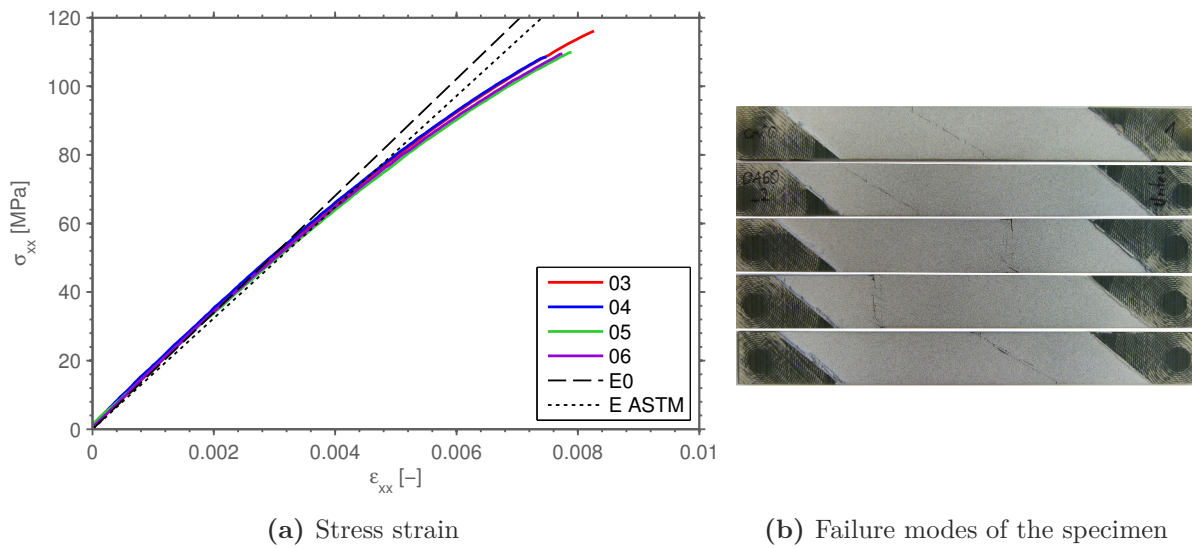


**Fig. 4.22:** Stress strain curves and failure modes from the BB30\_PT\_OA60 test series

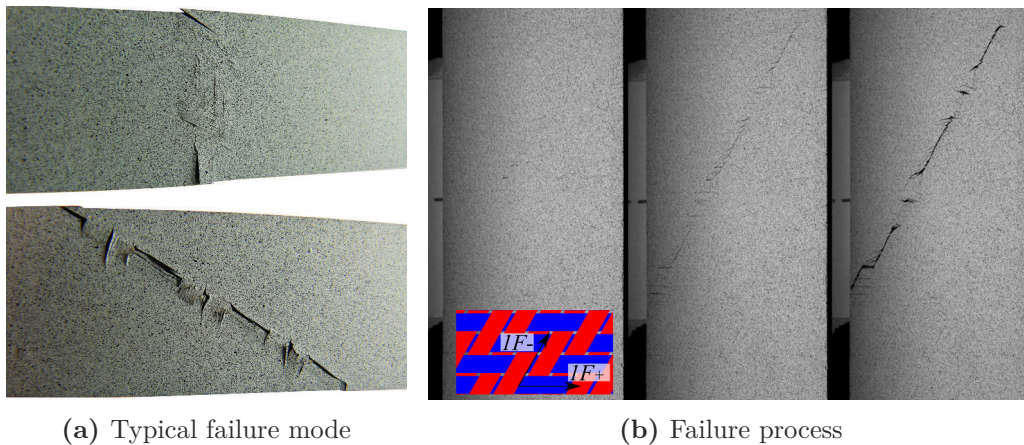


**Fig. 4.23:** Failure modes of the BB30\_PT\_OA60 test series

## OA90

The results of the OA90 test series are summarized in Table 4.13. Seven specimen were tested at the off-axis angle of  $90^\circ$ , which is equivalent to the 22-direction of the braid. Two specimen were used for loading/unloading experiments, while the others were loaded monotonically up till failure. All measured values show minor variations and the stiffness and strength of OA90 are the lowest values measured for all tensile off-axis series.

The stress-strain curves of the OA90 series are shown in Fig. 4.24a. A smooth degradation is observed for all specimen over the complete strain range, with the behavior being nearly identical for the tested specimen. The first cracking observed on the specimen is identical with the final load drop within the stress strain curve.

## Failure mode

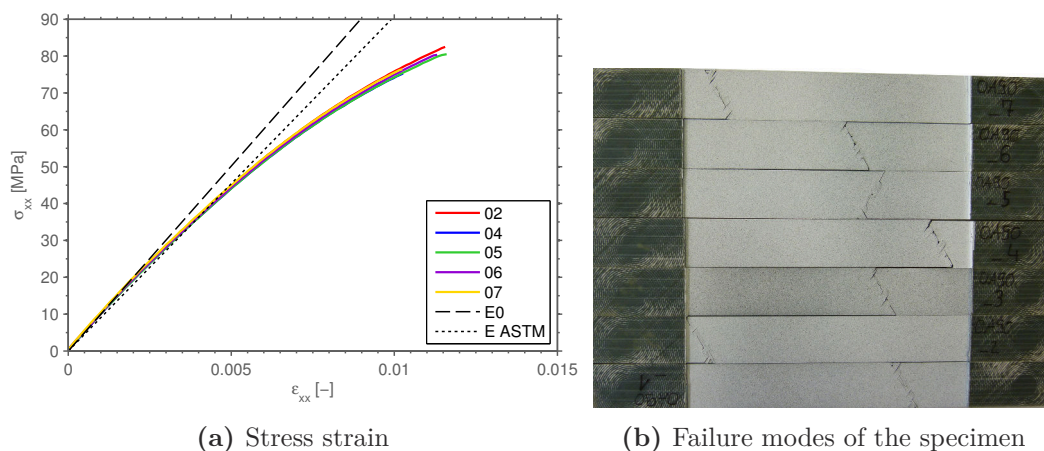
The failure modes observed on all coupons by postmortem inspection were similar to the

**Table 4.13.:** Test results from series BB30\_PT\_OA90

Test	Modulus ASTM <sup>1</sup> $E_x$ [MPa]	Modulus initial $E_x^0$ [MPa]	Poisson's ratio $\nu_{xy}$ [-]	Failure strain $\varepsilon_{OA90}^{UTS}$ [-]	Strength $\sigma_{OA90}^{UTS}$ [MPa]
PT_OA90_01 <sup>2</sup>	9244	10017	0.32	0.0105	76.7
PT_OA90_02	9158	9988	0.33	0.0116	82.7
PT_OA90_03 <sup>2</sup>	8595	10356	0.34	0.0113	80.2
PT_OA90_04	8940	9654	0.33	0.0103	75.4
PT_OA90_05	8930	9832	0.33	0.0116	80.5
PT_OA90_06	8981	9824	0.33	0.0113	80.5
PT_OA90_07	9124	10599	0.33	0.0102	76.5
AVG	8996	10039	0.33	0.0110	78.9
STDV	197	306	0.00	0.0006	2.5
CV [%]	2.2	3.0	1.2	5.1	3.2

<sup>1</sup>: evaluated within  $\varepsilon_{xx} = 0.001 - 0.003$     <sup>2</sup>: loading/unloading experiment

OA60 case: the final failure is dominated by transverse cracking that localizes into a single crack, along one of the yarn directions (Fig. 4.25a). As the yarn directions 1F+ and 1F- are oriented at the same angle to the load direction, the cracking is observed in either one of the two yarn directions (Fig. 4.24b). The high speed videos show that the failure of the specimen is introduced by transverse cracking in one of the yarn directions and followed by the shear-failure of the other yarn direction shown in Fig. 4.25b. The yarns transverse to the main crack are unable to transport the shear force over the crack and shear off, which manifests in several intra-yarn cracks over the width.

**Fig. 4.24:** Stress strain curves and failure modes from the BB30\_PT\_OA90 test series



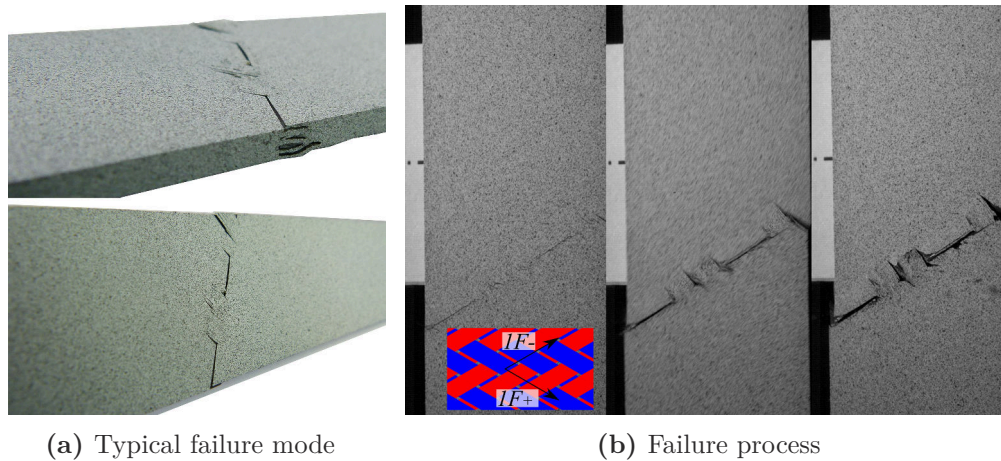


Fig. 4.25: Failure mode of the BB30\_PT\_0A90 test series

### Summary of the tensile off-axis experiments

The fiber volume fraction of the different off-axis test series varied in the range of 60%-62%. For the comparison of the tensile off-axis experiments, all properties measured were normalized to a fiber volume fraction of 60% according to the procedure given in Section 3.4.7. A summary of the elastic properties measured in the tensile off-axis experiments is given in Fig. 4.26. Both the initial elastic moduli and the one obtained in the strain range of 0.1% – 0.3% plotted over the off-axis angle  $\psi$  are shown in Fig. 4.26a. The difference between the initial modulus and the one obtained according to the standard [84] within the range of 0.1 – 0.3% axial strain is most prominent for the off-axis angles  $\psi = 0^\circ \dots 15^\circ$ , while the difference is small for the bigger off-axis angles. The dotted lines given for  $E_x$  and  $E_x^0$  represent the off-axis curves calculated from the measured elastic constants  $E_{11}, E_{22}, G_{12}$  and  $\nu_{12}$  by the equation

$$\frac{1}{E_\psi} = \frac{1}{E_{11}} \cos^4 \psi + \frac{1}{E_{22}} \sin^4 \psi + \left( \frac{1}{G_{12}} - \frac{2\nu_{12}}{E_{11}} \right) \sin^2 \psi \cos^2 \psi \quad (4.4)$$

As the shear modulus  $G_{12}$  was not measured, it was calculated by applying Eq. 4.4 to the  $\psi = 30^\circ$  off-axis experiment. The calculated off-axis curves show that the biaxial braided composites behave orthotropic and that the  $\psi = \theta$  experiment can be used to acquire the shear modulus.

To evaluate the influence of textile yarn architecture, the elastic properties are further compared to the properties of a angle-ply laminate. A comparison to two angle-ply laminates with  $(\pm 29^\circ)$  and  $(\pm 31^\circ)$  layup is given in Fig. 4.26a. The layup of the angle-ply laminates represents the range of braiding angles found on the coupons by optical sensor measurements. The elastic response of the laminates was calculated, neglecting yarn waviness, with the UD properties given in Table A.3. The stiffness measured experimentally from the braided composite is between 10% and 20% lower as the one obtained from the angle-ply laminate. The difference is mainly attributed to the fiber waviness in the braided composite. As the fiber stiffness dominates the properties for low off-axis angles  $\psi = 0 \dots 30^\circ$ , the knock-down due to waviness is more prominent for these cases.

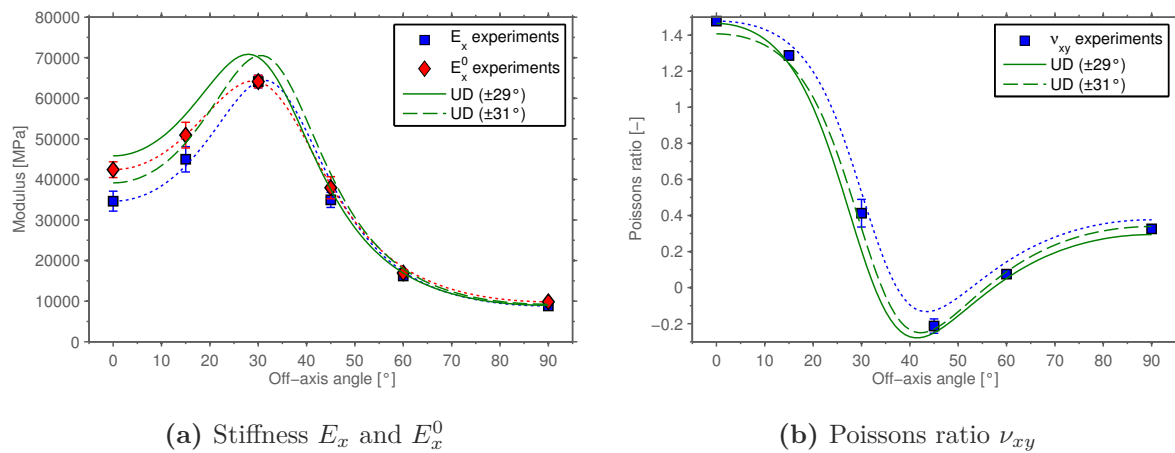


**Fig. 4.26:** Polar plot of elastic properties over the off-axis angle

The Poisson's ratio as a function of the off axis angle is given in Fig. 4.26b. The measured values over the off-axis angle agree well with the values calculated under the assumption of orthotropic behavior. The comparison to the ( $\pm 29^\circ$ ) and ( $\pm 31^\circ$ ) angle-ply laminates show only small deviations to the measured values, which mostly lie within the experimental scatter. The highest deviation is observed in the  $\psi = 30^\circ$  case, which is, as for the stiffness, mainly attributed to the fiber waviness in the braided composite.

A representative stress-strain curve for each tensile off-axis test series is presented in Fig. 4.27a. All stress-strain curves except for OA30 are nonlinear. The strength increases with the off-axis angle in the range of OA00-OA30. The highest strength is measured for OA30, where the load is aligned with one of the yarn directions, and a significant drop in the strength is observed for the higher off-axis angles OA45-OA90.

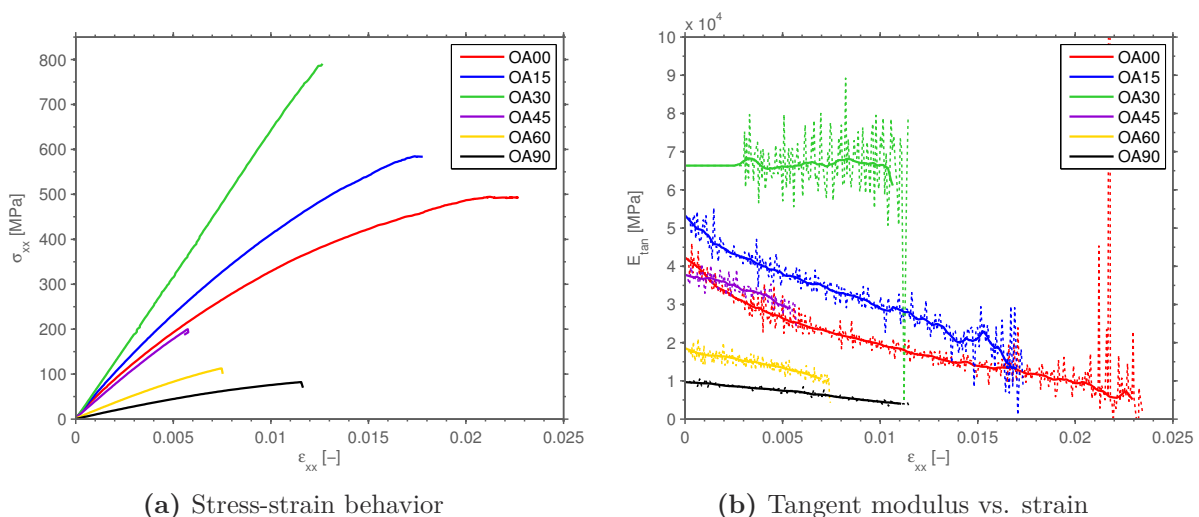


**Fig. 4.27:** Representative curves for stress and tangent modulus of the off-axis experiments

The highest strain to failure was measured for the OA00 test series, and drops with increasing off-axis angle for OA00-OA45. The OA45 test series has the lowest failure strain, which increases again for higher off-axis angles OA60-OA90. The difference in strength

and failure strains can be attributed to the stresses in the yarn directions, which can be evaluated by using an equivalent laminate model. The laminate model neglects the fiber waviness in the braided composites, but it helps to gain phenomenological understanding of the behavior, as yarns within a braid can be thought to follow a similar mechanical behavior as equivalent UD plies [95, 118]

For **0A00** and **0A15**, high strength and failure strain is believed to be due to the transverse yarn stress  $\sigma_{2F+/-}$  being compressive and inhibiting cracking introduced through shear stresses in the yarns. For **0A45**, the 1F+ yarn direction fails in transverse tension, which explains the brittle behavior and the low failure strain. For **0A60** and **0A90** the stiffness decreases faster compared to the strength, which increases the failure strain compared to **0A45**. For the fiber-dominated **0A30** test series, the failure strain is around 30% lower than the fiber failure strain given in the datasheet [176]. This decrease shows the influence of the textile architecture, as it is mainly attributed to strain concentration introduced through fiber waviness and transverse cracking.

Fig. 4.27b shows representative curves for the progression of tangent modulus in each off-axis case. The dotted lines are the tangent moduli obtained by finite difference, while the solid lines represent the curves calculated by regression of the stress-strain curve. For all off-axis angles except  $\psi = 30^\circ$  a significant decrease of the tangent modulus was observed. The tangent moduli progression can be separated into two main groups: while **0A00** and **0A15** decrease nonlinear, the decrease for **0A45**, **0A60** and **0A90** is linear and less within the same strain range. The tangent modulus decrease coincidences with the failure modes observed during the experiments, which involved a single crack for the test series **0A45**, **0A60** and **0A90** compared to a broad area of damage and delamination for **0A00** and **0A15**.

The degradation, i.e. decrease of stiffness, is smooth for all off-axis angles. This correlates with the observations regarding crack formation from DIC and high-speed camera: besides some edge-cracking observed for  $\psi = 0^\circ \dots 30^\circ$ , no aggregation of transverse or intra-yarn cracking was observed on the coupon surface prior to final failure. Thus, the degradation observed in the stress-strain curves is believed to be driven by microscopic effects on fiber/matrix scale rather than by macroscopic cracking, like e.g. intra-yarn cracking reported for triaxial braided composites in [45, 195].

The characteristics of cracking within the specimens was furthermore investigated with micrographs, which were extracted from the tested coupons. For each test series, micrographs with different orientations were cut from two coupons. Two micrographs were extracted for each coupon from the area of final failure and from an area, which showed no surface cracking during the experiment. The main goal of the investigations was to check, whether the cracks observed on the surface are representative for all plies within the laminate. The images from a **0A00** coupon are exemplarily shown in Fig. 4.28. For all off-axis angles, cracking within matrix or intra-yarn cracking was exclusively observed in the area of final failure. For the **0A45** series, some cracks were observed outside the location of final failure, which correlates with the results from DIC and high-speed camera recordings, as additional transverse cracking was observed for some of the **0A45** specimen. The observations from the micrographs lead to two major conclusions: the cracking pattern on the surface of the tested coupons is representative for all plies within the braided laminate and they confirm that the non-linear behavior observed in the stress-strain curves is driven by

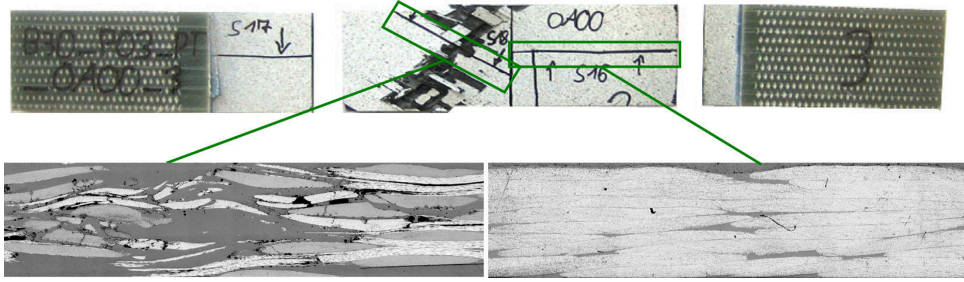


**Fig. 4.28:** Micrographs of cracking within a 0A00 specimen: cracks are solely observed in the region of macro-failure

microscopic damage events at the fiber/matrix scale as described in [170]. In addition, the first cracking observed was equal to the point of final failure for all test series.

#### 4.2.2. Tensile loading/unloading experiments

Loading/unloading experiments were conducted to investigate the mechanics of the non-linear deformation observed in the monotonic experiments. Two loading/unloading experiments have been conducted for each of the test series 0A00, 0A15, 0A45, 0A60 and 0A90. The specimens were loaded to a defined load level, unloaded to a small force and reloaded to the next load level. Four load levels were defined for each off-axis angle, where the load was increased up till failure in the fourth load cycle. It should be noted that the specimen were instantaneously re-loaded after reaching zero force, i.e. no information about time-dependency of the residual deformation has been acquired. However, the effect of stress and strain relaxation were reported to be small for ( $\pm 30^\circ$ ) carbon/epoxy braided composites by Kelkar and Whitcomb [26]. Thus viscous effects are unlikely to be dominant. The complete description of test procedure and the evaluation is given in Section 3.4.6.

The assembled stress-strain curves obtained from the loading/unloading experiments showed a similar behavior as the ones obtained in the monotonic experiments. Both strength and strain to failure were in all cases within the range obtained by monotonic loading, i.e. no effect of the unloading and reloading to the measured response of the specimen was found.

#### Stress-strain curves

A representative stress strain curve from a loading/unloading experiment for each off-axis angle tested is displayed in Fig. 4.29. Inelastic deformation is observed for all off-axis angles, with 0A00 and 0A15 showing the largest inelastic strains. For 0A45, the behavior is almost linear and only negligible inelastic strains are observed, whereas a small amount of inelastic deformation is observed for 0A60 and 0A90.

Fig. 4.30 gives an overview to the inelastic strain  $\varepsilon_{ie}$  and the damage variable  $d$  calculated from the stress-strain behavior of the experiments as described in Section 3.4.6. The lines refer to the average values, whereas the crosses mark the measurements. The x-axis in the plots is the unloading strain  $\varepsilon^{(1)}$  (cf. Fig. 3.23).

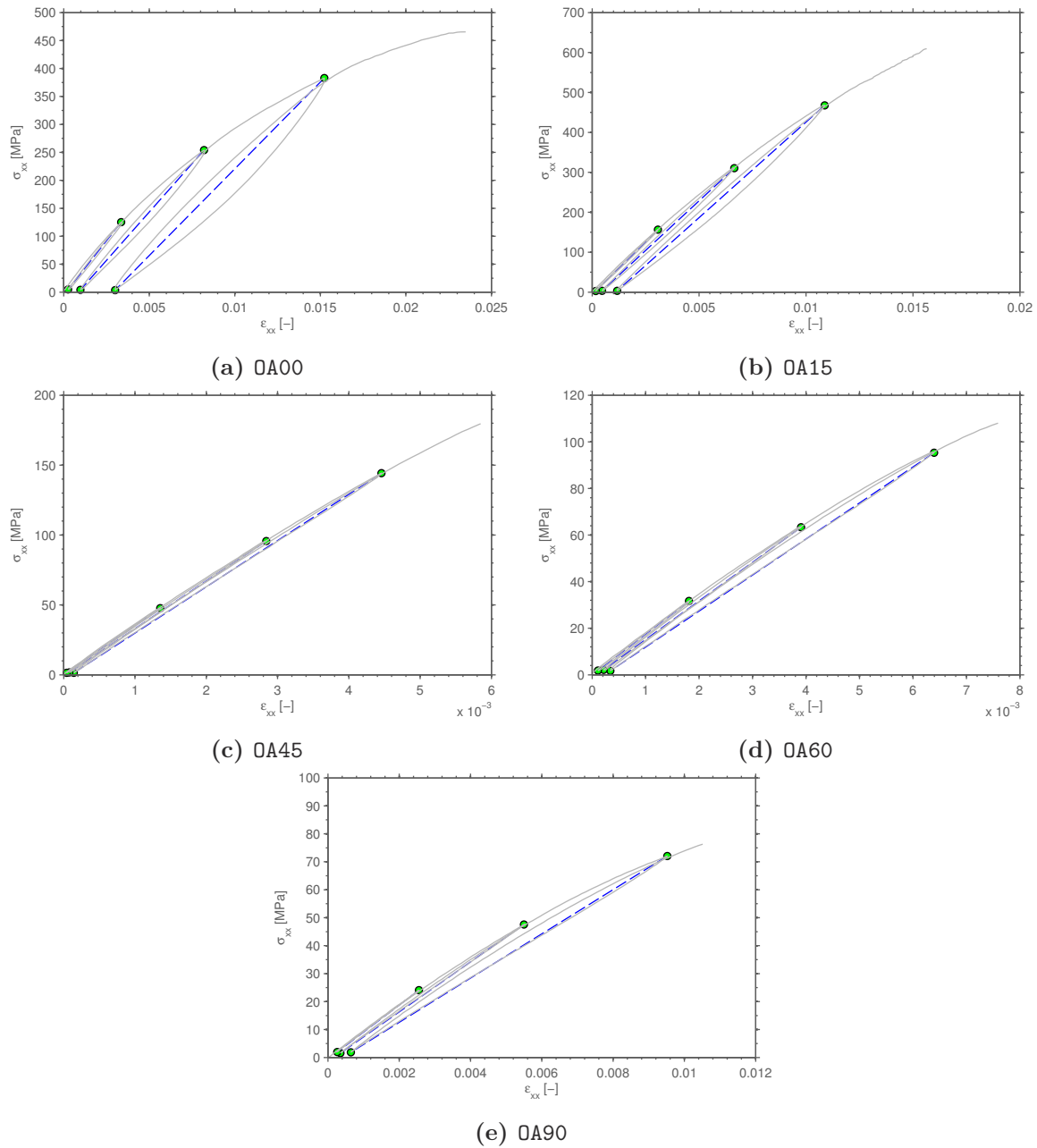


**Fig. 4.29:** Loading/unloading curves from the off-axis experiments

For the off-axis load-cases OA45, OA60 and OA90, the inelastic strain increases linearly with the applied strain (Fig. 4.30a) and the inelastic strains measured are generally lower compared to the other off-axis tests. In contrast to this, a nonlinear dependency is observed for OA00 and OA15: the inelastic strains increase for higher strain values, i.e. the inelastic deformation is believed to become dominant for larger strains. For the damage variable the dependency on the strain is also linear for OA45, OA60 and OA90. The slope is different for the OA45 experiments, but a high scatter of results was observed in these experiments, which is attributed to the fact that only minor nonlinearity was observed

for this load case. For OA00 and OA15 the dependency is nonlinear and contrary to the inelastic deformation, as the slope tends to decrease for higher strains.

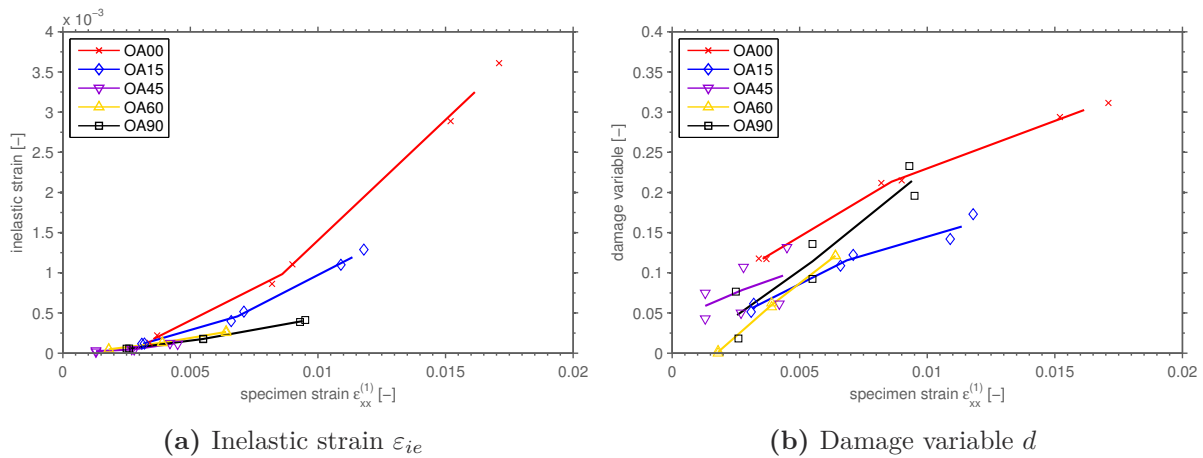


**Fig. 4.30:** Measures for inelastic deformation and damage from the loading/unloading experiments

Summarizing the loading/unloading experiments, a mixture of damage and inelastic deformation is driving the non-linear stress-strain behavior of the ( $\pm 30^\circ$ ) biaxial braided composites. Whereas values of similar ranges are obtained for material damage at all the off-axis experiments, inelastic strains are bigger for small off-axis angles. Fig. 4.31 compares the inelastic deformation observed in the experiments with the case of *ideal* inelastic deformation (cf. Eq. 3.19). The evaluation for the first cycle shows a big scatter, especially for higher off-axis angles. This is attributed to the small strains which are present during unloading of these experiments, where an evaluation error introduced by noise of the strain signal has a higher influence. The scatter is much lower for the second and third cycle, which reveal a clear trend: inelastic deformation has a higher influence for the small off-axis angles.

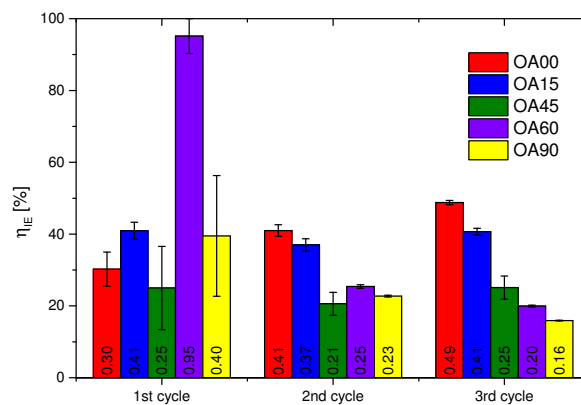


**Fig. 4.31:** Amount of inelastic deformation obtained from comparison to ideal inelastic unloading

The behavior can be explained by qualitatively evaluating the stresses in an equivalent laminate model. The higher influence of inelastic strains for small off-axis angles is mainly attributed to two reasons: firstly, the applied specimen stresses are higher for

these experiments, which results in higher shear stresses in the yarns. The nonlinear shear-behavior of the yarns is believed to be one of the main drivers for the inelastic behavior (cf. [117, 141, 170, 196]). Secondly, the stress state in the yarns is compressive in these cases, which additionally contributes to an inelastic deformation [141].

### 4.2.3. Compression

The compression tests were conducted according to *ASTM-D6641* with the combined loading compression (CLC) test fixture. Details about the test procedure and data acquisition are given in Section 3.4. The modulus for the compression test was evaluated according to the standard in a strain range of  $\varepsilon_{xx} = 0.1\% - 0.3\%$ , where the strain  $\varepsilon_{xx}$  is calculated as average from the two strain gauges. The test panels for **OA15**, **OA30**, **OA45** and **OA60** experiments were 4 mm thick to prevent buckling of the specimen during loading. Oblique tabs were not used for the compression test due to the limitations in specimen and tab size given by the test fixture. The failure pattern developed as in the tension tests along the yarn directions, thus in most cases the cracks were present in both, the gauge region and under the tabs. As this pattern of failure is driven by the yarn architecture and not introduced by local effects in the gripping, failure occurring in the gauge region and spreading into the gripping region was regarded as valid.

#### OA00

Six coupons were tested for the **PC\_OA00** test series. An overview to the test results is given in Table 4.14.

**Table 4.14.:** Test results from series **BB30\_PC\_OA00**

Test	Modulus	Strength	Failure strain	Bending		
	$E_x$ [MPa]	$\sigma_{OA00}^{UCS}$ [MPa]	$\varepsilon_{OA00}^{UCS}$ [-]	$\varepsilon_1$	$\varepsilon_2$	$\varepsilon^{UCS}$
PC_OA00_01	41377	329.67	0.0095	5.2	4.3	3.2
PC_OA00_02	39731	296.80	0.0088	-3.3	-1.7	-2.3
PC_OA00_03	42414	326.59	0.0101	-3.0	-2.8	-2.9
PC_OA00_04	40665	328.77	0.0112	2.5	0.6	-0.7
PC_OA00_05	39389	273.60	0.0080	0.0	0.4	0.5
PC_OA00_07	41678	291.09	0.0085	1.1	1.9	2.4
AVG	40876	307.75	0.0094			
STDV	1067	21.76	0.0011			
CV [%]	2.6	7.1	11.4			

$\varepsilon_1 = 0.001$ ,  $\varepsilon_2 = 0.003$ ; specimen 06 not tested

All experiments were valid regarding specimen bending, which was below 5% for all the tests. The Young's modulus varied little between the specimen, which is, as for the tension tests, related to variation of the braiding angle. The smaller scatter compared to the tension tests is attributed to the smaller gauge region and smaller overall dimensions

of the compression coupons. As the braiding angle varies systematically over the panel, less braiding angle variation is present in smaller specimens.

The stress-strain behavior of the specimen is shown in Fig. 4.32a and varies only little between the different experiments, which is an effect of the decreased braiding angle variation. The knee in the behavior of the specimen 03 is attributed to cracking under

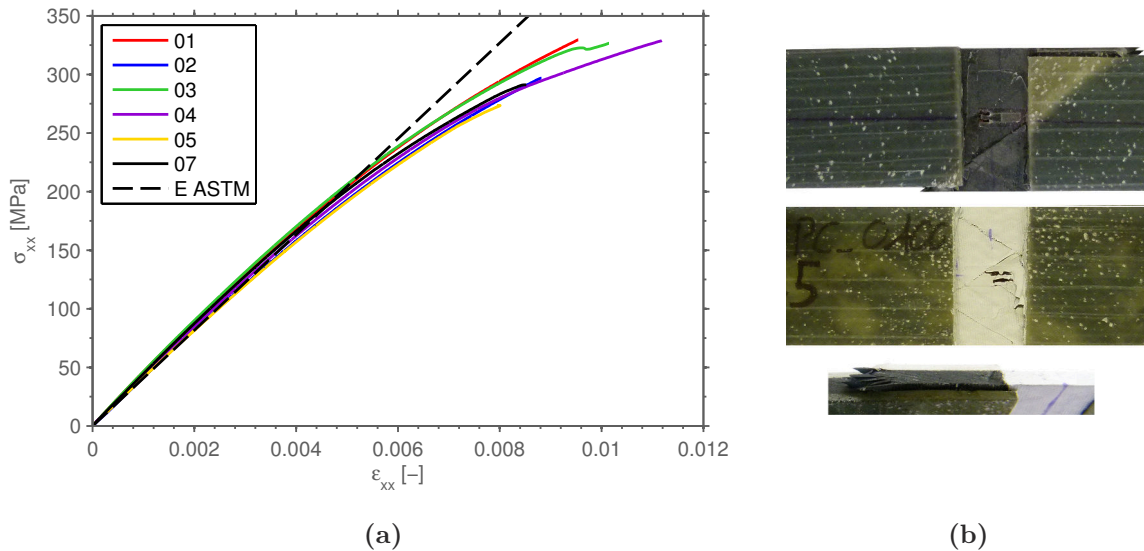


**Fig. 4.32:** Stress-strain curves and typical failure modes from the BB30\_PC\_OA00 test series

one of the two strain gauges directly before final failure.

Typical failure modes of the specimen are shown in Fig. 4.32b. All coupons failed within the gauge region by one or several cracks developing across the width of the coupon. The cracks were along one of the yarn directions, and thus running partly under the tabs. For the single crack failure, one crack along the yarn direction developed over the complete width of the coupon, while a zig-zag pattern of cracks was observed for the coupons with several cracks. No influence of the failure pattern to the strength or failure strain was observed, but the specimen failing in several cracks showed some residual strength after the first major load drop (not shown in Fig. 4.32a as the strain gauges failed with the first major load drop). As observed in the tensile experiments, the failure is abrupt and without previous specimen cracking. The damaged region of the coupon is rather small, comparable to the tensile experiments with high off-axis angles (OA45-OA90).

## OA15

Seven specimen were tested for the PC\_OA15 test series. For three specimen, increased bending values were measured at the beginning of the experiments (cf. Table 4.15), but as the bending decreased with further increasing load, the experiments were considered to be valid. The variance in stiffness, strength and failure strain between the experiments is very small, which, as for PC\_OA00, is attributed to the decreased braiding angle variation compared to the tensile tests. The stress-strain behavior (Fig. 4.32a) is slightly nonlinear up to a specimen strain of  $\epsilon_{xx} = 0.5\%$  and progresses nonlinear up till failure. All

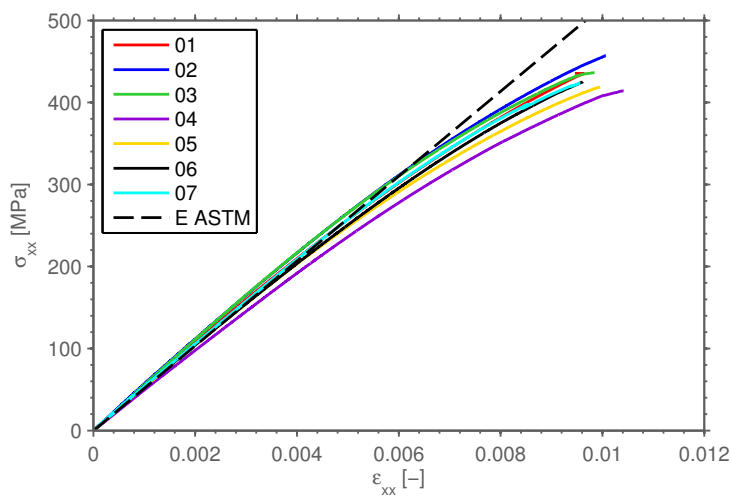


**Table 4.15.:** Test results from series BB30\_PC\_OA15

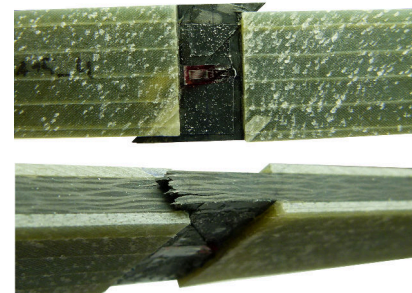
Test	Modulus $E_x$ [MPa]	Strength $\sigma_{OA15}^{UCS}$ [MPa]	Failure strain $\varepsilon_{OA15}^{UCS}$ [-]	Bending		
				$\varepsilon_1$	$\varepsilon_2$	$\varepsilon^{UCS}$
PC_OA15_01	52717	435.38	0.0095	-2.1	-1.2	-0.7
PC_OA15_02	53910	457.19	0.0101	0.6	0.8	0.7
PC_OA15_03	54631	436.44	0.0098	14.2	5.8	4.2
PC_OA15_04	47904	414.13	0.0104	11.8	7.7	8.2
PC_OA15_05	50714	418.58	0.0100	8.3	4.3	3.5
PC_OA15_06	50276	425.01	0.0096	-5.5	-5.5	-7.1
PC_OA15_07	51801	423.61	0.0096	16.9	10.7	8.7
AVG	51708	430.05	0.0098			
STDV	2136	13.40	0.0003			
CV [%]	4.1	3.1	3.1			

$$\varepsilon_1 = 0.001, \varepsilon_2 = 0.003$$

specimen failed in a single crack along the 1F+ direction, which is oriented  $45^\circ$  to the loading direction. A typical failure mode is shown in Fig. 4.33b: the failure is similar to the OA00\_PC series with a single crack running across the width of the coupon and the damaged region being limited to the cracking surface. Besides the main crack, no further damage is observed on the coupon.



(a)



(b)

**Fig. 4.33:** Stress-strain curves and typical failure modes from the BB30\_PC\_OA15 test series

### OA30

Seven specimen were tested for the PC\_OA30 test series. An overview to the test results is given in Table 4.16.

**Table 4.16.:** Test results from series BB30\_PC\_OA30

Test	Modulus	Strength	Failure strain	Bending		
	$E_x$ [MPa]	$\sigma_{OA30}^{UCS}$ [MPa]	$\varepsilon_{OA30}^{UCS}$ [-]	$\varepsilon_1$	$\varepsilon_2$	$\varepsilon^{UCS}$
PC_OA30_01	66367	618.73	0.0101	14.8	15.4	17.5
PC_OA30_02	64712	590.43	0.0100	35.6	18.1	13.2
PC_OA30_03	67677	672.81	0.0091	1.8	0.1	9.8
PC_OA30_04	64411	647.23	0.0127	0.6	-1.2	-12.4
PC_OA30_05	64249	580.31	0.0098	2.2	-0.3	-2.2
PC_OA30_06	64279	593.41	0.0109	1.9	2.4	6.1
PC_OA30_07	65572	633.10	0.0104	1.3	2.7	10.0
AVG	65324	619.43	0.0104			
STDV	1204	31.30	0.0011			
CV [%]	1.8	5.1	10.2			

$$\varepsilon_1 = 0.001, \varepsilon_2 = 0.003$$

Large values of specimen bending were present for two specimen (01 and 02) over the complete experiment up till failure (Fig. 4.34). Additionally, increased bending values at specimen failure were measured for the specimens 04 and 07. In the latter case, the increased bending values were due to preliminary surface cracking under one of the strain gauges, leading to a sudden overshoot of one of the strain signals. For the specimen 01 and

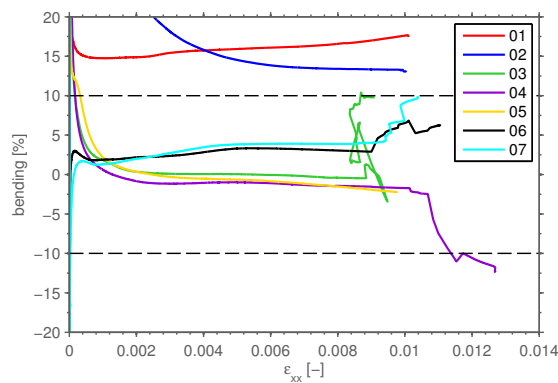


**Fig. 4.34:** Bending values measured for the BB30\_PC\_OA30 test series

02, increased bending was measured over the complete experiment, but as the specimen showed no significant difference in stiffness and strength compared to the specimen with lower bending values, they were considered valid. The increased values of bending are believed to be an effect of the comparable small strain gauge size: as the strain gauges

are smaller than a unit cell of the braided composite, local inhomogeneity of the strain field may be the cause of the difference in strain signals.

The stiffness and strength measured from the experiments showed low scatter, with the increased variation of the failure strain being attributed to the described preliminary strain gauge failures. The stress-strain behavior of the specimen is given in Fig. 4.35a: different to the tensile OA30 experiments, some nonlinearity can be observed in the compressive OA30 stress-strain curves. The jumps observed in some of the stress-strain curves (e.g. 03 and 06) are the consequence of the preliminary failure of one of the strain gauges.

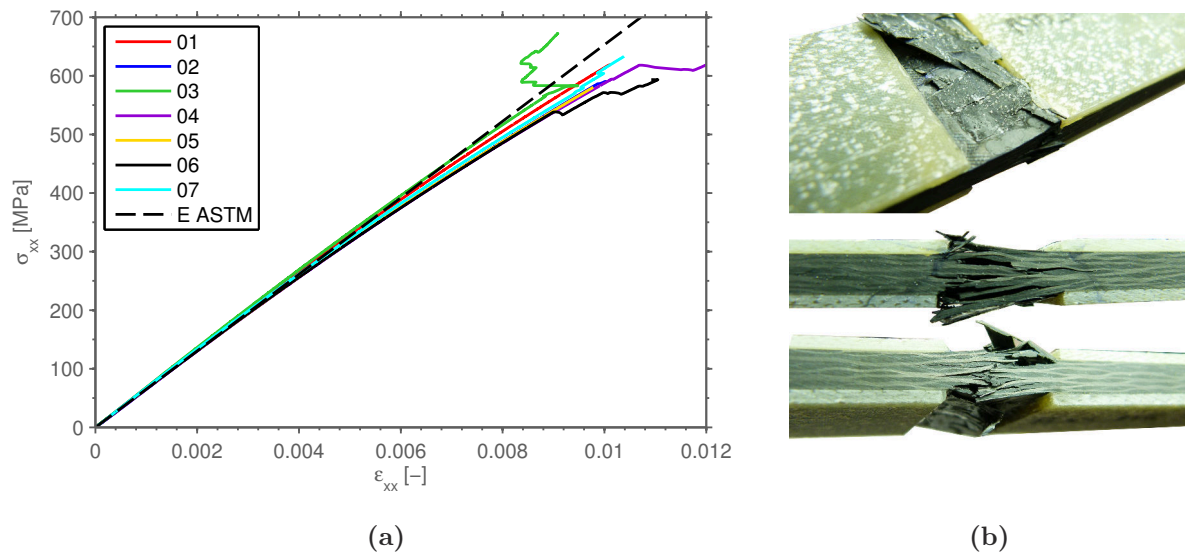


**Fig. 4.35:** Stress-strain curves and typical failure modes from the BB30\_PC\_OA30 test series

Typical failure patterns of the specimen are shown in Fig. 4.35b: all specimens failed with the major cracking being oriented along the 1F+ yarn direction, which is inclined  $60^\circ$  to the load axis. The plies of the braided laminates were spread open at the location of major cracking and a broad zone of damage within the gauge region is observed. The damage in the specimen includes transverse intra-yarn cracking, intra- and inter-ply delamination as well as yarn compressive failure. Compressive fiber failure is believed to control the failure behavior, as most yarns failed in the 1F- direction.

## OA45

For the PC\_OA45 test series, six specimen were tested, with an overview of the results given in Table 4.17. Bending values bigger than 10% were observed during the experiments for all specimens except one. For the specimen 03, 06 and 07, the bending decreased with loading, which indicates that the difference in strain between the two sides is not due to specimen bending. For the specimens 05 and 08, the measured bending value stayed almost constant and increased with loading, respectively. As the measured values for modulus, strength and failure strain of these specimen were in the range of the properties measured from the other tests, the specimens were considered valid. The stress-strain behavior of the specimen, shown in Fig. 4.36a, is almost linear until  $\epsilon_{xx} = 0.5\%$  and

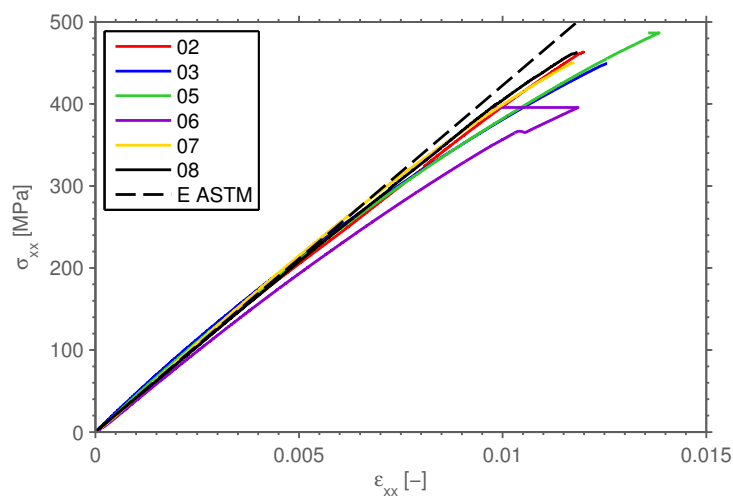
**Table 4.17.:** Test results from series BB30\_PC\_OA45

Test	Modulus $E_x$ [MPa]	Strength $\sigma_{OA45}^{UCS}$ [MPa]	Failure strain $\varepsilon_{OA45}^{UCS}$ [-]	Bending		
				$\varepsilon_1$	$\varepsilon_2$	$\varepsilon^{UCS}$
PC_OA45_02	41587	463.28	0.0120	4.3	-1.6	8.3
PC_OA45_03	43385	449.44	0.0126	32.2	17.5	7.2
PC_OA45_05	42961	486.62	0.0136	8.2	7.7	11.8
PC_OA45_06	39895	395.71	0.0119	16.2	11.1	4.9
PC_OA45_07	44067	450.10	0.0118	21.9	10.2	0.3
PC_OA45_08	41712	462.88	0.0118	-3.8	-15.1	-35.3
AVG	42268	451.34	0.0123			
STDV	1377	27.75	0.0006			
CV [%]	3.3	6.1	5.2			

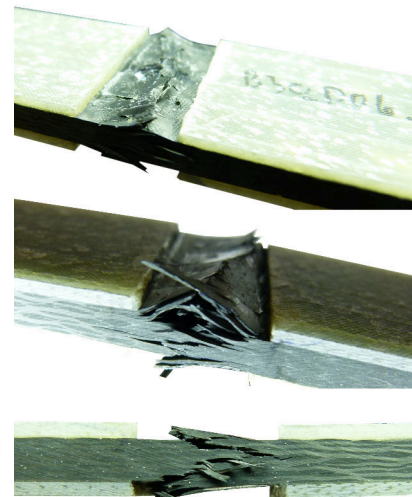
$\varepsilon_1 = 0.001$ ,  $\varepsilon_2 = 0.003$ ; specimen 01 and 04 not tested

progresses slightly nonlinear till failure. Failure was brittle in all cases, without any preliminary cracking observed before final failure.

Typical failure modes of the specimen are shown in Fig. 4.36b. All specimen failed with the major crack running along the 1F+ direction oriented  $75^\circ$  to the load axis. The plies are spread open similar to the PC\_OA30 case and the cracking is inclined through the thickness of the laminate. Crack propagation through the thickness shows a combination of transverse cracking and delamination. The crack pattern forms one or several wedges of material, which introduces the spreading of the braided plies.



(a)



(b)

**Fig. 4.36:** Stress-strain curves and typical failure modes from the BB30\_PC\_OA45 test series

**OA60**

Seven specimen were tested for the PC\_OA60 test series, with the results of the test series given in Table 4.18. Modulus, strength and failure strain showed only minor deviations

**Table 4.18.:** Test results from series BB30\_PC\_OA60

Test	Modulus	Strength	Failure strain	Bending		
	$E_x$ [MPa]	$\sigma_{OA60}^{UCS}$ [MPa]	$\varepsilon_{OA60}^{UCS}$ [-]	$\varepsilon_1$	$\varepsilon_2$	$\varepsilon^{UCS}$
PC_OA60_01	16529	317.44	0.0392	-5.4	-6.5	-3.7
PC_OA60_02	17392	315.74	- <sup>1</sup>	-1.2	-4.0	-29.9
PC_OA60_03	17144	314.26	0.0386	2.7	1.6	1.2
PC_OA60_04	17002	317.39	0.0371	0.7	0.9	-2.1
PC_OA60_05	18420	315.12	0.0363	5.1	4.1	1.8
PC_OA60_06	17096	310.61	0.0358	10.0	8.5	5.8
PC_OA60_07	18740	316.79	- <sup>1</sup>	-2.4	-2.0	-12.0
AVG	17475	315.34	0.0374			
STDV	744	2.22	0.0013			
CV [%]	4.3	0.7	3.5			

<sup>1</sup>: strain gauge failure

$\varepsilon_1 = 0.001$ ,  $\varepsilon_2 = 0.003$

between the tested specimen. The bending values were smaller than 10% in all cases, except for the specimen 02 and 07, where the one of the strain gauges failed, which lead to the increased bending values at failure. The average failure strain of the specimen was 3.7%, which is quite large compared to the other compressive off-axis test series, which failed at around 1% strain.

The increased failure strain also reflects in the stress-strain curves, which are nonlinear over the complete strain range. Similar to the other off-axis experiments, a smooth degradation until the point of failure is observed. For some of the specimen (e.g. 01 and 04), a slightly progressive stress-strain behavior just before final failure is present. This “stiffening” is not believed to be related to material behavior and is assumed to be due to a malfunction of the foil strain gauges. Similar effects are seen for the PC\_OA90 test series, but the cause of the error could not be identified clearly. Possible reasons for the behavior were assumed to be a contact of the strain gauge wire with the test fixture or issues with the foil bond.

Typical failure modes of the specimen are shown in Fig. 4.37b. All specimen failed with the major crack being oriented along the 1F+ yarn direction, which is at 90° to the load direction. Similar to the PC\_OA45 test series, a spreading of the plies within the gauge region was observed. The cracks are inclined through the thickness and the failure observed is a combination of transverse cracking and delamination.

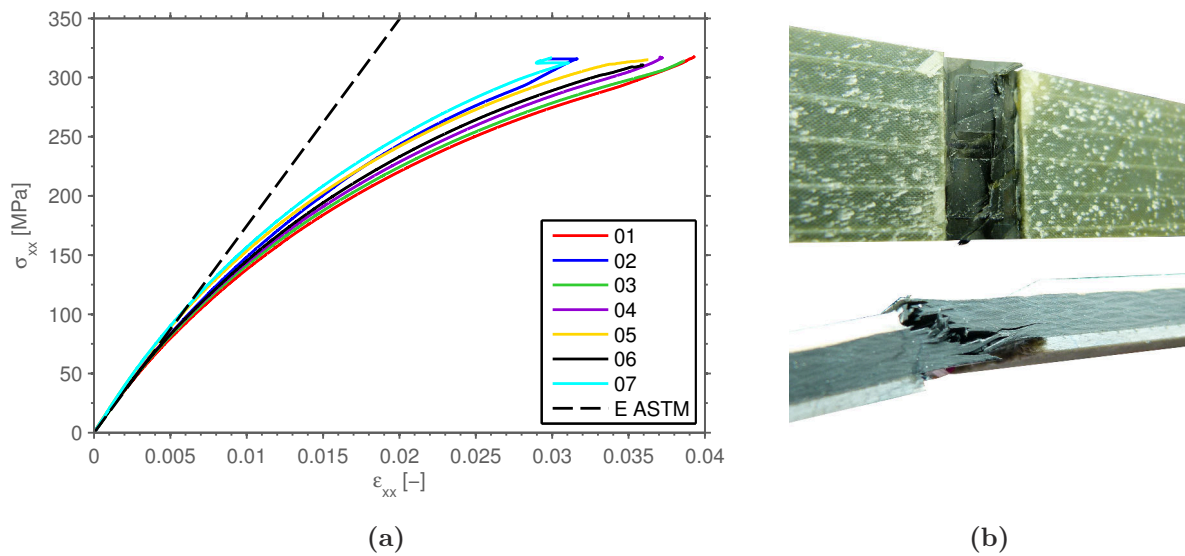


Fig. 4.37: Stress-strain curves and typical failure modes from the BB30\_PC\_OA60 test series

## OA90

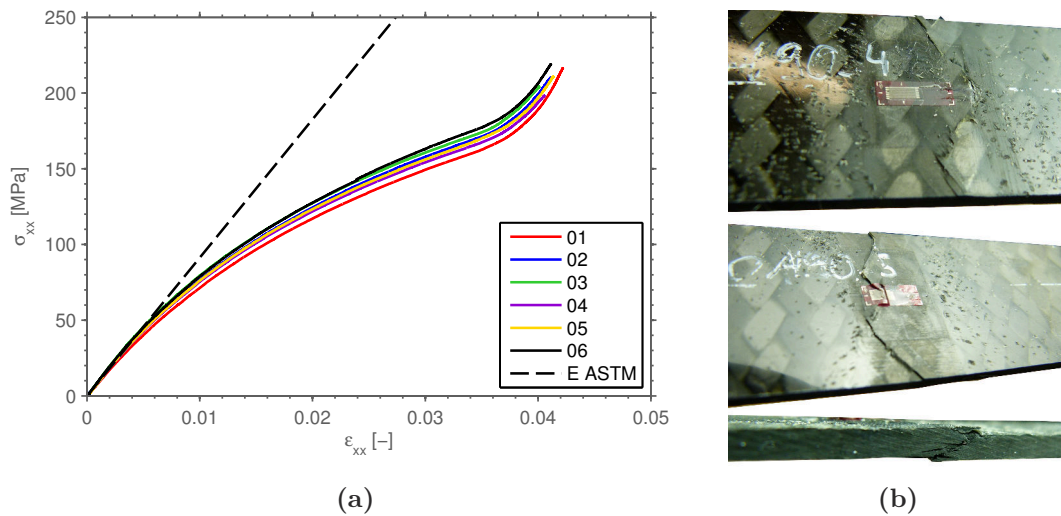
The results for the six specimen tested for the PC\_OA90 test series are summarized in Table 4.19.

Table 4.19.: Test results from series BB30\_PC\_OA90

Test	Modulus	Strength	Failure strain	Bending		
	$E_x$ [MPa]	$\sigma_{OA90}^{UCS}$ [MPa]	$\epsilon_{OA90}^{UCS}$ [-]	$\epsilon_1$	$\epsilon_2$	$\epsilon^{UCS}$
PC_OA90_01	8417	216.39	0.0422	-3.9	1.5	0.3
PC_OA90_02	9075	210.01	0.0411	-1.4	0.5	0.3
PC_OA90_03	9660	204.33	0.0401	-2.3	-1.7	-0.2
PC_OA90_04	9108	198.49	0.0406	-9.4	-5.1	-0.8
PC_OA90_05	9180	210.67	0.0414	-9.9	0.1	0.6
PC_OA90_06	9395	218.91	0.0411	-2.0	-2.4	-0.1
AVG	9139	209.80	0.0411			
STDV	380	6.89	0.0006			
CV [%]	4.2	3.3	1.6			

$$\epsilon_1 = 0.001, \epsilon_2 = 0.003$$

The variations of the results are small between the different specimen and the bending values calculated for the experiments are all within the acceptable range of 10% for all specimen. The average failure strain given by the strain gauge measurements was around 4%, but can be assumed to be higher due to the observations from the stress-strain curves. Fig. 4.38a shows that all stress strain curves measured in the experiments are progressive in the region above  $\epsilon_{xx} > 3.5\%$ .



**Fig. 4.38:** Stress-strain curves and typical failure modes from the BB30\_PC\_OA90 test series

This effect is similar to the one observed in the PC\_OA60 experiments and is assumed to be due to a malfunction of the strain gauge measurement. Linear extrapolation of the strain signal gave the failure strain to be around  $\epsilon_{xx} = 5\%$ . Neglecting the progressive region at the end, the stress strain behavior of all specimen shows a smooth degradation of the stiffness up till final failure. The failure observed for all specimen was abrupt, without preliminary cracking, as in the other off-axis test series. Typical failure patterns are shown in Fig. 4.38b. A zig-zag path of the major crack running across the width of the coupons is observed for all of the specimen. The crack runs along the yarn edges of the upper ply and is inclined through the thickness (Fig. 4.38b). Different to the PC\_OA45 and PC\_OA60 experiments, only minor spreading of the plies was seen in the PC\_OA90 experiments.

### Summary of the off-axis compression experiments

All properties were normalized to a fiber volume fraction of 60% for the comparison. The Young's moduli of the off-axis experiments are summarized in an off-axis plot in Fig. 4.39. Additionally, the off-axis moduli of ( $\pm 29^\circ$ ) and ( $\pm 31^\circ$ ) angle-ply laminates, neglecting yarn waviness (UD properties from Table A.3), are given. The elastic results are similar to the ones obtained from the tension tests: stiffness knockdown due to waviness is mainly seen for the load applied in one of the fiber directions ( $\psi = 30^\circ$ ) and for the lower off-axis angles ( $\psi = 0^\circ \dots 30^\circ$ ).

A representative stress-strain curve from every test series is shown in Fig. 4.40a. In difference to the tension tests, a nonlinear behavior is obtained for all off-axis angles. Also for the  $\psi = 30^\circ$  experiments, where one of the yarn directions is aligned with the load, a nonlinear stress-strain behavior was measured. The stress-strain curves show a stiffer behavior for  $\psi = 0 \dots 45^\circ$ , while  $\psi = 60 \dots 90^\circ$  behaves much softer. The highest strength is measured for the load aligned with one of the yarn directions  $\psi = 30^\circ$ , but different to the tensile tests similar strength are measured for  $\psi = 15^\circ$  and  $\psi = 45^\circ$  as well as for  $\psi = 0^\circ$  and  $\psi = 60^\circ$ . The failure strain is lower than 1% for  $\psi = 0^\circ \dots 30^\circ$  and

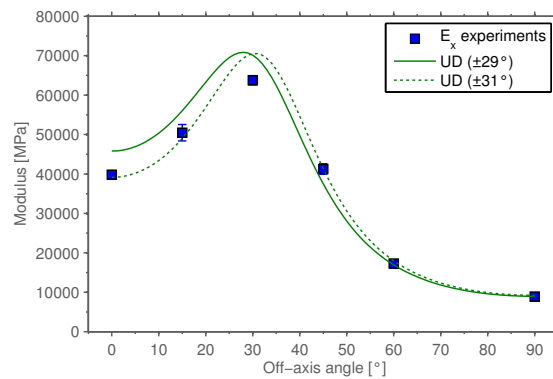


**Fig. 4.39:** Polar plot of elastic compressive properties over the off-axis angle

increases with increasing off-axis angle up to more than 4% for  $\psi = 90^\circ$ . The progression of tangent moduli show that the decrease of modulus is minimal for loading in one of the yarn directions ( $\psi = 30^\circ$ ), highest for the low off-axis angles  $\psi = 0^\circ$  and  $\psi = 15^\circ$  and lower for  $\psi = 45^\circ \dots 90^\circ$ .

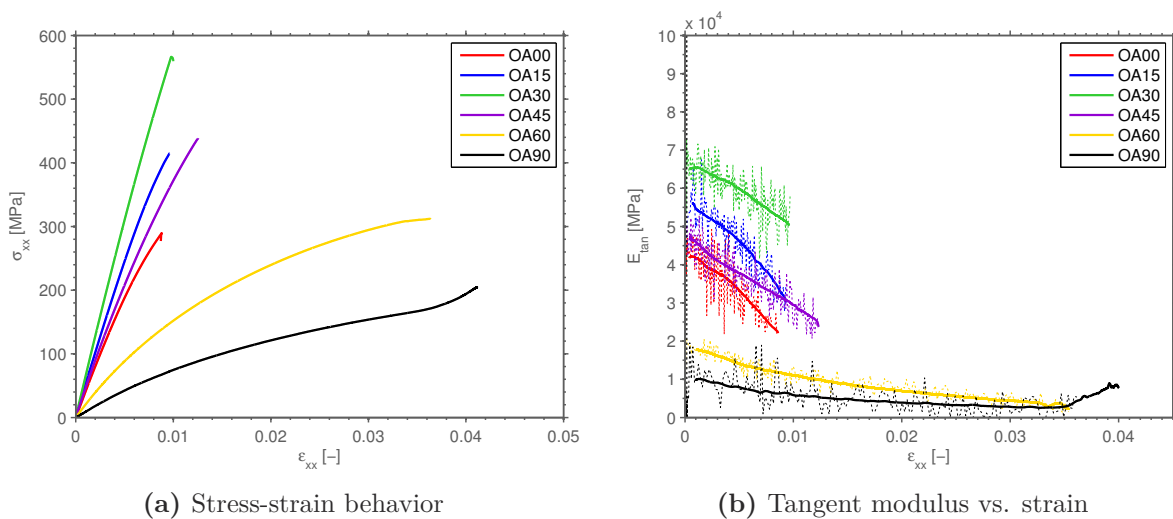


**Fig. 4.40:** Representative curves for stress and tangent modulus of the compressive off-axis experiments

Increased bending values, exceeding the normally permitted 10%, were observed in some of the specimen from the OA30 and OA45 test series. But no significant difference in the measured properties was observed in the specimen with high bending values. Thus, the high bending values are attributed to the inhomogeneity of the strain field on a braided composite: in OA30 and OA45 one of the yarn directions is oriented  $0^\circ$  respectively  $15^\circ$  to the load direction, which has the effect that a strain gauge can be placed completely on a straight region of the yarn, yielding a rather local strain value measured. However, the strain gauge size is a limitation of the test fixture used, and could only be avoided if using bigger specimen gauge sections in a different procedure in combination bigger strain gauges. Alternatively, DIC could be used in combination with a different test fixture, which allows proper illumination and view to the specimen. But the effort for



measurements drastically increases, as two DIC systems are needed to measure strain on both sides of the specimen. It can be concluded that the CLC test procedure used offers a good possibility for off-axis compression tests of braided composites. Alternative test procedures including bigger specimen gauge sections could be favorable, but the development of improved measuring techniques was out of scope of the presented investigations.

The failure patterns observed on the specimen by postmortem inspection (Fig. 4.41) can be grouped into 2 main failure modes: for OA00 and OA15, a single crack across the width occurred with no delamination between the plies and small damaged zone on the specimen. For OA30, OA45, OA60 and OA90 a broad damaged zone with delamination between the plies and the crack being inclined in the thickness direction was present. For OA30, compressive fiber failure was observed, while the other off-axis angles were dominated by transverse cracking. The OA90 test series failed in single crack across the coupon width, with the failure mode being similar to OA45 and OA60, but with less delamination and without spreading of the plies in the specimen.

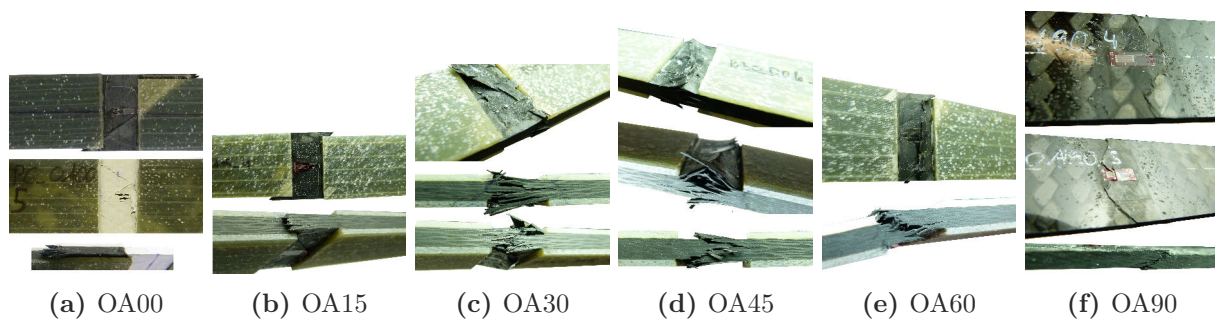


Fig. 4.41: Failure modes of the specimen observed in the compression tests

#### 4.2.4. Comparison of tension and compression off-axis experiments

For the comparison of tensile and compressive off-axis experiments, all properties were normalized to 60% FVF according to the procedure given in Section 3.4.7.

##### Stiffness

The comparison of tensile and compressive Young's moduli is given in Fig. 4.42. The modulus evaluated in the strain interval  $\varepsilon_{xx} = 0.1\% - 0.3\%$  is used for the comparison. The moduli obtained in tension and compression are very similar for all off-axis angles tested, with the OA00, OA15 and OA45 compressive moduli being slightly higher than the tensile ones. For OA00 and OA15 this is mainly attributed to the material volume tested being smaller for the compressive tests, which decreases the effects of braiding angle variation observed in the tensile tests. Additionally the stress-strain behavior of the compressive experiments was less nonlinear for low strains, i.e. the modulus  $E_x$  was closer to the initial modulus. For the OA45 test series, the difference is likely to be due manufacturing tolerances in the off-axis angle, which have a high effect on the stiffness of the OA45 experiments (cf. Fig. 4.39).

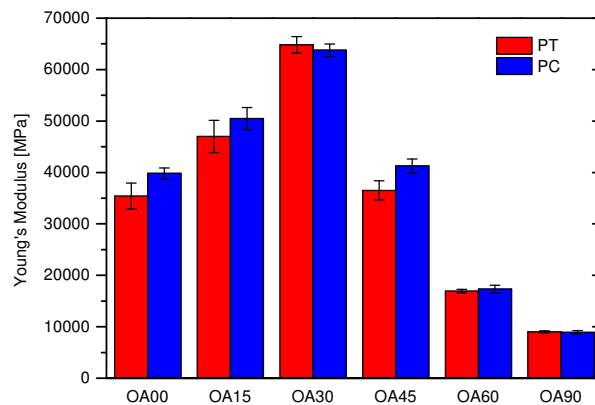


Fig. 4.42: Comparison of Young's moduli obtained from tension and compression off-axis experiments

### Strength, failure strain and failure modes

A comparison of the strength obtained from the tensile and compressive off-axis experiments is given in Fig. 4.43a. For both, tension and compression, the highest strength is observed in the OA30 case, where the load is aligned with one of the yarn directions. Comparing the strength between tension and compression, the tensile strength exceeded the compressive ones for the low off-axis angles  $0^\circ - 30^\circ$ , while an opposite effect is observed for the off-axis angles  $45^\circ - 90^\circ$ . For the failure strains given in Fig. 4.43b, a similar trend is observed. Here, the highest failure strains in tension are obtained in the OA00 load case, while the compressive failure strains are maximal for the OA90 experiments.

The difference in strength for the OA30 loading is believed to be due to the difference in longitudinal fiber strength in tension and compression. For the other off-axis angles, the

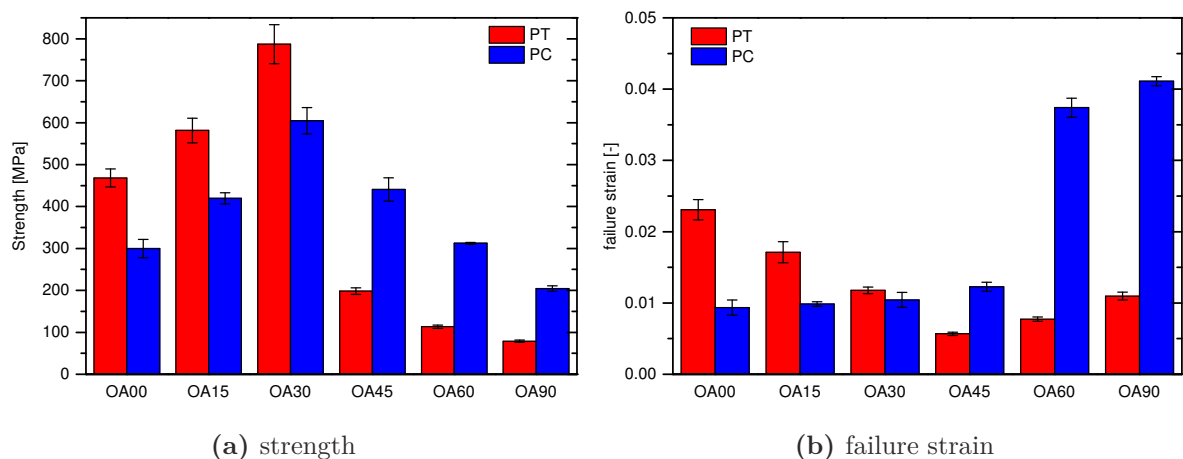


Fig. 4.43: Comparison of strength and failure strain from the off-axis experiments

failure modes observed were dominated by the transverse cracking, and the difference in strength and failure strain can be explained by evaluating a  $(\pm 30^\circ)$  equivalent laminate model. If a uniaxial tensile load is applied, the transverse yarn stress ( $\sigma_{2F+}, \sigma_{2F-}$ , cf. Fig. 3.1) is compressive for the off-axis angles  $\psi = 0^\circ$  and  $\psi = 15^\circ$  and tensile for the higher off-axis angles. For a uniaxial compressive stress, the sign of the transverse

yarn stress is opposite. The equivalent laminate model suggests two explanations for the difference in tensile and compressive strength:

- The transverse compressive strength of the yarns is, similar to UD composites, significantly higher as the transverse tensile strength. Thus, a failure with tensional transverse yarn stresses occurs at lower stresses.
- In the case of a transverse compressive yarn stress, cracks being initiated by shear stresses in the yarns may be kept closed by the transverse compression, i.e. higher shear stresses in the yarns are possible.

The comparison of failure stresses measured in the off-axis experiments shows that the mechanics of failure in biaxial braided composites follow the same trends as unidirectional composites, when the stresses in the yarn coordinate system are considered. Thus, the statement of Puck [95] can be approved, which encourages the application of UD failure theories to the yarn stresses for both, unit cells and macroscopic equivalent laminate models.

The differences observed between tensile and compressive loading are also reflected in the failure modes of the specimen compared in Fig. 4.44. Fiber failure is present in the OA30 experiments in tension and compression. For the other test series, the failure mode is shear-initiated transverse cracking, with a strong dependence of the failure patterns to the transverse yarn stress: a broad damaged area including delamination was observed in PT\_OA00 and PT\_OA15 experiments as well as in the PC\_OA45, PC\_OA60 and PC\_OA90 series, while failure by a single crack was observed for PC\_OA00 and PC\_OA15 and PT\_OA45, PC\_OA60 and PC\_OA90.

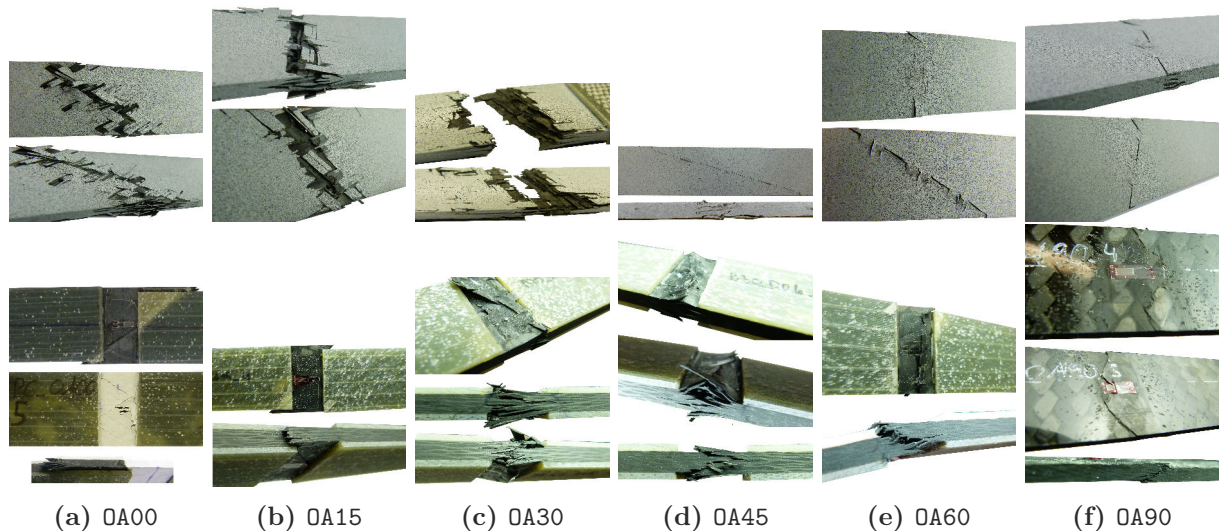


**Fig. 4.44:** Failure modes of the specimen observed in the tension (upper) and compression (lower) test series

### Stress-strain behavior

A comparison of the stress-strain behavior obtained from the off-axis experiments in tension and compression is given in Fig. 4.45. A representative stress-strain curve from each

test series is used. Overall, the stress-strain behavior is very similar in tension and compression. The biggest difference is seen for the OA45 test series, where the compressive response is stiffer compared to the tensile one. The difference is, as described above attributed to manufacturing tolerances regarding the off-axis angle. But besides the difference in initial stiffness for OA45, the stress strain curves are very similar. Additionally a slight difference is seen for the OA30 load case, where the compressive response is nonlinear in comparison to the linear response from the tensile test.

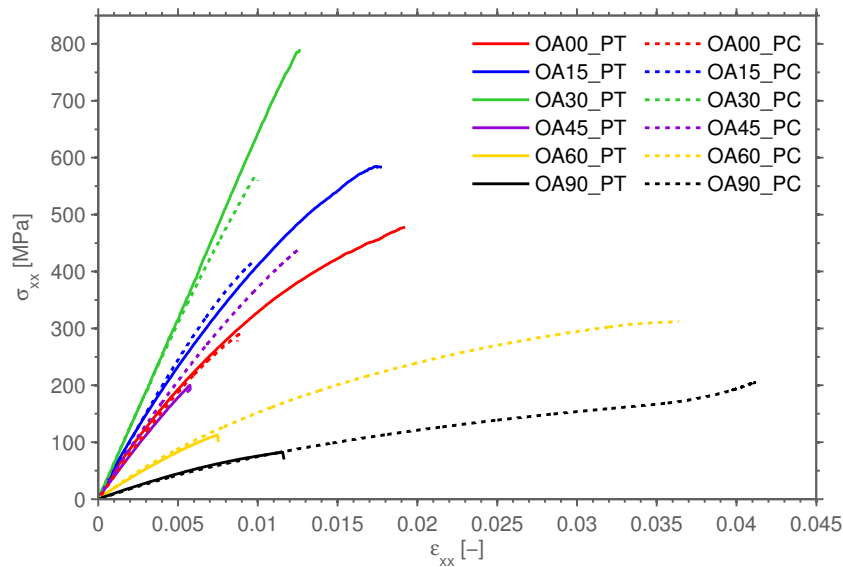


**Fig. 4.45:** Stress strain curves from tension and compression ( $\pm 30^\circ$ ) off-axis experiments

The similarity of the stress-strain behavior in tension and compression allows to draw conclusions about the drivers for the nonlinear deformation: as the same mechanics for the nonlinear deformation are present in tension and compression, the response of the biaxial braided composites is believed to be mainly governed by the shear behavior of the yarns. However, the small differences observed between tension and compression can be due to the additional influence of the transverse yarn stress.

## 4.3. Conclusion from experimental measurements

### 4.3.1. Yarn architecture characterization

Different methods for the characterization of the yarn architecture of biaxial braided composites have been investigated. As baseline technique, optical microscopy was used, and additional investigations using micro-CT and image analysis of surface scans were conducted. Optical microscopy was found to be an appropriate technique to acquire most of the yarn architecture parameters needed to build up a geometric model of the braided composites. Recommendations regarding the number and position of the samples required to achieve reliable results were summarized into a strategy for yarn architecture measurements. Micrographs were found to be not suitable to reliably measure the braiding angle. For this purpose, surface images were investigated with both hand measurements

and automated measurements using an optical sensor. The optical sensor proved to give more robust and detailed results, as a complete areal information is evaluated. Additional information on the yarn architecture regarding three-dimensional effects and nesting could be acquired by using micro-CT scanning. The shape and dimensions of the yarns were different near the surfaces, which questions to obtain yarn cross-section dimensions (e.g. yarn width) from surface scanning. Qualitative information of the yarn architecture could be extracted from the micro-CT scans, but a quantitative information was found to be more difficult to obtain, as an automated and robust segmentation of the CT-scans is required. This proved to be difficult due to the low contrast between matrix, longitudinal and transverse yarns.

All investigations presented here have been conducted on plane braided composite panels, but the strategy presented for yarn architecture characterization can also be applied to complete braided structures with variable yarn architecture on different regions of the component.

### 4.3.2. Mechanical characterization with tensile and compressive off-axis experiments

Off-axis experiments with a ( $\pm 30^\circ$ ) biaxial braided composite have been conducted to characterize elastic, non-linear and failure behavior. Oblique tabs have been found useful within the tensile test to improve the homogeneity of the strain field on the coupons. DIC and high-speed camera recording were used to get information about the strain field and the failure behavior in the tensile experiments. The combined loading compression test fixture together with foil strain gauges was used for the compression tests. Six test series with different off-axis angles were conducted in tension and compression. The off-axis angles allowed to introduce various combined stress states to the biaxial braided composites. The experiments yielded information about the stress-strain and failure behavior under combined loading and characterized the different failure modes of the investigated biaxial braided composite.

A high dependency of elastic properties, non-linearity of the stress-strain behavior and failure modes on the off-axis angles was observed. In the tensile experiments, a high influence of braiding angle variations on the mechanical properties was found in the OA00 and OA15 test series. A deviation in braiding angle angle of  $1.5^\circ$  created a difference in the stiffness and strength of the OA00 samples of 20% and 15%, respectively. As the braiding angle variation due to a s-shape of the yarns was present on all panels measured within this thesis, this variation of material properties is inherent. Similar variations of the braiding angle and thus changing material properties are expected on components produced by the same manufacturing process. Thus, a decreased braiding angle variation is crucial to achieve even and reproducible material properties.

The highest strength values in the experiments were measured for the load in yarn direction (OA30). The OA30 tensile strength was 30% higher as the compressive one, which is mainly attributed to the difference of tensile and compressive strength of the yarns. For the other off-axis angles, the strength was found to be dependent to the transverse stress state in the yarn, which was analyzed for the off-axis test cases with an equivalent laminate model. The strength was higher in the case, where the transverse

yarn stress was found to be compressive. This was in tension for OA00 and OA15 and in compression for OA45, OA60 and OA90.

While the stress-strain behavior was linear in tension for the braided composites when the load was aligned in the yarn direction (PT\_OA30), the behavior was nonlinear in all other load cases. Most of the experiments were also nonlinear for small strains, which lead to a big difference between the initial modulus  $E_x^0$  calculated by regression of the stress-strain curve and the elastic modulus  $E_x$  evaluated in a strain range from 0.1% – 0.3% axial strain. This implies that the elastic  $E_x$ , when used in a linear elastic models, only gives an approximate solution for the stress-strain relation. Furthermore, the usage of linear elastic models for biaxial braided composites is only valid for small loads, as the behavior is nonlinear over the complete strain range.

The comparison between PT and PC experiments showed that the stress-strain behavior for all off-axis angles was found to be very similar in tension and compression. This implies that the nonlinear stress-strain behavior of the biaxial braided composites is mainly driven by the shearing behavior of the yarns. Cyclic loading/unloading experiments in tension have been conducted to investigate the source of the nonlinear behavior. Both inelastic deformation and material damage was found within the cyclic experiments. The inelastic deformation was found to be more dominant for low off-axis angles, which was mainly related to the higher stresses present in the yarns for these experiments. Beside the phenomenological evaluation done for the experiments here, the stress-strain curves may be used as a basis for calibration of predictive models.

The failure modes observed in both, tensile and compressive experiments, were significantly influenced by the yarn architecture. In all experiments, the major cracking developed along one of the yarn directions of the braided composite. The failure modes observed in the specimen were fiber failure in tension and compression and shear-dominated transverse failure of the yarns. Fiber failure was observed in tension and compression for the load in the yarn direction (PT\_OA30, PC\_OA30) and additionally for the PT\_OA15 test series. Shear-dominated transverse failure of the yarns was observed either localized into a single crack (PT\_OA45, PT\_OA60, PT\_OA90 and PC\_OA00, PC\_OA15) or as broad failure spread accompanied with delamination and several intra-yarn cracking (PT\_OA00, PT\_OA15 and PC\_OA45, PC\_OA60, PC\_OA90). The failure mode was also found to be controlled by the transverse stress state in the yarns: for tensile stresses, the failure localizes into a single crack, while broad damage is present for compressive transverse stress.

Summarizing the mechanical characterization of biaxial braided composites with off-axis tension and compression experiments, the investigations proved to be very useful to achieve an understanding about the stress-strain and failure behavior of the braided composites. The high-speed camera used in the tension tests helped to develop an understanding of the failure process. Also the compression tests were found useful to develop a knowledge of the compressive failure of biaxial braided composites. The small strain gauges required for the CLC test fixture gave increased bending values for some experiments, but specimen buckling was not found to be problematic for the test series. The non-linear and failure behavior was found to be mainly driven by in-plane stresses and in-plane shear was dominant for nonlinear and failure behavior. The textile yarn architecture majorly influenced stress-strain behavior and failure modes, and simple equivalent laminate models were found to be useful to analyze the yarn stresses and explain effects

---

observed in the experiments. For all test series conducted, the first cracking in the braided laminates was found to coincide with the final failure of the specimen.

# 5. Geometric modeling and analytical predictions

Unit cell modeling is an established method for prediction of the nonlinear constitutive behavior of braided composites [39, 40, 45]. Basis for a unit cell model is the geometric description of yarns and matrix within the unit cell. The academic software package WiseTex [46] was used for geometric modeling of the biaxial braided unit cells within this thesis. WiseTex calculates the geometry of yarns and matrix based on yarn architecture input parameters.

The geometric modeling of the ( $\pm 30^\circ$ ) and ( $\pm 45^\circ$ ) braided composites, based on the yarn architecture parameters measured by optical microscopy, is described in this chapter. An assessment of the calculated geometric model is given by comparison of the WiseTex yarn geometry to the micro-CT scan of the ( $\pm 45^\circ$ ) braided composite. Based on the WiseTex geometric model, the braided composites' elastic behavior was predicted by using the micromechanics software TexComp [72]. The elastic predictions for ( $\pm 30^\circ$ ) and ( $\pm 45^\circ$ ) braided composites are compared to experimental results and parametric studies regarding yarn architecture variations are given. Furthermore, predictions based on analytically calculated yarn architecture parameters are compared to the ones based on measured parameters. Finally, the export of the yarn architecture geometry for finite element unit cell modeling is described.

## 5.1. Geometric model from WiseTex

The yarn architecture parameters given in Table 4.5 are used as an input for the geometric models. With the input, the yarn paths are calculated in WiseTex by using an energy minimization scheme: the fabric structure given by the braid pattern is divided into smaller parts, with the yarns in the undulation being represented by structural elements. The yarn path is approximated by a parametric function  $z(x)$  and the parameters of  $z$  are calculated by minimization of the structural elements' bending energy. A detailed description on the method can be found in [46].

### 5.1.1. Input parameters

The input parameters required to build up a unit cell model of a biaxial braid in WiseTex are given in Table 5.1. The input parameters can be separated into geometric parameters, defining the yarn geometry, and fiber/matrix mechanical parameters, which are stored in the WiseTex unit cell model for later usage in e.g. micromechanical calculations.

The parameters from optical microscopy given in Table 4.5 are used with the spacing adjusted to be equal to the yarn width. This is reasonable as the geometric model provided



by WiseTex does not include effects like yarn overlapping or yarn cross section deformation (cf. Fig. 4.2). Fiber mechanical properties were calculated by reverse engineering from UD experiments (Table A.1). The matrix mechanical data was taken from bulk matrix experiments (Table A.2).

**Table 5.1.:** Input parameters for WiseTex unit cell modeling

name	variable	source
<b>geometric data</b>		
yarn shape	-	micrographs
yarn height	$d_1$	micrographs
yarn width	$d_2$	micrographs
spacing	$p$	micrographs
braiding angle	$\theta$	optical sensor
<b>fiber data</b>		
filament diameter	$f_{fil}$	datasheet [176]
number of filaments	$N_{fil}$	datasheet [176]
fiber long. Young's modulus	$E_{f11}$	reverse engineering
fiber trans. Young's modulus	$E_{f22}$	reverse engineering
fiber shear modulus	$G_{f12}$	reverse engineering
fiber long. Poisson's ratio	$\nu_{f12}$	reverse engineering
fiber trans. Poisson's ratio	$\nu_{f23}$	estimated (no data available)
<b>matrix data</b>		
matrix Young's modulus	$E_m$	bulk matrix experiments
matrix Poisson's ratio	$\nu_m$	bulk matrix experiments

### 5.1.2. Unit cell geometry

The unit cell geometries for the BB30 and BB45 braids are shown in Fig. 5.1. For braiding angles unequal to  $45^\circ$ , a sheared unit cell is used. The thickness of the unit cell is twice the yarn thickness, which results in a fiber volume fraction of 54.4% for the BB30 and 53.5% for the BB45 unit cell. The unit cell fiber volume fractions thus deviates by 7% and 6.5% to the one experimentally measured from the braided panels of BB30 and BB45, respectively.

Reasons for the smaller fiber volume fractions present in the unit cell models are believed to be the deviations of the idealized geometric model to the real yarn architecture: effects like grown-together yarns, deformation of the yarn cross section, yarn cross section rotation or differences in the yarn architecture of the outer plies (cf. Section 4.1.4) are not considered in the WiseTex geometry model. As the correct fiber volume fraction is crucial for mechanical property prediction, an artificially increased packing density inside the yarns, yielding 60% unit cell fiber volume fraction, was used in the models. The approach of increased packing density is commonly used for analytical and FE unit cell models [22, 45, 57].

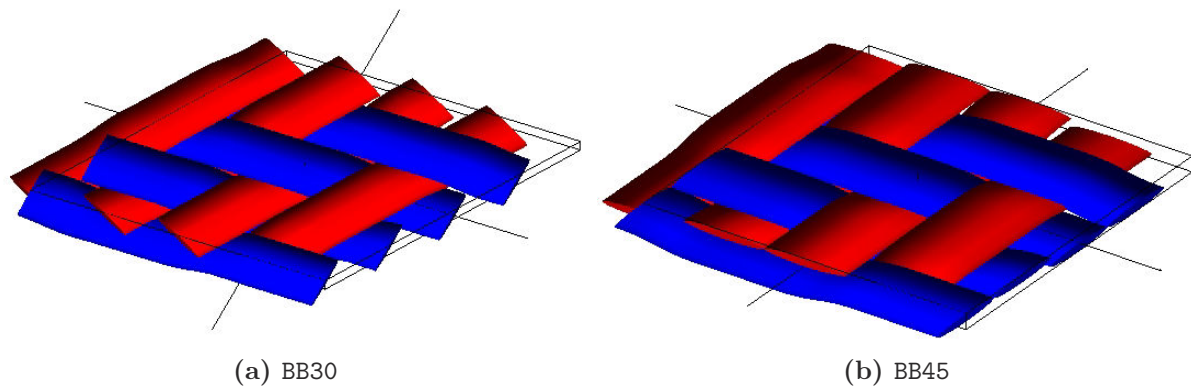


**Fig. 5.1:** Geometric models of the biaxial braided composites obtained from WiseTex

### 5.1.3. Comparison of unit cell geometry to micro-CT measurements

In order to assess the geometric model calculated by WiseTex, the yarn geometry was compared to the experimental results from the micro-CT measurements. One slice of the micro-CT data, with the WiseTex yarn geometry added to the CT image, is shown in Fig. 5.2. The comparison shows that the overall accordance of the geometric model to the micro-CT scan is reasonable. Besides local effects, attributed to yarn deformation and yarn path distortion, the yarn path is predicted well by WiseTex. The main deviations between the model and the real geometry can be summarized as: yarn cross-section deviation, penetration of adjacent plies and deviations from the idealized yarn path. Deviations from the idealized cross section are visible at different parts of the scan, and attributed to the yarn deformation during compaction. The penetration of adjacent (WiseTex) plies is marked in the figure, and is mainly attributed to the unit cell model thickness of the transverse yarns (red) being bigger as the thickness of the yarns in the CT scan. However, the displayed geometry of the model represents the transverse yarn cut in the center (i.e. thickest part), which is not the case for the CT-scan, where the ply position varies. Deviations of WiseTex and micro CT yarn path furthermore show, that the ideally straight part of the yarn is not straight in all cases.

No regularity in the deviations between CT-scans and geometric model is observed. Whether the models represents the yarn architecture well or deviates, depends on the position of the ply in the laminate (mold or vacuum bag side) as well as on the lateral



**Fig. 5.2:** Comparison of yarn geometry of WiseTex and from micro-CT scanning

position of the plies relative to each other. A characterization of these variations, as e.g. described in [55] can yield information for more precise yarn architecture models, but this requires improved techniques for micro-CT contrast increase and automated algorithms for image segmentation and shape detection, which was both beyond the scope of the current study. Furthermore, as the deviations are dependent on the laminate configuration and stacking, an improved geometric model would require additional information about the stacking of the plies relative to each other. For all plies in the laminate are to be modeled in a unit cell, the characterization effort and computational cost drastically increases. Furthermore, it is unlikely, that a distinct stacking, which needs to be defined as input, can be robustly achieved on a component. The focus of the unit cell modeling in the current thesis was on parametric and efficient unit cell modeling. Thus, single ply unit cell models were used to keep the model size small and the models efficient.

Summing up, the WiseTex geometry approximates the yarn path by idealized geometric shapes, which show a good overall accordance with micro-CT measurements. Local deviations can be observed between model and measurement, but for the goal of a predictive, efficient and parametric model, the choice of a single ply model based on an idealized yarn geometry is appropriate.

## 5.2. Elastic predictions

The geometric model from WiseTex was used for elastic predictions with the academic software TexComp [72, 112]. The elastic properties calculation within TexComp comprises several steps: the yarns in the textile are divided in small yarn segments and replaced by ellipsoids with equal geometric and constitutive properties. The aspect ratio of the ellipsoids is controlled by the local curvature of the yarn. All ellipsoid problems are solved by application of Eshelby's equivalent inclusion principle and the homogenization is done by using a Mori-Tanaka scheme [142].

A second prediction approach based on orientation averaging of was employed: A stiffness-averaging method was implemented into MATLAB, which is similar to the one proposed by Quek et al. [197] for triaxial braided composites. The undulation of the yarns is considered by stiffness-averaging of off-axis UD plies: the undulated yarn is modeled as a series of off-axis oriented UD plies assembled in iso-strain condition. For the yarn geometry, a cosine function was chosen in the undulation region and the yarns were assumed to be straight in the crossover region. Only two geometric parameters, namely width-to-height ratio of the yarns and the braiding angle are needed as input parameters for the geometry. The calculation of a UD ply stiffness matrix including yarn waviness is given by

$$C_{UD}^{wavy} = \frac{1}{N} \cdot \sum_{i=1}^N C_{UD}(\phi) \quad (5.1)$$

$C_{UD}(\phi)$  is the stiffness matrix of a UD ply with an out-of-plane angle of  $\phi$ , where  $\phi$  is calculated from the yarn path function. The stiffness matrix  $C_{UD}^{wavy}$  of one of the yarn directions is used within classical laminate theory to calculate the properties of an equivalent ( $\pm\theta^\circ$ ) laminate. A comprehensive description of the stiffness-averaging method is given in Appendix B.

### 5.2.1. Comparison of predictions to experiments

The results of the predictions are shown as off-axis polar plots of the axial modulus  $E_{xx}$  in Fig. 5.3, with the initial moduli of the BB30 and BB45 experiments given for comparison. The experimental characterization of the BB45 braided composites was conducted at the Polymer Competence Center Leoben, with the test results given in Table A.5.

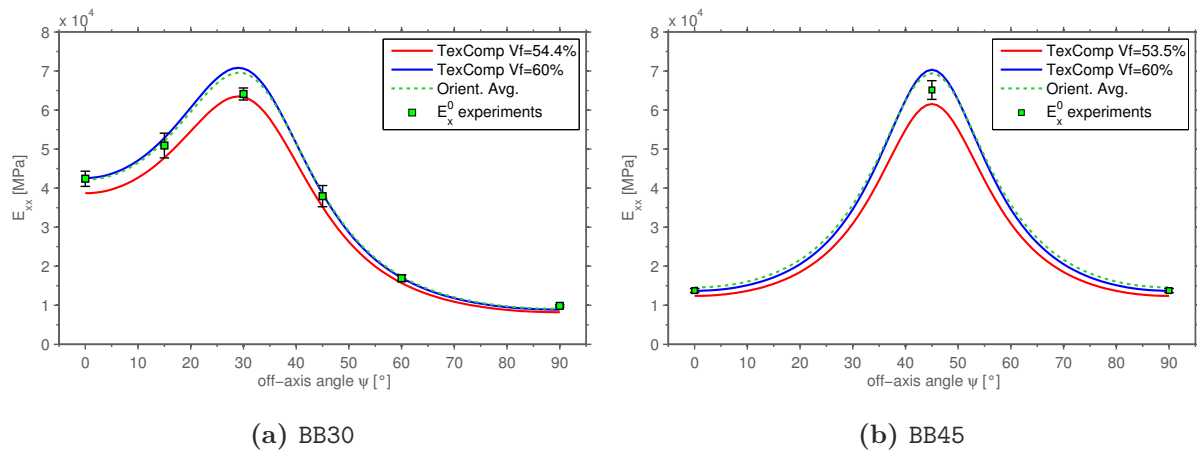


Fig. 5.3: Comparison of predicted elastic constants to experiments

For the TexComp results, two sets of predictions are given: the predictions based on the actual unit cell geometry given by WiseTex (54.4% respectively 53.3%) and the results obtained with the packing density scaled so that the total fiber volume fraction of the unit cell is 60%. The elastic constants at 60% FVF are 5%-10% higher, with the biggest difference being present in the yarn direction ( $\psi = \theta$ ). The results of the orientation averaging approach, using the same material properties and fiber volume fraction, are very similar to the ones obtained from TexComp. Comparison of the predictions with the experimental measured values yields good accordance for both braids investigated. Deviations between predictions and experiments are present in the yarn direction  $\psi = \theta$ , where the predicted stiffness is approximately 10% bigger for both BB30 and BB45. The difference is attributed to deviations of idealized and real yarn architecture and out-of-plane deformation effects, which are not covered by the analytical models. Further considerations regarding the out-of-plane deformation are given in Section 6.8. Despite the stiffness in yarn direction, all predicted elastic constants lie within the experimental scatter. Thus, both methods provide a fast and efficient way for elastic predictions of biaxial braided composites. Orientation averaging was found in close agreement to the results obtained by TexComp, and may be favorable if less information about the yarn architecture is available.

### 5.2.2. Effects of yarn architecture variation on elastic results

On the basis of the validation of WiseTex/TexComp results given in the previous section, parametric studies were conducted to evaluate the influence of changes in the yarn architecture to the elastic properties. Therefore, the yarn architecture input parameters

of BB30 and BB45 were varied within the bounds of the standard deviation found in the optical microscopy measurements (cf. Table 4.5).

### Yarn height

The variation of the yarn height yields for BB30 and BB45  $d_1 - \sigma_{d1} = 247 \mu\text{m}$  and  $252 \mu\text{m}$  and  $d_1 + \sigma_{d1} = 305 \mu\text{m}$  and  $312 \mu\text{m}$ , respectively. Two different schemes for yarn height change are investigated:

- (1) Solely the yarn height is changed. With the yarn width being constant, the fiber volume fraction also changes.
- (2) Yarn height and width are both changed, in order to keep the unit cell fiber volume fraction constant.

Both cases are relevant for braided composites: the first is achieved if the compaction pressure during infiltration of the braid is increased, while the second refers to the case that the yarns spread over a bigger area (e.g. mandrel cross section change). Fig. 5.4 shows a comparison of the variation compared to the model with the average yarn architecture values (*avg*) used. A similar trend is observed from both braiding angles: a decreased yarn height increases the stiffness of the braided composite. The effect of (1) on the mechanical behavior is bigger for both BB30 and BB45: the two effects of a fiber volume fraction change in the yarns and the change of waviness add up to the total increase or decrease of stiffness. The difference in stiffness is around 15%-20%, with the highest

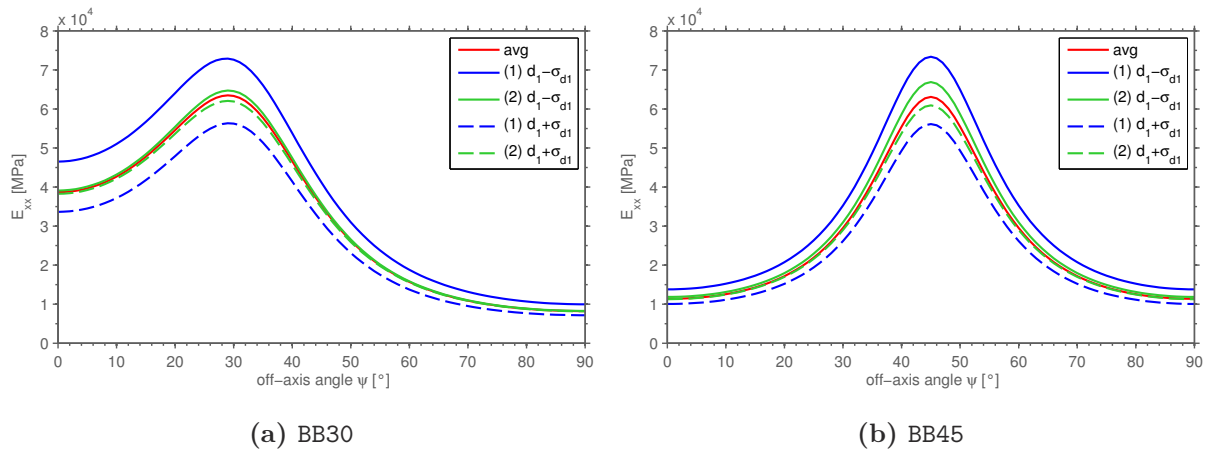


**Fig. 5.4:** Elastic behavior influence from yarn height variation

changes observed in axial and transverse direction. The second case (2) yields less changes of the elastic properties: the stiffness in the yarn directions of BB30 and BB45 changes by 2% and 8%, respectively, while the response is almost similar to the *avg* case for the other off-axis angles. The simulations show that the elastic properties for yarn height variations are sensitive to changes of the fiber volume fraction, while changes of yarn waviness at constant fiber volume fraction has less effects.

### Yarn width

The yarn width is varied for BB30 and BB45 in between  $d_2 - \sigma_{d_2} = 2829 \mu\text{m}$  and  $2831 \mu\text{m}$  and  $d_2 + \sigma_{d_2} = 3331 \mu\text{m}$  and  $3353 \mu\text{m}$ , respectively. Similar as for the yarn height, two cases are also distinguished for the yarn width variation: yarn width change with constant yarn height (1) and at constant FVF (2). The results shown in Fig. 5.5 that a higher width in the yarns not necessarily leads to increased mechanical properties: if the yarn height is constant with increasing yarn width, the fiber volume fraction decreases and the elastic properties suffer. In contrast, if the fiber volume fraction is kept constant, the wider yarns decrease the waviness, which increases the stiffness, where the biggest changes are, as for the yarn height, observed in the yarn direction.

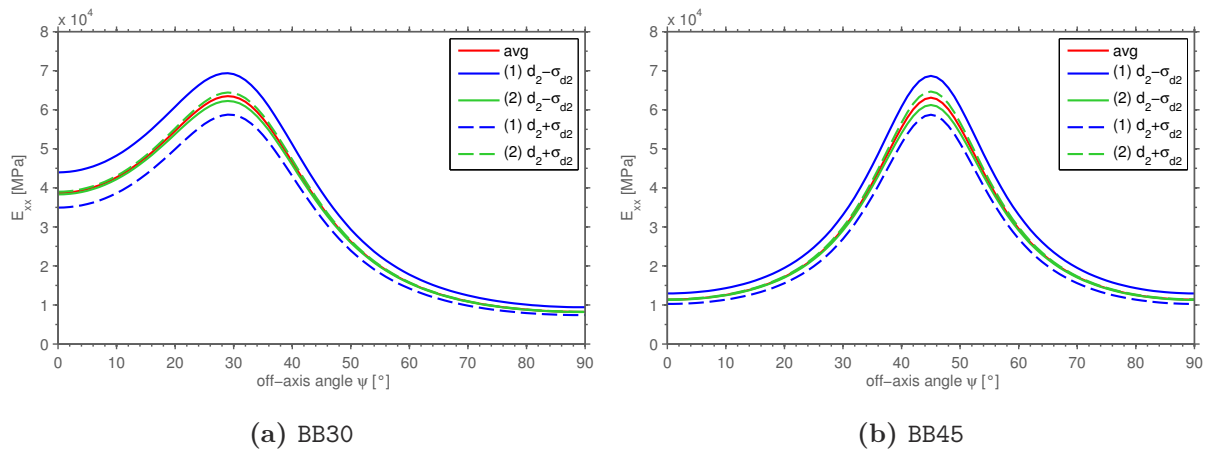


Fig. 5.5: Elastic behavior influence from yarn width variation

### Braiding angle

The braiding angle standard deviation was measured  $0.6^\circ$  for the BB30 and  $1.2^\circ$  for the BB45. Despite the rather small standard deviation, a systematic variation of the braiding angle due to the yarns' s-shape was observed on all panels. The elastic behavior predicted by TexComp is shown in Fig. 5.6. The biggest influence of the braiding angle is present for BB30 in the take-up direction and for BB45 in take-up and transverse direction. The stiffness in take-up direction changes by 5% for BB30 and by 7% for BB45. In opposite, the stiffness in yarn direction is not influenced by the braiding angle change, but the position of maximum stiffness changes with the braiding angle.

### Summary: effect of yarn architecture changes

The numerical investigations of elastic constants made with TexComp show a high sensitivity of the elastic behavior for the yarn architecture parameters varied within the bounds of the measured standard deviation. Changes of the unit cell fiber volume fraction were found to be the strongly affecting the biaxial braid stiffness. Changes of waviness at constant fiber volume fraction, which refers to the case of wider braid yarns, mainly influenced the stiffness in the yarn directions and the change of stiffness was smaller compared

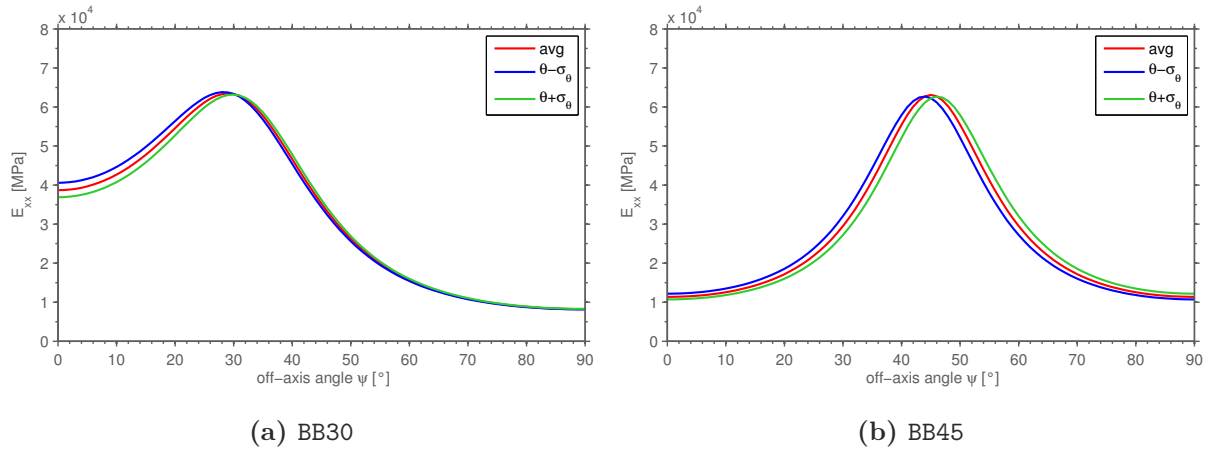


**Fig. 5.6:** Elastic behavior influence from braiding angle variation

to the cases where fiber volume fraction was changed. In addition, the braiding angle was found to have a high sensitivity to the stiffness in take-up direction, which correlates to the variation of stiffness observed in the BB30\_PT\_0A00 experiments (cf. Fig. 4.13a). Small changes of the braiding angle can considerably influence the stiffness of the braid, which emphasizes the relevance of considering yarn architecture changes for modeling of braided components.

### 5.3. Elastic predictions based on analytically calculated yarn architecture parameters

Analytical predictions for the yarn architecture can be favorable for application in the early design phase of braided components. Analytically calculated yarn architecture parameters were compared to the optical microscopy measurements in the previous chapter. Both sets of parameters given in Table 4.6 were used to investigate the possibility of using analytically calculated parameters for elastic property prediction.

The elastic constants, predicted on the basis of measured and analytically calculated yarn architecture parameters are given in Table 5.2. All properties except for the Poisson's ratio  $\nu_{12}$  of the BB30 braid, are overestimated when using the analytically calculated yarn architecture values. Young's and shear moduli are overestimated by around 10% for the BB45 and between 5% and 16% for the BB30 braided composite. The deviations of elastic properties outline the importance of optical microscopy for robust and precise yarn architecture characterization. Despite the deviations, analytical calculation of yarn architecture can be helpful for an early phase of design, when no detailed information on the yarn architecture is available. The presented approach of elastic predictions based on analytically calculated yarn architecture parameters yields similar results as the one outlined by Birkefeld et al. [33], with the advantage of the packing density not required to be estimated. Thus, the simplified approach for yarn architecture calculation, needing only fiber volume fraction, braiding angle and braiding process parameters as inputs, can be summarized as useful and to serve reasonable elastic predictions in the early phase of design, if no measurements of the yarn architecture are available.

**Table 5.2.:** Comparison of elastic constants predicted by the use of micrograph measurements and analytical predictions

	BB30			BB45		
	micrograph	analytical	deviation	micrograph	analytical	deviation
$E_{11}$ [MPa]	42590	47850	12.4%	13700	15220	11.1%
$E_{22}$ [MPa]	8881	10280	15.8%	13700	15220	11.1%
$G_{12}$ [MPa]	26610	28000	5.2%	34130	37810	10.8%
$\nu_{12}$ [-]	1.492	1.411	-5.4%	0.811	0.813	0.2%

## 5.4. Transfer of WiseTex geometry to finite element unit cell models

The geometric models inside WiseTex can be stored as either binary or XML<sup>1</sup>-type files.

If solely the geometry of the model shall be exported, WiseTex offers an export of the yarn geometry to an ASCII (*\*.cfl*) file. The *cfl* file stores the information of the unit cell and the yarns in a structured format, including unit cell dimensions, braiding angle and information about the geometric and material properties of the yarns defined in the model. An example of an *cfl* file for a biaxial braid with one type of yarn defined is:

```
14.2258905200649 14.2258905200649 0.552 # Unit cell dimensions
1.0472 # =2*theta opening angle of yarns [rad]
1 # number of yarn types
1 # Number of the yarn
Tenax HTS40 12K 800tex # designation of the yarn
E # shape of the cross-section
carbon fiber neu # name of the yarn fiber
0.0681 0.007 1.77 240 0.23 28 0.4 13 10 4300 1.8 # fiber data
1.5707963267949 # empirical fitting factor
616 # total number of sections
```

Furthermore, the information about the yarn architecture is stored segment-wise for every yarn. The number of segments in one yarn can be adjusted and is controlled by the *points per crimp interval* parameter within WiseTex. Every yarn segment includes information about the location, cross-section and orientation of the cross section:

```
## For every cross-section ##
1 # yarn type
76 # no. of cross-sections in yarn
-10.6694028054303 -6.16 0.138 # X Y Z coordinates of the current cross-section
0.187842969245378 # Length around the cross sections
3.08 0.276 # Principal cross-section axes, mm
0.0653168637087045 # Average curvature radius at the cross section center
0 -1 0 # Segment 1-axis, parallel to the major cross-section axis
0 0 1 # Segment 2-axis
1 0 0 # Segment 2-axis, tangent to the heartline.
0.691699604743083 # Fiber volume fraction inside a yarn
0.00129632941822128 # Yarn segment volume fraction
```

The *cfl*-file of the WiseTex model is used to import the yarn architecture data into the FE pre-processor Abaqus/CAE.

<sup>1</sup>XML: Extensive Markup Language



## 5.5. Conclusion on geometric modeling and analytical predictions

WiseTex was used to calculate the geometry of the biaxial braided composite unit cells. The geometry obtained from WiseTex was compared to the micro-CT measurements and a good agreement was found. Deviations were observed locally, where the micro-CT scan showed deviations from the idealized yarn cross section and yarn path shape. To include these local deviations into a geometric model, comprehensive evaluation of the CT-data (cf. [55]) and additional preforming simulation steps [82, 83] are required. In addition, the influence of adjacent plies on the geometry would require to model the complete braided laminate in a unit cell model. As the focus of FE unit cell modeling in this thesis was put to reduced, parametric and efficient unit cell models, the WiseTex geometry yielded an optimal choice. No additional simulation step is required to calculate the geometry and XML file format as well as command line capability allow integration of WiseTex into a FE modeling framework.

With the WiseTex geometry models, the elastic properties of the BB30 and BB45 braided composites could be calculated by using the analytical Mori-Tanaka approach implemented in TexComp. The predictions made with TexComp correlated well with experimental results with maximum 10% deviation being present in the yarn direction. In addition, a simple stiffness-averaging approach used for elastic property prediction yielded similar results as the WiseTex/TexComp modeling approach.

The WiseTex/TexComp model was further used for parametric studies showing a high dependency of the elastic behavior to yarn architecture input parameters: for yarn width and height changes, the effect of fiber volume fraction was dominant compared to the change of yarn waviness at constant fiber volume fraction. In addition, the braiding angle variations crucially affected the stiffness in take-up and transverse direction. Thus, also small braiding angle changes, e.g. introduced by the s-shape of the yarns, need to be considered in a structural simulation of a biaxial braided composite component.

## 6. Finite element unit cell modeling

This chapter describes the finite element (FE) unit cell models used within this thesis to predict the constitutive behavior of biaxial braided composites. The main purpose of the FE unit cell modeling was to predict the effect of the yarn architecture on the elastic, nonlinear and failure behavior of biaxial braided composites. The focus was on parametric and efficient models: with the goal of simulating a complex braided structure, unit cell simulations have to be able to calculate the constitutive behavior, which will later serve as input for macroscopic modeling, for a multitude of different yarn architectures. Thus, many different configurations of the unit cell need to be modeled and solved, yielding the main requirements for the FE unit cell models:

1. The model has to be parametric, i.e. modeling, solution and post-processing shall be automated without requiring manual operations like e.g. meshing in the pre- and post processing.
2. The model needs to be efficient. As many simulations are conducted for different yarn architectures, a fast modeling and solution is crucial.

These requirements led to the development of a new reduced FE unit cell modeling approach based on Cox's binary model [125]. In the novel Binary Beam Model (BBM), beams and continuum elements are used to model the yarns and matrix pockets in the biaxial braided composite unit cell. While the beam elements model the longitudinal properties of the yarns, the transverse and shear yarn properties and the properties of the matrix pockets are modeled in a smeared way by the so-called *effective medium* continuum elements. The reduced modeling approach yields advantages in efficiency and automation of model generation, when compared to the classical continuum unit cells [40, 45, 79]: continuum element unit cells serve a detailed representation of the 3D stress field in yarns and matrix, but often suffer meshing issues and poor element quality, connected to an increased numerical effort, when applied to high fiber volume fraction textile composites [37, 139]. Through the geometric idealizations introduced, these issues are not present in the BBM modeling approach.

The BBM modeling approach, implemented into a modeling framework in MATLAB, is described in the following sections. A short overview to the modeling framework, including the geometric modeling in WiseTex, geometry import into Abaqus/CAE, FE solution in Abaqus/Standard and post-processing is given. The constitutive laws, adapted to the reduced model formulation, are introduced: the model assumes linear elastic deformation in the beam elements and elastic-plastic behavior in the effective medium. Equations for the calculation of the yarn and effective medium material properties at different fiber volume fractions are introduced. This ensures the applicability of the unit cell modeling approach to braided composites with varying fiber volume fractions. Furthermore, the periodic boundary conditions for the rhombus unit cell used in the biaxial braided

composite simulations are given. The mesh-dependency, present in the stress-field of the effective medium, is removed by introducing an averaging procedure to calculate the yarn stress components at each beam node. Furthermore, the equations for the failure analysis using the BBM are defined.

BBM stress predictions in the yarns are compared to the solution of a classical continuum element unit cell. Elastic simulations with the unit cell under different out-of-plane boundary conditions are correlated to experimental measurements. Additionally, stress profiles at different out-of-plane boundary conditions are presented and an approach for the out-of-plane modeling of biaxial braided laminates is given. For the prediction of biaxial braided composites strength, a material parameter-identification approach based on experiments of biaxial braided composites was used. With the strength parameters calculated, the model predictions are finally validated by comparison to the experimental results from BB30 and BB45 off-axis experiments.

## 6.1. Framework for unit cell modeling

The approach for modeling and solution of the BBM FE unit cell was implemented into a MATLAB framework, which is outlined in Fig. 6.1. The framework allows to build, solve and post-process BBM unit cells without manual work, yielding a parametric and efficient modeling. First, the geometric, material and numeric input properties have to be defined in MATLAB. The framework builds a WiseTex XML file with the defined parameters and calculates the geometric model with WiseTexCL [74]. The calculated geometry is passed to a python script, which builds up the model in the Abaqus/CAE pre-processor, generating all the information required for solution and post-processing and finally writes the model to an ASCII *\*.inp* file. In an additional step, periodic boundary conditions are added to the model and the solution is started. The solution can be either linear elastic for the calculation of elastic properties or non-linear for strength prediction. All simulations were conducted with the implicit commercial FE solver *Abaqus/Standard*. After the FE solution is finished, the post-processing of the model is started, where another python script opens the Abaqus output-database (*ODB*), calculates the volume averaged stresses and writes these to the *ODB*. Depending on the type of solution, a failure analysis is conducted, returning the critical nodes for failure of the unit cell as well as the location of failure. Finally, the homogenized elastic constants (linear simulations) or the homogenized stress-strain behavior of the unit cell is calculated. Further information to the framework implementation is provided in Appendix E.3.

## 6.2. Binary Beam Model: modeling and idealizations

The main purpose of the BBM is to use a reduced representation of the textile yarn architecture, while preserving relevant details of the stress field of biaxial braided composite unit cells. The geometric idealization used within this thesis is similar to the one proposed by Cox and co-workers [125, 131, 198] in the Binary Model (BM): as shown in Fig. 6.2, the braided composite, consisting of yarn and matrix pocket volumes, is idealized by two independent sets of elements: 1D line elements at the yarn centerlines and 3D

<b>BBM Framework (MATLAB)</b>	
0. Input parameter definition	<ul style="list-style-type: none"> <li>- geometry</li> <li>- material properties</li> <li>- load</li> <li>- numeric parameters</li> </ul>
1. WiseTex XML / CL	<ul style="list-style-type: none"> <li>- create XML model</li> <li>- export geometry to ASCII-file</li> </ul>
2. Abaqus/CAE, Python scripting	<ul style="list-style-type: none"> <li>- read ASCII-file</li> <li>- create yarns + matrix block</li> <li>- assign material propertire, sections, mesh</li> <li>- find nodesets for gauge averaging</li> <li>- write INP-file</li> </ul>
3. Periodic boundary conditions (MATLAB)	<ul style="list-style-type: none"> <li>- find nodesets</li> <li>- calculate load(s)</li> <li>- include equations into INP-file</li> </ul>
4. Solving: Abaqus/Standard	<ul style="list-style-type: none"> <li>- linear-elastic / non-linear</li> </ul>
5. Post-Processing	<ul style="list-style-type: none"> <li>- Abaqus/CAE, Python</li> <li>- calculate volume-averaged stresses</li> <li>- apply failure criterion</li> <li>- output critical values to *.post-file</li> <li>- export constraint driver forces/displacements</li> <li>- MATLAB</li> <li>- calculate elastic constants</li> <li>- calculate homogenized stress-strain behavior</li> </ul>

**Fig. 6.1:** MATLAB-Framework for Binary Beam Model (BBM) unit cell

elements, defining the unit cell volume. Cox used truss elements for the yarns, based on the assumption that bending of the yarns is dominated by transverse shear, modeled by the effective medium. In the BBM, linear Timoshenko beam elements are used instead of truss elements. This allows to consider the influence of the yarn cross section on both the bending stiffness of the impregnated yarns and the bending-induced stress fluctuations in the yarns.

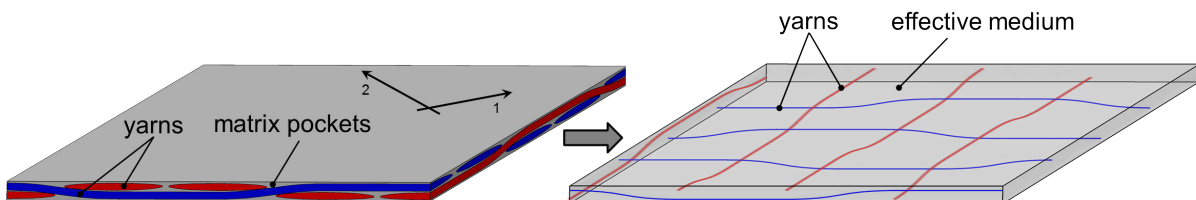


**Fig. 6.2:** Idea of BBM idealization

In the BBM, longitudinal and bending properties of the yarns are modeled by the Timoshenko beam elements, while transverse and shear properties of the yarns and the properties of the matrix pockets are represented in a smeared way by the 3D continuum elements of the effective medium. The impregnated yarn bending stiffness is influenced

by both, yarn material properties as well as shape and dimensions of the cross section. When loaded in the longitudinal direction, a stress concentration exists in the bending interval of the yarns. The stress on the upper and lower surface thus can be considerably higher as the yarn center stress (increase of 20% shown for a continuum unit cell model in Fig. 6.3). Thus yarn bending considerably influences the longitudinal failure of the yarns. Both effects, bending rigidity and stress concentration, can be considered by using the beam elements in the BBM.

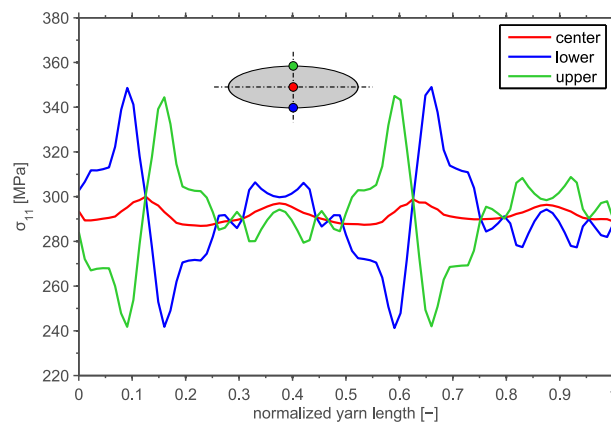


**Fig. 6.3:** Stress profile of a yarn loaded in longitudinal direction

The yarn geometry, exported from the WiseTex model, is used to define the coordinates, the tangential direction and the cross-sectional orientation of the beam elements. The yarn cross section of the WiseTex model is considered in the beam modeling by area and moments of inertia of the beams. The beam section properties are calculated from the yarn cross section dimensions:

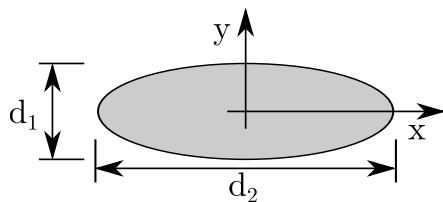


**Fig. 6.4:** Ellipse cross section

$$A_{yarn} = \frac{\pi}{4} d_1 d_2 \quad (6.1)$$

$$I_{xx} = \iint_A y^2 dA = \frac{\pi d_2 d_1^3}{64} \quad (6.2)$$

$$I_{yy} = \iint_A x^2 dA = \frac{\pi d_1 d_2^3}{64} \quad (6.3)$$

$$I_{zz} = \iint_A r^2 dA = \frac{\pi d_2^3 d_1^3}{16(d_2^2 + d_1^2)} \quad (6.4)$$

Where  $A_{yarn}$  is the area of the yarn and  $I_{xx}$ ,  $I_{yy}$  and  $I_{zz}$  are the second moments of inertia for bending and torsion of the elliptical cross-section given in Fig. 6.4. As given by the WiseTex model, all yarn cross-section properties are defined constant along the yarn paths. Size and shape of the WiseTex unit cell define the effective medium volume, i.e. the BBM unit cell includes four yarns in each direction and has the shape of a rhombus for braiding angles  $\theta \neq 45^\circ$ . Smaller unit cells of braided composites as e.g. given in [39, 199] can be used for finite element modeling to reduce the computational cost of the solution. However, as the BBM modeling approach yielded a very efficient solution even with the larger rhombus unit cell given by WiseTex, the unit cell volume was not reduced further.

### 6.2.1. Coupling of yarns and matrix

Two types of finite element meshes, a continuum mesh and a beam element mesh are used in the BBM. As the meshes of beam and continuum elements are not naturally consistent, i.e. do not share nodes, their degrees of freedom (DOFs) need to be coupled. The coupling can be either introduced by forcing consistent meshing of beam and continuum elements or alternatively by introducing constraint equations between beam and continuum nodes. Consistent meshing requires a fine continuum mesh and can, nevertheless, result in distorted continuum elements, yielding an increased numerical cost and a poor quality of stress and strain predictions. The usage of multi-point-constraint equations for coupling was reported for the Binary Model [133, 136] and for continuum element unit cells [124, 138] and thus was used for the BBM. The multi-point constraints coupling of the beam elements and continuum elements and can be easily established inside Abaqus by using the *embedded elements* function.

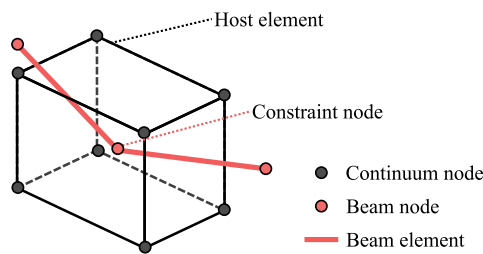


**Fig. 6.5:** Embedding of beam elements

The *embedded elements* function couples the translational DOFs of beam elements to the continuum elements. As shown in Fig. 6.5, each beam element node is assigned to the overlapping continuum host element. The beam node displacements are calculated from the displacements of the continuum element nodes, by interpolation of the beam node's relative position inside the host element. The rotational DOFs of the beam element are not constraint, thus the torsional behavior of

the yarns is solely controlled by the beam torsional stiffness. Introducing the coupling removes the requirement of consistent meshes from beam and continuum elements. However, the mesh size of the effective medium continuum elements was chosen in a way, that all yarns were embedded similar into the *effective medium*: the number of continuum elements along  $1/4$  of the unit cell edge should be an uneven integer to have all beams placed in-plane centered in one continuum element (cf. Fig. 6.6).

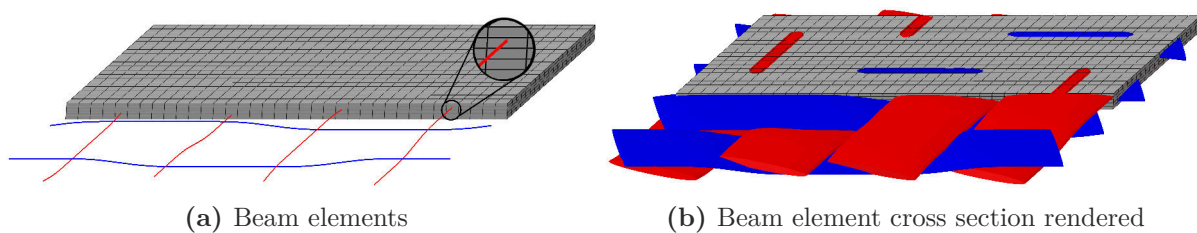


**Fig. 6.6:** BBM unit cell with embedded beam elements (half of the effective medium elements removed)

## 6.3. Constitutive laws

Material properties for beam and continuum elements need to be defined for the BBM. As the beam elements represent the axial and bending stiffness of the yarns, longitudinal yarn properties, namely axial modulus and strength of the yarns, are required for the beam

elements. The effective medium models the smeared transverse and shear properties of yarns as well as the properties of the matrix pockets. As the effective medium is defined isotropic, only shear and transverse modulus are required as elastic properties. Furthermore, yarn transverse tensile and compressive strength as well as yarn shear strength are required to evaluate transverse yarn failure. For modeling of non-linear deformation prior to final failure, a plasticity model was defined in the effective medium, which requires material parameters for pressure-dependence and hardening.

The constitutive properties of beam and effective medium elements depend on the packing density  $p_d$  in the yarns and on the unit cell fiber volume fraction  $\varphi_f$ . Thus, a parametric unit cell model needs the constitutive properties to be available at different fiber volume fractions. As most experimental investigations solely provide results for one specific fiber volume fraction, yarn and matrix constitutive properties are calculated by fiber/matrix micromechanics: fiber and matrix properties are calculated by reverse-engineering from UD experiments at a known fiber volume fraction, and can further be used to calculate yarn and effective medium properties at any desired fiber volume fraction. A variety of methods is available for micromechanics of UD composites, ranging from detailed FE unit cell calculations [41, 118], advanced analytical methods like e.g. methods of cells or multicontinuum technology [57, 113] to closed-form analytical formulae [24, 51]. Closed-form analytical equations were chosen in the current work, as they offers the advantage of straightforward and efficient implementation into the BBM modeling framework and do not require an additional analysis step. Analytical formulae do of course not represent the current state of research in micromechanical modeling, but they provide an simple and efficient way to scale both, elastic and strength properties to different fiber volume fractions.

### 6.3.1. Volume fractions

Constitutive property definition in the BBM requires consideration of the volume fractions inside a unit cell: as the beam elements (BE) have the yarn cross section prescribed and model the yarn longitudinal and bending stiffness, the packing density is used to calculate their properties. The beam elements introduce stiffness in their longitudinal direction, while the transverse and shear properties of the yarns and the matrix pocket properties are represented in a smeared way by the effective medium (EM). Thus, the composite properties at the unit cell fiber volume fraction are used for the effective medium elements.

$$\begin{aligned} P^{BE} &= f(P^{UD}, \varphi = p_d) \\ P^{EM} &= f(P^{UD}, \varphi = \varphi_f) \end{aligned} \tag{6.5}$$

### 6.3.2. Elastic properties

The elastic properties of beam and effective medium continuum elements are derived from the elastic properties of a yarn. As the yarn can be assumed to behave transversely isotropic, yarn properties are calculated from UD micromechanics. Different property assignments for the Binary Model have been proposed by Cox and co-workers [125, 131, 133]. The elastic properties assigned to the BBM follow similar ideas as the ones given

by Cox for the Binary Model. The fiber and matrix properties given in Table A.1 and Table A.2 are used throughout the simulations.

### Effective medium

The effective medium represents the matrix-dominated properties of shear and transverse behavior of the yarns and the behavior of the matrix. The effective medium can be either defined transversely isotropic or isotropic [131], with the latter yielding the advantage that no material orientation needs to be defined for the effective medium. As an unique material orientation definition in the effective medium is not possible for the braided composite unit cells modeled, an isotropic effective medium definition is used for the BBM, which has been showed to give appropriate results for the Binary Model [131, 133]. The off-axis experiments showed that in-plane shear and transverse behavior of the yarns dominate the mechanical behavior of biaxial braided composites. Thus, the effective medium was assigned with these elastic constants. The elastic constants are calculated with Chamis' micromechanical equations [200]:

$$E^{EM} = E_{22} = \frac{E_m}{1 - \sqrt{\varphi_f}(1 - E_m/E_{f22})} \quad (6.6)$$

$$G^{EM} = G_{12} = \frac{G_m}{1 - \sqrt{\varphi_f}(1 - G_m/G_{f12})} \quad (6.7)$$

The fiber volume fraction of the unit cell  $\varphi_f$  is used, as the effective medium represents the smeared properties of yarns and matrix pockets (Fig. 6.7). The Poisson's ratio of the effective medium yields

$$\nu^{EM} = E^{EM}/(2 \cdot G^{EM}) - 1. \quad (6.8)$$

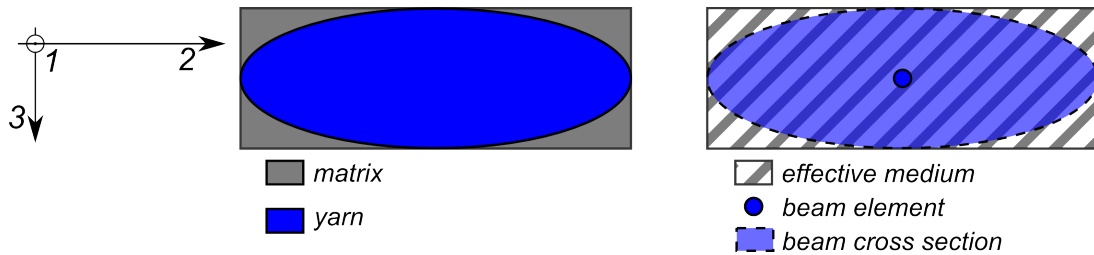


**Fig. 6.7:** Continuum yarn embedded in resin compared to a beam element embedded in effective medium in the BBM

### Yarns

The longitudinal stiffness of a yarn with the packing density  $p_d$  can be calculated by the rule of mixtures

$$E_{11}^Y = E_{f1} \cdot p_d + E_m \cdot (1 - p_d) \quad (6.9)$$

For the stiffness of the beam elements, the volume doubling present in the BBM has to be considered (Fig. 6.7): the yarn cross section is assigned to the beam element embedded



in the effective medium and thus the yarn volume in the BBM is filled twice, by the effective medium and the beam element. Using the yarn stiffness from Eq. 6.9 would result in an artificially stiffened behavior, thus the stiffness introduced by the effective medium has to be considered in the beam element constitutive definition. The beam elements stiffness is calculated by equalizing the stiffness of a yarn-in-matrix representation and the BBM as shown in Fig. 6.7

$$E_{11}^{CM} = E_{11}^{BBM} \quad (6.10)$$

$$E_{11}^Y \cdot \varphi_Y + E_m \cdot (1 - \varphi_Y) = E^{BE} \cdot \varphi_Y + E^{EM} \quad (6.11)$$

$E_{11}^{CM}$  and  $E_{11}^{BBM}$  are based on the assumption of equal strains of yarn and matrix, and beam element and effective medium, in the 11-direction. The equation solved to  $E^{BE}$  and with  $E_{11}^Y$  substituted from Eq. 6.9 and  $\varphi_Y = \varphi_f/p_d$  yields the beam element stiffness:

$$E^{BE} = E_{11}^Y - \left( E_m + \frac{p_d}{\varphi_f} \cdot (E^{EM} - E_m) \right) \quad (6.12)$$

### 6.3.3. Strength properties

The failure analysis within the BBM is based on failure criteria originally developed for UD composite materials. The yarn longitudinal stresses extracted from beam elements and the transverse stresses from the effective medium are used within the failure analysis. UD failure criteria were shown to be appropriate for prediction of failure and damage initiation within the yarns of textile composite unit cells (cf. e.g. [24, 45, 47, 140]). The strength input properties needed for a failure analysis with the BBM are yarn tensile and compressive longitudinal and transverse strength and yarn in-plane shear strength. Similar to the elastic constants, these parameters need to be available at arbitrary fiber volume fractions. Murthy and Chamis [200] presented a set of analytical equations in the framework of the Integrated Composite Analyzer (ICAN), which allow to calculate the composites UD strength properties based on fiber and matrix constituent properties.

The yarn longitudinal strength properties were calculated by using the rule of mixtures equations, proposed in the ICAN models:

$$X_T = \varphi_f \cdot X_{f,T} + (1 - \varphi_f) \cdot X_{f,T} \cdot E_m/E_{f11} \quad (6.13)$$

$$X_C = \varphi_f \cdot X_{f,C} + (1 - \varphi_f) \cdot X_{f,C} \cdot E_m/E_{f11} \quad (6.14)$$

In addition to the rule-of-mixtures equations, a compressive strength value for microbuckling and one for delamination is given in [200]. However, both equations yielded unrealistic strength values for high fiber volume fractions, and thus the rule of mixtures equations were used for the BBM. The longitudinal fiber strength values in tension  $X_{f,T}$  and compression  $X_{f,C}$ , calculated by reverse-engineering from UD experiments, are given in Table A.1. The increase of strength with fiber volume fraction predicted by the rule of mixtures yielded a good correlation to internal experimental data with a similar material at various fiber volume fractions [201].

For the transverse yarn strength, also some approaches for micromechanical calculation of strength properties are available. Ruijter [51] e.g. used the equations given for the ICAN

model by Chamis and Lomov et al. [24] used an alternative approach published originally by Rosen. The values calculated from the two approaches are compared in Fig. 6.8. The transverse properties decrease with the fiber volume fraction for both approaches. The comparison of the predicted values with internal experimental data [201] showed that both predictions do not yield realistic values. The model used by Lomov [24] predicts a decrease of properties with fiber volume fraction largely above the measured values and the ICAN model results in zero strength properties at a fiber volume fraction of around 85%. Ivanov et al. [45] published an alternative approach, assuming the transverse and

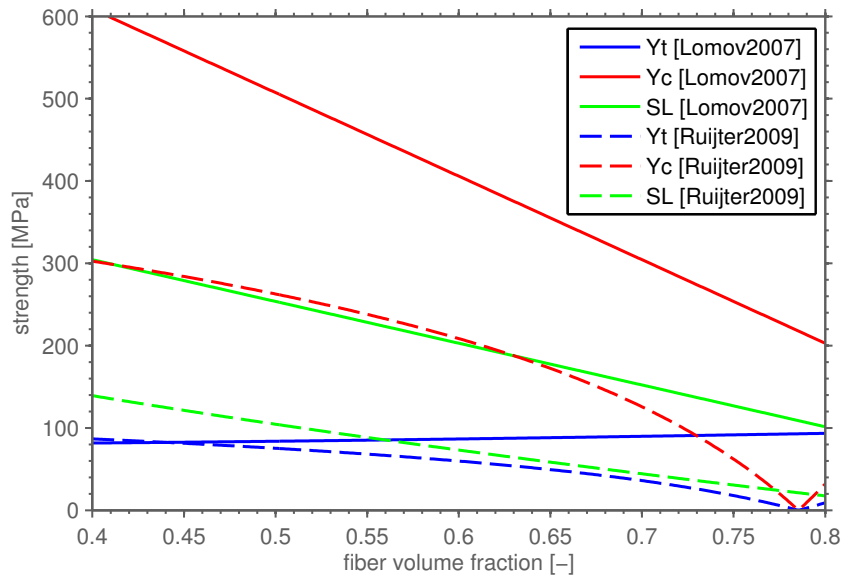


**Fig. 6.8:** Strength properties plotted over fiber volume fraction, from [24, 51]

shear strength properties to be constant for different fiber volume fractions. The approach was successfully used with a unit cell model for prediction of triaxial braided composites damage initiation and progression. Due to the lack of the simple models to represent a reasonable dependence of strength properties to the fiber volume fraction, Ivanov's approach was used, keeping the transverse and shear strength parameters for the BBM constant over the fiber volume fraction:

$$Y_T(\varphi_f) = Y_T \quad Y_C(\varphi_f) = Y_C \quad S_L(\varphi_f) = S_L \quad (6.15)$$

The transverse strength properties used in the BBM simulations are given in Table 6.7. It is important to note, that the complex mechanics of transverse and shear failure of UD composites, which involve damage and plastic deformation in the matrix and fiber-matrix interface failure [41], cannot be covered by analytical considerations. However, detailed analysis models require additional experimental validation, which was out of the scope of the current work. Thus, constant transverse strength properties were considered appropriate as a first approach.

### 6.3.4. Plasticity model

The off-axis experiments of the ( $\pm 30^\circ$ ) biaxial braided composites showed considerable nonlinear behavior before final failure. Investigations on crack occurrence and position showed the nonlinear behavior is due to microscopic cracking (cf. [170]), and the loading/unloading experiments revealed that the stress-strain nonlinearity is due to both inelastic deformation and material damage. For the Binary Model, Flores et al. [136] showed that matrix-induced nonlinearities in ceramic-matrix composites can be considered in the simulations by using a Drucker-Prager plasticity model. A similar approach was chosen in the BBM to account for the nonlinear deformation prior to final failure. Using a plasticity criterion to model the nonlinearities, introduced by damage and inelastic effects cf. Section 4.2.2, is valid in this case as only monotonically increasing loads are considered within the BBM simulations. The nonlinear deformation of braided composites was related to the shear and transverse behavior of the yarns and is thus in the BBM assigned to the effective medium elements. For efficient implementation of the unit cell simulations within Abaqus, a linear Drucker-Prager plasticity model with associated flow and nonlinear shear hardening was defined in the effective medium continuum elements. The Drucker-Prager yield criterion allows to consider the pressure-dependence of yielding commonly reported for composite materials [172, 202, 203].

The Drucker-Prager yield criterion is given as :

$$f(\boldsymbol{\sigma}) = \sigma_e - b \cdot \sigma_m - a = 0 \quad (6.16)$$

Where  $\sigma_e$  is the von Mises stress,  $\sigma_m$  is the hydrostatic part of the stress tensor and  $a, b$  are material parameters that define the yield stress and the pressure-dependence. The parameter  $b = \tan(\beta)$  is related to the pressure dependence, with  $\beta$  being the so-called friction angle of the material shown in Fig. 6.9a, defining the slope of the yield curve in the plane of von Mises stress and the hydrostatic pressure.

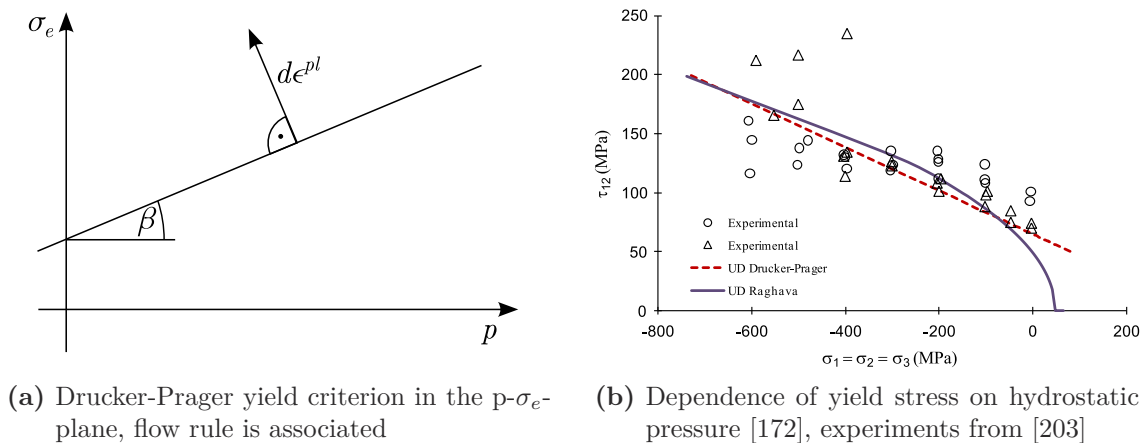


**Fig. 6.9:** Pressure dependence of the DP-plasticity model ( $-p = \sigma_m = \sigma_1 = \sigma_2 = \sigma_3$ )

The value of  $\beta$  was for the BBM unit cell simulations extracted from the publication of Vyas et al. [172]. Vyas et al. summarized experimental results from Shin and Pae [203], who tested the in-plane shear behavior of carbon/epoxy composites under several hydro-

static pressure states (cf. Fig. 6.9b). The friction angle was obtained by linear regression to the experimental results:

$$\beta = \tan^{-1} \left( \sqrt{3} \cdot \frac{\Delta\tau_{12}}{\Delta p} \right), \quad (6.17)$$

which yielded a friction angle of  $\beta = 17.7^\circ$ . The flow rule of the plasticity model was chosen fully-associated, i.e. the plastic flow is orthogonal to the yield surface (Fig. 6.9a).

Besides the pressure-dependence, the hardening behavior of the effective medium within the Drucker-Prager yield criterion needs to be defined. As considerable hardening was observed in the braided composites off-axis experiments, assuming ideal plastic deformation, like given by Flores et al. [136], is not suitable. The hardening was defined by using the shear-stress over shear-strain curve from a ( $\pm 45^\circ$ ) UD experiment, shown in Fig. 6.10. The progressive stress-strain behavior ultimately before final failure was not used for the

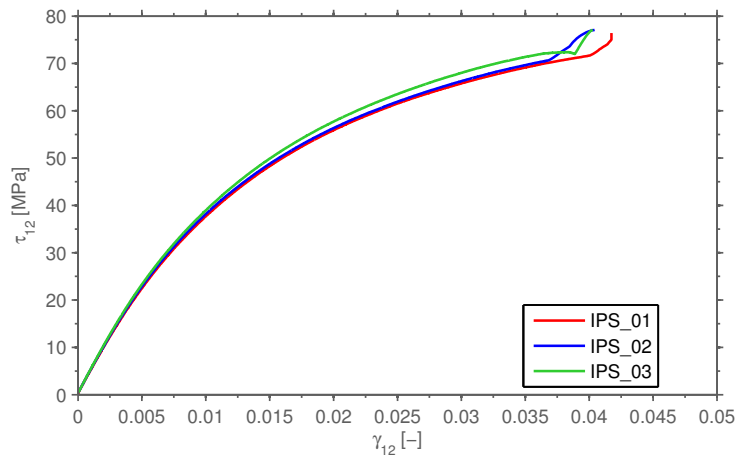


**Fig. 6.10:** In-plane shear stress-strain curves used for hardening definition [204]

hardening definition, as it was introduced through failure of the foil strain gauges used. A least square fit method was used to calculate the hardening curve from the experimental results, with the hardening function  $a = r(\gamma_{12}^{pl})$  defined linear-exponential as proposed by Flatscher [141]:

$$r = \tau_{12}^y = \begin{cases} \tau_{12}^0 + c_1 \cdot \gamma_{12}^{pl} & \text{for } \gamma_{12}^{pl} < \gamma_{12}^{pl*} \\ K \cdot (\gamma_{12}^{pl})^{\frac{1}{m}} & \text{for } \gamma_{12}^{pl} > \gamma_{12}^{pl*} \end{cases} \quad (6.18)$$

The plastic part of the shear strain is calculated from

$$\gamma_{12}^{pl} = \gamma_{12} - \tau/G, \quad (6.19)$$

where  $G$  is the shear modulus evaluated in the range of  $\gamma_{12} = 0.05 - 0.25\%$ . The coefficients  $K$ ,  $m$  and  $\tau_{12}^0$  are extracted from the experimentally measured curve by regression and the transition point  $\gamma_{12}^{pl*}$  as well as the parameter  $c_1$  are calculated by forcing the value

and slope of the two parts of the hardening curve given in Eq. 6.18 to be equal at the point  $\gamma_{12}^{pl*}$ :

$$\gamma_{12}^{pl*} = \left( \frac{\tau_{12}^0}{c_1 \cdot \left(1 - \frac{1}{m}\right)} \right)^m \quad (6.20)$$

$$c_1 = \frac{K}{m} \cdot (\gamma_{12}^{pl*})^{\left(\frac{1}{m}-1\right)} \quad (6.21)$$

The input parameters for the Drucker-Prager plasticity criterion are summarized in Table 6.1.

**Table 6.1.:** Material properties defined for the Drucker-Prager plasticity model

pressure dependence	hardening		
$\beta$ [°]	$\tau_{12}^0$ [MPa]	$K$ [MPa]	$1/m$ [-]
17.7	24.8	172	0.2295

## 6.4. Periodic boundary conditions

All unit cell calculations were conducted with periodic boundary conditions basing on the equations given by Pahr [144] and Anthoine [145] described in Section 2.6.4. A rhombus-shaped unit cell is used for the braided composites (Fig. 6.11),

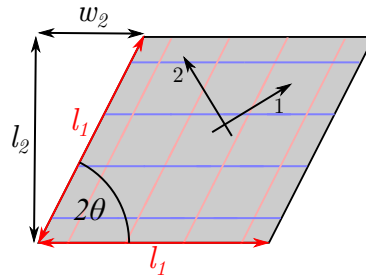


**Fig. 6.11:** Rhombus unit cell used for the BBM

which yields the periodicity tensor of the unit cell:

$$\mathbf{P} = [\mathbf{p}^1 \quad \mathbf{p}^2 \quad \mathbf{p}^3] = \begin{bmatrix} p_1^1 & p_1^2 & p_1^3 \\ p_2^1 & p_2^2 & p_2^3 \\ p_3^1 & p_3^2 & p_3^3 \end{bmatrix} = \begin{bmatrix} l_1 & w_2 & 0 \\ 0 & l_2 & 0 \\ 0 & 0 & l_3 \end{bmatrix} = \begin{bmatrix} l_1 & l_1 \cos 2\theta & 0 \\ 0 & l_1 \sin 2\theta & 0 \\ 0 & 0 & l_3 \end{bmatrix}, \quad (6.22)$$

with  $\theta$  being the braiding angle,  $l_1$ ,  $l_2$  and  $w_2$  as given in Fig. 6.11 and  $l_3$  being the thickness of the unit cell.

### 6.4.1. Coupling equations

The periodic boundary conditions are implemented into the FE unit cell calculations based on the equations given in [205]. The basic relations are given for the displacements of adjacent faces (naming cf. Fig. 6.12), connected by the periodicity vectors  $\mathbf{p}_i$

$$\mathbf{p}_1 : \quad \mathbf{u}^A - \mathbf{u}^B - \Delta \mathbf{u}^{AB} = 0 \quad (6.23)$$

$$\mathbf{p}_2 : \quad \mathbf{u}^C - \mathbf{u}^D - \Delta \mathbf{u}^{CD} = 0 \quad (6.24)$$

$$\mathbf{p}_3 : \quad \mathbf{u}^E - \mathbf{u}^F - \Delta \mathbf{u}^{EF} = 0 \quad (6.25)$$

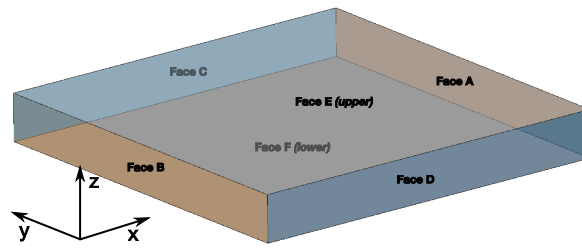


Fig. 6.12: Naming convention for the faces of the unit cell

The first two equations refer to plane periodicity, while spatial periodicity is modeled, if the third equation is added. The relations for faces and the corner nodes of the unit cell are given by the combining the equations above according to the periodicity vectors connecting the edges or corner nodes. The last part of the equations  $\Delta \mathbf{u}^{IJ}$  is given by the macroscopic stress or strain introduced into the unit cell. The concept of non-physical *constraint driver* (CD) nodes (cf. e.g. [51]) is used to introduce macroscopic loads in the BBM unit cell. Six constraint driver nodes, each connected to a macroscopic stress or strain tensor component, are added to the model. The complete equations for implementations of the periodic boundary conditions are given in Appendix F.

For shear stresses or strains to be introduced, either for  $\varepsilon_{ij}$ ,  $\varepsilon_{ji}$  or both, are available. Using only one of the shear strains DOFs introduces a simple shear deformation, while pure shear is achieved if both constraint drivers are displaced identically. For the BBM simulations, the macroscopic deformation tensor of the unit cell was assumed to be symmetric, which is equal to applying a pure shear. This was achieved by introducing an additional equation for each shear strain in the form

$$u_1^{CDn} - c_n \cdot u_2^{CDn} = 0 \quad (6.26)$$



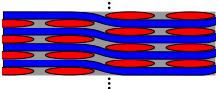
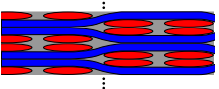
where  $u_{1,2}^{CDn}$  are the DOFs of one of the shear constraint-driver nodes and  $c_n$  is the ratio of the unit cell dimensions in the plane where the shear strain is acting; e.g.  $c_1 = l_1/l_2$  for the in-plane shear strain. Either displacements or forces are introduced into the unit cell yielding the desired strain or stress state, respectively. The stresses and strains are calculated from the constraint driver forces and displacements by the equations given in Appendix F.

### 6.4.2. Out-of-plane boundary conditions

In the BBM simulations, a macroscopic plane stress of the unit cell was assumed. Thus, for both, plane and spatial periodicity, the out-of-plane behavior of the unit cell needs to be defined. Different out-of-plane boundary conditions can be related to different laminate stacking sequences of adjacent braid plies. To introduce a desired out-of-plane behavior, the displacement in z-direction of the lower face of the unit cell face is either restricted (*fixed*) or left free to deform (*free*). The out-of-plane boundary conditions are summarized in Table 6.2. For plane periodicity, the *fixed* solution refers to the case of a two-ply laminate stacked symmetric on top of each other (*SYM*), while the unconstrained out-of-plane deformation refers to a single ply laminate (*SUC*). The two cases for spatial periodicity refer to a laminate with an infinite number of plies, stacked in-phase (*IP*) or out-of-phase (*OP*).

In all out-of-plane boundary conditions, the unit cell is not constraint to undergo a macroscopic deformation in z-direction, i.e. a macroscopic strain  $\langle \varepsilon_{zz} \rangle$  is present due to the transverse contraction. The different out-of-plane boundary conditions described above rather influence the microscopic (periodic) part of the z-displacements inside the unit cell.

**Table 6.2.:** Out-of-plane boundary condition cases

name	plane periodicity (2D)		spatial periodicity (3D)	
	2Dfree ( <i>SUC</i> )	2Dfixed ( <i>SYM</i> )	3Dfree ( <i>IP</i> )	3Dfixed ( <i>OP</i> )
ply number	1	2	$\infty$	$\infty$
stacking case	-	symmetric	in-phase	out-of-phase
boundary condition	upper and lower face free to deform	upper face free to deform	upper and lower face restricted by periodicity	upper and lower face stay plane
				

### 6.4.3. Unit cell loading

In-plane loading was used for the BBM simulations. The constraint drivers connected to out-of-plane deformation were left free to deform, considering effects of transverse contraction. All simulations were conducted load-controlled, i.e. the macroscopic stress state was prescribed to the unit cell. For the off-axis load cases, the load was introduced into the unit cell by transformation of the applied stress into the material coordinate system (12) of the braid:

$$\begin{bmatrix} \langle \sigma_{11} \rangle \\ \langle \sigma_{22} \rangle \\ \langle \tau_{12} \rangle \end{bmatrix} = \mathbf{T}(-\psi) \cdot \begin{bmatrix} \langle \sigma_{xx} \rangle \\ \langle \sigma_{yy} \rangle \\ \langle \tau_{xy} \rangle \end{bmatrix} \quad (6.27)$$

With the transformation matrix  $\mathbf{T}$  given in Eq. D.9.

## 6.5. Stress analysis: volume averaging

Stress fields obtained from unit cell simulations are commonly used for prediction of failure within yarns and matrix pockets. However, Sihn et al. [206, 207] showed that singularities can exist in the stress field inside a textile composite unit cell and concluded that even fine FE models fail to give an accurate prediction of the stress values near the singularity. Cox [134] also addressed the issue of using point-value stresses for the prediction of failure within textile composites: as detailed and refined models in combination with fracture mechanics drastically increase the computational cost, relative coarse mesh representations leading to an averaging of stresses and strains are reported to be favorable. However, the models with coarse mesh representation of the textile yarn architecture suffer the drawback that the stress and strain fields are mesh dependent, as averaged over the finite elements.

In the BBM, similar as in the Binary Model, 1D elements are embedded into a 3D medium. This would theoretically result in a stress singularity in the effective medium at the position of the beam nodes. As the effective medium is discretized, the singularity is averaged over the elements leading to a mesh-dependent solution. For the BBM, this effect can be shown for different mesh sizes used on the same model: Fig. 6.13 shows the von Mises stress field inside the effective medium of a BB45 BBM unit cell for two different mesh-sizes. For the coarser mesh (left), the averaging over the larger elements leads to smaller maximum stresses inside the effective medium.

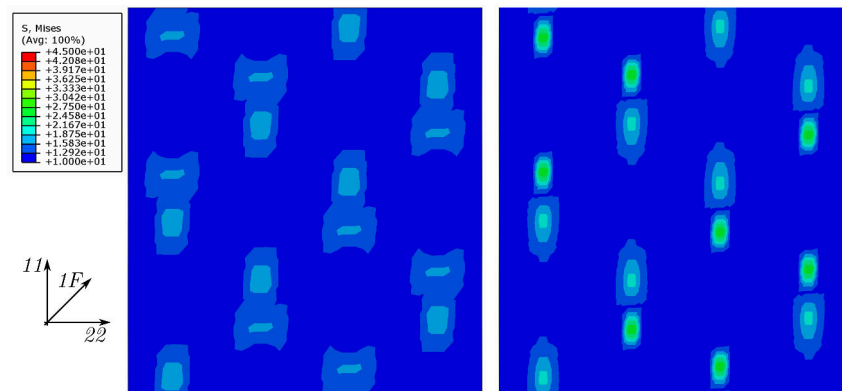


**Fig. 6.13:** Comparison of von Mises stress in the effective medium for different effective medium mesh sizes (left: 0.44 mm, right 0.27 mm)

To overcome the issue of mesh-dependency, Cox, Yang and Co-Workers [132–135] proposed a spatial averaging procedure for the effective medium strains called gauge-averaging. Applying the averaging is motivated by phenomenological considerations regarding textile composite failure modes, which are connected to stresses averaged over a certain length or volume [135]. Volume-averaging was shown to remove mesh-dependence from the strain field [132] and the comparison of averaged strains correlated well with DIC-measurement [135].



The approach of gauge-averaging was adapted for biaxial braided composites within the BBM. A cylindrical gauge-volume appropriate for non-orthogonal textile composites was chosen and the volume-averaging was directly applied to the effective medium stress field, as stress-based failure prediction was employed. The method described in the following section was implemented in the BBM modeling framework and the gauge-averaged stresses were used for failure prediction.

### 6.5.1. Averaging volume shape

Cox and Co-Workers [132–135] proposed cuboid-shaped averaging volumes for the spatially averaging of stresses and strains. A cuboid of the volume

$$(1/2 \text{ tow width}) \times (1/2 \text{ tow width}) \times (\text{tow thickness})$$

was shown to provide a mesh-independent solution [132]. A cuboid-shape averaging volume is suitable for composites with orthogonal textile yarn architecture, but yields no optimal solution for non-orthogonal textile composites such as braided composites: to account for the different yarn orientations at different braiding angles, a shearing of the cuboid would be required. However, this would result in different shapes of averaging volumes for different braiding angles. To define a unique averaging volume for different braiding angles, a cylinder-shaped volume with the symmetry-axis oriented along the unit cell thickness direction was chosen (Fig. 6.14). The cylinder height was equal to the yarn

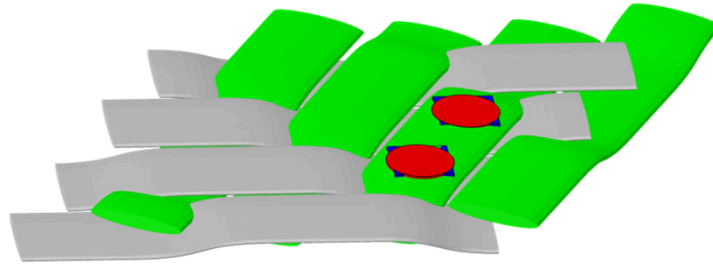


**Fig. 6.14:** Cylindrical gauge volumes used for volume averaging of strains (red) and volume proposed in [133]

height and the diameter of the cylinder was calculated from volume-equivalence to the cubic volume proposed by Yang and Cox [133]:

$$d_{cyl} = \frac{d_2}{\sqrt{\pi}} \quad (6.28)$$

For each beam node, the effective medium nodes in the surrounding volume spanned by the cylinder with the diameter  $d_{cyl}$  are searched in the undeformed unit cell model and assigned as the averaging region. After the finite element solution procedure, the volume averaging is conducted for all beam nodes in each result step. The volume averaged stress at a beam node  $m$  with the averaging volume  $\Omega^m$  is given by:

$$\bar{\sigma}_{ij}^m = \frac{1}{N} \sum_{n=1}^N \sigma_{ij}^{EMnode=n}, \forall n \in \Omega^m. \quad (6.29)$$

The averaging is conducted for all stress components in the beam node coordinate system and the volume averaged stress tensor for each beam node is written to the Abaqus output-database-file (*odb*).

### 6.5.2. Averaging volume size

In order to validate the choice of the averaging volume size, a factor scaling the gauge cylinder diameter (gauge factor **gf**) was introduced. The resulting stress profiles from BBM simulations with different gauge factors are exemplarily shown in Fig. 6.15. The stresses were extracted from the transverse (2F) yarns in a BB45 unit cell pulled into the 1F yarn direction. Both, in- and out-of-plane stress profiles have sharp peaks attributed to stress singularities for the small averaging volume **gf=0.25**. These sharp peaks are not present for the stresses being averaged over the proposed gauge volume (**gf=1**). Furthermore, the stress profile of another unit cell simulation with identical gauge factor **gf=1** and the element size increased by 50% is shown. The gauge averaged stress profiles with different mesh refinements correlate well. Thus it can be concluded that a mesh-independent solution of the effective medium stress field in the BBM can be achieved, if the stress is averaged over the proposed gauge volume (**gf=1**).

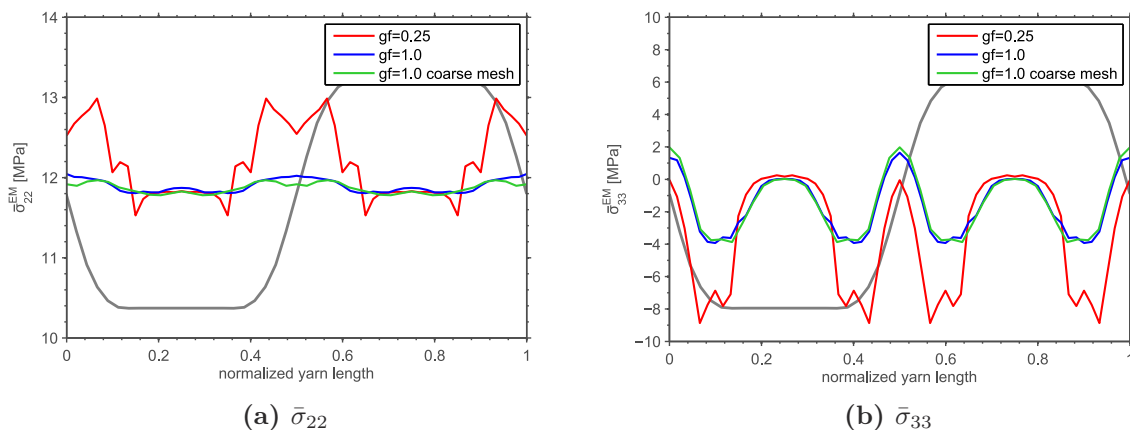


**Fig. 6.15:** Gauge averaged stresses with different gauge volumes (**gf** = 0.25, 1), and different mesh refinements (yarn path given in gray)

## 6.6. Failure analysis

The failure in the BBM model was predicted by using failure criteria applied on the yarn stress tensor given at each beam node. Based on the observations from the off-axis experiments, yarn longitudinal, transverse and shear failure were considered for the prediction of failure.

Using a failure criterion just yields the macroscopic stress at failure initiation, but gives no information about the progression of failure, i.e. what happens after the failure is initiated. In the off-axis experiments, observation of first failure in the yarns coincided with the final failure of the specimen. Based on these observations the first failure predicted by the failure criteria was treated as final failure within the BBM calculations.

### 6.6.1. Yarn stresses in the BBM

Yielding accurate yarn stress predictions from the BBM requires additional considerations regarding the properties of yarns and matrix: while the phases are explicitly modeled in a continuum element unit cell, the properties are split up to beam and continuum elements in the BBM. The material definition for the beam elements considers the volume overlapping present for beam and effective medium continuum elements, by subtracting the doubled part of the stiffness, cf. Eq. 6.9. Thus, the yarn longitudinal stress has to be calculated by adding the gauge-averaged stress component  $\bar{\sigma}_{11}^{EM}$  in the effective medium to the beam element stress  $\sigma_{11}^{BE}$ :

$$\sigma_{11}^Y = \sigma_{11}^{BE} + \bar{\sigma}_{11}^{EM} \quad (6.30)$$

The transverse stresses in the yarn are derived by considering a simple modeling case: If a single yarn inside the BBM is stressed in transverse tension, the strain of the model is equal to the one in a continuum unit cell, as the stiffness is identical. However, as the EM yields a lower stiffness as the yarn in transverse direction ( $E_{22}^Y < E^{EM}$ ), the stress needs to be corrected with the ratio of effective medium and yarn stiffness:

$$\sigma_{ii}^Y = \bar{\sigma}_{ii}^{EM} \cdot \frac{E_{ii}(\varphi = \kappa)}{E^{EM}} \quad (6.31)$$

$$\tau_{ij}^Y = \bar{\tau}_{ij}^{EM} \cdot \frac{G_{ij}(\varphi = \kappa)}{G^{EM}} \quad (6.32)$$

Both corrections of the stresses are conducted inside the BBM modeling framework. The corrected stresses are used for the continuum element unit cell comparison and the yarn failure criterion.

### 6.6.2. Failure criterion

Longitudinal failure of the yarns in tension and compression was predicted by using the maximum stress criterion:

$$f_{E,YLt} = \frac{\sigma_{11}^Y}{X_T} = 1, \quad \text{for } \sigma_{11}^Y > 0 \quad (6.33)$$

$$f_{E,YLc} = \frac{-\sigma_{11}^Y}{X_C} = 1, \quad \text{for } \sigma_{11}^Y < 0 \quad (6.34)$$

The stress exposure  $f_{E,i}$  equals one for fiber failure in tension and compression. Either tensile ( $X_T$ ) or compressive strength ( $X_C$ ) of the yarn is used based on the longitudinal yarn stress  $\sigma_{11}^Y$  given in Eq. 6.30. Longitudinal yarn failure is evaluated at five distinct points of the beam cross section given in Table 6.3. This includes the effects of stress concentrations introduced by yarn bending into the yarn longitudinal failure (cf. Fig. 6.19).

Transverse failure of the yarns was predicted by using the plane-stress (2D) formulation of Puck's phenomenological failure criterion [127]. The criterion distinguishes three different transverse failure modes, considering the different mechanics of transverse fail-

**Table 6.3.:** Points for stress evaluation on the beam cross section (cf. Fig. 6.4)

Name	center	upper	lower	left	right
x	0	0	0	-a	a
y	0	b	-b	0	0

ure in tension and compression. The plane-stress formulation of the criterion yields a closed-form solution for all failure modes, avoiding an iterative fracture angle search, as required in the 3D version of the criterion. Comparative simulations were made by using the Pucks 3D failure criterion, but as the results of 2D and 3D Puck criterion were very similar, the 2D version of the criterion was used. Three different criteria representing the different transverse yarn failure modes are available:

---

yarn transverse failure mode A:

for ( $\sigma_{22}^Y > 0$ ):

$$f_{E,YT,A} = \sqrt{\left(\frac{\tau_{12}^Y}{S_L}\right)^2 + \left(1 - p_{\perp\parallel}^t \frac{Y_t}{S_L}\right)^2 \left(\frac{\sigma_{22}^Y}{Y_t}\right)^2} + p_{\perp\parallel}^t \frac{\sigma_{22}^Y}{S_L} \quad (6.35)$$

yarn transverse failure mode B

for ( $\sigma_{22}^Y < 0$  and  $0 \leq \left|\frac{\sigma_{22}^Y}{\tau_{12}^Y}\right| \leq \left|\frac{R_{\perp\perp}^A}{\tau_{12,c}^Y}\right|$ )

$$f_{E,YT,B} = \frac{1}{S_L} \left( \sqrt{(\tau_{12}^Y)^2 + (p_{\perp\parallel}^c \sigma_{22}^Y)^2} + p_{\perp\parallel}^c \sigma_{22}^Y \right) \quad (6.36)$$

yarn transverse failure mode C

for ( $\sigma_{22}^Y < 0$  and  $0 \leq \left|\frac{\sigma_{22}^Y}{\tau_{12}^Y}\right| > \left|\frac{R_{\perp\perp}^A}{\tau_{12,c}^Y}\right|$ )

$$f_{E,YT,C} = \left[ \left( \frac{\tau_{12}^Y}{2(1+p_{\perp\perp}^c)S_L} \right)^2 + \left( \frac{\sigma_{22}^Y}{Y_c} \right)^2 \right] \frac{Y_c}{(-\sigma_{22}^Y)} \quad (6.37)$$

with

$$R_{\perp\perp}^A = \frac{S_L}{2p_{\perp\parallel}^c} \left( \sqrt{1 + 2p_{\perp\parallel}^c \frac{Y_c}{S_L}} - 1 \right) \quad p_{\perp\perp}^c = p_{\perp\parallel}^c \frac{R_{\perp\perp}^A}{S_L} \quad \tau_{12c} = S_L \sqrt{1 + p_{\perp\perp}^c}$$


---

The gauge-averaged and corrected stresses ( $\sigma_{ii}^Y$  and  $\tau_{ij}^Y$ ) as given in Eq. 6.31-Eq. 6.32 are used for transverse failure. The failure modes given by Puck for inter-fiber-failure refer to yarn transverse failure modes in the BBM. As the gauge-averaged stresses represent the average stress state of the yarn at the beam node position, one transverse yarn stress exposure value is calculated for each beam element node. The inclination parameters used in the equations are given in Table A.4.

## 6.7. Comparison to continuum unit cell

The BBM is a low-order representation unit cell modeling approach for biaxial braided composites. For a failure analysis with the unit cell model, the stress fields predicted by the model need to capture the relevant effects within the material. In order to assess the stress fields predicted with the BBM unit cell model, a continuum unit cell (CUC) with an identical geometry was built and solved for comparison. The CUC model was built with the academic software MeshTex [79], which creates a FE volume mesh based on a WiseTex geometry. MeshTex includes an interpenetration-correction algorithm, changing yarn-path and yarn shape, which ensures to have no overlapping volumes in the unit cell. A detailed description on the procedure used in MeshTex is given in [24].

A WiseTex geometric model was used for both, continuum and BBM unit cell calculations. The yarn architecture parameters measured from the micrographs (cf. Table 4.5), yielded a tight geometric model that could not be meshed properly with volume elements. Thus yarn spacing and unit cell thickness were increased in the geometric model. The geometric parameters used are given in Table 6.4. The continuum unit cell yields a slightly different yarn path (Fig. 6.16), which is due to the interpenetration correction that is not required in the BBM modeling approach.

**Table 6.4.:** Geometric parameters of BBM and continuum unit cell

yarn architecture		unit cell dimensions		volume fractions	
$d_1$ [mm]	3.0915	$l_1$ [mm]	13.2	$\varphi_f$	42.54%
$d_2$ [mm]	0.283	$l_2$ [mm]	13.2	$\varphi_Y$	63.30%
$p$ [mm]	3.3	$l_3$ [mm]	0.65	$p_d$	67.20%
$\theta$ [°]	45				

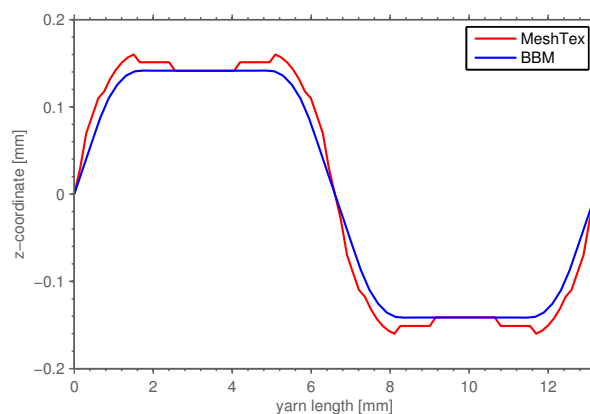


**Fig. 6.16:** Comparison of yarn MeshTex and BBM yarn paths

The in-plane elastic constants calculated from the two models given in Table 6.5 are very similar. The BBM predicts slightly smaller elastic constants in the 11- and 22-direction, which is mainly attributed to the difference in yarn paths and shapes. The elastic constants were calculated for two out-of-plane boundary condition cases: for *SUC*, upper and lower face are left free to deform, while the deformation of the unit cell lower

surface is fixed for *SYM*. The braided composite unit cell warps out-of-plane, as shown in Fig. 6.17, in the case the two yarn directions being stressed unequally. Thus, the difference is mainly influencing the shear modulus of the BB45 unit cell. The comparison shows, that the BBM captures the effect of out-of-plane deformation on the elastic behavior accurately.

**Table 6.5.:** Comparison of elastic constants from BBM and continuum unit cell (CUC)

	CUC		BBM	
	SUC	SYM	SUC	SYM
$E_{11}$ [MPa]	11421	11434	10120	10143
$E_{22}$ [MPa]	11377	11443	10120	10143
$G_{12}$ [MPa]	13791	23790	13553	24383
$\nu_{12}$ [-]	0.776	0.779	0.795	0.800

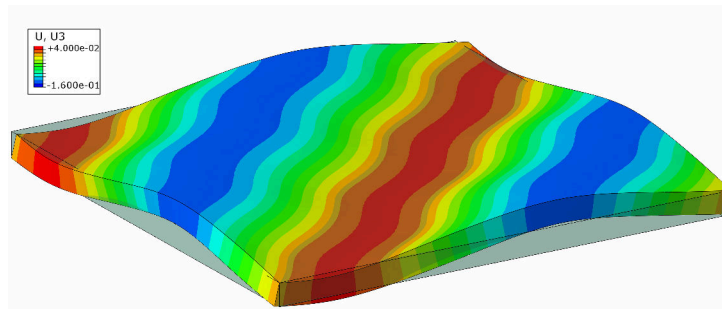


**Fig. 6.17:** Out-of-plane deformation of the BBM unit cell

### 6.7.1. Yarn stress profiles

For the stress profile comparison, two distinct load cases were considered: a tensile stress of 100 MPa was applied in one of the yarn directions (1F) and in the take-up-direction (11), cf. Fig. 6.18. Each of the cases was solved for both, *SUC* and *SYM* out-of-plane boundary condition. While the stress profiles in the *SYM* case are mainly influenced by the yarn architecture, the stress profiles in the *SUC* case superimpose effects of the yarn architecture and out-of-plane unit cell warping. The stress profiles of all yarns in one direction are identical, when shifted for half the undulation wavelength per yarn (cf. [39]). Thus, a single stress profile per yarn direction needs to be considered for the comparison. For the in-plane stress profile comparison, mainly the  $\sigma_{1F}$  loadcase is considered, as the  $\sigma_{11}$  loadcase was found to give similar results.

#### Yarn longitudinal stress

The comparison of longitudinal yarn stresses in the yarn oriented along the load is given in Fig. 6.19. Three section points are considered: yarn center, yarn upper surface and yarn lower surface. For both cases, the stress in the center of the yarn correlates very well between BBM and CUC. For the *SYM* case given in Fig. 6.19a, the maximum stress in the

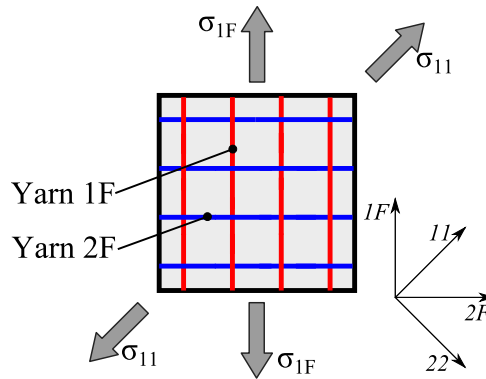


**Fig. 6.18:** Load cases for stress profile comparison between BBM and CUC

undulation interval, present at upper and lower surface, is nearly identical predicted by BBM and CUC. The position of the maximum stress in the undulation interval is slightly shifted for the BBM, which is mainly attributed to two reasons: the yarn path between the models is slightly different (cf. Fig. 6.16) and the support provided by the transverse yarns (2F) is localized for the BBM as the cross section is not explicitly modeled. This also reflects in the case of free out-of-plane deformation shown in Fig. 6.19b, where the stress peak predicted by the BBM is around 30% higher compared to the CUC. The cross section being not modeled explicitly in the BBM provides less constraint to the out-of-plane warping (cf. Fig. 6.17) and provides higher bending stresses. However, the *SUC* boundary condition reflecting a single unit cell is of minor relevance for most braided composite laminates, consisting of two or more plies.

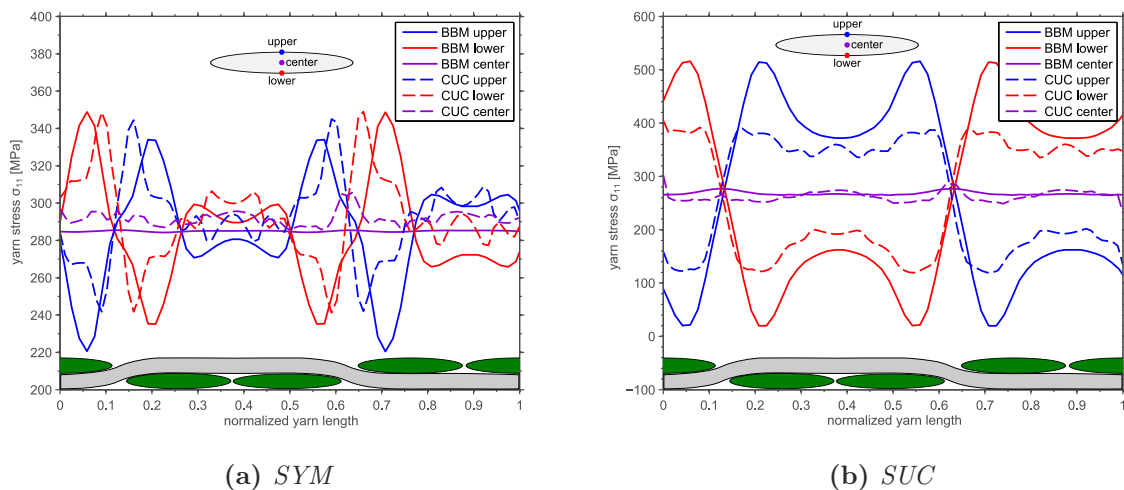


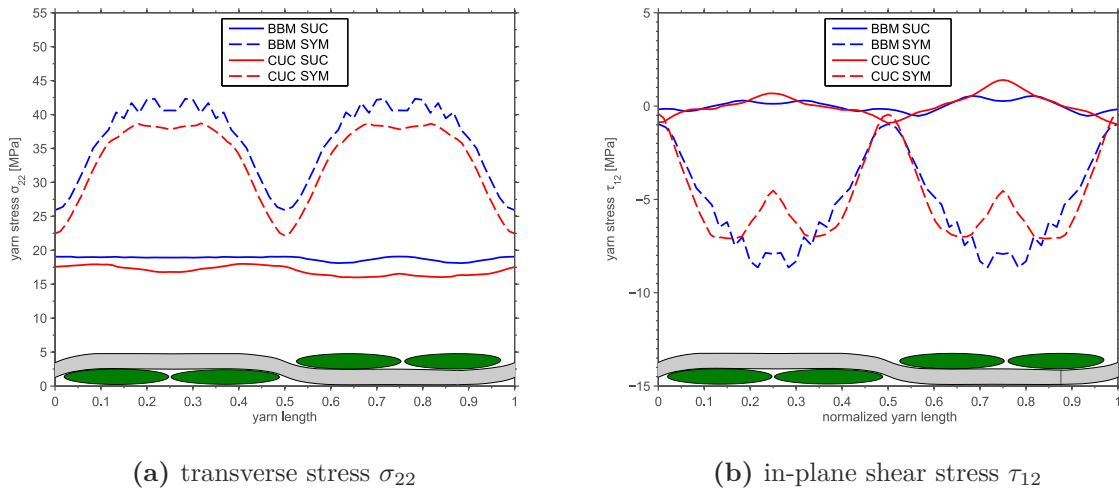
**Fig. 6.19:** BBM yarn 1F stress profile (upper, center, lower refer to the positions on the cross section)

### Yarn in-plane transverse and shear stress

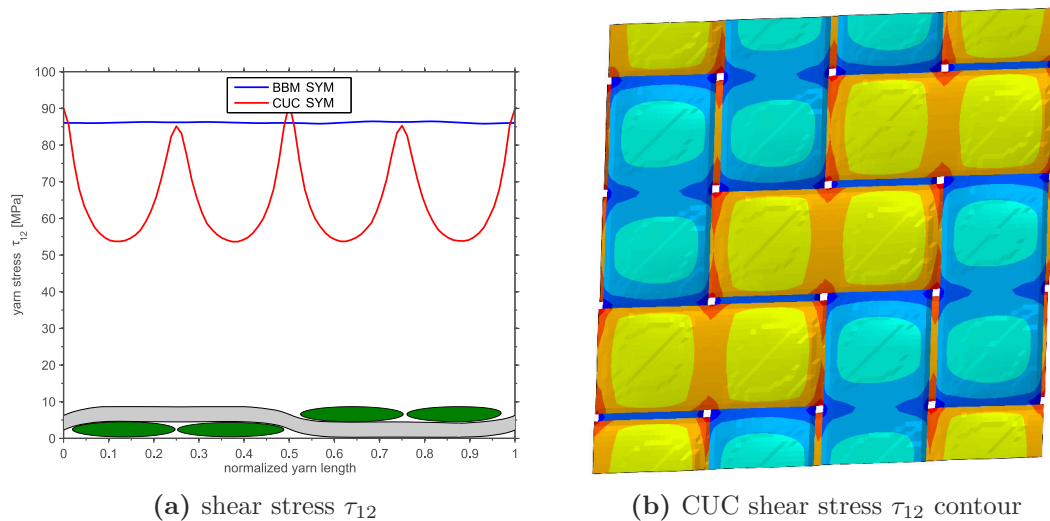
The transverse stresses are compared at the center of yarn 2F (cf. Fig. 6.18), which is oriented orthogonal to the load. The comparison of the transverse normal stress is shown in Fig. 6.20a. The stress profiles from BBM and CUC agree well: in both out-of-plane

boundary conditions, the shape of the stress profile is reproduced well by the BBM. The BBM transverse stresses deviate in both cases by less than 10%, which is a good agreement for the low-order yarn representation given in the BBM.

A comparison of the shear stress profiles is given in Fig. 6.20b. For the *SYM* case, only small shear stresses are present in the yarns. For the *SUC* case, the unit cell warping introduces shear stresses in the straight part of the yarn, which is predicted by both, BBM and CUC. The stress profiles are identical, except for the local minimum between the crossing yarns given for the CUC, which can not be observed in the BBM stress profile.

(a) transverse stress  $\sigma_{22}$ (b) in-plane shear stress  $\tau_{12}$ **Fig. 6.20:** BBM yarn 2F stress profile (evaluated at the center of the yarn)

The deviation of shear stress profiles becomes more evident when considering the stress profile for the loading applied in take-up direction shown in Fig. 6.21a: where stress peaks

(a) shear stress  $\tau_{12}$ (b) CUC shear stress  $\tau_{12}$  contour**Fig. 6.21:** Shear stress distribution on the yarn surface for loading in take-up direction (11)

between the yarns are observed in the CUC unit cell model, a constant shear stress is present in the BBM model. The shear stress peaks in the CUC model are introduced by



the cross section edges of the yarns (Fig. 6.21b), thus, the constant shear stress in the BBM is an artifact of the modeling abstractions: rotational DOFs are not coupled between beam and continuum elements and the cross sections are not explicitly modeled. Such local variations of the stress field, introduced by the yarn cross-section shape can, as a consequence of the model idealizations, not be represented by the BBM. However, for the case of the in-plane shear stress, the sharp stress peaks predicted by the idealized geometry CUC model are unlikely to be present in the real material: the yarn cross sections in the straight region were shown to grow together in the micro-CT scans (Fig. 4.9), which is believed to reduce the shear stress peaks.

### Out-of-plane yarn stresses

The out-of-plane yarn stresses predicted by the BBM are compared to stresses in the center of the CUC yarns. Two typical stress profiles are shown in Fig. 6.22, which is the out-of-plane normal stress  $\sigma_{33}$  and the transverse shear stress  $\sigma_{23}$ , both for for the load applied in the take-up direction. For the cases of the  $\sigma_{33}$  stress profile shown in

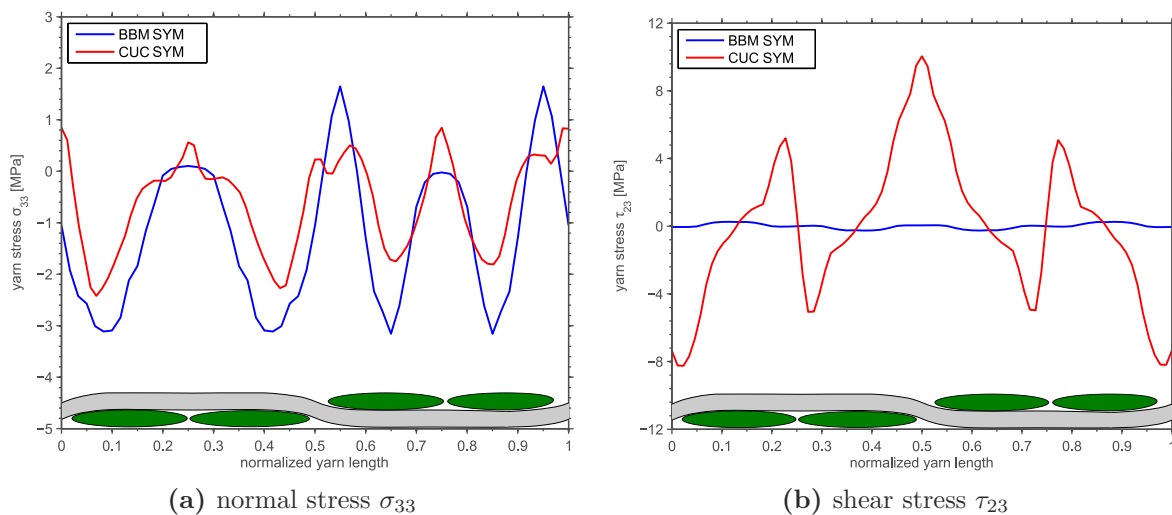


**Fig. 6.22:** Comparison of out-of-plane stress profiles for loading in the take-up direction 11

Fig. 6.22a, BBM and CUC agree well, while bigger deviations are observed for  $\tau_{23}$ , shown in Fig. 6.22b. The reason for good agreement in the  $\sigma_{33}$  case and the deviation in the  $\tau_{23}$  profile can be attributed to the sources of the stress variations: the transverse normal stresses  $\sigma_{33}$  are mainly introduced by the compression of the crossing yarns to each other (Fig. 6.22a), while the transverse shear stresses  $\tau_{23}$  in the yarn are rather due to local effects. The maximum stress introduced in the undulation interval by local compression of the yarn cross-section edges to the longitudinal yarn (Fig. 6.22b). Effects of yarn-to-yarn interaction (like for  $\sigma_{33}$ ) are represented well in the BBM stress profiles, while the effects mainly introduced by the local cross sectional geometry (like for  $\tau_{23}$ ) cannot be represented, as the cross section geometry does not influence the coupling between beam and continuum elements. Other load cases and out-of-plane stress components lead to similar results.

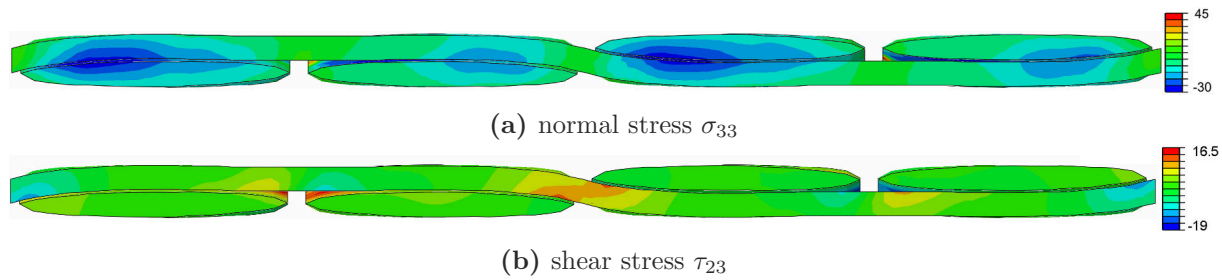


**Fig. 6.23:** Out-of-plane stress distribution in the yarns of the CUC for 11-loading

### 6.7.2. Summary and conclusion of comparison

The stress profiles predicted by the binary beam model and a continuum element unit cell were compared for a BB45 unit cell and found to correlate well. The normal stresses longitudinal and transverse to the yarn directions were in good agreement. The effects of out-of-plane deformation are represented well for transverse and shear stresses, but are overpredicted for the yarn longitudinal stresses in the BBM. Out-of-plane transverse and shear stresses, which are calculated in the BBM by volume-averaging, correlated well in most of the considered cases. Bigger deviations between the stress profiles of BBM and CUC were present for local stress peaks, which are introduced by the yarn cross sectional shape.

Concluding the comparison, the stresses mainly introduced by the mechanics of the yarns (e.g. yarn bending stresses) or by the interaction of yarns (e.g. yarn-to-yarn compression) are captured well by the BBM unit cell. In opposite, the stress peaks arising from local yarn cross-section interaction require the cross-section to be explicitly modeled, and are thus not captured by the BBM. However, based on the idea of gauge averaging, stresses averaged over a certain gauge volume are driving the failure process. Thus, these local stress fluctuations are considered less relevant for failure initiation and propagation. This is supported by the results published by Schultz and Garnich [57] and Ivanov et al. [45], who used stresses averaged over a certain region to predict the damage initiation and progression of triaxial braided composites.

## 6.8. Elastic predictions

The BBM unit cell was used to predict the elastic properties of BB30 and BB45 braided composites. The unit cell geometries are given in Section 5.1.2 and are based on the yarn architecture parameters from optical microscopy. The packing density in the yarns was set to  $p_d = 76.2\%$  for the BB30 and  $p_d = 76.3\%$  for the BB45 braid to achieve a unit cell fiber volume fraction of 60% in both cases. The elastic material parameters of yarns and effective medium were calculated from the fiber and matrix properties given in Table A.1 and Table A.2. The element size for effective medium and beam elements was chosen 0.2 mm, yielding around 70,000 elements in total. The BBM unit cell models were pre-processed, solved and post-processed in around 3 minutes on a desktop PC.

Three unit cell load cases, namely uniaxial stress in 11- and 22-direction and in-plane shear stress, were required to calculate the elastic constants of the braided composites

under the assumption of plane stress. The equations for the calculation of the elastic constants are given in Appendix F.

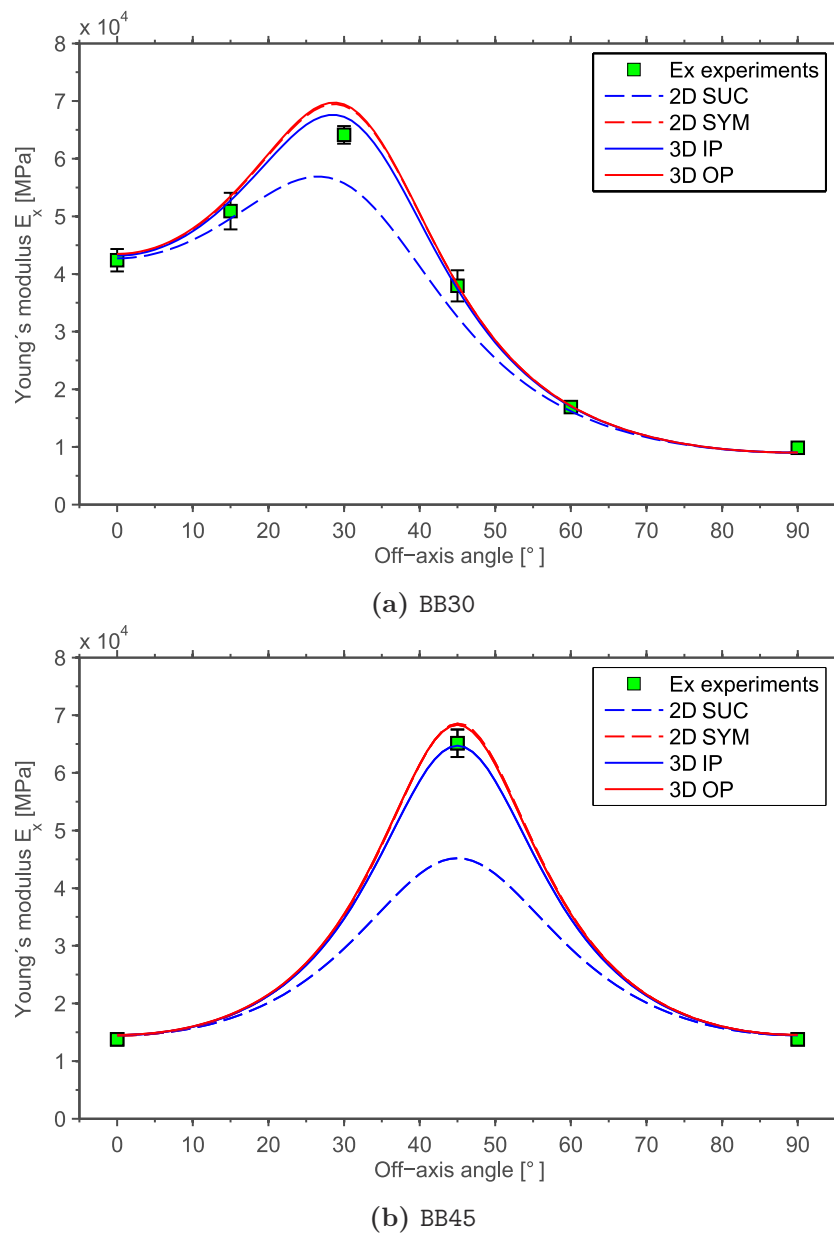


**Fig. 6.24:** Young's modulus  $E_x$  predicted by the BBM compared to experimental results

An off-axis polar plot of the predicted elastic modulus, with the off-axis experimental results given for comparison, is shown in Fig. 6.24. The initial modulus  $E_x^0$ , calculated from the tensile experimental data by regression of the stress-strain curve, is used for comparison to the linear elastic finite element solution. For both braiding angles, four unit cell simulations with different out-of-plane boundary conditions, as described in Table 6.2, were conducted. In the micro-CT scan of the BB45 braided composite, no distinct stacking configuration was seen, thus none of the idealized stacking configurations is present in a real braided composite laminate. However, as the unit cell simulations were conducted

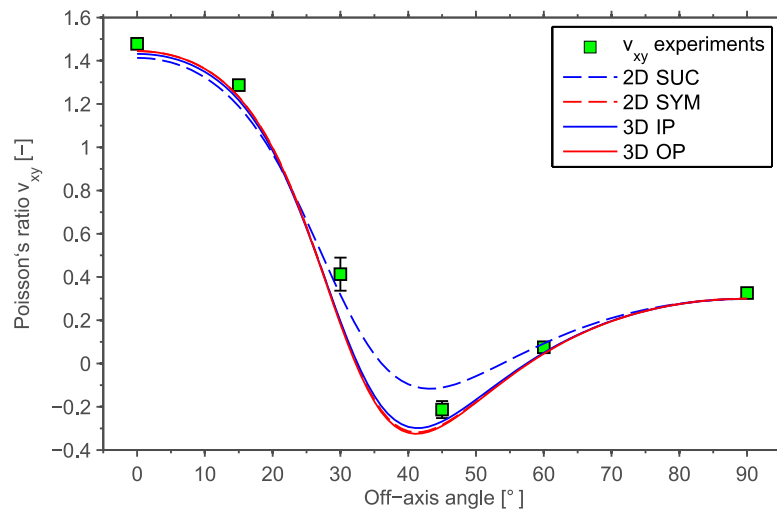
with a single unit cell, the main goal of the comparison was to find the idealized stacking configurations yielding the best approximation of a mixed stacking case.

For both braiding angles, the different out-of-plane boundary conditions mainly influence the stiffness in the the yarn direction (off-axis angle  $\psi = \theta$ ). For this load case, a high longitudinal stress is present in one of the yarn directions, while the longitudinal stress in the other yarn direction is comparable small, which introduces the out-of-plane warping of the unit cell and softens the response. The stiffness reduction is most prominent for the *SUC* boundary condition, which equals a single ply laminate, where no constraint is given to the out-of-plane deformation. For the stacking of adjacent plies being out-of-phase (cf. Table 6.2), similar results are obtained for two plies (*SYM*) and an infinite number of plies (*OP*). For the out-of-phase stacking, the out-of-plane deformation is locked, as the adjacent plies tend to deform out-of-plan contrarily. This leads to zero out-of-plane warping, giving an upper bound for the stiffness. If 3D periodicity with *IP* stacking is assumed, the adjacent plies give a certain support and restrict the out-of-plane deformation, thus the response in yarn direction is slightly softer compared to the *OP* case.

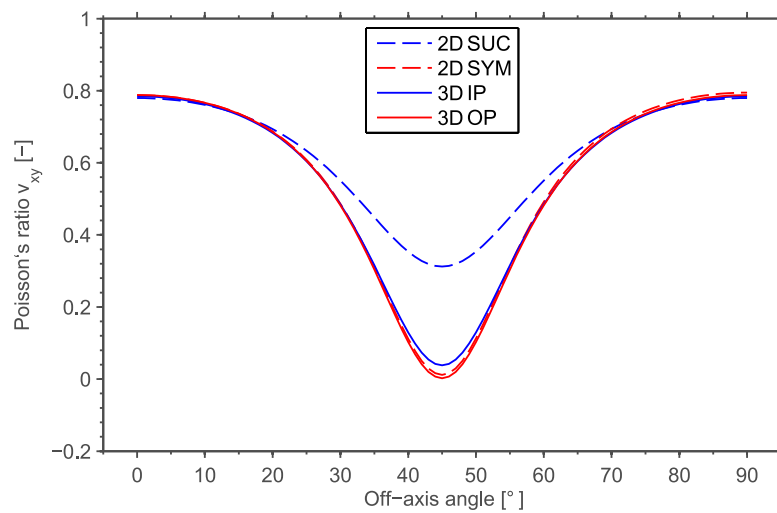
Comparing the predicted elastic constants to the experiments, the *IP* stacking yields the best approximation for the biaxial braided laminates behavior. As the real stacking does not match the *OP* case, a certain amount out-of-plane deformation of the braided composites can be assumed to be present if loaded off-axis. Thus, the *IP* out-of-plane boundary condition is considered the most realistic for a mixed stacking, which can be assumed to be present in most braided laminates. A more detailed investigation of the effect of stacking to the predicted properties may be obtained by introducing special boundary conditions as presented by Ivanov et al. [208, 209]. This may lead to improved results for modeling a distinct stacking, but for predictions of mechanical properties, the information of laminate stacking is unlikely to be available. Thus, the *IP* out-of-plane boundary condition can be summarized to yield realistic results for stiffness and out-of-plane deformation of mixed stacking biaxial braided composite laminates.

The Poisson's ratios calculated by the BBM with the different out-of-plane boundary conditions are compared to the experimental measured ones in Fig. 6.25. For the BB45 braided composite, no experimental data on the Poisson's ratio was available, thus only the simulation results are shown. Comparing the different out-of-plane boundary conditions, the results of the cases considering two or more plies (*SYM*, *IP*, *OP*) are very similar, while the *SUC* solution overestimates the transverse contraction. The biggest deviation for both braiding angles is seen for an off-axis angle of  $\psi = 40 - 50^\circ$ . The comparison to the experimental data of the BB30 braid shows, as for the Young's modulus, that the *IP* solution yields a good correlation. The deviations observed between prediction and experiments for the off-axis angles  $\psi = 30^\circ$  and  $\Psi = 45^\circ$  are mainly attributed to the idealizations made for the effective medium constitutive model.

A comparison of the elastic moduli calculated with the BBM to the analytical predictions made with TexComp is given in Fig. 6.26. The TexComp results for both, BB30 and BB45 are very similar to the *OP* solution of the BBM, with the stiffness in yarn direction, predicted by TexComp, being 2-3% bigger. The elastic modulus in take-up and transverse direction of the TexComp model is 3-5% lower. The deviations for the matrix-dominated values are believed to be due to the different micromechanical methods used for the yarn elastic properties (Mori-Tanaka in TexComp, Chamis equations in the



(a) BB30



(b) BB45

**Fig. 6.25:** Comparison of predicted Poisson's ratios at different out-of-plane boundary conditions

BBM). The differences in yarn direction show that proper modeling of the influence of waviness on the yarn longitudinal behavior requires considering both, the stiffness knock-down of the yarn itself introduced by the undulation and the softening introduced by the out-of-plane deformation. Therefore, the BBM, which allows to consider different laminate stacking configurations, yields a more precise and realistic prediction of the stiffness, while the TexComp modeling overestimates the yarn stiffness. Furthermore, it should be noted that the effect becomes even more prominent, if laminates with a smaller number of plies ( $n < 4$ ) are used.

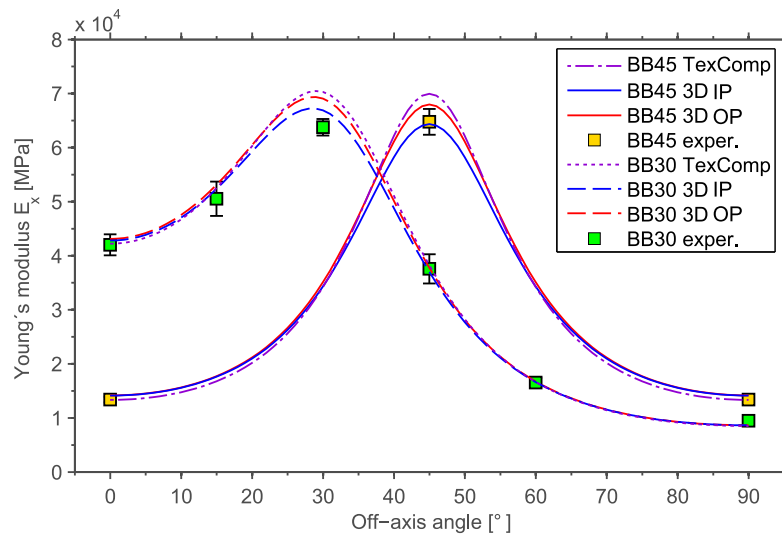


Fig. 6.26: Comparison of elastic BBM results to Mori-Tanaka homogenization (TexComp)

## 6.9. Parametric study: out-of-plane boundary conditions

It was shown in the previous section that out-of-plane boundary conditions of unit cell calculations considerably influence the elastic results. In addition to the elastic influence, the out-of-plane warping of the unit cell introduces an additional bending stress into the yarn stress profiles. As the additional bending can have a considerable effect on the predicted failure stresses, the influence of out-of-plane unit cell warping to the yarn stresses was evaluated in a parametric study: the stresses in the yarns and the failure loads were evaluated for load in the yarn direction at different out-of-plane boundary conditions. For the stress-profile study, the *IP* case, which was found to be a good approximation for the elastic behavior, is compared to the case of maximal and minimal out-of-plane deformation of a single-ply unit cell (*SUC*) and 3D-periodic *OP* stacking, respectively. The unit cell calculations were conducted linear elastic for a BB30 and BB45 unit cell. A stress of 100 MPa was applied in the yarn (F-) direction, as shown in Fig. 6.27.

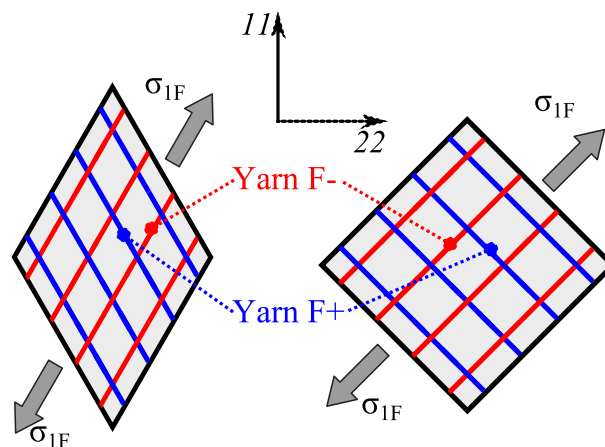
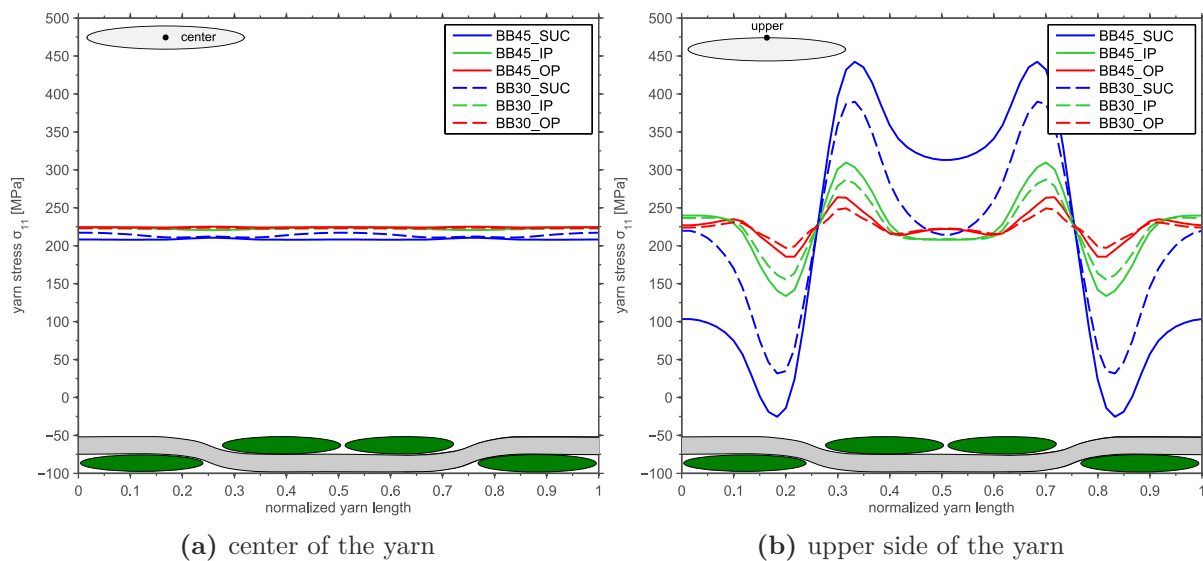


Fig. 6.27: Load cases considered for the out-of-plane boundary condition study

The longitudinal stress profiles were evaluated in one of the yarns in loading direction (*Yarn F-*). The resulting stress profiles are shown in Fig. 6.28. The longitudinal stress



**Fig. 6.28:** Longitudinal yarn stress profiles in the *yarn F-*

in the center of the yarn shown in Fig. 6.28a is insensitive to the out-of-plane boundary condition applied. For *IP* and *OP* of both, BB30 and BB45, almost identical stresses are predicted, while the *SUC* solution yields 3-7% lower stresses in the yarn center. In opposite, major deviations between the out-of-plane boundary conditions are seen for the longitudinal stress at the upper point of the yarn cross section. For the BB45, the lowest stresses in the undulation interval are predicted for the *OP* case, while the peak stress increases by 18% for the *IP* case and 68% for the *SUC* case. In addition, the location stress peak is shifted more towards the straight region of the yarn, the more out-of-plane deformation being present. The increased maximum stresses for the *SUC* and *IP* case are induced by yarn bending through the local out-of-plane deformation of the unit cell (cf. Fig. 6.17). The investigations for BB30 show similar effects as the BB45 stress profiles, but the maximum stresses are lower. However, the difference in stress peaks is of similar range as for the BB45 braid.

The transverse and shear stress profiles in a yarn oriented transverse to the load (*F+*) are shown in Fig. 6.29. For both braiding angles, the same effects of the out-of-plane deformation are observed: while the solutions for *IP* and *OP* boundary conditions are nearly identical, the *SUC* solution deviates significantly. The transverse stress in the *SUC* case is more than twice the one observed in the *IP* and *OP* case. Negligible shear stresses are present in the yarns of the BB45 in the *IP* and *OP* case, while shear stresses in the straight region are introduced by the warping in the *SUC* case. For the transverse stresses, the influence of unit cell warping is similar for both braiding angles, but for the shear stresses it is increased in the BB45 unit cell.

The out-of-plane normal and shear stresses predicted with the different out-of-plane boundary conditions are shown in Fig. 6.30 and Fig. 6.31. For the normal stresses  $\sigma_{33}$ , the influence of the out-of-plane boundary conditions is contrary to the one observed for the in-plane stresses: the biggest stresses are present for the *OP* boundary condition.

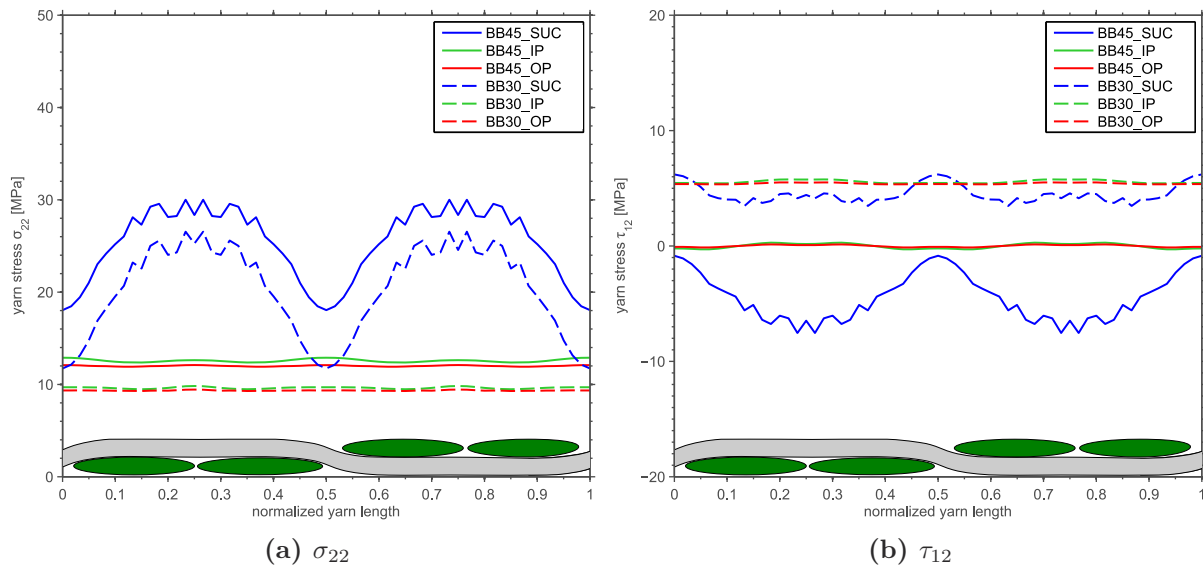


**Fig. 6.29:** Transverse and shear yarn stress profiles in *yarn F+*

The stress profile in the *SUC* case is similar, with the peak stresses being smaller, while the *IP* case predicts the lowest stresses. The high stresses in the *OP* case are due to the compression of the yarns to each other, which is introduced through the suppressed out-of-plane deformation. This is similar for the *SUC* solution, where the bended yarns introduce transverse compression. As the *IP* case models infinite plies, deforming in a similar way, the compression of the yarns to each other is minimal in this case.

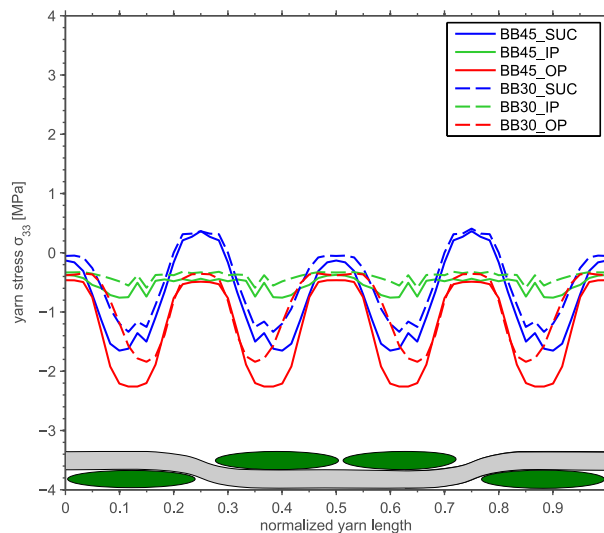


**Fig. 6.30:** Transverse normal stress  $\sigma_{33}$  in *yarn F-*

For the out-of-plane shear stresses shown in Fig. 6.31, the highest stresses are present in the case of *IP* stacking. This is due to the fact that adjacent unit cell deforming similar mainly introduce the support by transverse shear stresses. As not out-of-plane deformation is present in the *OP* case, only minor transverse shear stresses are observed. The *SUC* case, where the transverse shear stresses are induced by the big out-of-plane



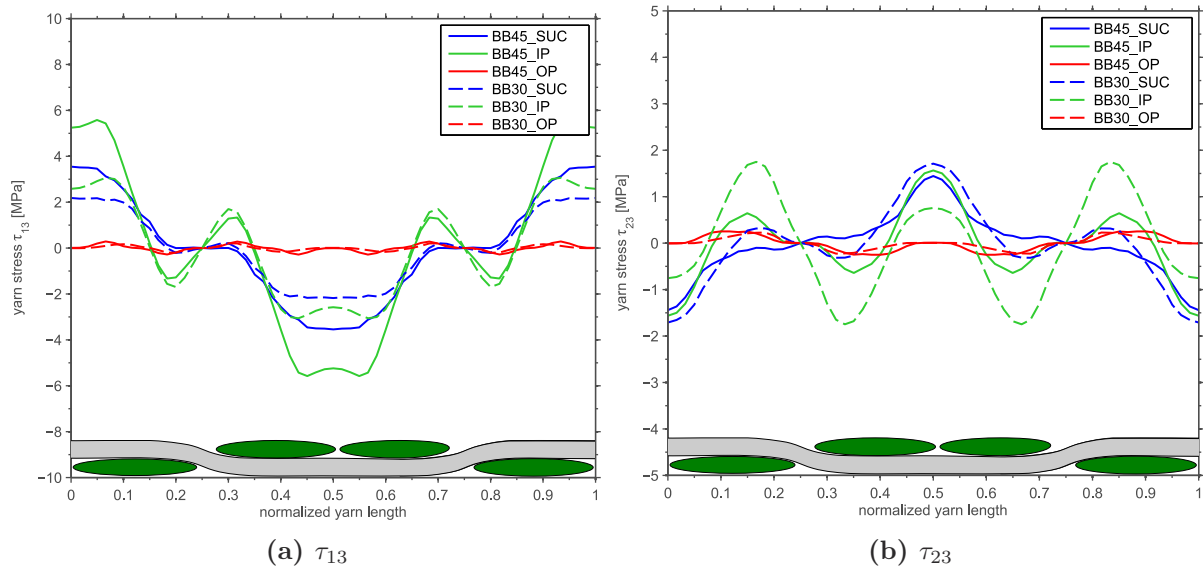


**Fig. 6.31:** Transverse shear yarn stress profiles in *yarn F*-

warping, shows similar stress profiles as the *IP* unit cell, with the stress peaks being smaller for  $\tau_{13}$  and similar for  $\tau_{23}$ .

### 6.9.1. Nonlinear deformation and failure

In addition to the linear simulations, the influence of the out-of-plane boundary conditions to the nonlinear deformation and the failure loads predicted by BBM unit cell simulations was investigated. The simulations included a nonlinear geometry formulation and the Drucker-Prager plasticity model in the effective medium. The load case considered was, as for the stress profiles, load in one of the yarn directions. The homogenized stress-strain curves from the BB30\_0A30 and the BB45\_0A45 simulations are given in Fig. 6.32. The linear (*lin*) stress-strain curves, given for comparison, were obtained from the linear elastic simulations.

For both braiding angles, similar effects are seen in the stress-strain behavior: The simulations with *IP* and *OP* soften under the load, while the *SUC* case stiffens with the load applied. For the *SUC* case, the large out-of-plane deformation of the unit cell dominates the nonlinear deformation by stiffening the yarn response, which leads to the global stiffening of the unit cell. The decrease of stiffness, observed in the *IP* and *OP* nonlinear simulations is mainly due to plastic deformation in the effective medium. For the the *IP* case, also some stiffening of the yarns due to the out-of-plane deformation is present, however, this effect is superimposed with the plastic deformation in the effective medium.

The unit cell strength for the nonlinear simulations was predicted by evaluating longitudinal fiber failure. Due to the increased stress concentration in the undulation interval of the *SUC* model, the lowest strength is predicted in this case. The *SUC* strength is 24% and 30% lower compared to the *OP* strength for BB30 and BB45, respectively. The difference in strength is lower in magnitude as compared to the peak stress difference observed in the linear elastic simulations. For the high out-of-plane deformation present in the

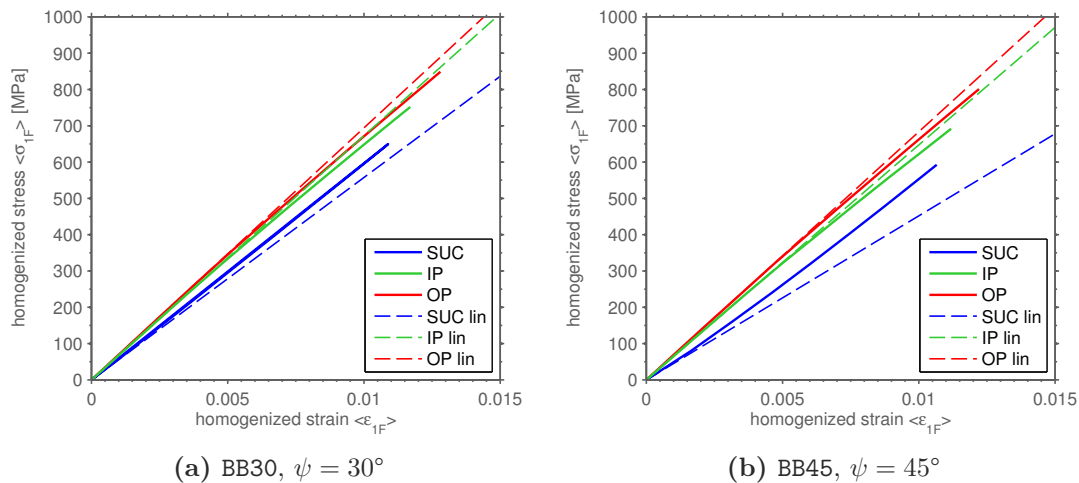


**Fig. 6.32:** Comparison of linear and nonlinear solutions for different out-of-plane boundary conditions

*SUC* case, the nonlinear geometric analysis leads to a stiffening of unit cell and a smaller out-of-plane deformation compared to the linear case. In the case of the *IP* configuration, the strength is 11% lower for the BB30 case and 18% lower for BB45 case, when compared to the *OP* configuration. This difference is of similar magnitude as the difference in stress peaks observed for the linear elastic simulations. Thus, nonlinear geometric effects have less impact on the results for *IP* and *OP* boundary conditions.

To further investigate the effect of nonlinear geometry for the BB30 unit cell in *IP* configuration. The yarns in biaxial braided composites can be considered as discrete reinforcing structure, which may align with the load (scissoring [94]) or straighten (reducing the waviness) under load. The influence of these effects on the deformation of a BB30 is shown in Fig. 6.33. Note that a linear-elastic effective medium constitutive law was

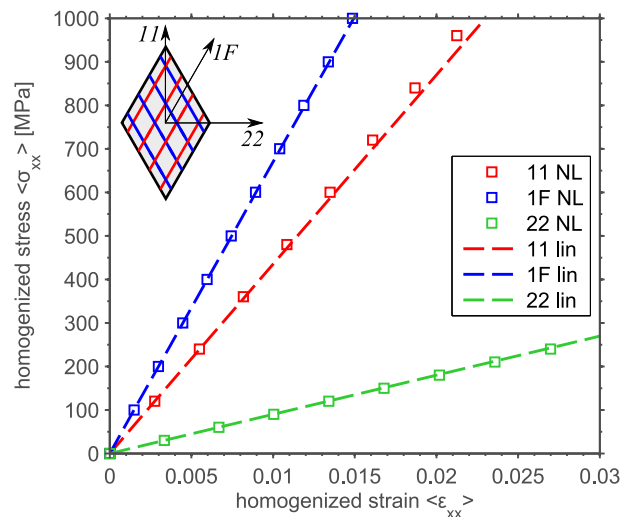


**Fig. 6.33:** Comparison of linear and nonlinear geometry for BB30 in *IP* configuration

used for these simulations. For tension in transverse direction (22) and tension in tension in yarn direction (1F), linear and nonlinear deformation yield identical results. A

slight stiffening of the unit cell response is observed in the take-up (11) direction, which is due to alignment of the  $\pm 30^\circ$  yarns with the load. However, the impact of this effect is small compared to the nonlinear effects due to material softening observed in the off-axis experiments.

### 6.9.2. Summary out-of-plane boundary conditions

The comparison of yarn stress profiles from identical unit cells simulated with different out-of-plane boundary conditions showed a major effect of the chosen boundary condition to the stress profiles. Especially the *SUC* condition lead to a high out-of-plane deformation, introducing additional stresses. The *IP* and *OP* boundary conditions differ less, with a maximum difference of 20% for the yarn longitudinal stress. As no correlation to experimental results is possible, no clear recommendation for a ideal choice of boundary condition can be identified from the stress profile comparison. However, the *IP* boundary condition, which was found to be well suited for elastic predictions, also yielded reasonable results for the yarn stresses, when considering a mixed stacking case as observed in the micro-CT scans. Thus, the *IP* boundary condition will be used for the nonlinear simulations described in the next sections.

## 6.10. Prediction of failure and comparison to experiments

The simulations for failure prediction were conducted for the BB30 and BB45 braided composites with the geometric models given in Section 5.1.2. All simulations included the elastic-plastic material definition of the effective medium and spatial periodicity with *IP* stacking.

### 6.10.1. Parameter identification

The elastic predictions done with the BBM based on constituent material parameters from experiments with UD composite laminates. A similar approach was investigated for the strength predictions, taking the strength properties from the same series of UD experiments. The failure of the braided composite is in the BBM predicted by applying failure criteria to the yarn stress tensor calculated. The yarns within a textile composite behave, transversely isotropic and thus the strength parameters for the yarns can be directly extracted from UD experiments. Due to the high packing density in the yarn of braided composites ( $p_d \approx 70\%$ ), a special manufacturing process for high volume fraction UD laminates of similar fiber/matrix combination is required. The properties were measured from UD coupons, produced by UD braiding and infused with the VAP process, yielding laminates with a fiber volume fraction of 66%. The experiments in tension and compression were conducted according to an in-house standard procedure at the *Polymer Competence Center Leoben*. The shear properties were not tested and thus taken from [204]. The experimental measured strength properties are given in Table 6.6.

The measured strength properties were scaled to the fiber volume fraction present in the yarn according to the procedure given in Section 6.3.3 and used for unit cell simulations of the BB30 in take-up and transverse direction. The predicted stress-strain behavior is

**Table 6.6.:** Experimental strength values for HTS40 / RTM6 normalized to 60% FVF

$X_T$ [MPa]	$X_C$ [MPa]	$Y_T$ [MPa]	$Y_C$ [MPa]	$S_L$ [MPa] <sup>1</sup>
1836	905	47	164	71.3

<sup>1</sup>: taken from [204]

shown in Fig. 6.34. For both, OA00 and OA90 load, the stiffness and non-linear deformation predicted by the BBM model yields excellent correlation to the experiments. However, the failure stresses calculated by the BBM model underestimate the experimentally measured stresses by 25% for the OA00 loading and by 40% for the OA90 loading. The failure predicted by the model is intra-yarn failure in compression (mode C) for the OA00 and tension (mode A) for the OA90 case. Further load cases that were simulated with the material data from Table 6.6 yielded similar magnitudes of strength underestimation.

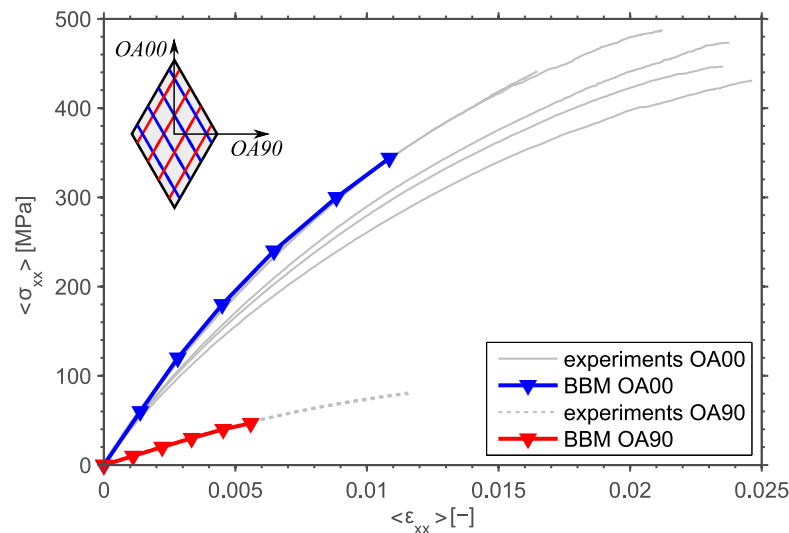


**Fig. 6.34:** Comparison of BBM simulations with UD strength parameters and BB30 experiments

The deviation between the BBM predictions with UD strength parameters and experimental results is mainly believed to be due to the input parameters being not appropriate for the behavior to be modeled. For UD laminates, the effect of thin plies known as *in-situ*-effect yields increased matrix-dominated properties in dependence of the ply position in the laminate and the ply thickness. Properties determined by UD experiments were found to be inappropriate for predicting matrix-dominated failure within a composite laminate. A similar effect is believed to be present for the biaxial braided composites investigated in this work: the transverse cracking in the yarn is believed to be dependent on the boundary conditions given by the textile architecture of crossing and undulating yarns. The process of failure and thus the material properties obtained by UD experiments are unlikely to be representative for the yarns in braided composites. For the *in-situ* effect in UD laminated composites, Camanho et al. [159] presented an analytical approach for the calculation of *in-situ* strength in laminates. But as the approach assumes specific

boundary conditions for crack opening, these equations are unlikely to be representative for braided composites. Due to this, an alternative approach will be used in this thesis: the strength parameters required for the yarns will be identified by the comparison of BBM-simulations of biaxial braided composites with according experimental results. A similar approach has been used by Cox, Yang and Co-Workers [133, 136] to obtain critical strain values for failure within the Binary Model. As the failure criteria presented in Section 6.6 require five independent input parameters for yarn longitudinal, transverse and shear failure prediction, five distinct load cases will be used for the parameter identification. The strength parameters are identified within the simulations by an iterative best-fit procedure. An overview to the load cases and the identified parameters is given in Table 6.7.

**Table 6.7.:** Load cases for parameter identification and identified strength values

Strength	$X_T$ [MPa]	$X_C$ [MPa]	$Y_T$ [MPa]	$Y_C$ [MPa]	$S_L$ [MPa]
Model	BB30	BB30	BB30	BB30	BB45
Load Case	PT_OA30	PC_OA30	PT_OA90	PT_OA00	PT_OA00
Value <sup>1</sup>	2192	1545	82	174	112

<sup>1</sup>: values given for 60% fiber volume fraction

### 6.10.2. Comparison to experiments

The BBM predictions are compared to the BB30 and BB45 off-axis experiments. For all off-axis angles characterized experimentally, nonlinear simulations were conducted with the load introduced into the unit cell calculated by Eq. 6.27. The stress-strain curves and strength predicted by the BBM simulations are compared to the experimental results given in Chapter 4 for the BB30. The BB45 tensile and compressive experiments in take-up (OA00) and yarn direction (OA45) were conducted at the *Polymer Competence Center Leoben*, with an overview to the experiments is given in Appendix A.1. All BBM unit cell simulations were nonlinear, including the elastic-plastic material model in the effective medium. A linear geometric formulation was used, as the effects of nonlinear geometry observed were small and the linear geometry models showed an improved convergence for compressive loads. The element size for effective medium and beam elements was chosen 0.2 mm, which yielded 70,000 elements in total. The off-axis stresses applied to the unit cell were calculated according to Eq. 6.27. The unit cell failure stress was obtained from the first longitudinal or transverse failure occurring within the yarns.

#### BB30 tension

The results of the BBM simulations in tension are compared to the off-axis experiments in Fig. 6.35. Only the experimental stress-strain curves of the monotonically loaded specimen are shown for clarity. The point, where the BBM stress-strain curves end is the point, where failure was predicted in the unit cell model.

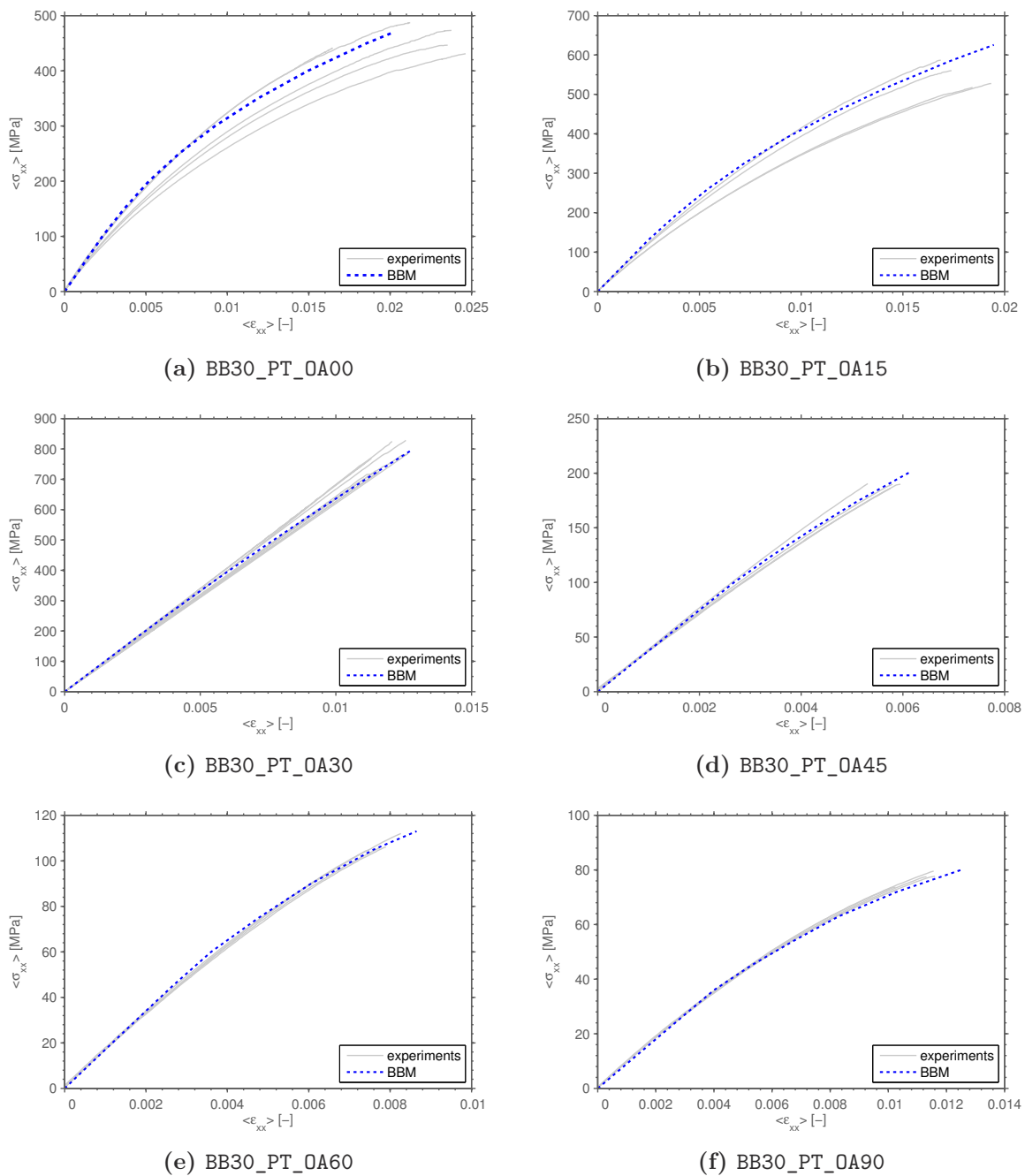


**Fig. 6.35:** Comparison of non-linear BBM-simulations with tensile off-axis experiments

The shape of the stress-strain curves, i.e. the decrease of the tangent modulus is predicted excellent by the BBM unit cell. For the 0A00 and 0A15 experiments, where a larger scatter was observed in the experimental measured stiffness, the BBM simulations agree with the response of the stiffer stress-strain curves (Fig. 6.35a, 6.35b). The reason for this is mainly found in the braiding angle: the variations of stiffness in the experiments could be assigned to braiding angle variations on the panels. The braiding angle was predominantly found to be bigger as the nominal  $30^\circ$ , resulting in a softer response of most

specimen. For tension applied in the yarn direction (0A30), the stress-strain behavior of the BBM unit cell is slightly nonlinear, while the experimental stress-strain curves show a linear response Fig. 6.35c. The source of the deviation is difficult to evaluate, as the 0A30 stress-strain curves had to be linearized at the beginning of the experiment (cf. Section 4.2.1). The nonlinear stress-strain behavior predicted by the BBM is due to plastic deformation of the effective medium, i.e. the plasticity model is likely to overestimate the decrease in stiffness in this case. In contrast, for the higher off-axis angles 0A45, 0A60 and 0A90, the predicted response is in excellent agreement with the experiments (Fig. 6.35d-6.35f). Thus the effective medium plasticity model works accurate for matrix-dominated load cases, but slightly overestimates the nonlinear deformation, if the load is mainly carried by the longitudinal yarn stiffness.

For the assessment of the strength prediction, the values of 0A00, 0A30 and 0A90 are not considered quantitatively, as these load cases were used for the parameter identification and thus match the experimentally measure strength. In the case of 0A00, the failure mode predicted was compressive intra-yarn failure (mode C), which matches with the observations on the failure mode and process in the experiments. For the 0A15 load case, the BBM simulations overestimate the average experimental strength by 12%, which is attributed to the braiding angle variations. The failure mode predicted for 0A15 is compressive intra-yarn failure (mode C) in the 1F- direction, while yarn tensile rupture was observed in the experiments. However, the stress exposures of yarn longitudinal and transverse failure are very close in the model and the difference in failure modes is believed to be due to an interaction of transverse cracking and longitudinal yarn failure. For 0A30, the predicted failure mode is yarn longitudinal failure in the 1F- direction, as observed in the experiments. In the yarn direction transverse to the load (1F+) the model does not predict preliminary transverse failure, which is in accordance with the experiments, where no cracking was observed in the transverse yarn direction. For the off axis load cases 0A45 and 0A60, the predictions made by the BBM unit cell are nearly identical to the experimentally measured values. The failure mode for these load cases, as well as for 0A90, is tensile transverse yarn failure (mode A). This is in accordance with the experimental observations for these load cases, where the final failure appeared as tensile cracking in the 1F+ direction.

Summarizing the comparison to the tensile experiments, the nonlinear deformation of the braided composites is modeled well by the BBM model and the predicted failure stresses agree well with the experimental measured values. Except for 0A15, the failure modes predicted match the observations from the experiments.

### **BB30 compression**

The comparison of the BBM simulations to the off-axis compression experiments is given in Fig. 6.36. The predicted non-linear deformation is in good agreement with the experiments. In most cases, the non-linear deformation is slightly overestimated by the model, resulting in a softer response of the simulations for higher strains. Except the 0A30, the trend is similar for all cases: the initial stiffness is predicted accurate by the BBM, but with increasing strains, the predicted response is softer as the measured one. The reason for this behavior could be due to the calibration of the plasticity model: the pressure dependence of the model is calibrated with published test data from a similar material

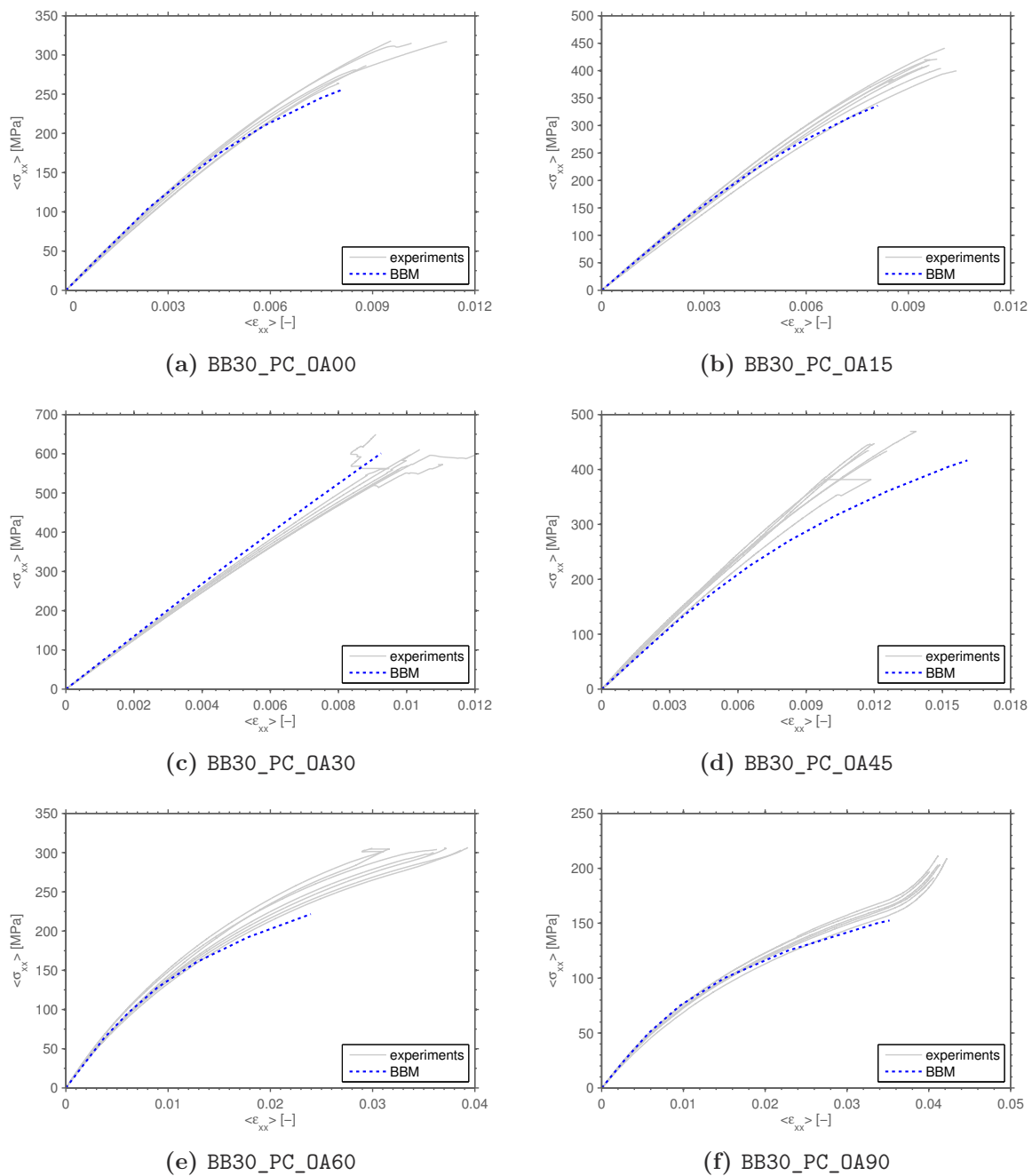


**Fig. 6.36:** Comparison of non-linear BBM-simulations with tensile off-axis experiments

and the flow is assumed to be associated, which is due to the lack of experimental data for HTS40/RTM6 material not validated for the current material. In addition, the hardening curve, which was used identical for tension and compression was calibrated for the tension test and could be different in compression. The deformation behavior is different for the 0A30 case: the measured response is stronger nonlinear compared to the BBM response. The nonlinear deformation in the experiments is believed to be due to the increase of waviness under compressive loads, which the linear geometric model does not represent.



For the **0A45** the increased deviation between measured and predicted stress-strain curves is due to the difference of initial modulus of model and experiment, which is believed to be introduced by manufacturing tolerances of the coupons: the **0A45** mechanical properties are very sensitive to the off-axis angle and the compressive modulus measured was considerably higher as the tensile one (cf. Fig. 4.42). This suggests the off-axis angle in the experiments being lower than the nominal one, which introduces the difference in stiffness. However, summarizing the stress-strain comparison in compression, the nonlinear deformation is predicted accurate by the **BBM** for all off-axis angles.

The strength predicted by the **BBM** correlates well with the experiments in the **0A30** and **0A45** case, but is underestimated in the other off-axis load cases. As the **0A30** case (Fig. 6.36c) was used for the parameter identification of the compressive yarn strength, the prediction meets the experiments. The failure mode in this case is yarn failure in compression, which correlates with the observations from the experiments. For the **0A00** and the **0A15** test series (Fig. 6.36a-6.36b), the strength is underestimated by the model by 15% and 20%, respectively. For both test series, the failure mode predicted is transverse tensile yarn failure (mode A), which correlates with the experiments, where the **PC\_00** and **PC\_15** failed into a single tensile crack (cf. Fig. 4.41). The deviation in strength is mainly attributed to stress concentrations from local out-of-plane deformation of the yarns in the unit cell: as the yarn-to-effective medium coupling using the **MPCs** is localized at the beam nodes, a local out-of-plane deformation of the unit cell at the undulation intervals of the yarn is present. The out-of-plane deformation introduces additional stress concentrations in the yarns, leading to a predictions of a lower strength in the unit cell simulations. Using a nonlinear geometry formulation could reduce the effects of local stress concentrations, but it lead to convergence issues with the **BBM** unit cell: for compressive loads with nonlinear geometry, the yarns are twisted along their length, drastically softening the unit cell response and finally resulting in a non-convergence of the **FE** problem. The twisting is due to the fact that the rotational **DOFs** of the beams are not coupled into the effective medium, which is an artifact in the model formulation. A solution could be to introduce an improved constraint method, coupling both, rotational and translational, degrees of freedom from the beam nodes.

For the **0A45** test series, the predicted strength lies within the experimental scatter and the failure mode predicted is transverse compressive failure in the **1F+** yarn direction. The mode and location of failure correlate well with the experiments, which showed an through-the-thickness inclined crack in the **1F+** direction. Comparing the unit cell predictions higher off-axis angles **0A60** and **0A90** to the experiments, the compressive strength is underestimated by 29% and 25% respectively. The failure mode predicted is yarn transverse compressive failure (mode C) in the **1F+** direction for **0A60** and simultaneous mode C failure in both yarn directions for **0A90**. The predicted failure modes correlate with the experiments, where thickness-inclined cracks were observed in both test series. The large deviation between the models and the experiments could not be assigned to modeling assumptions in the **BBM**, and it is rather believed that the difference comes from the experiments: the **CLC** test fixture requires specimen with small gauge sections and thus local stress concentrations induced by the fixture can have a major effect. In both test series, the cracking of the specimen was near the load introduction and the **0A90** series showed a zig-zag pattern where the cracks were stopped at the tab location. Thus,

it is believed that the cracking was inhibited by the load introduction in the experiments, increasing the maximum force and thus strength measured. The theory is supported by the test results obtained from Birkefeld [193] for an biaxial braided composites of identical fiber/matrix combination: the compressive strength measured by Birkefeld in the  $11$ -direction is identical to the one measured in this thesis (Cichosz: 299.8 MPa, Birkefeld: 299.1 MPa), while the strength in  $22$ -direction measured by Birkefeld is 24% lower as the one measured in this thesis (Cichosz: 204.4 MPa, Birkefeld: 155.7 MPa). The issue is believed to be particular for braided composites, as they BB30 has a very high Poisson's ratio ( $\nu_{yx}^{OA90} \approx 1.5$ ), triggering additional stresses in the material if the deformation is constraint.

### BB45 tension and compression

The BBM unit cell simulations were additionally compared to BB45 experiments. The BB45 braided composites were manufactured with an identical procedure as described in this thesis (cf. Section 3.2.2) for the BB30. The comparison of stress-strain behavior from BBM and the experiments is given in Fig. 6.37. No stress-strain curves were available for

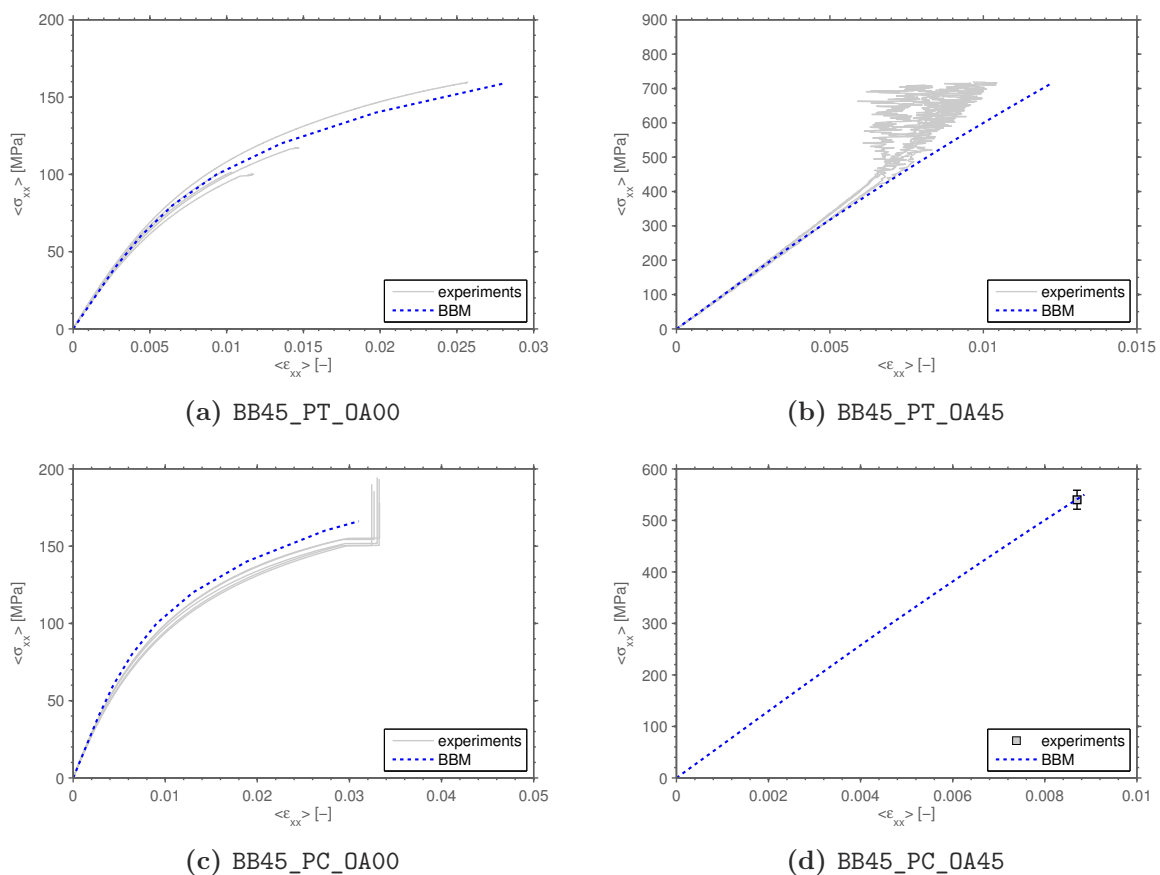


**Fig. 6.37:** Comparison of non-linear BBM-simulations with tensile off-axis experiments

the OA45 compression experiments, thus only the strength value is given in the plot. For tension and compression in take-up direction (OA00, Fig. 6.37a, 6.37c), the stress-strain

behavior of simulations and experiments agrees well. In the tension experiments, the foil strain gauges, used to measure the strain on the specimen, failed preliminary and thus only one stress-strain curve is available up to the failure strain. In compression, the initial stiffness and thus the stresses over the complete strain range are slightly overestimated by the BBM unit cell model, which is likely to be due to a braiding angle deviation of the specimen. As in tension, the foil strain gauges failed preliminary at approximately 3% compressive strain, which marks the point of abrupt load increase at constant strain in the experimental stress-strain curves. For the load applied in the yarn direction (0A45, Fig. 6.37b, 6.37d), the comparison of the stress-strain curve in tension yields a good accordance between simulation and experiment. The oscillations in the experimental curves are due to a blistering of the stochastic DIC-pattern.

The strength predicted by the BBM unit cell model agree well with the experimentally measured ones. The BB45\_PT\_0A00 was used for parameter identification and thus is not used for assessment of the predictions. For the load applied in the yarn direction, the predicted tensile and compressive strength lie within the experimental scatter, while the compressive strength in the take-up direction is underestimated by 13%. This is, as for the BB30\_PC\_0A00 case attributed to the local out-of-plane deformation of the unit cell. In general, the BBM unit cell predictions made for BB45 can be judged as very accurate.

The BBM unit cell predicts transverse yarn failure in the yarn orthogonal to the load direction as first failure for the BB45\_PT\_0A45. Failure is predicted at a stress of 582 MPa, which correlates with experimental observations of surface-cracking on the specimen forming between 450-550 MPa. In this case, as the load could be further increased and the 1F-yarn direction was mainly stressed in longitudinal direction, transverse yarn failure was ignored and yarn longitudinal failure was used to predict the strength.

## 6.11. Conclusion on FE unit cell modeling

In this chapter, a novel unit cell modeling approach, the Binary Beam Model (BBM) was proposed for modeling the constitutive behavior of biaxial braided composites. The modeling approach was integrated into a MATLAB framework, thus parametric unit cell models can be built without requiring manual work e.g. for meshing or post-processing of the models.

The modeling idealizations base on Cox's Binary Model and were improved in terms of considering the effects introduced by yarn waviness: beam elements, modeling longitudinal and bending stiffness and strength of the yarns are embedded into effective medium continuum elements. The beam elements allow to consider the influence of yarn waviness and yarn cross-section on stiffness and stress fluctuations in the yarns. Constitutive laws for both, effective medium and beam elements have been proposed for the BBM. The yarn's constitutive law was chosen linear elastic and considers the volume doubling of beam and continuum elements. A Drucker-Prager plasticity model was introduced for the effective medium, which allows to model nonlinear deformation prior to final failure.

For the matrix-dominated stresses, which are extracted from the effective medium, an averaging approach based on the idea of volume-averaging was introduced: the averaging removes the mesh-dependency from the effective medium stress field, while preserving local stress fluctuations introduced by the textile yarn architecture of the braided com-

posites. The stress profiles calculated by the BBM were compared to classical continuum element unit cell results, and a good correlation was obtained for the stress variations present over the complete cross section of the yarns. A major difference was found for the in-plane shear stress, which yields from the modeling idealizations: rotational DOFs of the beams are not coupled with the effective medium continuum elements and thus no influence of yarns crossovers is modeled. However, the in-plane shear stress predicted by the BBM was conservative compared to the continuum unit cell. Overall, the correlation of BBM and continuum element unit cell was found to be excellent, yielding a good basis for failure prediction.

Periodic boundary conditions were used for all simulations and the application of different idealized out-of-plane boundary conditions was investigated. The effect of the chosen out-of-plane boundary condition on the elastic predictions and stress profiles was found to be severe: the stiffness in the yarn direction was changed up to 40% depending on the out-of-plane boundary condition and the stress maxima varied up to 70%. Assuming a single unit cell in the simulations was found to be not appropriate for the simulation of a braided laminate with variable stacking of the plies. The comparison of the elastic behavior under different out-of-plane boundary conditions showed that the *IP* stacking correlated best with the experimental results. As the *IP* stacking yielded realistic results for the stress profiles, this boundary condition was chosen for further calculations. The *IP* stacking idealization, which represents identical stacking of an infinite number of plies, was found to be a good solution for parametric and predictive calculations.

Strength parameters measured from UD experiments of the same fiber/matrix combination were found to be inappropriate for failure modeling in the yarns. Similar to the *in-situ* effect known for UD composites, the strength properties of a yarn inside a textile composite are believed to be controlled by the boundary conditions given to the crack formation and propagation inside the yarn. Thus, a parameter identification approach based on experiments of biaxial braided composites was used to identify the strength properties used within the BBM. Five experiments out of the off-axis test series were chosen to calibrate the strength properties required for the yarns.

The BBM model predictions were compared to the results of tensile and compressive BB30 and BB45 off-axis experiments. The non-linear deformation predicted under tensile and compressive loads correlated well with the experiments, approving the modeling approach of using a Drucker-Prager plasticity model in the effective medium. A deviation to the experiments was found for the slight nonlinear deformation predicted by the model for the tension applied in one of the yarn directions ( $\Psi = \theta$ ). The deviation could be attributed to nonlinear geometric effects like yarn stretching and yarn alignment, not considered in the presented BBM formulation. The off-axis failure predictions correlated well in tension, with the failure stresses and the failure modes being predicted accurately. In compression, the failure modes predicted by the BBM simulations matched the ones found in the experiments, but deviations to the failure stresses determined experimentally have been found for just a few of the loadcases. The deviations were mainly attributed to the out-of-plane deformation behavior of the BBM unit cell under compression, increasing the maximum yarn stress. In addition, it was found that the compressive test results in transverse (22) direction differ significantly from the ones obtained by Birkefeld [193] with a Celanese test fixture. While the BBM results underestimate the strength measured in

the off-axis compression experiments with the CLC test fixture, it matches the strength given in [193].

Summarizing the finite element unit cell simulations, the BBM model provides an accurate and efficient tool to simulate the effect of a textile yarn architecture on the elastic and nonlinear behavior of biaxial braided composites. The model correlates well with classical predictions and experimental investigations, and thus builds a good basis for predicting yarn-architecture dependent solutions of the constitutive behavior of biaxial braided composites. The predicted response from the BBM can further be used as an input for macroscopic modeling.

# 7. Macroscopic modeling of biaxial braided composites

Macroscopic modeling approaches are necessary for efficient modeling and simulation of structural components made from biaxial braided composites. Explicit modeling of the yarn architecture, like it is done in unit cell modeling, is not suitable for structural simulation from both, modeling effort and computational cost. Thus, a macroscopic approach based on shell element modeling is introduced. The assumption of plane-stress, used within most shell elements, was shown to be meaningful for braided composites, as the textile reinforcement is two-dimensional. Two types of approaches based on CLT will be employed:

1. Linear and analytical predictions, solely using CLT equations and first failure prediction.
2. Nonlinear predictions, including plastic deformation and damage, implemented into a material subroutine in the finite element code Abaqus/Explicit.

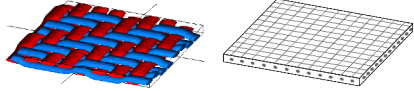
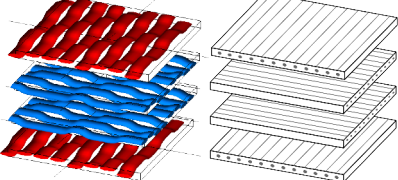
The analytical approach will be used to determine the macroscopic input properties based on the FE unit cell modeling results. Two methods for analytical predictions, either modeling the two yarn directions of the braided composites in separate plies, or smearing the properties into one orthotropic ply, are compared in terms of elastic and strength prediction. Furthermore, predictions for different failure criteria are compared and validated with the off-axis experiments. Due to the analytical model being limited to linear deformation, a nonlinear modeling approach, including plasticity and damage, is presented.

## 7.1. Analytical modeling approaches

Using CLT-based plane-stress modeling is common for macroscopic modeling approaches of woven and braided composites (cf. [12, 34, 117, 210, 211]). Beside the computational efficiency, the shell elements modeling yields the advantage that a distinct laminate stacking, i.e. different braiding angles in a braided laminate, can be modeled within a single element, by using thickness integration points.

Two different approaches, shown in Table 7.1, will be considered for analytical modeling: the smeared ply approach (SPA), common for modeling of woven fabrics [117], and the angle ply approach (APA), reported for biaxial and triaxial braided composites [12, 210]. For the SPA, the behavior of the braided composites is modeled within a single orthotropic ply. The input properties are given as the stiffness and strength of the braided composite in take-up and transverse direction and in-plane shear. Thus, the

**Table 7.1.:** Macroscopic modeling approaches for biaxial braided composites

	<b>Smeared Ply Approach (SPA)</b>	<b>Angle Ply Approach (APA)</b>
		
idealization	one orthotropic ply	four equivalent yarn plies $(\pm\theta)_S$
input		
<i>elastic</i>	$E_{11}^{BB}, E_{22}^{BB}, G_{12}^{BB}, \nu_{12}^{BB}$	$E_{11F}^{eq}, E_{22F}^{eq}, G_{12F}^{eq}, \nu_{12F}^{eq}, \theta$
<i>strength</i>	$X_T^{BB}, X_C^{BB}, Y_T^{BB}, Y_C^{BB}, S_L^{BB}$	$X_T^{eq}, X_C^{eq}, Y_T^{eq}, Y_C^{eq}, S_L^{eq}$
calibration	direct input from BB unit cell simulation / experiments	elastic: inverse CLT strength: calibration to load cases

braiding angle is not modeled explicitly, but included in the input properties. On the opposite, the APA considers the braiding angle, by modeling the braided composite as an angle ply laminate. A symmetric  $(\pm\theta)_S$  laminate of four equivalent yarn plies is used for each braided composite layer, excluding bending-extension effects which are present for a two-ply  $(\pm\theta)$  unsymmetrical laminate. The input properties of the APA are the elastic and strength properties of the equivalent yarn plies: these properties include the effects of yarn waviness and cannot be obtained directly from unit cell simulations or experiments.

Both methods yield advantages and drawbacks: the SPA input is straightforward to obtain from experimental or unit cell modeling results. Five unit cell load cases or experiments are required for elastic and strength calibration. However, only limited information is given by the SPA about the failure behavior, as neither the yarn direction failing nor the failure mode of the yarns can be determined. For the APA, the material properties are not given directly by unit cell simulations or experiments and thus require a calibration procedure. The elastic properties can be calculated from closed-form equations given as *inverse CLT* by Zebdi et al.[119] and strength properties are determined by an iterative correlation procedure of the macroscopic model to the unit cell results. However, the APA yields major advantages for failure prediction, as the braiding angle is included in the yarn stress calculation and thus failure prediction. Additionally, following the recommendations given by Puck [95], who noted that the mechanics of wavy yarn plies are similar to the ones of UD plies, common UD failure criteria can be applied to the yarn plies. Thus, the critical yarn direction and the yarn ply failure mode can be predicted.

### Stress calculation and failure criteria

The analytical predictions of failure for both, SPA and APA, are based on failure criteria, applied to the stress vectors available in the approach. For the SPA, the stresses in the 12-material coordinate system are employed ( $\sigma_{11}, \sigma_{22}, \tau_{12}$  cf. Fig. 7.1), while the APA failure predictions are based on the yarn ply stresses ( $\sigma_{11F+/-}, \sigma_{22F+/-}, \tau_{12F+/-}$  cf. Fig. 7.1).

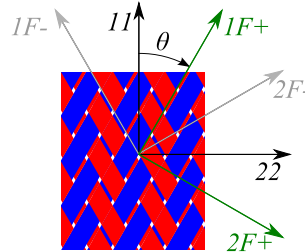


Fig. 7.1: Coordinate system used for the braided composites

The stresses in the equivalent yarn plies can be derived by application of CLT, which yields for the case of a  $(\pm\theta)_S$  braided composite a closed-form equation for the in-plane stresses:

$$\boldsymbol{\sigma}_{F+/-} = \mathbf{Q}^{\text{eq}} \cdot \boldsymbol{\varepsilon}_{F+/-} = \mathbf{Q}^{\text{eq}} \cdot \mathbf{T}(\pm\theta)^{-T} \cdot \boldsymbol{\varepsilon}_{BB} \quad (7.1)$$

Where  $\boldsymbol{\sigma}_{F+/-}$  is the in-plane stress vector of the yarn plies,  $\mathbf{Q}^{\text{eq}}$  is the stiffness matrix of the equivalent yarn ply,  $\mathbf{T}(\pm\theta)$  is the transformation matrix given in Eq. D.9 and  $\boldsymbol{\varepsilon}_{BB}$  is the in-plane strain vector of the angle-ply laminate.

For the SPA predictions, the maximum stress criterion is used, as the basing assumptions for application of phenomenological criteria as e.g. Puck are not given for an orthotropic ply, representing both yarn directions. All stress components are compared to the biaxial braided composite strength values, yielding the most critical failure mode:

$$f_{E,Lt}^{BB} = \frac{\sigma_{11}}{X_T^{BB}} = 1, \text{ for } \sigma_{11} > 0 \quad f_{E,Lc}^{BB} = \frac{-\sigma_{11}}{X_C^{BB}} = 1, \text{ for } \sigma_{11} < 0 \quad (7.2)$$

$$f_{E,Tt}^{BB} = \frac{\sigma_{22}}{Y_T^{BB}} = 1, \text{ for } \sigma_{22} > 0 \quad f_{E,Tc}^{BB} = \frac{-\sigma_{22}}{Y_C^{BB}} = 1, \text{ for } \sigma_{22} < 0 \quad (7.3)$$

$$f_{E,SL}^{BB} = \frac{|\tau_{12}|}{S_L^{BB}} = 1 \quad (7.4)$$

For the APA, two sets of criteria, namely Puck 2D and maximum stress criterion, are used. For Puck 2D, yarn ply transverse failure is predicted by Eq. 6.35-6.37 (with yarn ply stresses and strength employed) and yarn ply longitudinal failure is predicted by the maximum stress criterion (Eq. 7.5). For the maximum stress, all failure stress exposures are calculated by comparing the equivalent ply stresses to the corresponding strength values (Eq. 7.5-Eq. 7.7).



$$f_{E,Lt} = \frac{\sigma_{11F}}{X_T^{eq}} = 1, \text{ for } \sigma_{11F} > 0 \quad f_{E,Lc} = \frac{-\sigma_{11F}}{X_C^{eq}} = 1, \text{ for } \sigma_{11F} < 0 \quad (7.5)$$

$$f_{E,Tt} = \frac{\sigma_{22F}}{Y_T^{eq}} = 1, \text{ for } \sigma_{22F} > 0 \quad f_{E,Tc} = \frac{-\sigma_{22F}}{Y_C^{eq}} = 1, \text{ for } \sigma_{22F} < 0 \quad (7.6)$$

$$f_{E,SL} = \frac{|\tau_{12F}|}{S_L^{eq}} = 1 \quad (7.7)$$

## 7.2. Input property determination for SPA and APA method

The input properties required for APA or SPA can be obtained from unit cell simulations, like presented in Chapter 6. Alternatively, experiments of biaxial braided composites could be used. While the experimental approach may be feasible, if only few yarn architecture configurations are considered, the unit cell simulations offer a more efficient method for calibration of the approaches to various yarn architectures.

### 7.2.1. Input for SPA

The elastic properties for the SPA are achieved directly from the unit cell simulations of a biaxial braided composite. The elastic constants are calculated from linear elastic simulations, presented in Section 6.8. For the strength properties, five nonlinear simulations are required: tension and compression in take-up and transverse direction and in-plane shear. Alternatively, five experimental test cases, with equal load directions as for the unit cell strength calculation are needed.

### 7.2.2. Input for APA

The APA requires input properties for the equivalent yarn plies, representing undulated yarns embedded in matrix from one fiber direction of a biaxial braided composites. These properties can be calculated from unit cell simulations. The unit cell simulations yield the stiffness matrix of the braided composite given in the material coordinate system (cf. Fig. 7.1).

$$\mathbf{Q}^{BB} = f(E_{11}^{BB}, E_{22}^{BB}, G_{12}^{BB}, \nu_{12}^{BB}) \quad (7.8)$$

The elastic constants of the equivalent plies can be calculated following the *inverse CLT* approach published by Zebdi et al. [119]. The stiffness matrix of the braided composite  $\mathbf{Q}^{BB}$  can be written as

$$\mathbf{Q}^{BB} = \frac{1}{2} (\bar{\mathbf{Q}}^{+\theta} + \bar{\mathbf{Q}}^{-\theta}), \quad (7.9)$$

where  $\bar{\mathbf{Q}}^{\pm\theta} = \mathbf{T}^{-1}(\pm\theta) \cdot \mathbf{Q} \cdot \mathbf{T}^{-T}(\pm\theta)$  are the stiffness matrices of the equivalent plies in the global  $1\mathcal{2}$ -coordinate system and  $\mathbf{T}$  is the transformation matrix given in Eq. D.9. Eq. 7.9 can be re-written to

$$\mathbf{Q}^{BB} = \frac{1}{2} \begin{bmatrix} 2 \cdot \bar{Q}_{11}^{+\theta} & 2 \cdot \bar{Q}_{12}^{+\theta} & 0 \\ 2 \cdot \bar{Q}_{12}^{+\theta} & 2 \cdot \bar{Q}_{22}^{+\theta} & 0 \\ 0 & 0 & 2 \cdot \bar{Q}_{66}^{+\theta} \end{bmatrix}, \quad (7.10)$$

as for arbitrary braiding angles, the components of the  $\bar{\mathbf{Q}}^{\theta}$  and  $\bar{\mathbf{Q}}^{-\theta}$  stiffness matrices yield:

$$\bar{Q}_{11}^{+\theta} = \bar{Q}_{11}^{-\theta} \quad \bar{Q}_{22}^{+\theta} = \bar{Q}_{22}^{-\theta} \quad \bar{Q}_{12}^{+\theta} = \bar{Q}_{12}^{-\theta} \quad \bar{Q}_{66}^{+\theta} = \bar{Q}_{66}^{-\theta} \quad \text{and} \quad (7.11)$$

$$\bar{Q}_{16}^{+\theta} = -\bar{Q}_{16}^{-\theta} \quad \bar{Q}_{26}^{+\theta} = -\bar{Q}_{26}^{-\theta} \quad \bar{Q}_{61}^{+\theta} = -\bar{Q}_{61}^{-\theta} \quad \bar{Q}_{62}^{+\theta} = -\bar{Q}_{62}^{-\theta} \quad (7.12)$$

$\bar{\mathbf{Q}}^{\pm\theta}$  is the yarn ply stiffness matrix in the material coordinate system, thus can be written as a function of the unknown components of the yarn ply stiffness matrix  $\mathbf{Q}^{eq}$  (in the yarn  $1F\pm$  coordinate system):

$$\begin{aligned} \bar{Q}_{11}^{+\theta} = \bar{Q}_{11}^{-\theta} &= Q_{11}^{eq} \cdot c^4 + 2 \cdot (Q_{12}^{eq} + 2 \cdot Q_{66}^{eq}) s^2 c^2 + Q_{22}^{eq} \cdot s^4 \\ \bar{Q}_{22}^{+\theta} = \bar{Q}_{22}^{-\theta} &= Q_{11}^{eq} \cdot s^4 + 2 \cdot (Q_{12}^{eq} + 2 \cdot Q_{66}^{eq}) s^2 c^2 + Q_{22}^{eq} \cdot c^4 \\ \bar{Q}_{12}^{+\theta} = \bar{Q}_{12}^{-\theta} &= (Q_{11}^{eq} + Q_{22}^{eq} - 4 \cdot Q_{66}^{eq}) \cdot s^2 c^2 + Q_{12}^{eq} \cdot (s^4 + c^4) \\ \bar{Q}_{66}^{+\theta} = \bar{Q}_{66}^{-\theta} &= (Q_{11}^{eq} + Q_{22}^{eq} - 2 \cdot Q_{12}^{eq} - 2 \cdot Q_{66}^{eq}) \cdot s^2 c^2 + Q_{66}^{eq} \cdot (s^4 + c^4) \end{aligned} \quad (7.13)$$

With  $c = \cos \theta$ ,  $s = \sin \theta$  and  $\theta$  being the braiding angle. Inserting Eq. 7.13 into Eq. 7.10 yields a linear system of four equations for the four unknown components of the stiffness matrix  $\mathbf{Q}^{eq}$  and thus delivers a unique solution for the stiffness matrix components of the equivalent ply:

$$\begin{bmatrix} Q_{11}^{BB} \\ Q_{22}^{BB} \\ Q_{12}^{BB} \\ Q_{66}^{BB} \end{bmatrix} = \begin{bmatrix} c^4 & s^4 & 2s^2c^2 & 4s^2c^2 \\ s^4 & c^4 & 2s^2c^2 & 4s^2c^2 \\ s^2c^2 & s^2c^2 & s^4 + c^4 & -4s^2c^2 \\ s^2c^2 & s^2c^2 & -2s^2c^2 & s^4 + c^4 - 2c^2s^2 \end{bmatrix} \cdot \begin{bmatrix} Q_{11}^{eq} \\ Q_{22}^{eq} \\ Q_{12}^{eq} \\ Q_{66}^{eq} \end{bmatrix} \quad (7.14)$$

However, for  $\theta = 45^\circ$  the equation system given in Eq. 7.14 is singular, and an additional constraint needs to be introduced. In this thesis, the ratio of longitudinal and transverse stiffness  $Z$  extracted from the BB30 was used:

$$\left( \frac{E_{11}^{eq}}{E_{22}^{eq}} \right)_{\theta=45^\circ} = \left( \frac{Q_{11}^{eq}}{Q_{22}^{eq}} \right)_{\theta=45^\circ} = Z = \left( \frac{E_{11}^{eq}}{E_{22}^{eq}} \right)_{\theta=30^\circ} \quad (7.15)$$

Eq. 7.15 reduces the system of four equations given in Eq. 7.14 to a three equation system that can be uniquely solved. The elastic constants of the equivalent ply are calculated from the compliance matrix, obtained by inversion:

$$\mathbf{S}^{eq} = (\mathbf{Q}^{eq})^{-1} \quad (7.16)$$

$$E_{11}^{eq} = \frac{1}{S_{11}^{eq}} \quad E_{22}^{eq} = \frac{1}{S_{22}^{eq}} \quad G_{12}^{eq} = \frac{1}{S_{66}^{eq}} \quad \nu_{12}^{eq} = -\frac{S_{11}^{eq}}{S_{22}^{eq}} \quad (7.17)$$

With the equivalent elastic constants assigned to the APA equivalent laminate, the in-plane elastic response of the APA is identical to the one obtained with SPA. The equations have been implemented into a MATLAB function (*InverseCLT\_BB.m*, cf. Appendix E.2), the elastic constants of the equivalent yarn plies calculated for BB30 and BB45 are given in Table 7.2.

**Table 7.2.:** Elastic constants of the equivalent yarn plies calculated by inverse CLT

	$E_{11}^{eq}$ [MPa]	$E_{22}^{eq}$ [MPa]	$G_{12}^{eq}$ [MPa]	$\nu_{12}^{eq}$ [-]
BB30	126006	6887	4522	0.221
BB45	121144	7629	4063	0.323

### Strength properties

The strength properties for the APA model, when obtained from unit cell modeling results, are connected to the failure criterion used, and cannot be determined analytically like shown for the elastic constants. Thus, the calculation of the equivalent yarn ply strength will be based on an iterative correlation of the APA model to distinct unit cell load cases, cf. Fig. 7.2.

The off-axis experiment showed that the failure modes change with the off-axis angle applied, thus the equivalent ply strength parameters are calculated by application of appropriate load cases. Basically, any multi-axial load case may be chosen for the calibrations, as arbitrary loads can be introduced into both, BBM unit cell and APA model. However, the choice of load cases was restricted to off-axis loading, as this offers the advantage that off-axis coupon experiments could be used instead for the calibration. In both cases, the input for the calibration are the tensile or compressive strength of the braided composite at five off-axis angles:

$$\sigma_{OA\psi}^{UTS/UCS}, \psi = \psi_i \quad i = 1 \dots 5$$

Which yields the five strength parameters required in the failure criteria. For each load case, the failure stress is extracted from the BBM simulation and the APA laminate model is loaded with the unit cell failure load and the strength is adjusted, for the APA model predicting the same macroscopic failure stress.

By applying this procedure, the fluctuations in the stress field of the unit cell model are considered within the material parameters used in the APA model. To ensure that the method is valid, identical failure modes have to be predicted by APA and the unit cell.

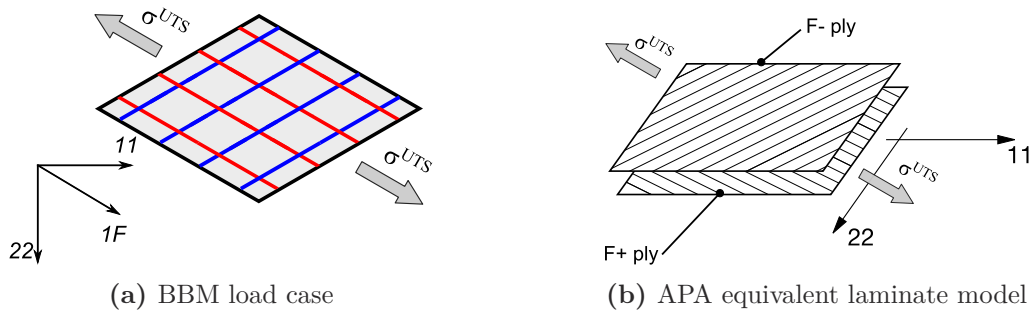


**Fig. 7.2:** BBM unit cell and APA equivalent laminate model load case

The load cases chosen for the calibration depend on the yarn architecture and the braiding angle. The longitudinal tensile and compressive strength of the equivalent ply can be obtained for the loading applied in the yarn direction ( $\psi = \theta$ ). For the transverse strength of the equivalent ply, the choice of load cases is more difficult: as the equations of the Puck 2D criterion for transverse failure modes A and C include both, transverse and shear strength parameters, no independent solution for the yarn ply strength can be obtained. Thus, an iterative procedure, including all load cases with transverse yarn failure, was used to fit the equivalent yarn ply transverse strength parameters. The choice of load cases for the BB30 was based on the stress state in the yarns and the failure modes in the unit cell simulations: OA90 in tension and compression was chosen for the calibration of  $Y_T^{eq}$  and  $Y_C^{eq}$  and the in-plane shear strength  $S_L^{eq}$  was calibrated under OA00 tensile loading. For the BB45, the in-plane shear strength  $S_L^{eq}$  of the equivalent ply was also obtained from tensile loading in take-up direction (OA00). However, it was found that the transverse strength parameters have only minor effects on the failure behavior of the BB45 over the complete range of off-axis angles. This is in accordance with the results of Fouinneteau [12], who found transverse failure of  $1 \times 1$  biaxial braided composites to be negligible. Thus, the transverse yarn ply strength was for the BB45 alternatively calibrated from the transverse yarn failure under PT\_OA45 loading. The macroscopic stress value, where transverse yarn failure was present in the BB45\_PT\_OA45 simulation, was used for the calibration. As no preliminary transverse failure under compression in 1F-direction was present in the BBM unit cell simulations, the value  $Y_C^{eq}$  was taken from the yarn material parameters given in Table 6.7.

The calibration of the APA was done for both, maximum stress and Puck 2D criterion, with the results for BB30 and BB45 summarized in Table 7.3. The strength values given can be interpreted as *in-situ* values (as described by Schultz and Garnich [57]) for the undulated yarns in a braided composite. The influence of the yarn architecture is e.g. present for the longitudinal direction, where the strength parameters are reduced by 30%-40% compared to the yarn strength parameters in the BBM.

**Table 7.3.:** Calculated strength values and load cases used for strength correlation

BB30 calibration					
	$X_T^{eq}$ [MPa]	$X_C^{eq}$ [MPa]	$Y_T^{eq}$ [MPa]	$Y_C^{eq}$ [MPa]	$S_L^{eq}$ [MPa]
	PT_OA30	PC_OA30	PT_OA90	PC_OA90	PT_OA00
Puck 2D	1487.8	1126.5	50.1	102.5	90.2
Max stress	1487.8	1126.5	41.8	79.6	103.4
BB45 calibration					
	$X_T^{eq}$ [MPa]	$X_C^{eq}$ [MPa]	$Y_T^{eq}$ [MPa]	$Y_C^{eq}$ [MPa]	$S_L^{eq}$ [MPa]
	PT_OA45	PC_OA45	PT_OA45 <sup>1</sup>	- <sup>2</sup>	PT_OA00
Puck 2D	1343.1	1035.3	70.3	174.0 <sup>2</sup>	85.1
Max stress	1343.1	1035.3	70.3	174.0 <sup>2</sup>	79.1

<sup>1</sup>: calibrated from transverse failure in the F+ yarn direction

<sup>2</sup>: not calibrated

### 7.3. Analytical failure prediction with APA and SPA

The in-plane stress failure envelopes predicted using the APA and SPA model are shown for the BB30 and BB45 braided composites in Fig. 7.3 and Fig. 7.4. The axes of the failure envelopes represent the stress components in the material coordinate system. For the APA, the failure envelopes were calculated by evaluating the Puck 2D failure criteria in both yarn plies, with the most critical value of the two plies used to calculate the failure stress. Thus, the earliest failure predicted was used to construct the failure envelopes. In addition to the failure envelopes, the results from the off-axis experiments are given in the plots.

For the SPA, the failure envelopes is cuboid-shaped, regardless of the braiding angle. The difference between SPA failure envelopes at different braiding angles is given by the dimensions, defined by the input values of strength in the material axes. The BB45 envelope is quadratic in the  $\sigma_{11}$ - $\sigma_{22}$  plane as, take-up and transverse direction strength are equal. The highest strength value yields for both braiding angles in shear: with the fibers oriented off-axis ( $\pm\theta$ ), shearing mainly introduces stresses in the longitudinal direction of the fibers, resulting in a high shear stiffness and strength of the braided composites.

The APA failure envelopes differ significantly from the SPA envelopes. The orientation and shape of the of the failure is influenced by the braiding angle: for BB45 the orientation of the failure envelope is  $45^\circ$ , while the orientation of the envelope is shifted more towards the  $\sigma_{11}$ -axis for the BB30. This is due to the yarn ply stresses  $\sigma_{F+}/\sigma_{F-}$  being used for the prediction of failure, inherently including the braiding angle. Thus, e.g. a biaxial  $\sigma_{11}$ - $\sigma_{22}$  stress state for the BB45, equivalent to longitudinal tension in both yarn directions yields a higher failure stress value as uniaxial  $\sigma_{11}$  tension, where the yarns are mainly stresses in shear. In addition, for both braiding angles, the failure stress at a combined  $\sigma_{11}$ - $\sigma_{22}$  stress state decreases with a shear stress introduced: A shear stress  $\tau_{12}$  introduces additional

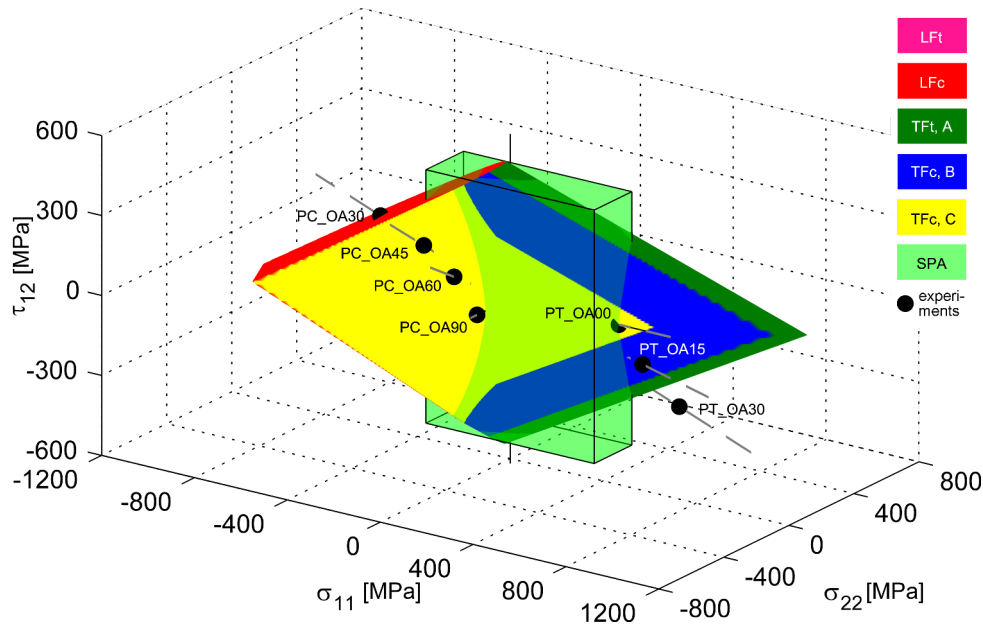


Fig. 7.3: Comparison of 3D failure envelopes from SPA and APA for BB30

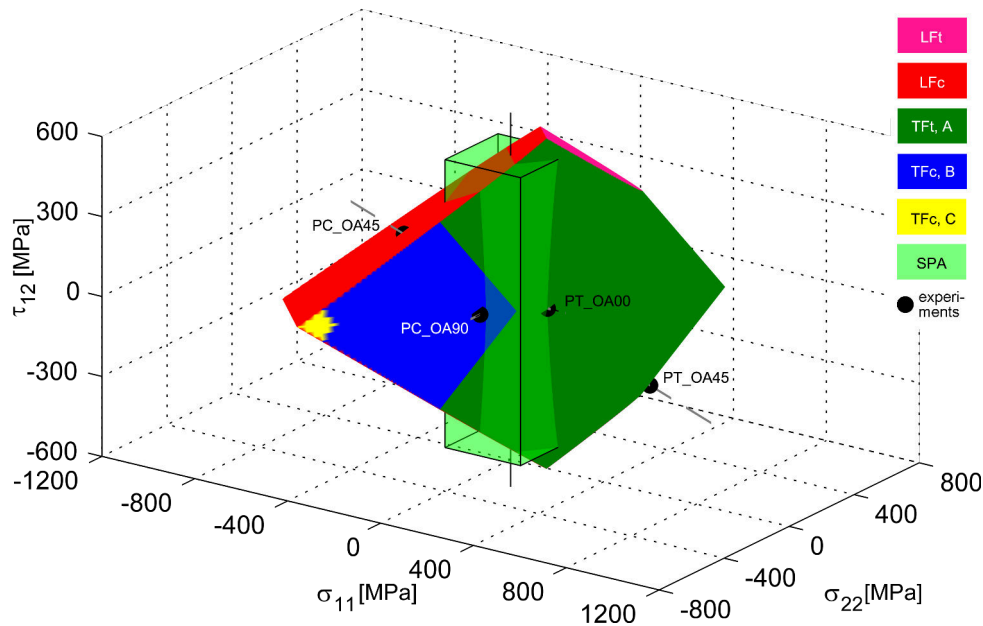


Fig. 7.4: Comparison of 3D failure envelopes from SPA and APA for BB45

stresses in the yarns, which mainly affects the load cases, where stresses are introduced in the yarn direction. The failure modes predicted by the APA method are mainly yarn transverse failure modes, which is in accordance with the off-axis experiments.

A comparison of the APA and SPA predictions to the off-axis experiments is given as a  $\sigma_{11}$ - $\sigma_{22}$  cut of the failure envelopes in Fig. 7.5. The failure stresses from the off-axis experiment results are projected to the plane. It is important to note that all off-axis experiments except OA00 and OA90 have a non-zero shear stress component, thus the 2D comparison can only yield qualitative results: e.g. BB30\_PC\_OA30 and BB45\_PC\_OA45,

lying on the 3D failure envelopes (cf. Fig. 7.3 and Fig. 7.4) are projected inside the failure envelope for the 2D representation. However, the off-axis experiments confirm the shape of the APA failure envelope. The off-axis load cases in yarn direction show that the orientation of the failure envelopes is captured accurately by the APA approach. In opposite, the SPA approach does not consider the braiding angle and thus strongly underestimate the failure stresses for load cases in yarn direction. In addition, for the tension/compression quadrants, the SPA is non-conservative and predicts higher failure stresses as the APA approach. A combination of tension and compression in the material coordinate system results in high shear stresses in the yarns, and thus the SPA predictions are not considered realistic. However, as tension-compression stress states cannot be achieved by off-axis testing, this needs additional experimental verification.

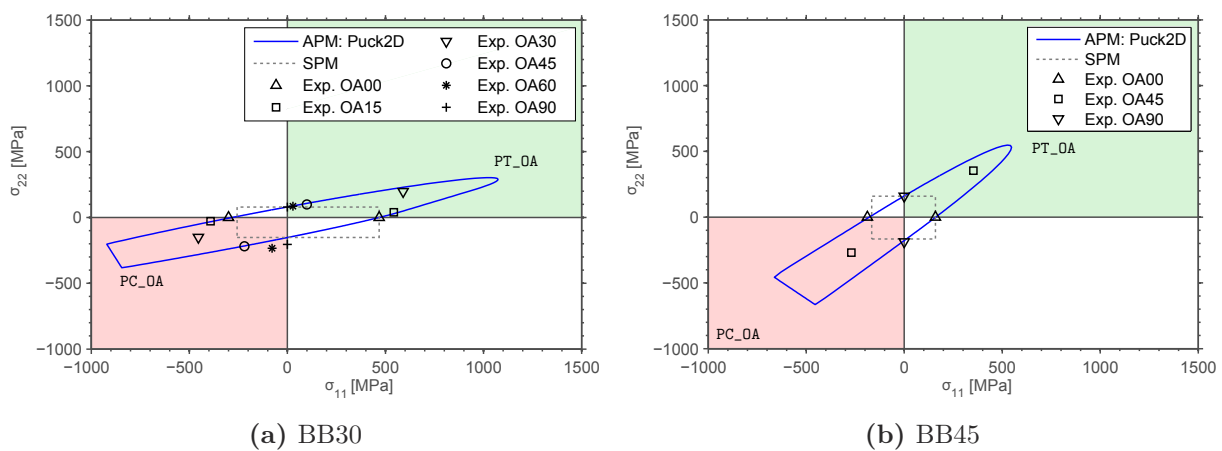
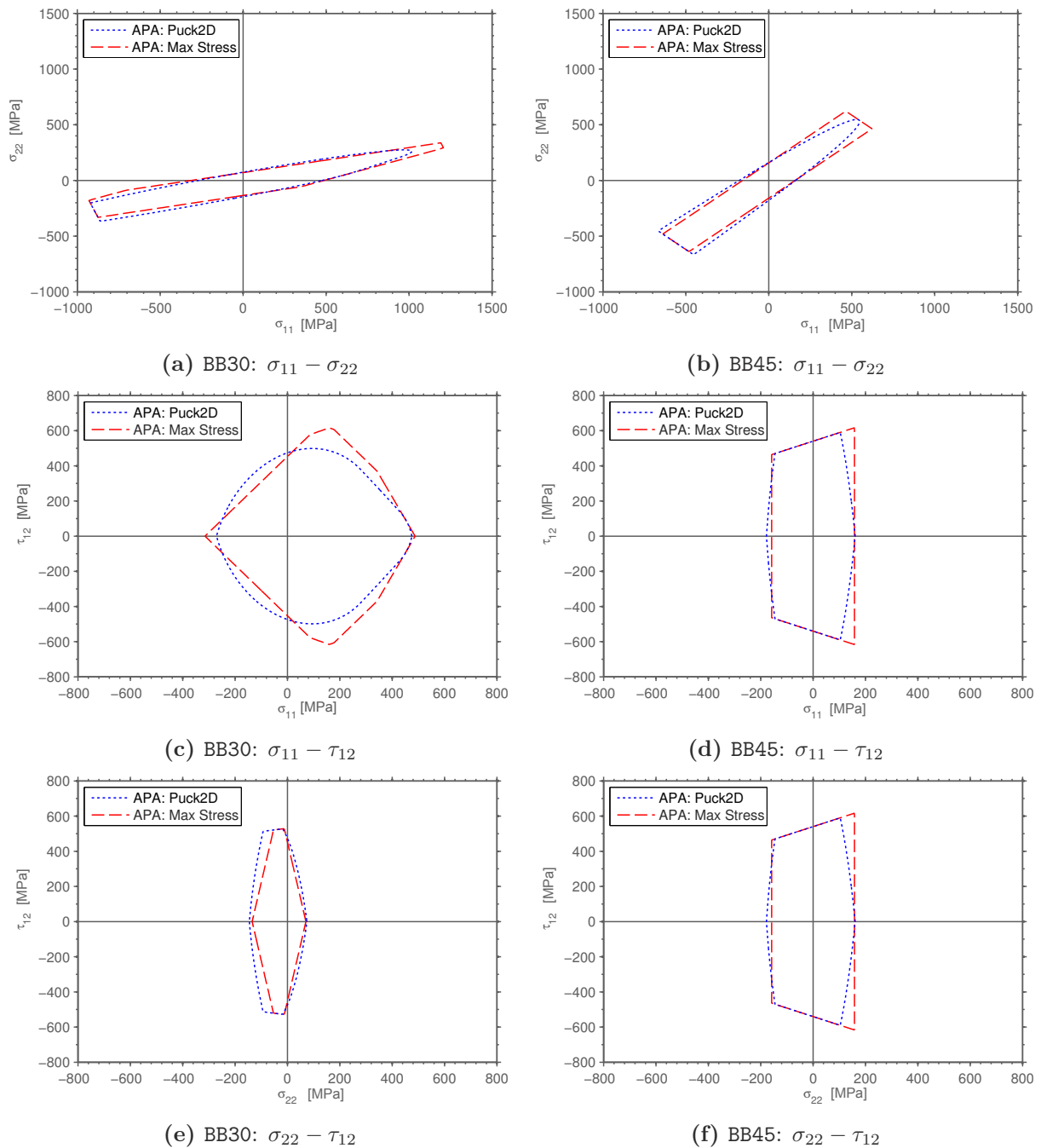


Fig. 7.5:  $\sigma_{11}$ - $\sigma_{22}$  failure envelopes for BB30 and BB45 braided composites

Concluding the comparison, the APA approach yields more realistic results for braided composites. The SPA approach, giving accurate results for woven fabrics, where the maximum strength is present along the material axes, fails to consider the influence of the braiding angle on the failure envelope. In opposite, the highest failure stresses being present in the yarn direction is captured well by the APA, as the yarn ply stresses are used for the failure prediction. Based on the results of the comparison, the APA was used for the failure predictions presented further.

## 7.4. Comparison of failure criteria for APA

In the APA, the biaxial braided composites are modeled as equivalent yarn plies, which enables either application of rather simple criteria like maximum stress or phenomenological criteria like Puck 2D, originally developed for UD plies. To investigate the influence of the failure criterion used, Puck 2D and maximum stress failure criteria are compared for the BB30 and BB45 braided composites. The strength parameters for both criteria are given in Table 7.3. The 2D failure envelopes in the planes, given by the in-plane stress components, are shown in Fig. 7.6. In general, the predictions from the two criteria, are very similar, but some differences can be observed from the comparison.



**Fig. 7.6:** BB30 and BB45 failure envelopes with different criteria

The  $\sigma_{11}$ - $\sigma_{22}$  failure envelopes (Fig. 7.6a and 7.6b) show that none of the two criteria is in general more conservative. This is mainly due to the maximum stress criterion not considering stress interaction, which is covered by the Puck criterion: for transverse tension in the yarn plies ( $\sigma_{2F+}/2F- > 0$ ) the bearable shear stress is reduced (Puck mode A), while a shear stress higher than the uniaxial shear strength can be carried for moderate transverse compressive stresses (Puck mode B). Including the transverse stress interaction, also has an effect for the BB45 in uniaxial tension/compression in the 11-



direction (cf. Fig. 7.6d): the maximum stress criterion predicts shear failure of the yarn plies, with identical failure stresses in tension and compression. For the Puck criterion, different failure modes (mode A in tension, mode B in compression) are predicted, leading to an increased failure stress in compression, also observed in the coupon experiments (cf. Table A.5).

For the regions, where Puck and maximum stress criterion are identical, e.g. the straight part of the failure envelope in Fig. 7.6c and Fig. 7.6d, fiber failure is present, which is predicted by the maximum stress criterion in both cases.

In addition, some deviations between the failure envelopes are due to the different yarn ply strength values obtained for the two criteria in the calibration (cf. Table 7.3): for uniaxial compression in the 11-direction of the BB30, the Puck criterion predicts higher failure stresses (cf. Fig. 7.6c), which is due to the yarn ply transverse tension strength ( $Y_T^{eq}$ ) obtained in the calibration.

The comparison of different failure criteria within the APA approach shows, that the failure envelopes predicted by the maximum stress criterion do not differ significantly to the ones predicted by the Puck 2D criterion. Thus, the major effect to the failure envelope is given by the braiding angle, used in the calculation of the stresses  $\sigma_{F+/F-}$ . However, the Puck criterion is beneficial for shear-dominated load cases, where the influence of the transverse stress is considered by the different failure modes of the Puck criterion, while the failure stress is predicted identically in tension and compression by the maximum stress criterion.

## 7.5. APA application to test cases

The APA failure predictions are compared to the off-axis experiments in the off-axis failure envelopes given in Fig. 7.7 and Fig. 7.8. In the off-axis failure envelopes, the theoretical failure stresses for all failure modes (longitudinal failure  $LF$ , transverse failure  $TF$ , shear failure  $SF$ ) of the two yarn plies  $F+$  and  $F-$  are given. The lowest failure stress value yields the critical failure mode.

The results from maximum stress and Puck 2D criterion for the BB30 braided composite are shown in Fig. 7.7. For the Puck criterion, the predictions in tension and compression (Fig. 7.7a and Fig. 7.7b) correlate well with the experimental results. In tension, the failure stresses for  $\psi = 15^\circ$  and  $30^\circ$  underestimate the experimental results: for  $\psi = 15^\circ$ , the failure load is predicted is 12% lower and the failure mode predicted is transverse yarn failure instead of fiber failure observed in the experiments. The deviation is believed to be due to the linear prediction, which does not consider stress-redistribution by plastic deformation of the yarns under shear. For tension in the yarn direction ( $\psi = 30^\circ$ ), transverse failure of the  $F+$  yarn direction is predicted in advance of the yarn rupture in the  $F-$  direction. For compression, the predictions agree well with the experimental results for  $\psi = 0^\circ$ - $45^\circ$ , while the failure stresses are underestimated for  $\psi = 60^\circ$ - $90^\circ$ . This deviation is attributed to the calibration using the BBM modeling results, which also underestimated the strength for these off-axis angles.

The maximum stress criterion predictions in tension (Fig. 7.7c) also agree well with the off-axis experiments. For compression, the predictions made with the maximum stress criterion are slightly less accurate: the failure stress for the take-up direction ( $\psi = 0^\circ$ ) is

overestimated, while the strength values for the higher off-axis angles ( $\psi = 45^\circ$ - $90^\circ$ ) are underestimated.

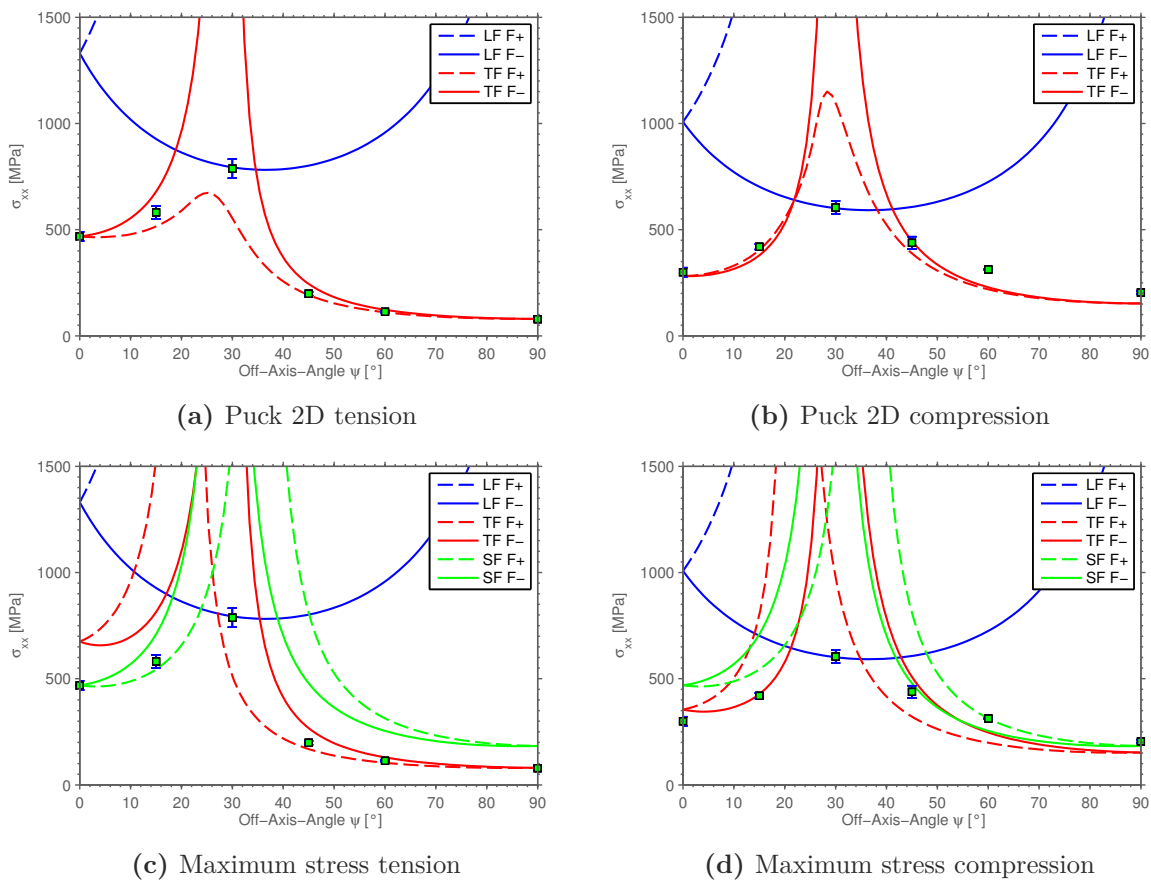
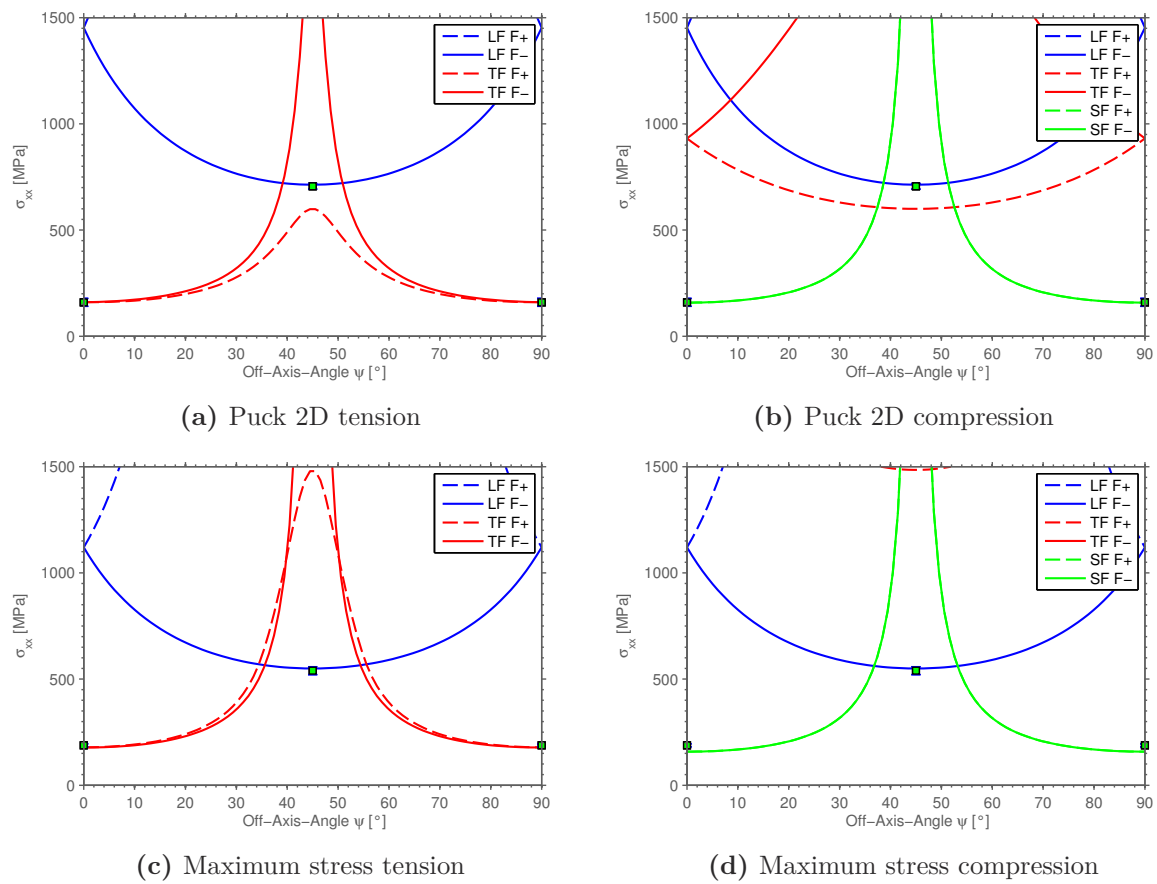


Fig. 7.7: BB30 off-axis failure envelopes

The predictions for the BB45 braided composite are compared in Fig. 7.8. Both failure criteria agree well with the experimental values. For tension in the yarn direction ( $\Psi = 45^\circ$ ), the first failure predicted is for both criteria the transverse failure of the F+ yarns (cf. Fig. 7.8a and Fig. 7.8b). For the BB45, the preliminary F+ yarn failure was also observed in the experiments, however, the predicted stress for transverse failure is, as for the BBM model, slightly overestimated. For compression, the failure stress in take-up ( $\psi = 0^\circ$ ) direction is slightly underpredicted from the maximum stress criterion (Fig. 7.8d). This is, as for the higher off-axis angles of the BB30, due to the maximum stress criterion neglecting interaction of transverse and shear stresses. In opposite, the Puck 2D prediction meets the experimental result.

### 7.5.1. Discussion and conclusion of linear predictions

Concluding the comparison of failure predictions from maximum stress and Puck 2D criteria to the experiments, both criteria yielded reasonable results. The deviations observed for the Puck 2D criterion are mainly due to the fact that the linear analysis does not consider the non-linear material behavior of the yarn plies. In addition, due to the



**Fig. 7.8:** BB45 off-axis failure envelopes

fact that the APA stiffness and strength parameters were calibrated to the BBM simulations, the deviations observed for the compressive failure stresses under high off-axis angles, observed for the BBM, were also present for the APA predictions. The maximum stress criterion predictions were less accurate in comparison to the experiments. Thus, interaction of transverse stresses and different transverse failure modes in tension and compression, which is both considered by the Puck criterion, is believed to be crucial for modeling failure of braided composites.

A drawback from the linear predictions was present for the tension applied in the yarn direction ( $\psi = \theta$ ): the first failure predicted for both braided composites was transverse failure of the yarns, which meets the experimental observations for BB45, but was not observed in the BB30 experiments. In both cases, the linear predictions failed to give the information, if a load increase is possible after the first failure. For structural simulation, the first failure predicted needs to be considered critical, which is appropriate for most off-axis cases considered, but underestimates the failure stress when yarn longitudinal tensile stresses dominate. In addition, the analytical model lacks to consider the influence of non-linear deformation in the yarn plies, which can have an influence on both, failure strain and failure mode predicted.

## 7.6. Nonlinear constitutive law

To overcome the limitations reported in the previous section, a nonlinear constitutive model (BB\_APA\_NL) has been developed and implemented into the commercial finite element code Abaqus/Explicit. The main idea of the constitutive model was based on the APA: both equivalent yarn plies of the biaxial braided composite are represented in a single shell element integration point, employing UD constitutive laws for the equivalent yarn plies. An overview to the implemented constitutive law is given in Fig. 7.9: the constitutive model includes two levels, the yarn ply and the biaxial braided (BB) ply level. The material properties, required for the BB\_APA\_NL are, similar to the analytical APA, defined for the yarn plies (Table 7.1) and assembled to yield the BB properties. The braiding angle is updated in each iteration by using the strains of the integration point. With the updated braiding angle, the strain increment is transformed into the yarn ply coordinate system of F+ and F- yarn ply, with plasticity and damage laws being evaluated in both yarn plies (red box in Fig. 7.9). The plastic strain increment is calculated, updating the elastic strain, which is furthermore used to calculate the damaged stiffness matrix of both yarn plies. The two stiffness matrices are then re-assembled to the BB stiffness matrix and with the elastic strain of the BB ply known, the nominal stresses can be calculated and returned to the FE solver.

### 7.6.1. Input properties

The input properties for the BB\_APA\_NL are similar to the ones required for the analytical APA given in Table 7.1. In addition, the yield stress and hardening curve of the equivalent yarn ply under in-plane shear needs to be defined. The hardening parameters required are obtained by least-squares regression of the UD ( $\pm 45^\circ$ ) experimental data given in Fig. 6.10. In addition, the fracture toughness of the equivalent yarn plies for the failure modes considered, namely longitudinal tensile, longitudinal compressive, transverse tensile and transverse compressive, have to be given. As no experimental data for the fiber/matrix combination used was available, the material properties were taken from [141]. The additional input parameters required are summarized in Table 7.4.

**Table 7.4.:** Additional material parameters required for BB\_APA\_NL

fracture toughness				hardening parameters		
$G^{Lt}$	$G^{Lc}$	$G^{Tt}$	$G^{Tc}$	$K$	$m$	$\tau_{12F}^{y,0}$
N/mm	N/mm	N/mm	N/mm	N/mm <sup>2</sup>	-	N/mm <sup>2</sup>
89.8	78.3	0.2	0.8	188.9	3.28	13.71

### 7.6.2. Braiding angle update

The strain increment is passed to the VUMAT in the  $12$  coordinate system and has to be transformed in the yarn ply coordinate system by using the braiding angle. As the fiber

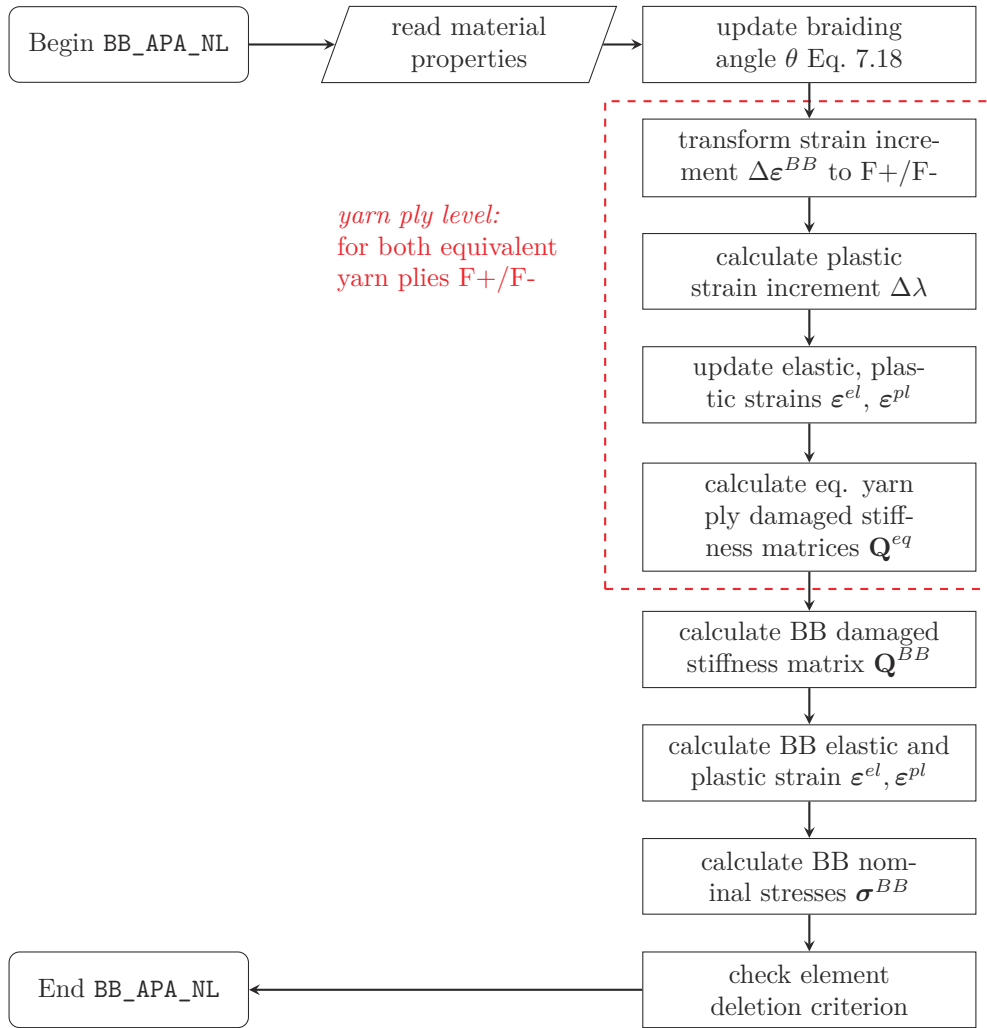


Fig. 7.9: Flowchart for VUMAT BB\_APA\_NL

orientation changes during deformation, the braiding angle is updated by using the axial and transverse strain in the  $12$  coordinate system, as given by [12]:

$$\theta = \tan^{-1} \left( \tan(\theta^0) \cdot \frac{1 + \varepsilon_{22}}{1 + \varepsilon_{11}} \right) \quad (7.18)$$

Considering braiding angle change can be deactivated in the BB\_APA\_NL.

### 7.6.3. Strain increment transformation

The strain and strain increment are provided to the material subroutine in the material  $(12)$  coordinate system. As both yarn directions can be believed to be strained identically, the strain and strain increment in the yarn plies can be obtained by coordinate transformation:

$$\begin{aligned} \Delta \varepsilon_{F+} &= \mathbf{R} \mathbf{T}(\theta) \mathbf{R}^{-1} \Delta \varepsilon_{BB} \\ \Delta \varepsilon_{F-} &= \mathbf{R} \mathbf{T}(-\theta) \mathbf{R}^{-1} \Delta \varepsilon_{BB} \end{aligned} \quad (7.19)$$

With  $\Delta\boldsymbol{\varepsilon}_{F+/F-}$  and  $\Delta\boldsymbol{\varepsilon}_{BB}$  being the strain increment in the yarn ply F+/F- and the braid coordinate system, respectively (cf. Fig. 7.1). The transformation matrix  $\mathbf{T}$  is given in Eq. D.9. The BB\_APA\_NL internally uses the engineering shear strain, thus the Reuter matrix  $\mathbf{R}$  is used within the transformation.

#### 7.6.4. Plasticity model

For the BB\_APA\_NL, a 1D plasticity law was implemented on the yarn ply level, to account for the plastic deformation observed in the off-axis experiments. Plastic deformation of UD composites is commonly reported in literature [117, 159, 170, 172, 212], with different plasticity criteria proposed. For the yarn plies in the biaxial braided composites, a rather simple approach was chosen, considering plastic deformation solely under in-plane shear, as proposed by Johnson [117] and Fouinneteau [12] for woven and braided fabric composites, respectively. Thus, the yarn plies are assumed to deform elastic in longitudinal and transverse direction and elastic-plastic under in-plane shear:

$$\varepsilon_{11F}^{pl} = \varepsilon_{22F}^{pl} = 0 \quad \gamma_{12F}^{pl} \neq 0$$

The yield criterion used is:

$$f = |\tau_{12F}| - \tau_{12F}^{y,0} - r(\alpha) = 0 \quad (7.20)$$

Where  $\tau_{12F}^{y,0}$  is the initial in-plane shear yield stress and  $r(\alpha)$  is the isotropic hardening law, defined as a function of the accumulated plastic strain  $\alpha$ . Plastic flow was assumed to be associated and a power-law was used for hardening:

$$r(\alpha) = K \cdot \alpha^{(1/m)} \quad (7.21)$$

The deformation is elastic for  $f < 0$  and plastic deformation occurs for stress states on the yield surface  $f = 0$ . The plastic strain increment is given as

$$d\gamma_{12F}^{pl} = d\lambda \frac{\partial f}{\partial \tau_{12F}} = d\lambda \operatorname{sgn}(\tau_{12F}), \quad (7.22)$$

where  $\operatorname{sgn}$  is the signum function and  $d\lambda \geq 0$  is the plastic multiplier to be determined, which gives the change of the accumulated plastic strain  $d\alpha = d\lambda$ . The accumulated plastic strain  $\alpha$  is calculated by integration of the plastic strain increments:

$$\alpha = \int_0^{\gamma_{12F}^{pl}} \operatorname{sgn}(\tau_{12F}) d\gamma_{12F}^{pl} \quad (7.23)$$

Plastic deformation is considered in the case of an undamaged yarn ply. As soon as one of the yarn ply damage parameters is unequal to zero, the plastic strain stays constant.

#### Numerical implementation

The yield criterion in Eq. 7.20 includes the hardening function  $r(\alpha)$ , yielding a nonlinear equation that needs to be solved in every increment. The equation is solved numerically,

by using an implicit predictor-corrector algorithm: based on an elastic test step, the plastic strain increment is calculated iteratively with a Newton-algorithm. An overview of the numerical implementation is given in Fig. 7.10. For the test step, the strain increment is

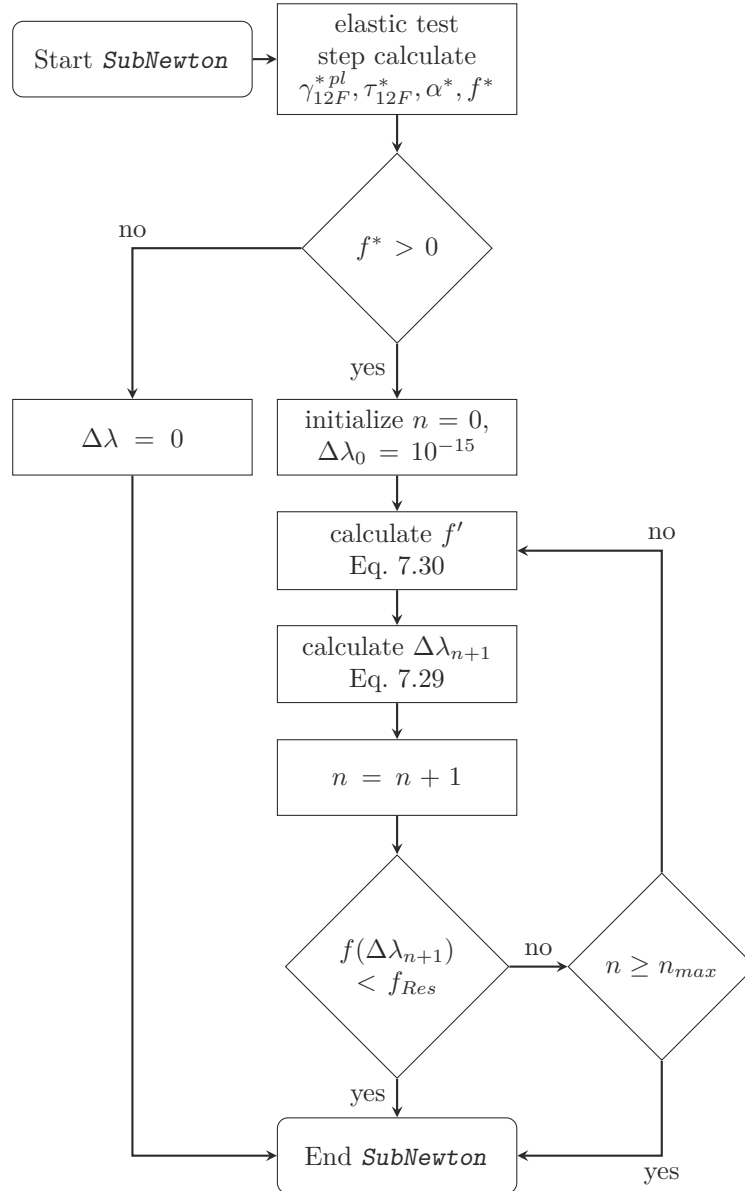


**Fig. 7.10:** Flowchart for integration of constitutive equation

assumed purely elastic:

$$\gamma_{12F}^{*pl(k+1)} = \gamma_{12F}^{pl(k)} \quad (7.24)$$

$$\tau_{12F}^{*(k+1)} = G_{12}^{eq} \cdot (\gamma_{12F}^{(k+1)} - \gamma_{12F}^{p(k)}) \quad (7.25)$$

$$\alpha^{*(k+1)} = \alpha^{(k)} \quad (7.26)$$

With  $(k + 1)$  being the current strain increment to be solved. For the test value of the yield function  $f^* \leq 0$ , the elastic test step is accepted and the plastic strain increment is

set to zero. If  $f^* > 0$ , a plastic corrector is introduced to relax the stress state satisfying  $f^{(k+1)} = 0$ . To calculate the unknown plastic multiplier  $\Delta\lambda$ , the unknown stress in the current increment is written as a function of the test stress and the plastic multiplier:

$$\tau_{12F}^{(k+1)} = \tau_{12F}^{*(k+1)} - \Delta\lambda \cdot G_{12}^{eq} \cdot \frac{\partial f^{(k+1)}}{\partial \sigma} \quad (7.27)$$

Eq. 7.27 is inserted into the plasticity criterion Eq. 7.20, which gives:

$$\begin{aligned} f^{(k+1)}(\Delta\lambda) &= |\tau_{12F}^{*(k+1)}| - \Delta\lambda G_{12}^{eq} - \left( \tau_{12F}^{y,0} + r(\alpha^{(k)} + \Delta\lambda) \right) \\ &= |\tau_{12F}^{*(k+1)}| - \Delta\lambda G_{12}^{eq} - \tau_{12F}^{y,0} - K \cdot (\alpha^{(k)} + \Delta\lambda)^{(1/m)} = 0 \end{aligned} \quad (7.28)$$

Eq. 7.28 is nonlinear equation of  $\Delta\lambda$  and is solved by using a Newton algorithm, given as

$$\Delta\lambda_{n+1} = \Delta\lambda_n - \frac{f(\Delta\lambda_n)}{f'(\Delta\lambda_n)}, \quad (7.29)$$

where  $n$  marks the increment of the newton-algorithm. The derivation  $f'$  of the yield criterion is:

$$f' = \frac{\partial f}{\partial \Delta\lambda} = -G_{12}^{eq} - \frac{K}{m} (\alpha + \Delta\lambda)^{(1/m-1)} \quad (7.30)$$

At the beginning of the constitutive equation integration,  $\Delta\lambda$  needs to be assigned a small value to ensure  $f$  to be differentiable. If the Newton algorithm does not converge after  $n_{max} = 100$  iterations, a warning message is printed and the iteration is stopped. When the Newton iteration converges,  $\Delta\lambda$  is known and stress, plastic strain increment and accumulated plastic strain are updated:

$$\gamma_{12F}^{pl(k+1)} = \gamma_{12F}^{pl(k)} + \Delta\lambda \operatorname{sgn}(\tau_{12F}) \quad (7.31)$$

$$\tau_{12F}^{(k+1)} = G_{12}^{eq} \cdot (\gamma_{12F}^{(k+1)} - \gamma_{12F}^{pl(k+1)}) \quad (7.32)$$

$$\alpha^{(k+1)} = \alpha^{(k)} + \Delta\lambda \quad (7.33)$$

### Elastic and plastic yarn ply strain

With the plastic strain increment in the yarn plies known, the elastic and plastic strains can be updated:

$$\boldsymbol{\varepsilon}_N = \boldsymbol{\varepsilon}_N^{old} + \Delta\boldsymbol{\varepsilon}_N \quad (7.34)$$

$$\boldsymbol{\varepsilon}_N^{el} = \boldsymbol{\varepsilon}_N - \boldsymbol{\varepsilon}_N^{pl} = \boldsymbol{\varepsilon}_N - \begin{bmatrix} 0 \\ 0 \\ \gamma_{12N}^{pl} \end{bmatrix} \quad (7.35)$$

With  $N \in F+, F-$  and  $\boldsymbol{\varepsilon}, \boldsymbol{\varepsilon}^{el}, \boldsymbol{\varepsilon}^{pl}$  being the total, elastic and plastic strain, respectively.



### 7.6.5. Damage model

The damage model in the yarn plies is based on the anisotropic damage model for UD composites published by Lapczyk and Hurtado [165]. The damage evolution is defined with the use of fracture energies, removing the mesh-dependency in the softening regime. For the BB\_APA\_NL, the damage model was adapted to use the Puck 2D criterion for damage initiation. Three damage variables for yarn longitudinal, transverse and shear failure are introduced. The damaged stiffness matrix, as given by [165], yields:

$$\mathbf{Q}^{eq} = \frac{1}{D} \begin{bmatrix} (1 - d_L)E_{11}^{eq} & (1 - d_L)(1 - d_T)\nu_{21}E_{11}^{eq} & 0 \\ (1 - d_L)(1 - d_T)\nu_{12}E_{22}^{eq} & (1 - d_T)E_{22}^{eq} & 0 \\ 0 & 0 & D(1 - d_S)G_{12}^{eq} \end{bmatrix}, \quad (7.36)$$

with

$$D = 1 - (1 - d_L)(1 - d_T)\nu_{12}\nu_{21}$$

and  $d_L$ ,  $d_T$ ,  $d_S$  being the internal damage variables introduced for yarn longitudinal, transverse and shear damage. The damage variables are zero in the undamaged state and grow until 1, which is equivalent to full damage. The damage variables used in the stiffness matrix have different values for tension and compression, which are assigned based on the sign of the according normal stress:

$$d_L = d_{Lt} \frac{\{\sigma_{11F}\}}{|\sigma_{11F}|} + d_{Lc} \frac{\{-\sigma_{11F}\}}{|\sigma_{11F}|} \quad (7.37)$$

$$d_T = d_{Tt} \frac{\{\sigma_{22F}\}}{|\sigma_{22F}|} + d_{Tc} \frac{\{-\sigma_{22F}\}}{|\sigma_{22F}|} \quad (7.38)$$

With the Macauley bracket operator  $\{x\} = \frac{x+|x|}{2}$ . The damage variable for shear failure is calculated as a linear combination of the yarn longitudinal and transverse damage variable:

$$d_S = 1 - (1 - d_{Lt})(1 - d_{Lc})(1 - d_{Tt})(1 - d_{Tc}) \quad (7.39)$$

The damage initiation criterion is evaluated by using effective quantities, basing on the idea of Lemaitre [163]. With the elastic yarn ply strain updated, the effective stress vector of the yarn plies can be calculated by using the yarn plies' undamaged stiffness matrix:

$$\tilde{\boldsymbol{\sigma}}_{F+/F-} = \mathbf{Q}^{eq,0} \boldsymbol{\varepsilon}_{F+/F-}^{el} \quad (7.40)$$

The undamaged stiffness matrix is obtained from Eq. 7.36, with  $d_L = d_T = d_S = 0$ . The effective stress values are used to calculate the stress exposures from the maximum stress criterion given in Eq. 7.5 for longitudinal failure and the Puck 2D criterion given in Eq. 6.35-Eq. 6.37 for transverse failure. Four damage initiation values for yarn longitudinal (L) and transverse (T) failure in tension (t) and compression (c) are used:  $f_{E,Lt}$ ,  $f_{E,Lc}$ ,  $f_{E,Tt}$ ,  $f_{E,Tc}$ . If one of the stress exposure values exceeds one, the corresponding damage variable is calculated.

The damage variables calculation is based on the publication of Lapczyk and Hurtado [165], with the equations adapted to the Puck initiation criterion used. Equiva-

lent values of stresses and strains are used, removing the mesh-dependency for damage-progression. The damage variables for the different failure modes are given by:

$$d_I = \frac{\delta_{I,eq}^f (\delta_{I,eq} - \delta_{I,eq}^0)}{\delta_{I,eq} (\delta_{I,eq}^f - \delta_{I,eq}^0)} \quad (7.41)$$

with  $I \in Lt, Lc, Tt, Tc$ .  $\delta_{I,eq}$  is the equivalent displacement of the failure modes, with the superscripts 0 and  $f$  for the equivalent displacements at damage initiation and fully damaged state ( $d_I = 1$ ), respectively. The equivalent displacement at failure is calculated from:

$$\delta_{I,eq}^f = \frac{2G^I}{\sigma_{I,eq}^0} \quad (7.42)$$

Where  $G^I$  is the fracture toughness of the active mode. The values of the failure mode damage variables are defined monotonically increasing ( $\dot{d}_I \geq 0$ ). The equivalent displacements for the different failure modes are given in Table 7.5, where  $L_c$  is the equivalent element length, given from Abaqus/Explicit [76].

**Table 7.5.:** Equivalent displacements and stresses used for damage variable calculation

mode	$\delta_{I,eq}$	$\sigma_{I,eq}$
long. tensile ( $\tilde{\sigma}_{11} \geq 0$ )	$L_c \{\varepsilon_{11}\}$	$\frac{L_c \{\tilde{\sigma}_{11}\} \{\varepsilon_{11}\}}{\delta_{eq}^{ft}}$
long. compression ( $\tilde{\sigma}_{11} \leq 0$ )	$L_c \{-\varepsilon_{11}\}$	$\frac{L_c \{-\tilde{\sigma}_{11}\} \{-\varepsilon_{11}\}}{\delta_{eq}^{fc}}$
trans. tensile ( $\tilde{\sigma}_{22} \geq 0$ )	$L_c \sqrt{\{\varepsilon_{22}\}^2 + \gamma_{12}^2}$	$\frac{L_c \{\tilde{\sigma}_{22}\} \{\varepsilon_{22}\} + \tilde{\tau}_{12} \gamma_{12}}{\delta_{eq}^{mt}}$
trans. compression ( $\tilde{\sigma}_{22} \leq 0$ )	$L_c \sqrt{\{-\varepsilon_{22}\}^2 + \gamma_{12}^2}$	$\frac{L_c \{-\tilde{\sigma}_{22}\} \{-\varepsilon_{22}\} + \tilde{\tau}_{12} \gamma_{12}}{\delta_{eq}^{mc}}$

$\{x\}$  refers to the Macauley bracket operator  $\{x\} = \frac{x+|x|}{2}$

### 7.6.6. Stress calculation

The nominal stress of the BB ply is calculated from the elastic strain and BB damaged stiffness matrix. Therefore, the damaged stiffness matrices of the equivalent yarn plies are transformed to the BB coordinate system with

$$\bar{\mathbf{Q}}^{\pm\theta} = \mathbf{T}(\pm\theta)^{-1} \mathbf{Q}^{eq} \mathbf{T}(\pm\theta)^{-T}. \quad (7.43)$$

The BB stiffness matrix  $\mathbf{Q}^{BB}$  is then obtained from the yarn ply stiffness matrices  $\bar{\mathbf{Q}}^{\pm\theta}$  according to Eq. 7.9. The elastic strain of the BB ply is obtained by averaging the transformed elastic strains from the yarn plies:

$$\varepsilon_{BB}^{el} = \frac{1}{2} \cdot \left( (\mathbf{R} \mathbf{T}(\theta) \mathbf{R}^{-1} \varepsilon_{F+}^{el}) + (\mathbf{R} \mathbf{T}(-\theta) \mathbf{R}^{-1} \varepsilon_{F-}^{el}) \right) \quad (7.44)$$

The nominal stress of the BB ply is finally calculated from

$$\sigma_{BB} = \mathbf{Q}^{BB} \varepsilon_{BB}^{el}. \quad (7.45)$$

### 7.6.7. Material point deletion

A criterion for material point deletion is defined, setting all stress components of the material point to zero. For the BB\_APA\_NL subroutine, two different criteria for material point deletion are used. The material point is deleted, if either both yarn directions fail in transverse failure (cf. e.g. BB30\_PT\_OA90 experiments Fig. 4.25), or if one of the yarn directions fails in longitudinal direction (cf. e.g. BB30\_PT\_OA30 experiments Fig. 4.19).

### 7.6.8. Implementation

The constitutive law was implemented as a Fortran *VUMAT* material user subroutine inside the commercial FE code Abaqus/Explicit. An overview about the user-defined input properties for the subroutine are given in Appendix E.4.

## 7.7. BB\_APA\_NL model validation

The BB\_APA\_NL model is validated by comparison to the off-axis experiments. The predictions are obtained from single shell (S4R) element simulations in Abaqus/Explicit. For the off-axis load cases, a shear deformation is introduced under the uniaxial stress applied, thus, the boundary conditions of the simulations, shown in Fig. 7.11, were set to not constraint shear deformation of the element. Furthermore, two equations were introduced,

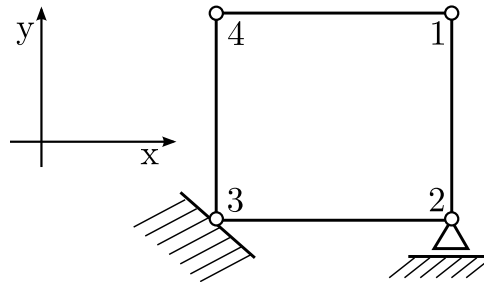


Fig. 7.11: Boundary conditions for single element simulations

ensuring unconstrained transverse and shear deformation:

$$u_x^{N4} - u_x^{N1} = u_x^{N2} \quad (7.46)$$

$$u_y^{N4} - u_y^{N1} = 0 \quad (7.47)$$

The off-axis loads were introduced into the element by applying forces to node 1 and node 2 and rotating the material coordinate system by the off-axis angle. The simulations have been conducted without consideration of finite yarn rotations, as the unit cell calculations and the material parameter calibration did not consider this effect. The elastic, strength and nonlinear material parameters used within the simulations are given in Table 7.2, 7.3 and 7.4, respectively.

### 7.7.1. Nonlinear deformation

The stress-strain behavior predicted by the BB\_APA\_NL for the off-axis tensile load cases is shown in Fig. 7.12. For comparison, the stress-strain curves obtained from the monotonic off-axis tension experiments (cf. Section 4.2.1) are given. The experimentally observed

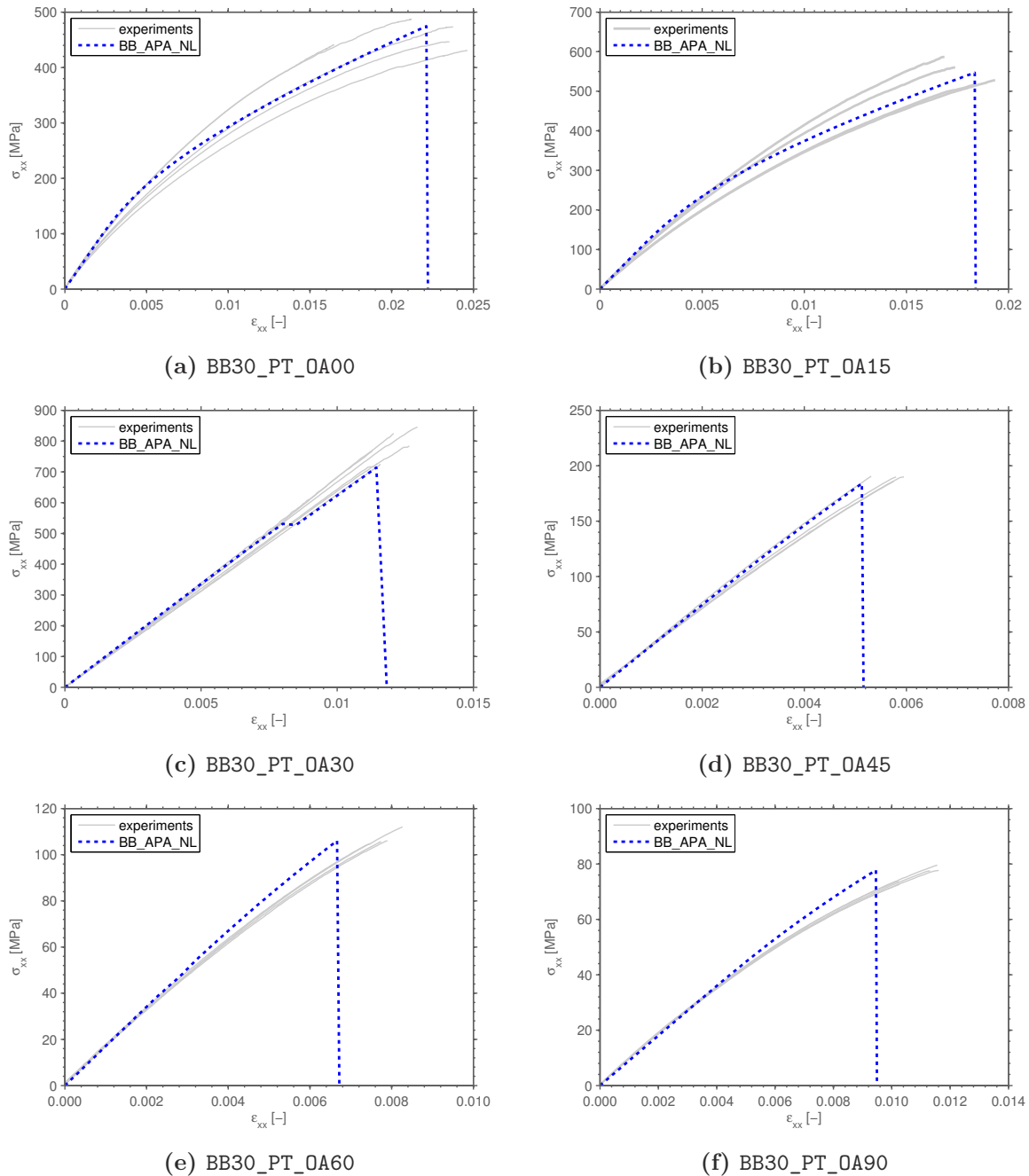


**Fig. 7.12:** Comparison of BB30\_PT predicted stress-strain behavior to off-axis experiments

non-linear stress-strain behavior is predicted accurately by the model, for both linear (e.g. OA30 and OA45) and strongly nonlinear (e.g. OA00 and OA15) load cases. For OA60 and OA90, the behavior is less nonlinear, which is predicted well for moderate strains up to

$\varepsilon_{xx} = 0.004$ , but the decrease of modulus is slightly underpredicted for higher strains. As the decrease of modulus was predicted well by the BBM unit cell, the deviation is believed to be due to neglecting the influence of transverse stress ( $\sigma_{22F}$ ) in the 1D yield criterion. For the OA30 case, where the load is applied in the F- yarn direction, a discontinuity in the predicted stress-strain curve is present at a stress of approximately 550 MPa, which is not observed in the experiments. This is due to a transverse tensile failure, predicted in the F+ yarn ply (oriented  $60^\circ$  to the load), which was not observed in the off-axis experiments and the unit cell simulations.

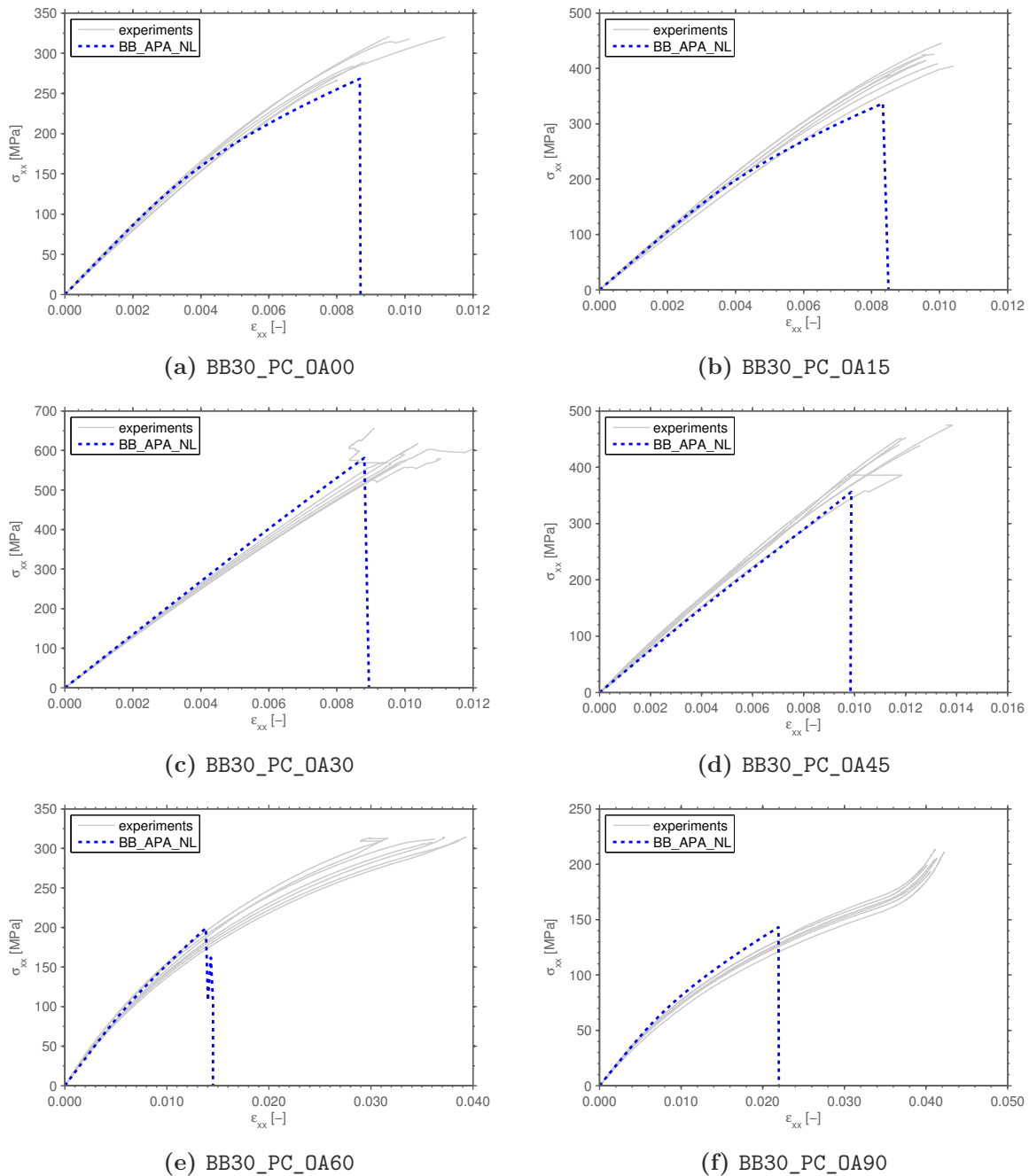


**Fig. 7.13:** Comparison of BB30\_PC predicted stress-strain behavior to off-axis experiments

The model predictions for the BB30 off-axis compression load cases are compared to the experiments in Fig. 7.13. As for the tensile off-axis load cases, the predictions agree well with the experiments for both, linear and nonlinear behavior. The response is, as in tension, nonlinear for OA00, OA15, OA60, OA90 and rather linear for OA30 and OA45. The small deviations between experimental stress-strain curves and the predictions are attributed to the transverse stress influence to the plastic deformation in the yarn plies. It is noted that the underprediction of the strength in the OA60 and OA90 case is of similar magnitude as observed in the BBM simulations, which were taken as basis for the calibration of the macroscopic models. Possible reasons for these deviations were discussed in Section 6.10.2.

A comparison of the predicted response to the experimental results for the BB45 is given in Fig. 7.14. As no experimental stress-strain curves were available for the BB45\_PC\_OA45,

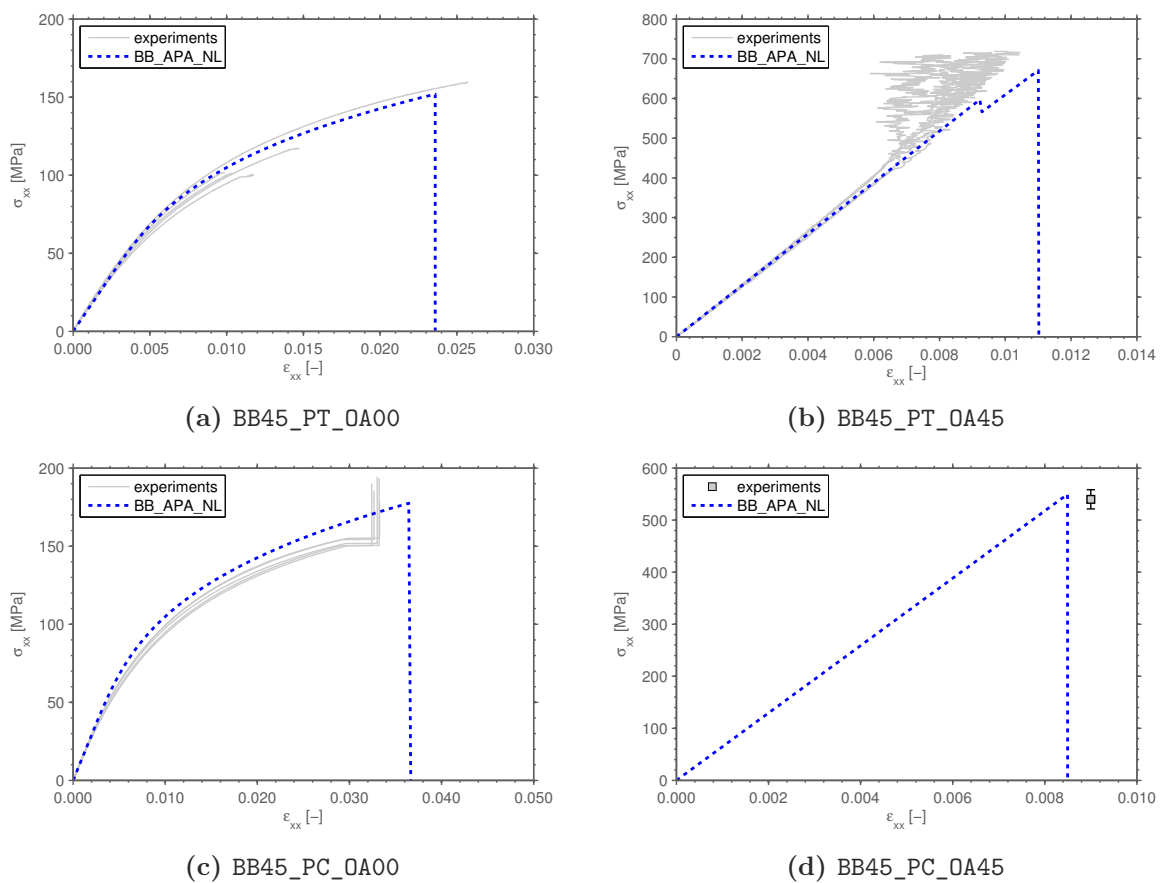


**Fig. 7.14:** Comparison of BB45 predicted stress-strain behavior to experiments

only the strength is given. The nonlinear response in tension and compression in the take-up direction (OA00) is predicted well by the model. In the tension and compression OA00 test series, the foil strain gauges failed before final failure, i.e. the end point of the experimental stress-strain curves does not represent the point of final failure. The linear response predicted for the load in yarn direction correlates well with the experiments. As for the tensile loading in yarn direction of the BB30, a preliminary failure is predicted in the F+ yarn ply, which is oriented orthogonal to the load. The transverse failure

was also observed in the F+ yarns in the experiments, but no discrete load drop was visible. Thus, the effect of transverse cracking is in this case overestimated by the linear softening damage model. However, no detailed investigation of this effect was possible, as the DIC strain signal was very noisy for higher strains, which was due to a blistering of the stochastic DIC pattern.

Summarizing the comparison of the stress-strain predictions, the 1D plasticity model used in the BB\_APA\_NL allows to represent the dominant nonlinear effects observed in the biaxial braided composites. The decrease of modulus was predicted accurate for various load cases, ranging from linear (e.g. BB30\_OA30), slightly nonlinear (e.g. BB30\_OA90) and strongly nonlinear (e.g. BB30\_OA00). Thus, the in-plane shear behavior of the yarn plies can be believed to be dominant for the nonlinear deformation of biaxial braided composites.

### 7.7.2. Failure prediction

The failure in the BB\_APA\_NL approach was predicted by applying the damage initiation and progression approach described in Section 7.6.5. The ultimate failure of the material point was in all cases given either by both yarn directions failing in transverse direction immediately after each other or by longitudinal failure of one of the yarn plies. The predicted failure stresses, strains and failure modes are compared to the off-axis experiments and analytical predictions.

The comparison of predictions to experiments for the BB30 tensile off-axis load cases is given in Table 7.6. The failure stresses predicted by BB\_APA\_NL (NL) and analytical APA

**Table 7.6.:** Comparison of BB30 tensile predictions from BB\_APA\_NL (NL) and analytical APA (lin) to off-axis experiments (exp)

	strength [MPa]			failure strain [%]			failure mode		
	NL	lin	exp.	NL	lin	exp.	NL	lin	exp.
PT_OA00	475	468	468±22	2.2	1.1	2.3±0.14	Tc	Tc	Tc
PT_OA15	547	515	581±30	1.8	1.0	1.7±0.15	Lt	Tc	Lt
PT_OA30	736	555	787±45	1.2	0.8	1.2±0.04	Lt	Tt	Lt
PT_OA45	184	192	198±8	0.5	0.5	0.6±0.02	Tt	Tt	Tt
PT_OA60	106	111	114±4	0.7	0.7	0.8±0.03	Tt	Tt	Tt
PT_OA90	78	80	79±3	0.9	0.9	1.1±0.06	Tt	Tt	Tt

(lin) correlate well and lie mostly within the experimental scatter. The largest deviation between linear and BB\_APA\_NL predictions is present for the fiber-dominated load cases in OA15 and OA30: for OA15, the analytically predicted failure stress is around 5% lower compared to the BB\_APA\_NL prediction. This is due to considerable plastic deformation being present in the nonlinear predictions, leading to a stress-redistribution and changing the failure mode to longitudinal failure. For the OA30 case, the first failure predicted by both models is transverse failure in the F+ yarn direction oriented 60° to the load. For the BB\_APA\_NL prediction, final failure is in the longitudinal direction of the F- yarn ply, oriented in load direction, which correlates with the experimental observations. The strength predicted by the nonlinear model being lower as the experimentally measured

one is due to the overpredicted softening after transverse failure (cf. Fig. 7.12c). Beside these two cases, the failure modes are predicted identically by linear and nonlinear model and correlate well with the experimental results.

A major difference between linear and nonlinear predictions is present in the failure strain: in the cases, where the deformation is strongly nonlinear, the failure strain predicted by the BB\_APA\_NL model is up to twice as large as the linearly predicted one. The nonlinear predictions correlate well with the experiments, while the linear model largely underpredicts the failure strains.

The comparison of predictions and experiments for the compressive BB30 off-axis cases is given in Table 7.7. For all off-axis cases, the failure stresses predicted by the BB\_APA\_NL model are slightly less than the ones predicted linearly. The deviation is mainly due to the fact that the material parameters for both models were obtained by correlation of the linear model to the unit cell calculations (cf. Table 7.3). Thus, the effects of plastic deformation, present in the BB\_APA\_NL model, are not included. The predicted failure strength strongly underestimating the experimental results for OA60 and OA90, is mainly due to the calibration to the BBM unit cell results. The failure strains are, beside these two cases, predicted accurately and the failure modes match the experimental observations.

**Table 7.7.:** Comparison of BB30 compressive predictions from BB\_APA\_NL (NL) and analytical APA (lin) to off-axis experiments (exp)

	strength [MPa]			failure strain [%]			failure mode		
	NL	lin	exp.	NL	lin	exp.	NL	lin	exp.
PC_OA00	268	281	300±21	0.9	0.7	0.9±0.11	Tt	Tt	Tt
PC_OA15	337	379	420±13	0.8	0.7	1.0±0.03	Tt	Tt	Tt
PC_OA30	581	601	605±31	0.9	0.9	1.0±0.11	Lc	Lc	Lc
PC_OA45	356	389	438±29	1.0	1.0	1.2±0.06	Tc	Tc	Tc
PC_OA60	199	219	312±2	1.4	1.3	3.7±0.13	Tc	Tc	Tc
PC_OA90	143	153	204±7	2.2	1.7	4.1±0.06	Tc	Tc	Tc

The failure predictions for the BB45 braid are compared to the experimental results in Table 7.8. As for the other cases, the predicted strength values correlate well with

**Table 7.8.:** Comparison of BB45 tensile and compressive predictions from BB\_APA\_NL (NL) and analytical APA (lin) to off-axis experiments (exp)

	strength [MPa]			failure strain [%]			failure mode		
	NL	lin	exp.	NL	lin	exp.	NL	lin	exp.
PT_OA00	160	161	159±19	2.7	1.1	>2.5 <sup>1</sup>	Tt	Tt	- <sup>3</sup>
PT_OA45	671	598	706±13	1.1	1.1	1.1 <sup>2</sup>	Lt	Tt	Lt
PC_OA00	178	178	188±7	3.6	1.2	>3 <sup>1</sup>	Tc	Tc	- <sup>3</sup>
PC_OA45	550	550	540±19	0.8	0.8	0.9 <sup>2</sup>	Lc	Lc	- <sup>3</sup>

<sup>1</sup>: failure strain not measured due to preliminary strain gauge failure

<sup>2</sup>: failure strain not measured, calculated from strength and elastic modulus

<sup>3</sup>: no information about failure mode



the experimental results. The difference in the BB\_PT\_OA45 case is attributed to the overestimation of damage of the transverse yarns, similarly observed in the BB30\_PT\_OA30 simulation. For this case, the linear model predicts transverse failure, underestimating the strength. The strain measurement in the experiments was not available up till final failure, as either the foil gauge bond failed or transverse cracking destroyed the DIC stochastic pattern on the coupon surface. However, the measured maximal strains approve the nonlinear modeling approach, as the linear model strongly underestimated the failure strains.

## 7.8. Conclusion on macroscopic modeling

Analytical linear, as well as a nonlinear modeling approach based on CLT have been used for failure prediction of biaxial braided composites. The analytical failure modeling, presented in Section 7.1, included two approaches, SPA and APA. For both approaches, input property assignment strategies based on results from FE unit cell calculations or experiments have been given. For the APA, the properties of the equivalent yarn plies, including the yarn waviness present in braided composites, have been derived by applying an inverse CLT approach for elastic properties and an iterative calibration procedure for the strength parameters. The predictions from SPA and APA have been compared to the off-axis experimental results in Section 7.3. The comparison showed that the SPA, commonly used for woven fabrics, lacks to represent the characteristics of the failure envelopes, being influenced by the braiding angle. The APA represents well the braiding angle influence, by basing the failure predictions on the equivalent yarn ply stresses.

Two failure criteria, the maximum stress and the Puck 2D failure criterion, were compared within the APA predictions in Section 7.4. The results from the two criteria were very similar, emphasizing that the yarn architecture and braiding angle, given by the yarn ply properties and the ply angle, respectively, are majorly affecting the failure envelope shape. However, the Puck 2D gave slightly better results, considering the different mechanics of yarn ply transverse failure under tension and compression. The predictions compared well to the off-axis experiments, with the first failure predicted coinciding with the final failure in the experiments for most cases. An exception were the cases, where the load applied was tensile in the yarn direction: preliminary transverse failure in the crossing yarn was predicted. Summing up, the analytical failure prediction correlated well with final failure in most of the cases, but underestimated the failure load for tension in yarn direction.

As the analytical predictions did not include the effects of plastic deformation, observed in the experiments, a nonlinear constitutive model for FE simulations was further introduced. The model bases on the APA and considers both yarn directions in a single material point of a shell element. Plastic deformation is considered in shear of the equivalent yarn plies and a damage law, including linear softening after damage initiation, was used.

The comparison of the linear and nonlinear modeling showed that the failure stresses predicted did not differ significantly and were in good correlation with the experimental results. An improvement of the predictions is given by the nonlinear model, for tensile loading in the yarn directions, where linear predictions are limited to the first failure,

occurring in the yarn ply oriented transverse to the load. Furthermore, the failure strain predictions for the cases with strong nonlinear deformation prior to final failure could be significantly improved with the nonlinear model. The deformation predicted by the linear model is not conservative, which is of major importance for structural simulations, as load re-distribution induced by the nonlinear deformation can significantly change the predictions. The comparison of the model predictions to the off-axis experiments showed a good correlation for the BB30 and BB45 braided composites. The deviation present for the high off-axis angles for BB30 under compression were also observed in the unit cell simulations and are thus attributed to the calibration of the material parameters to the unit cell simulations.

Summing up, linear and nonlinear approach yield accurate failure stress predictions, with the first failure predicted being identical with the final failure in the experiment. This is not the case for fiber-dominated load cases, where the nonlinear model predicts a further load increase after the first failure, which is in agreement with the experiments. Furthermore, the failure modes and failure strains are predicted more accurately by the nonlinear model.

With the models discussed in this chapter, a basis for macroscopic modeling of biaxial braided composites has been provided. The models use the framework of classical laminate theory and can be straightforwardly applied for the structural simulation of braided components.

## 8. Conclusions and future work

The goal of the presented research work was to create an approach for failure modeling of braided composites, applicable for simulations on structural components. This required to consider both, detailed unit cell modeling and experimental characterization to predict the yarn architecture influence on elastic, nonlinear and failure properties, and macroscopic modeling suitable for component simulation. From the literature review, presented in Chapter 2, the main working points of the thesis were identified as:

- Define a methodology for robust yarn architecture characterization, yielding a robust input for geometric modeling.
- Mechanical characterization of biaxial braided composites under combined stress states, to provide a phenomenological description of failure and serve a basis for model validation.
- Predict the influence of the yarn architecture on the mechanical behavior with unit cell modeling, including geometric modeling, analytical elastic predictions and non-linear FE unit cell simulations.
- Develop a macroscopic modeling approach for biaxial braided composite failure prediction, applicable to structural components.

### 8.1. Discussions and conclusions

In Chapter 3, the experimental techniques, used for yarn architecture and mechanical characterization, were given. The manufacturing process using closed cylindrical preforms, which are slit and draped into a flat preform shape, was found to be appropriate for high-quality specimen production. Quality assurance over the complete specimen production is crucial to obtain reproducible results. Optical sensor fiber orientation measurements were found suitable for braiding angle characterization. However, the scanned images included artifacts, which required the application of an automated data reduction routine.

The precision of thickness measurements of the specimen using a caliper was investigated: focus-variation measurements of the wavy vacuum-bag surface showed that caliper measurements are appropriate for the braided composites investigated. Deformation measurements using DIC were found to be useful for obtaining the specimen strain. Comparison of different techniques for average strain calculation from DIC measurements showed that considering the complete spatial strain distribution of the specimen is required for braided composites. Local strain measurements are prone to local effects, resulting in considerable deviations of the failure strain.

The first part of Chapter 4 presented the experimental results, obtained from yarn architecture characterization. The yarn architecture parameters required for the geometric models could, with exception of the braiding angle, be reliably measured from optical microscopy. A study on a ( $\pm 45^\circ$ ) braided composite panel showed that the sample position on the braided panel has no significant effect on the results. Furthermore, it was shown that 6-8 micrograph sections provide an appropriate number of measurements to identify differences in the magnitude of half the standard deviation. The braiding angle was obtained from surface scans of the braided composites by two methods: hand measurements from images and automated evaluation with an optical sensor. Both methods yielded a variable braiding angle transverse to the take-up direction, which was attributed to the s-shape of the yarns, caused by friction and gravity-effects during the braiding process. The average values obtained from the two methods compared well, but the hand-measurements provided slightly higher braiding angle values, attributed to the local measurements at yarn crossing points. Summing up, the sensor-measurements were found to be beneficial for application to structural components, offering an automated evaluation and an spatial measurement over the complete image.

Micro-CT was used for evaluation of 3D effects in the yarn architecture. Quantitative evaluation was less accurate, which is due to the reduced contrast and resolution of the CT-scans compared to micrographs. However, qualitative information regarding local variations of yarn cross-sections can be useful for improved geometric modeling.

Finally, analytically calculated yarn architecture parameters were compared to the measured values, yielding 10%-20% underestimation of the yarn height and good correlation for the other values. Attention needs to be paid, as underestimating the yarn height leads to non-conservative mechanical predictions (cf. Section 5.3).

The experimental results from the off-axis tension and compression testing of ( $\pm 30^\circ$ ) 2x2 braided composites were presented in the second part of Chapter 4. Off-axis testing introduces combined stress states into the material, triggering different fiber and matrix dominated failure modes.

A high dependence of mechanical properties on the braiding angle was found for loading in take-up direction: A braiding angle decrease of  $1.5^\circ$  yielded a strength increase of 15%. Similar braiding variations are expected on braided components, emphasizing the need of considering local braiding angle variations in structural simulation. The stress-strain behavior was, except for the load in yarn direction, nonlinear for all off-axis angles measured. Especially for the load in take-up direction, the initial modulus was more than 20% higher as the one obtained in the strain range given in the ASTM standard ( $\varepsilon_{xx} = 0.1-0.3\%$ ). In contrast, for the complete strain range till failure, the ASTM modulus overestimates the stiffness.

The tensile loading/unloading experiments showed that both inelastic deformation and damage are driving the nonlinear deformation, with the first being dominant for low off-axis angles ( $\psi = 0^\circ, 15^\circ$ ). Post-mortem microscopy investigations revealed intra-yarn cracking solely in the proximity of the macroscopic failure of the specimen. Thus, nonlinear deformation was mainly attributed to microscopic damage on fiber-matrix scale, commonly reported for UD composites under shear [159, 170]. This was also supported by the compressive stress-strain behavior being very similar to the tensile one.

Failure of the specimen was, except for the load in yarn direction, dominated by transverse yarn cracking. The strength values for the cases with transverse failure were found to be majorly influenced by the yarn transverse stress: for the same off-axis angle, the strength was higher in tension or compression, when the transverse yarn stress was compressive. A similar trend was observed in the failure modes of the coupons, being similar for the yarn transverse stresses sign being equal. The high-speed camera videos, used for the tensile experiments, showed that the first cracking occurring on the specimen surface coincided with the final failure of the specimen. Similar observations were made for the compressive experiments, yielding the conclusion that stable intra-yarn crack development like reported for triaxial braids [210] has less effect on the failure of biaxial braided composites.

The geometric unit cell modeling of the biaxial braided composites, conducted with the software WiseTex, was presented in Chapter 5. The geometric models compared well with the micro-CT measurements. Deviations in yarn shape and local nesting effects of the plies were identified as the cause for the reduced fiber volume fraction within the unit cells. Analytical predictions with the micromechanics software TexComp were in reasonable agreement with experimental results. Parametric studies yielded fiber volume fraction and braiding angle being the parameters majorly influencing the elastic constants.

The finite element unit cell modeling approach used for failure prediction of biaxial braided composites was presented in Chapter 6. The Binary Beam Model was formulated as an extension of the Binary Model [125]: by modeling the yarns with beam elements, stress concentration due to yarn bending could be included in the model, while keeping the numerical efficiency. Nonlinear behavior could efficiently be included using a Drucker-Prager plasticity model and volume averaging was shown to eliminate mesh-dependence in the effective medium stress field.

The stress profiles calculated by the BBM were compared to a classical continuum unit cell model, yielding a good correlation for most stress components. A deviation was present for stress fluctuations, introduced by the yarn cross section, which are not covered in the BBM: the coupling of beam and continuum elements does not include the cross-section definition.

With the periodic boundary conditions defined for the finite element unit cell, different out-of-plane boundary conditions, referring to laminate stacking configurations, were investigated for elastic solution and stress prediction. The out-of-plane boundary conditions had a major effect on predicted elastic behavior and stress fields, which varied up to 40% and 70%, respectively. For the random stacking observed in the braided laminates, considered in this work, 3D periodic boundary conditions with in-phase stacking were found to yield appropriate results.

The BBM predictions were compared to the off-axis experiments, yielding an excellent agreement for stiffness and non-linear behavior. For the failure prediction, strength parameters extracted from UD experiments were found to strongly underestimate the strength, thus a parameter identification based approach on biaxial braided composite experiments was used. The failure predictions of the BBM compared well with the off-axis experiments in tension and reasonable in compression. For the compressive load cases, nonlinear geometric effects, not considered in the simulation, could be causing the

deviations. However, also stress concentration effects in the compressive experiments, influencing the crack initiation and growth, could be a reason for the deviations. Thus, further experimental and numerical work is required for improved compressive failure predictions of biaxial braided composites.

Approaches used for macroscopic modeling were presented in Chapter 7. Due to computational efficiency, shell element and classical laminate theory based modeling was chosen. The input properties for the macroscopic models were obtained from unit cell modeling or experimental results: this yields the advantage that stress fluctuations, introduced by the textile yarn architecture, are considered in the material properties. Two analytical prediction methods were compared: the SPA, considering the stresses in the material coordinate system, and the APA, considering the stresses in equivalent yarn plies. From analytical failure predictions, it could be concluded the failure modeling based on the stresses in equivalent yarn plies (APA) is favorable for braided composites. Two failure criteria, maximum stress and Puck 2D, were used in the APA, both yielding a good agreement to the unit cell modeling and off-axis experimental results. However, the interaction of stresses for transverse failure prediction, considered in the Puck 2D criterion, was shown to improve the results.

Basing on the analytical APA modeling, a nonlinear modeling approach (BB\_APA\_NL), considering plastic deformation and damage was implemented into a material user subroutine of the finite element code Abaqus/Explicit. The BB\_APA\_NL stress-strain predictions yielded good agreement to the experimental results, approving the 1D plasticity model used. Considering nonlinear deformation significantly improved the failure strain prediction compared to the analytical model. The linear-softening damage model used was shown to work accurate for matrix-dominated load cases, but overestimated the effects of transverse cracking for fiber-dominated load cases. Summing up, considering the nonlinear deformation behavior of biaxial braided composites is crucial for structural simulation, as the deformation can be predicted more accurately and effects of load-redistribution can be considered.

The work presented on modeling of braided composites demonstrates the potential of multi-scale modeling. Finite element unit cells provide an insight to the mechanical behavior, considering the details of the textile yarn architecture. The BBM unit cell model presented allows computationally efficient and parametric modeling of biaxial braided composites, while preserving relevant details of the stress field. Furthermore, the macroscopic methods presented can be used for structural simulation, while incorporating the effects of yarn architecture by obtaining the mechanical properties from unit cell results. The modeling framework presented is straightforward applicable to structural simulation of biaxial braided components.

## 8.2. Potential future work

Every new method or model opens the door for a number of possible improvements. Some points for potential future research, arising from the research work conducted in the framework of this thesis, are given below.

### Yarn architecture

- Evaluate micro-CT scans quantitatively for yarn architecture characterization. This requires contrast enhancement and 3D segmentation methods for yarns and matrix.

### Mechanical characterization

- Investigate improved methods for compression testing, avoiding issues with specimen bending and crack growth under the loading tabs, both encountered with the CLC test fixture. New test methods require: larger gauge sections, reduction of shear-extension coupling, DIC measurement, and high-speed camera recordings.
- The off-axis characterization should be extended to more braiding angles; stress states that cannot be tested with off-axis experiments, should be characterized by using multi-axial testing.

### Unit cell modeling

- Investigate refined geometric modeling approaches with CT-scan results to obtain more realistic fiber volume fractions in the unit cells.
- Improving the accuracy of the BBM stress fields in the effective medium by new coupling methods for beam and continuum elements, considering the yarn cross section and coupling both, rotational and translational DOFs.
- Investigate experimental methods for measuring yarn strength and numerical methods to scale strength parameters to different fiber volume fractions.
- Extend the investigations on out-of-plane boundary conditions with comparisons to DIC measurements of the out-of-plane deformation. This requires a higher DIC-resolution on the specimen and experiments with laminates of different ply numbers.

### Macroscopic modeling

- The applicability of the proposed macroscopic modeling methods for braided laminates with a small number of plies ( $n < 4$ ) needs to be investigated. For these cases, the local out-of-plane deformation can become more prominent.
- Apply an improved plasticity model for the equivalent yarn plies, considering the influence of transverse stresses. Furthermore, coupling of damage and plasticity can be addressed based on the loading/unloading experiments conducted in this work.
- The effect of transverse yarn damage was overestimated for the models used, when the load applied was in one of the yarn directions. This requires additional experimental investigation, to obtain reliable data about the damage initiation and progression as well as improved damage models, to consider the stable damage development observed in the transverse yarns.

# A. Material properties

Fiber material properties (Table A.1) were obtained by reverse engineering from UD experiments, using Chamis' micromechanics equations (Eq. D.1-Eq. D.6). The matrix (RTM6) material properties given in Table A.2. The UD experiments have been conducted at the *Polymer Competence Center Leoben*, Austria.

**Table A.1.:** HTS40 fiber properties, shear modulus and strength from [204]

elastic		strength	
$E_{f11}$ [MPa]	218400	$X_{f,T}$ [MPa]	3040
$E_{f22}$ [MPa]	18100	$X_{f,C}$ [MPa]	1499
$G_{f12}$ [MPa]	21800		
$\nu_{f12}$ [-]	0.305		

RTM6 material properties obtained from bulk matrix experiments at the *Polymer Competence Center Leoben*, Austria.

**Table A.2.:** RTM6 material properties

$E_m$ [MPa]	$\nu_m$ [-]
2890	0.35

For 60% fiber volume fraction this yields the properties given in Table A.3

**Table A.3.:** Elastic constants of a HTS40/RTM6 UD ply with  $\varphi_f = 60\%$

$E_{11}$ [MPa]	$E_{22}$ [MPa]	$G_{12}$ [MPa]	$\nu_{12}$ [-]
131900	8300	4100	0.29



Inclination parameters used for failure analysis with Puck's 2D failure criterion.

**Table A.4.:** Inclination parameters for Puck 2D criterion (from [213])

$p_{\perp\parallel}^t$	$p_{\perp\parallel}^c$	$p_{\perp\perp}^t$
0.35	0.3	0.25

## A.1. BB45 test results

**Table A.5.:** Elastic and strength properties of ( $\pm 45^\circ$ ) biaxial braided composite

Test series	Modulus ASTM			Modulus initial		
	MEAN [MPa]	STD [MPa]	CV [%]	MEAN [MPa]	STD [MPa]	CV [%]
B45_PT_OA00	13760	547	4.0	15804	800	5.1
B45_PT_OA45	65136	2282	3.5	63092	1442	2.3
B45_PC_OA00	12857	408	3.2	-	-	-
B45_PC_OA45	62333	1458	2.3	-	-	-

Test series	Strength			
	MEAN [MPa]	STD [MPa]	CV [%]	$\varphi_f^1$ [%]
B45_PT_OA00	159.4	18.6	11.7	56.8
B45_PT_OA45	705.9	13.1	1.9	62.9
B45_PC_OA00	187.8	7.1	3.8	58.8
B45_PC_OA45	539.7	18.5	3.4	61.7

<sup>1</sup>: fiber volume fraction of the panels, the results given are normalized to a fiber volume fraction of 60% according to Eq. 3.24-Eq. 3.25

## B. Orientation averaging for biaxial braided composites

The equations given here are implemented into the MATLAB routine `OrientationAveraging.m`.

### Input

- Elastic constants of fibers and matrix
- Fiber volume fraction of the braided composite
- Yarn height  $d_1$ , yarn width  $d_2$  and braiding angle  $\theta$

### Equations

The properties of the (straight) UD segments are calculated by Chamis' micromechanical formulae (Eq. D.1-Eq. D.6). The 3D stiffness matrix is calculated as:

$$\mathbf{C} = \mathbf{S}^{-1} = \begin{bmatrix} S_{11} & S_{12} & S_{12} & 0 & 0 & 0 \\ S_{12} & S_{22} & S_{23} & 0 & 0 & 0 \\ S_{12} & S_{23} & S_{22} & 0 & 0 & 0 \\ 0 & 0 & 0 & S_{44} & 0 & 0 \\ 0 & 0 & 0 & 0 & S_{44} & 0 \\ 0 & 0 & 0 & 0 & 0 & S_{66} \end{bmatrix}^{-1} \quad (\text{B.1})$$

with the assumption of transversal isotropy

$$E_{22} = E_{33}, \quad G_{12} = G_{13}, \quad \nu_{12} = \nu_{13}, \quad G_{23} = \frac{E_{33}}{2(1 + \nu)}. \quad (\text{B.2})$$

The compliance matrix components yield:

$$\begin{aligned} S_{11} &= \frac{1}{E_{11}} & S_{22} &= \frac{1}{E_{22}} & S_{12} &= -\frac{\nu_{12}}{E_{11}} \\ S_{23} &= -\frac{\nu_{31}}{E_{33}} & S_{44} &= \frac{1}{G_{13}} & S_{66} &= \frac{1}{G_{23}} \end{aligned} \quad (\text{B.3})$$

The stiffness matrix is transformed in the global system by the angle  $\phi$ :

$$\mathbf{C}_{UD}(\phi) = \mathbf{T}^T \mathbf{C} \mathbf{T} \quad (\text{B.4})$$

With

$$\mathbf{T} = \begin{bmatrix} \cos^2 \phi & 0 & \sin^2 \phi & 0 & \cos \phi \sin \phi & 0 \\ 0 & 1 & 0 & 0 & 0 & 0 \\ \sin^2 \phi & 0 & \cos^2 \phi & 0 & -\cos \phi \sin \phi & 0 \\ 0 & 0 & 0 & \cos \phi & 0 & -\sin \phi \\ -2 \cos \phi \sin \phi & 0 & 2 \sin \phi \cos \phi & 0 & \cos^2 \phi - \sin^2 \phi & 0 \\ 0 & 0 & 0 & \sin \phi & 0 & \cos \phi \end{bmatrix}^{-1} \quad (\text{B.5})$$

The out-of-plane yarn angle  $\phi$  is given by the yarn geometry with  $A = d_1/2$  and  $\lambda = 2d_2$ :

$$\phi = \tan^{-1} \left( \frac{dy}{dx} \right) \quad (\text{B.6})$$

and the yarn path function:

$$y(x) = \begin{cases} A \cdot \cos(2 \cdot \pi x / \lambda) & x = 0 \dots d_2 \\ -A & x = d_2 \dots 2 \cdot d_2 \\ -A \cdot \cos(2 \cdot \pi x / \lambda) & x = 2 \cdot d_2 \dots 3 \cdot d_2 \end{cases} \quad (\text{B.7})$$

The stiffness matrix of a wavy ply is:

$$C_{UD}^{wavy} = \frac{1}{3 \cdot d_2} \cdot \int_{x=0}^{3 \cdot d_2} C_{UD}(\phi) dx = \frac{1}{N} \cdot \sum_{i=1}^N C_{UD}(\phi_i) \quad (\text{B.8})$$

The elastic constants of the biaxial braided composite are calculated by an equivalent laminate model as given in Eq. D.10 and Eq. D.11.

## C. Definition of RUC and RVE

The definition for the terms *Repeating Unit Cell* (RUC) and *Representative Volume Element* (RVE) are based on the publication from Pindera et. al. [143]. It is important to note that the concepts of RUC and RVE have not been used consistent in the literature: RUCs are designated RVE and vice versa.

### C.1. Representative Volume Element

The RVE concept is based on the statistical homogeneity: a RVE is the smallest sub-volume of a microstructure that has the same volume fractions and same statistical distributions as the complete material (c.f. Fig. C.1(a)). The sub-volume response is identical as the response of the complete material when either homogenous traction or displacement boundary conditions are applied. Examples for RVE could a volume with statistical distributed fibers in a unidirectional composite that has the same fiber volume fraction and the same arrangement of fibers as the one measured from a real material. If the RVE size is chosen appropriate, the strain energy density is identical for either displacement or traction boundary conditions applied, resulting in the same homogenized material properties.

### C.2. Repeating Unit Cell

The RUC concept bases on a periodic microstructure of the material (see Fig. C.1(b)). The RUC is the smallest volume of microstructure, which is able to reproduce the complete microstructure through replication (translation and rotation) of the volume. Note that due to practical reasons it is sometimes feasible to use a bigger sub-volume of the material. The response of the sub-volume is identical to the response of the complete material when periodic boundary conditions are applied to the RUC.

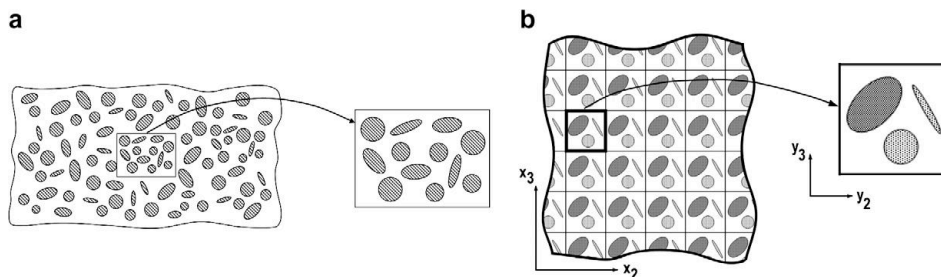


Fig. C.1: Definition of RUC and RVE according to [143]

# D. Normalization of properties for braided composites

## D.1. UD properties for the equivalent laminate

Chamis' micromechanical equations [200] are used to calculate the UD properties from fiber and matrix properties. The indexes  $f$  and  $m$  denote the constituent properties of fiber and matrix

$$E_{11} = \varphi_f E_{f11} + (1 - \varphi_f) E_m \quad (\text{D.1})$$

$$E_{22} = E_{33} = \frac{E_m}{1 - \sqrt{\varphi_f}(1 - E_m/E_{f22})} \quad (\text{D.2})$$

$$G_{12} = G_{13} = \frac{G_m}{1 - \sqrt{\varphi_f}(1 - G_m/G_{f12})} \quad (\text{D.3})$$

$$G_{23} = \frac{G_m}{1 - \varphi_f(1 - G_m/G_{f23})} \quad (\text{D.4})$$

$$\nu_{12} = \nu_{13} = \nu_m + \varphi_f(\nu_{f12} - \nu_m) \quad (\text{D.5})$$

$$\nu_{23} = \varphi_f \nu_{f23} + (1 - \varphi_f)(2\nu_m - \frac{\nu_{12}}{E_{11}} E_{22}) \quad (\text{D.6})$$

## D.2. Equivalent laminate properties

The stiffness matrix  $\mathbf{Q}$  of an equivalent ply yields

$$\mathbf{Q} = \begin{bmatrix} Q_{11} & Q_{12} & 0 \\ Q_{12} & Q_{22} & 0 \\ 0 & 0 & Q_{66} \end{bmatrix} \quad (\text{D.7})$$

with

$$Q_{11} = \frac{E_{11}}{1 - \nu_{12}\nu_{21}} \quad Q_{22} = \frac{E_{22}}{1 - \nu_{12}\nu_{21}} \quad Q_{12} = \frac{\nu_{12}E_{22}}{1 - \nu_{12}\nu_{21}} = \frac{\nu_{21}E_{11}}{1 - \nu_{12}\nu_{21}} \quad Q_{66} = G_{12}$$

The stiffness matrix is transformed to the material coordinate system (of the biaxial braided composite)

$$\bar{\mathbf{Q}}^{UD\pm\theta} = \mathbf{T}^{-1}(\pm\theta) \cdot \mathbf{Q} \cdot \mathbf{T}^{-T}(\pm\theta) \quad (\text{D.8})$$

with  $\mathbf{T}$  the transformation matrix

$$\mathbf{T}(\phi) = \begin{bmatrix} \cos^2 \phi & \sin^2 \phi & 2 \cos \phi \sin \phi \\ \sin^2 \phi & \cos^2 \phi & -2 \cos \phi \sin \phi \\ -\cos \phi \sin \phi & \cos \phi \sin \phi & \cos^2 \phi - \sin^2 \phi \end{bmatrix} \quad (\text{D.9})$$

The elastic constants are obtained from the compliance matrix of the biaxial braided composite:

$$\mathbf{s}^{BB} = [\mathbf{Q}^{BB}]^{-1} = \left[ \frac{1}{2} (\bar{\mathbf{Q}}^{UD+\theta} + \bar{\mathbf{Q}}^{UD-\theta}) \right]^{-1} \quad (\text{D.10})$$

$$E_{11}^{BB} = \frac{1}{S_{11}^{BB}} \quad E_{22}^{BB} = \frac{1}{S_{22}^{BB}} \quad G_{12}^{BB} = \frac{1}{S_{66}^{BB}} \quad \nu_{12}^{BB} = -\frac{S_{11}^{BB}}{S_{22}^{BB}} \quad (\text{D.11})$$

### D.3. Normalization

Young modulus in load direction:

$$\frac{1}{E_{\psi}^{BB}} = \frac{1}{E_{11}^{BB}} \cos^4(\psi) + \left[ \frac{1}{G_{12}^{BB}} - \frac{2\nu_{12}^{BB}}{E_{11}^{BB}} \right] \sin^2 \psi \cos^2 \psi + \frac{1}{E_{22}^{BB}} \sin^4(\psi) \quad (\text{D.12})$$

The experimentally measured Young's modulus  $E_X^{exp}$ , in off-axis direction  $\psi$ , with the experimental fiber volume fraction  $\varphi_{exp}$  is normalized to  $\varphi_{norm}$ :

$$E_x^{norm} = E_x^{exp} - (E_{\psi}^{BB}(\varphi_{exp}) - E_{\psi}^{BB}(\varphi_{norm})) \quad (\text{D.13})$$

$E_x^{norm}$  is the normalized value and  $E_{\psi}^{BB}(\varphi_{exp}), E_{\psi}^{BB}(\varphi_{norm})$  are determined by the procedure described above.

## E. Software codes

### E.1. Optical sensor data reduction

The analysis script *braiding\_angle\_analysis.m* is included in a folder on the attached DVD. A short description of input required and output printed is given in the user manual.

### E.2. Inverse CLT

The inverse CLT approach has been implemented into the MATLAB function *InverseCLT\_BB.m*. The script and a user manual are included on the DVD attached to this thesis.

### E.3. BBM modeling framework

The BBM modeling framework programmed in MATLAB and Python is included in the folder *BinaryBeamModel* on the DVD attached to this thesis. The framework is started using the file

```
.\BinaryBeamModel\Tool\30_MATLAB\32_Framework\Master_File30.m
```

Explanations to the input parameters are given in the user manual.

### E.4. Abaqus VUMAT: BB\_APA\_NL

The input requires 23 parameters to be defined. The input properties, together with an example input are given in the user manual. The Fortran subroutine is included in a folder of the DVD attached to this thesis.

# F. Periodic boundary conditions

## F.1. Constrain driver displacements and forces

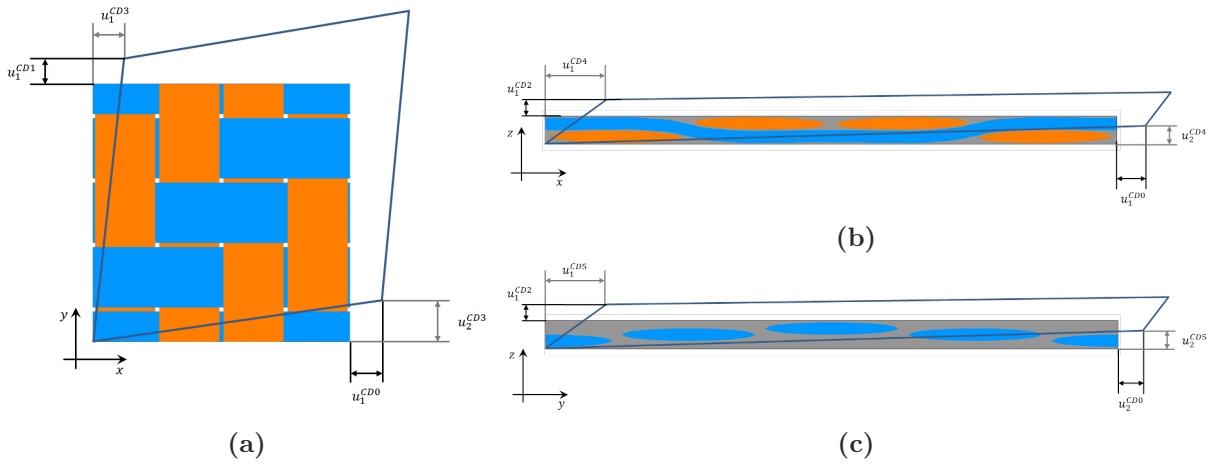


Fig. F.1: Constraint driver deformations

Table F.1.: Macroscopic stresses / strains and corresponding constraint driver displacements

stress	strain	CD displacement
$\sigma_{xx}$	$\epsilon_{xx}$	$u_1^{CD0}$
$\sigma_{yy}$	$\epsilon_{yy}$	$u_1^{CD1}$
$\sigma_{zz}$	$\epsilon_{zz}$	$u_1^{CD2}$
$\tau_{xy}$	$\gamma_{xy}$	$u_{1,2}^{CD3}$
$\tau_{xz}$	$\gamma_{xz}$	$u_{1,2}^{CD4}$
$\tau_{yz}$	$\gamma_{yz}$	$u_{1,2}^{CD5}$

$$\mathbf{U} = \begin{bmatrix} u_1^{CD0} & u_1^{CD3} & u_1^{CD4} \\ u_2^{CD3} & u_1^{CD1} & u_1^{CD5} \\ u_2^{CD4} & u_2^{CD5} & u_1^{CD2} \end{bmatrix} \quad \mathbf{F} = \begin{bmatrix} F_1^{CD0} & F_1^{CD3} & F_1^{CD4} \\ F_2^{CD3} & F_1^{CD1} & F_1^{CD5} \\ F_2^{CD4} & F_2^{CD5} & F_1^{CD2} \end{bmatrix} \quad (\text{F.1})$$



## F.2. Loading of the unit cell

### F.2.1. Strain controlled loading

Calculate constraint driver displacements from macroscopic strain tensor:

$$\mathbf{U} = \langle \boldsymbol{\varepsilon} \rangle \cdot \mathbf{P} \quad (\text{F.2})$$

The displacements are prescribed to the unit cell and the macroscopic stress tensor is calculated from the constraint driver forces, given by the FE solution:

$$\langle \boldsymbol{\sigma} \rangle = \frac{1}{2V} (\mathbf{F} \cdot \mathbf{P}^T + \mathbf{P} \cdot \mathbf{F}^T) \quad (\text{F.3})$$

### F.2.2. Stress controlled loading

Calculate constraint driver forces from macroscopic stress tensor:

$$\mathbf{F} = V \cdot \langle \boldsymbol{\sigma} \rangle (\mathbf{P}^T)^{-1} \quad (\text{F.4})$$

The forces are prescribed to the unit cell and the macroscopic strain tensor is calculated from the constraint driver displacements, given by the FE solution:

$$\langle \boldsymbol{\varepsilon} \rangle = \frac{1}{2} (\mathbf{U} \cdot \mathbf{P}^{-1} + (\mathbf{P}^{-1})^T \cdot \mathbf{U}^T) \quad (\text{F.5})$$

## F.3. Elastic constants calculation

- Elastic constants are calculated under plane stress assumption and the unit cell response is assumed orthotropic in the (12) material coordinate system.
- Three loadcases required to calculate the 2D orthotropic elastic constants, with the magnitude of loading  $C$  being arbitrary.

### Macroscopic constitutive equation

$$\begin{bmatrix} \langle \varepsilon_{11} \rangle \\ \langle \varepsilon_{22} \rangle \\ \langle \gamma_{12} \rangle \end{bmatrix} = \begin{bmatrix} S_{11} & S_{12} & S_{16} \\ S_{21} & S_{22} & S_{26} \\ S_{61} & S_{62} & S_{66} \end{bmatrix} \cdot \begin{bmatrix} \langle \sigma_{11} \rangle \\ \langle \sigma_{22} \rangle \\ \langle \sigma_{12} \rangle \end{bmatrix} \quad (\text{F.6})$$

Orthotropy holds true if

$$S_{16} = S_{26} = S_{61} = S_{62} = 0. \quad (\text{F.7})$$

The elastic constants are obtained from

$$E_{11} = 1/S_{11} \quad E_{22} = 1/S_{22} \quad G_{12} = 1/S_{66} \quad \nu_{12} = -S_{21}/S_{11}. \quad (\text{F.8})$$

**Normal load in 11-direction**

$$\text{Loading : } \quad \langle \boldsymbol{\sigma} \rangle = C \cdot \begin{bmatrix} 1 & 0 & 0 \\ 0 & 0 & 0 \\ 0 & 0 & 0 \end{bmatrix} \quad (\text{F.9})$$

Calculation of  $S$ -Matrix entries:

$$S_{11} = \frac{\langle \varepsilon_{11} \rangle}{\langle \sigma_{11} \rangle} \quad S_{21} = \frac{\langle \varepsilon_{22} \rangle}{\langle \sigma_{11} \rangle} \quad S_{61} = \frac{\langle \varepsilon_{12} \rangle + \langle \varepsilon_{21} \rangle}{\langle \sigma_{11} \rangle} \quad (\text{F.10})$$

**Normal load in 22-direction**

$$\text{Loading : } \quad \langle \boldsymbol{\sigma} \rangle = C \cdot \begin{bmatrix} 0 & 0 & 0 \\ 0 & 1 & 0 \\ 0 & 0 & 0 \end{bmatrix} \quad (\text{F.11})$$

Calculation of  $S$ -Matrix entries:

$$S_{12} = \frac{\langle \varepsilon_{11} \rangle}{\langle \sigma_{22} \rangle} \quad S_{22} = \frac{\langle \varepsilon_{22} \rangle}{\langle \sigma_{22} \rangle} \quad S_{62} = \frac{\langle \varepsilon_{12} \rangle + \langle \varepsilon_{21} \rangle}{\langle \sigma_{22} \rangle} \quad (\text{F.12})$$

**In-plane shear load (12)**

$$\text{Loading : } \quad \langle \boldsymbol{\sigma} \rangle = C \cdot \begin{bmatrix} 0 & 1 & 0 \\ 1 & 0 & 0 \\ 0 & 0 & 0 \end{bmatrix} \quad (\text{F.13})$$

Calculation of  $S$ -Matrix entries:

$$S_{16} = \frac{2 \langle \varepsilon_{11} \rangle}{\langle \sigma_{12} \rangle + \langle \sigma_{21} \rangle} \quad S_{26} = \frac{2 \langle \varepsilon_{22} \rangle}{\langle \sigma_{12} \rangle + \langle \sigma_{21} \rangle} \quad S_{66} = \frac{2(\langle \varepsilon_{12} \rangle + \langle \varepsilon_{21} \rangle)}{\langle \sigma_{12} \rangle + \langle \sigma_{21} \rangle} \quad (\text{F.14})$$

**F.4. Coupling equations**

For the implementation of the periodic boundary conditions, the surfaces of the unit cell need to be split up in faces (excluding edges and masternodes), edges (excluding masternodes) and masternodes (corner nodes). The naming of unit cell faces, edges and masternodes is given in Fig. F.2.

**F.4.1. Coupling equations for 2D periodicity****Equation for faces**

$$\begin{aligned} u_1^A - u_1^B - u_1^{CD0} &= 0 & u_1^C - u_1^D - u_1^{CD3} &= 0 \\ u_2^A - u_2^B - u_2^{CD3} &= 0 & u_2^C - u_2^D - u_1^{CD1} &= 0 \\ u_3^A - u_3^B &= 0 & u_3^C - u_3^D &= 0 \end{aligned}$$

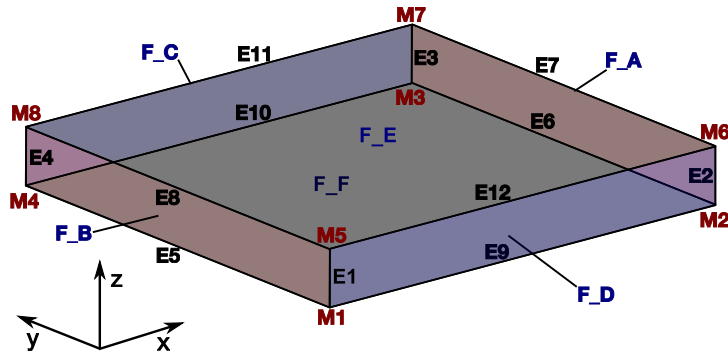


Fig. F.2: Naming convention for faces (F), edges (E) and master nodes (M)

### Equation for edges

$$u_1^{E2} - u_1^{E1} - u_1^{CD0} = 0$$

$$u_2^{E2} - u_2^{E1} - u_2^{CD3} = 0$$

$$u_3^{E2} - u_3^{E1} = 0$$

$$u_1^{E4} - u_1^{E1} - u_1^{CD3} = 0$$

$$u_2^{E4} - u_2^{E1} - u_1^{CD1} = 0$$

$$u_3^{E4} - u_3^{E1} = 0$$

$$u_1^{E7} - u_1^{E8} - u_1^{CD0} = 0$$

$$u_2^{E7} - u_2^{E8} - u_2^{CD3} = 0$$

$$u_3^{E7} - u_3^{E8} = 0$$

$$u_1^{E11} - u_1^{E12} - u_1^{CD3} = 0$$

$$u_2^{E11} - u_2^{E12} - u_1^{CD1} = 0$$

$$u_3^{E11} - u_3^{E12} = 0$$

$$u_1^{E3} - u_1^{E1} - u_1^{CD0} - u_1^{CD3} = 0$$

$$u_2^{E3} - u_2^{E1} - u_1^{CD1} - u_2^{CD3} = 0$$

$$u_3^{E3} - u_3^{E1} = 0$$

$$u_1^{E6} - u_1^{E5} - u_1^{CD0} = 0$$

$$u_2^{E6} - u_2^{E5} - u_2^{CD3} = 0$$

$$u_3^{E6} - u_3^{E5} = 0$$

$$u_1^{E10} - u_1^{E9} - u_1^{CD3} = 0$$

$$u_2^{E10} - u_2^{E9} - u_1^{CD1} = 0$$

$$u_3^{E10} - u_3^{E9} = 0$$

**Equation for masternodes**

$$\begin{array}{ll}
u_1^{M2} - u_1^{M1} - u_1^{CD0} = 0 & u_1^{M3} - u_1^{M1} - u_1^{CD0} - u_1^{CD3} = 0 \\
u_2^{M2} - u_2^{M1} - u_2^{CD3} = 0 & u_2^{M3} - u_2^{M1} - u_1^{CD1} - u_2^{CD3} = 0 \\
u_3^{M2} - u_3^{M1} = 0 & u_3^{M3} - u_3^{M1} = 0 \\
u_1^{M4} - u_1^{M1} - u_1^{CD3} = 0 & u_1^{M6} - u_1^{M5} - u_1^{CD0} = 0 \\
u_2^{M4} - u_2^{M1} - u_1^{CD1} = 0 & u_2^{M6} - u_2^{M5} - u_2^{CD3} = 0 \\
u_3^{M4} - u_3^{M1} = 0 & u_3^{M6} - u_3^{M5} = 0 \\
u_1^{M7} - u_1^{M5} - u_1^{CD0} - u_1^{CD3} = 0 & u_1^{M8} - u_1^{M5} - u_1^{CD3} = 0 \\
u_2^{M7} - u_2^{M5} - u_1^{CD1} - u_2^{CD3} = 0 & u_2^{M8} - u_2^{M5} - u_1^{CD1} = 0 \\
u_3^{M7} - u_3^{M5} = 0 & u_3^{M8} - u_3^{M5} = 0
\end{array}$$

**F.4.2. Coupling equations for 3D periodicity****Equation for faces**

$$\begin{array}{lll}
u_1^A - u_1^B - u_1^{CD0} = 0 & u_1^C - u_1^D - u_1^{CD3} = 0 & u_1^E - u_1^F - u_1^{CD4} = 0 \\
u_2^A - u_2^B - u_2^{CD3} = 0 & u_2^C - u_2^D - u_1^{CD1} = 0 & u_2^E - u_2^F - u_1^{CD5} = 0 \\
u_3^A - u_3^B - u_2^{CD4} = 0 & u_3^C - u_3^D - u_2^{CD5} = 0 & u_3^E - u_3^F - u_1^{CD2} = 0
\end{array}$$

**Equation for edges**

$$\begin{aligned}
u_1^{E2} - u_1^{E1} - u_1^{CD0} &= 0 & u_1^{E3} - u_1^{E1} - u_1^{CD0} - u_1^{CD3} &= 0 \\
u_2^{E2} - u_2^{E1} - u_2^{CD3} &= 0 & u_2^{E3} - u_2^{E1} - u_1^{CD1} - u_2^{CD3} &= 0 \\
u_3^{E2} - u_3^{E1} - u_2^{CD4} &= 0 & u_3^{E3} - u_3^{E1} - u_2^{CD4} - u_2^{CD5} &= 0 \\
u_1^{E4} - u_1^{E1} - u_1^{CD3} &= 0 & u_1^{E6} - u_1^{E5} - u_1^{CD0} &= 0 \\
u_2^{E4} - u_2^{E1} - u_1^{CD1} &= 0 & u_2^{E6} - u_2^{E5} - u_2^{CD3} &= 0 \\
u_3^{E4} - u_3^{E1} - u_2^{CD5} &= 0 & u_3^{E6} - u_3^{E5} - u_2^{CD4} &= 0 \\
u_1^{E7} - u_1^{E5} - u_1^{CD0} - u_1^{CD4} &= 0 & u_1^{E8} - u_1^{E5} - u_1^{CD4} &= 0 \\
u_2^{E7} - u_2^{E5} - u_2^{CD3} - u_1^{CD5} &= 0 & u_2^{E8} - u_2^{E5} - u_1^{CD5} &= 0 \\
u_3^{E7} - u_3^{E5} - u_2^{CD4} - u_1^{CD2} &= 0 & u_3^{E8} - u_3^{E5} - u_1^{CD2} &= 0 \\
u_1^{E10} - u_1^{E9} - u_1^{CD3} &= 0 & u_1^{E11} - u_1^{E9} - u_1^{CD3} - u_1^{CD4} &= 0 \\
u_2^{E10} - u_2^{E9} - u_1^{CD1} &= 0 & u_2^{E11} - u_2^{E9} - u_1^{CD1} - u_1^{CD5} &= 0 \\
u_3^{E10} - u_3^{E9} - u_2^{CD5} &= 0 & u_3^{E11} - u_3^{E9} - u_2^{CD5} - u_1^{CD2} &= 0 \\
u_1^{E12} - u_1^{E9} - u_1^{CD4} &= 0 & & \\
u_2^{E12} - u_2^{E9} - u_1^{CD5} &= 0 & & \\
u_3^{E12} - u_3^{E9} - u_1^{CD2} &= 0 & & 
\end{aligned}$$

**Equation for masternodes**

$$\begin{aligned}
u_1^{M2} - u_1^{M1} - u_1^{CD0} &= 0 & u_1^{M3} - u_1^{M1} - u_1^{CD0} - u_1^{CD3} &= 0 \\
u_2^{M2} - u_2^{M1} - u_2^{CD3} &= 0 & u_2^{M3} - u_2^{M1} - u_1^{CD1} - u_2^{CD3} &= 0 \\
u_3^{M2} - u_3^{M1} - u_2^{CD4} &= 0 & u_3^{M3} - u_3^{M1} - u_2^{CD4} - u_2^{CD5} &= 0 \\
u_1^{M4} - u_1^{M1} - u_1^{CD3} &= 0 & u_1^{M5} - u_1^{M1} - u_1^{CD4} &= 0 \\
u_2^{M4} - u_2^{M1} - u_1^{CD1} &= 0 & u_2^{M5} - u_2^{M1} - u_1^{CD5} &= 0 \\
u_3^{M4} - u_3^{M1} - u_2^{CD5} &= 0 & u_3^{M5} - u_3^{M1} - u_1^{CD2} &= 0 \\
u_1^{M6} - u_1^{M1} - u_1^{CD0} - u_1^{CD4} &= 0 & u_1^{M7} - u_1^{M1} - u_1^{CD0} - u_1^{CD3} - u_1^{CD4} &= 0 \\
u_2^{M6} - u_2^{M1} - u_2^{CD3} - u_1^{CD5} &= 0 & u_2^{M7} - u_2^{M1} - u_1^{CD1} - u_2^{CD3} - u_1^{CD5} &= 0 \\
u_3^{M6} - u_3^{M1} - u_2^{CD4} - u_1^{CD2} &= 0 & u_3^{M7} - u_3^{M1} - u_2^{CD4} - u_2^{CD5} - u_1^{CD2} &= 0 \\
u_1^{M8} - u_1^{M1} - u_1^{CD3} - u_1^{CD4} &= 0 & & \\
u_2^{M8} - u_2^{M1} - u_1^{CD1} - u_1^{CD5} &= 0 & & \\
u_3^{M8} - u_3^{M1} - u_2^{CD5} - u_1^{CD2} &= 0 & & 
\end{aligned}$$

## F.5. Implementation into FE unit cell model

- The equations are implemented into the analysis in the with the `*equation` command into the Abaqus input-file [76].
- The equations are defined for complete nodesets of the faces / edges / masternodes. Therefore, identically ordered nodesets on opposing sides are required. The ordering is done within the MATLAB-script `pbm_creator.m`
- All operations required for the application of periodic boundary conditions are done within the MATLAB-script `pbm_creator.m`, which takes the unit cell `inp` file as input.

### Suppress rigid body motion

To suppress the rigid body motion of the unit cell, the displacements in x-, y- and z-direction of the masternode 1 are fixed. All rigid body rotations are suppressed implicitly by the coupling of shear strain constraint drivers given in Eq. 6.26.

## G. Supervised student theses

Thesis type	Date	Student	Title
Semester	10/2010	Pascal Traub	Materialmodellierung eines 2D-Geflechtes in WiseTex
Semester	04/2011	Florian Kozak	Modellierung von geflochtenen Faserverbundcrashboxen
Semester	06/2011	Daniel Türk	Auslegung eines geflochtenen Fahrradrahmens aus CFK
Semester	07/2011	Ludwig Eberl	Strukturanalyse eines Hochleistungs-Rennruderbootes
Bachelor	10/2011	Monika Humbs	Charakterisierung und Materialmodellierung von geflochtenen Verbundwerkstoffen
Master	11/2011	Gasper Kokelj	FE Simulation of the Braiding Process
Diploma	12/2011	Tobias Wehrkamp-Richter	Strength Analysis of Biaxial Braided Carbon Composites Under Tension
Semester	02/2012	Martin Haubold	Vernetzung von FE-Einheitszellen für geflochtene Verbundwerkstoffe
Diploma	09/2012	Johannes Bueckle	Festigkeitsvorhersage von Biaxialgeflechtem mit FE-Einheitszellen
Semester	09/2012	Florian Kozak	Geometrierstellung von FE-Einheitszellen für geflochtene Verbundwerkstoffe
Bachelor	10/2012	Michael Sams	Berechnung von geflochtenen Verbundwerkstoffen mit FE-Einheitszellen
Semester	01/2013	Christoph Hannich	Auslegung eines geflochtenen Fahrradrahmens aus CFK
Semester	06/2013	Philipp Huber	Experimentelle Charakterisierung eines biaxialen CFK-Geflechtes
Diploma	09/2013	Christoph Hannich	Implementierung und Validierung eines makroskopischen Materialgesetzes für biaxial geflochtene Verbundwerkstoffe

# Bibliography

- [1] <http://www.manager-magazin.de/unternehmen/autoindustrie/elektroauto-herstellung-bmw-faehrt-i3-produktion-um-40-prozent-hoch-a-964633.html>. accessed: 02/05/14.
- [2] <http://www.bmw.com/com/de/insights/corporation/bmwi/concept.html>. accessed: 13/05/14.
- [3] Soden P, Kaddour A, and Hinton M. Recommendations for designers and researchers resulting from the world-wide failure exercise. *Composites Science and Technology*, 64(3-4):589 – 604, 2004.
- [4] Nguyen LH, Horejsi K, Bartz K, Noisternig J, Filsinger J, and Steinhilber M. Resin Infusion with Braided Preform Concept for Aircraft Fuselage Frames. In *SEICO 11*, Paris, March 28-29 2011.
- [5] Schürmann H. *Konstruieren mit Faser-Kunststoff-Verbunden*. Springer-Verlag Berlin Heidelberg, 2007.
- [6] Long A. *Design and Manufacture of Textile Composites*. Woodhead Publishing Limited. Taylor & Francis, Cambridge England, 2006.
- [7] Cox BN and Flanagan G. *Handbook of Analytical Methods for Textile Composites*. Number 4750 in NASA Contractor Report. Langley Research Center, March 1997.
- [8] Dölle N. FVK-Anwendungen bei Daimler - Lessons learned. In *CCeV Automotive Forum*, Neckarsulm, 24 June 2010.
- [9] National Composites Network. HYBRIDMAT 3:Advances in the manufacture of advanced structural composites in aerospace. Technical report, National Composites Network, 2006.
- [10] A&P Technology. GENx engine. <http://www.braider.com/Case-Studies/GENx-Engine.aspx>. Accessed: 13/02/2014.
- [11] Rüger O. Preforming: Stand der Technik & Ausblick. <http://www.carbon-composites.eu/>, 13 October 2009. accessed 24/02/2014.
- [12] Fouinneteau M. *Damage and failure modelling of carbon and glass 2D braided composites*. PhD thesis, Cranfield University School of Applied Sciences, 2006.
- [13] Hu J. *3-D Fibrous Assemblies: Properties, Applications And Modelling Of Three-Dimensional Textile Structures*. Woodhead Publishing Series in Textiles. Woodhead Publishing Limited, Cambridge England, 2008.



- [14] Erber A, Birkefeld K, and Drechsler K. The Influence of Braiding Configuration on Damage Tolerance of Drive Shafts. In *SEICO 09, SAMPE Europe 30th. International Jubilee Conference and Forum*, Paris, France, 23-25 March 2009.
- [15] Lomov S, Verpoest I, and Robitaille F. Manufacturing and internal geometry of textiles. In Long AC, editor, *Design and manufacture of textile composites*. Woodhead Publishing Limited, Cambridge England, 2005.
- [16] Potluri P, Rawal A, Rivaldi M, and Porat I. Geometrical modelling and control of a triaxial braiding machine for producing 3D preforms. *Composites Part A: Applied Science and Manufacturing*, 34(6):481 – 492, 2003.
- [17] A&P Technology. Damage-Tolerant Fan Casings for Jet Engines. Technical report, National Aeronautics and Space Administration, September 2006.
- [18] Wettemann T. Kostenaspekte beim Einsatz neuer Composite-Technologien – ein Fallbeispiel. In *Bayern Innovativ: Clustertreffen neue Werkstoffe*, Augsburg, 13 October 2007.
- [19] A&P Technology. Applications in Braid Technology. [https://depts.washington.edu/amtas/events/amtas\\_08spring/AP\\_braiding.pdf](https://depts.washington.edu/amtas/events/amtas_08spring/AP_braiding.pdf). accessed: 14/02/14.
- [20] de Haan P. Development of a composite trailing arm for a helicopter main landing gear. In *Proceedings of the International Symposium on Composites Manufacturing for Aircraft Structures*, Marknesse, The Netherlands, 6-7 October 2010.
- [21] Gardiner G. Airbus A350 Update. *High-Performance Composites*, 20:32–39, 2012.
- [22] Byun JH and Chou TW. Process-microstructure relationships of 2-step and 4-step braided composites. *Composites Science and Technology*, 56(3):235 – 251, 1996.
- [23] Birkefeld K, von Reden T, and Boehler P. Analysis and Process Simulation of Braided Structures. In *Proceedings of the 4th EUCOMAS*, Hamburg, 07 February 2012.
- [24] Lomov SV, Ivanov DS, Verpoest I, Zako M, Kurashiki T, Nakai H, and Hirose S. Meso-FE modelling of textile composites: Road map, data flow and algorithms. *Composites Science and Technology*, 67(9):1870 – 1891, 2007.
- [25] Charlebois KM, Boukhili R, Zebdi O, Trochu F, and Gasmi A. Evaluation of the Physical and Mechanical Properties of Braided Fabrics and their Composites. *Journal of Reinforced Plastics and Composites*, 24(14):1539–1554, 2005.
- [26] Kelkar AD and Whitcomb JD. Characterization and Structural Behavior of Braided Composites. Technical Report DOT/FAA/AR-08/52, U.S. Department of Transportation Federal Aviation Administration, January, 2009.

- [27] Pickett A, Erber A, von Reden T, and Drechsler K. Comparison of analytical and finite element simulation of 2D braiding. *Plastics, Rubber and Composites*, 38(9-10):387–395, 2009.
- [28] Kokelj G. *FE Simulation of the braiding process*. Diploma thesis, Institute for Carbon Composites, Technische Universität München, Munich, December 2011.
- [29] Du Gw and Popper P. Analysis of a Circular Braiding Process for Complex Shapes. *Journal of the Textile Institute*, 85(3):316–337, 1994.
- [30] Akkerman R and Villa Rodriguez B. Braiding simulation for RTM preforms. In *Proceedings of the 8th International Conference on Textile Composites, TexComp-8*, Nottingham, UK, 16-18 October 2006.
- [31] Long A. Process modelling for liquid moulding of braided preforms. *Composites Part A: Applied Science and Manufacturing*, 32(7):941 – 953, 2001.
- [32] Tsai JS, Li SJ, and Lee LJ. Microstructural Analysis of Composite Tubes Made from Braided Preform and Resin Transfer Molding. *Journal of Composite Materials*, 32(9):829–850, 1998.
- [33] Birkefeld K, Röder M, von Reden T, Bulat M, and Drechsler K. Characterization of Biaxial and Triaxial Braids: Fiber Architecture and Mechanical Properties. *Applied Composite Materials*, 19:259–273, 2012.
- [34] Pickett A and Fouinneteau M. Material characterisation and calibration of a meso-mechanical damage model for braid reinforced composites. *Composites Part A: Applied Science and Manufacturing*, 37(2):368 – 377, 2006.
- [35] Uozumi T, Kito A, and Yamamoto T. CFRP using braided preforms/RTM process for aircraft applications. *Advanced Composite Materials*, 14(4):365–383, 2005.
- [36] Lomov SV, Huysmans G, and Verpoest I. Hierarchy of Textile Structures and Architecture of Fabric Geometric Models. *Textile Research Journal*, 71(6):534–543, 2001.
- [37] Potter E, Pinho S, Robinson P, Iannucci L, and McMillan A. Mesh generation and geometrical modelling of 3D woven composites with variable tow cross-sections. *Computational Materials Science*, 51(1):103 – 111, 2012.
- [38] Crookston J, Ruijter W, Long A, Warrior N, and Jones I. A Comparison Of Mechanical Property Prediction Techniques Using Conformal Tetrahedra and Voxel-Based Finite Element Meshes for Textile Composite Unit Cells. In *Finite element modelling of textiles and textile composites*, St-Petersburg, 26-28 September 2007.
- [39] Goyal D. *Analysis of Linear Elasticity and Non-Linearity Due to Plasticity and Material Damage in Woven and Biaxial Braided Composites*. PhD thesis, Texas A&M University, 2007.

- [40] Qu P, Guan X, Jia Y, Lou S, and Nie J. Effective elastic properties and stress distribution of 2D biaxial nonorthogonally braided composites. *Journal of Composite Materials*, 46(8):997–1008, 2012.
- [41] Melro AR. *Analytical and numerical modelling of damage and fracture of advanced colposites*. PhD thesis, University of Porto, Februar 2011.
- [42] Ladevèze P, Allix O, Deü JF, and Lévêque D. A mesomodel for localisation and damage computation in laminates. *Computer Methods in Applied Mechanics and Engineering*, 183(1-2):105 – 122, 2000.
- [43] ASTM D3171 (1999). *Standard Test Methods for Constituent Content of Composite Materials*. ASTM International, 100 Barr Harbor Drive, PO Box C700, West Conshohocken, PA 19428-2959, United States.
- [44] Byun JH. The analytical characterization of 2-D braided textile composites. *Composites Science and Technology*, 60(5):705 – 716, 2000.
- [45] Ivanov DS, Baudry F, Van Den Broucke B, Lomov SV, Xie H, and Verpoest I. Failure analysis of triaxial braided composite. *Composites Science and Technology*, 69(9):1372 – 1380, 2009.
- [46] Verpoest I and Lomov SV. Virtual textile composites software WiseTex: Integration with micro-mechanical, permeability and structural analysis. *Composites Science and Technology*, 65:2563 – 2574, 2005.
- [47] Carvalho ND, Pinho S, and Robinson P. Numerical modelling of woven composites: Biaxial loading. *Composites Part A: Applied Science and Manufacturing*, 43(8):1326 – 1337, 2012.
- [48] Huang ZM and Ramakrishna S. Towards Automatic Designing of 2D Biaxial Woven and Braided Fabric Reinforced Composites. *Journal of Composite Materials*, 36(13):1541–1579, 2002.
- [49] Matveev MY, Long AC, Jones IA, and Lu G. Modelling Effects of Geometric Variability on Mechanical Properties of 2D Textile Composites. In *Proceedings of the 19th International Conference of Composite Materials*, Montreal, Canada, 28 July - 2 August 2013.
- [50] Ruijter W, Crookston J, and Long A. Effects of Variable Fibre Density on Mechanical Properties of a Plain Weave Glass Reinforced Polyester. In *16th International Conference on Composite Materials*, 2007.
- [51] Ruijter W. *Analysis of mechanical properties of woven textile composites as a function of textile geometry*. PhD thesis, University of Nottingham, 2008.
- [52] Adanur S. *Handbook of Weaving*. Taylor & Francis, 2000.
- [53] Ivanov DS. *Damage analysis of textile composites*. PhD thesis, Katholieke Universiteit Leuven, 2009.

- [54] Owens BC, Whitcomb JD, and Varghese J. Effect of Finite Thickness and Free Edges on Stresses in Plain Weave Composites. *Journal of Composite Materials*, 44(6):675–692, 2010.
- [55] Vanaerschot A, Cox BN, Lomov SV, and Vandepitte D. Stochastic framework for quantifying the geometrical variability of laminated textile composites using micro-computed tomography. *Composites Part A: Applied Science and Manufacturing*, 44(0):122 – 131, 2013.
- [56] Lomov S, Verpoest I, Peeters T, Roose D, and Zako M. Nesting in textile laminates: geometrical modelling of the laminate. *Composites Science and Technology*, 63(7):993 – 1007, 2003.
- [57] Schultz J and Garnich M. Meso-scale and multicontinuum modeling of a triaxial braided textile composite. *Journal of Composite Materials*, 47(3):303–314, 2013.
- [58] Chen B and Chou TW. Compaction of woven-fabric preforms: nesting and multi-layer deformation. *Composites Science and Technology*, 60(12-13):2223 – 2231, 2000.
- [59] Chen B, Lang EJ, and Chou TW. Experimental and theoretical studies of fabric compaction behavior in resin transfer molding. *Materials Science and Engineering: A*, 317(1-2):188 – 196, 2001.
- [60] Lomov SV, Huysmans G, Luo Y, Parnas RS, Prodromou A, Verpoest I, and Phelan FR. Textile composites: modelling strategies. *Composites Part A: Applied Science and Manufacturing*, 32(10):1379 – 1394, 2001.
- [61] Pearce N and Summerscales J. The compressibility of a reinforcement fabric. *Composites Manufacturing*, 6(1):15 – 21, 1995.
- [62] Potluri P and Manan A. Mechanics of non-orthogonally interlaced textile composites. *Composites Part A: Applied Science and Manufacturing*, 38(4):1216 – 1226, 2007.
- [63] Desplentere F, Lomov S, Woerdeman D, Verpoest I, Wevers M, and Bogdanovich A. Micro-CT characterization of variability in 3D textile architecture. *Composites Science and Technology*, 65(13):1920 – 1930, 2005.
- [64] Crookston JJ. *Prediction of elastic behaviour and initial failure of textile composites*. PhD thesis, University of Nottingham, 2004.
- [65] Djukic LP, Herszberg I, Walsh WR, Schoeppner GA, Prusty BG, and Kelly DW. Contrast enhancement in visualisation of woven composite tow architecture using a MicroCT Scanner. Part 1: Fabric coating and resin additives. *Composites Part A: Applied Science and Manufacturing*, 40(5):553 – 565, 2009.
- [66] Miene A. Bildanalytische Qualitätssicherung in der Preformfertigung. In *5. Sitzung der Arbeitsgruppe „Werkstoff- und Bauteilprüfung“*, Augsburg, Germany, 05 March 2010.

- [67] Thumfart S, Palfinger W, Stöger M, and Eitzinger C. Accurate Fibre Orientation Measurement for Carbon Fibre Surfaces. In Wilson R, Hancock E, Bors A, and Smith W, editors, *Computer Analysis of Images and Patterns*, volume 8048 of *Lecture Notes in Computer Science*, pages 75–82. Springer Berlin Heidelberg, 2013.
- [68] Thanner P and Palfinger W. Qualitätssicherung von Carbonfaserteilen mittels Bildverarbeitung. In *Handhabungstechnik, Der Schlüssel für eine automatisierte Herstellung von Composite-Bauteilen*, Augsburg, 8 July 2010.
- [69] Pickett AK, Sirtautas J, and Erber A. Braiding Simulation and Prediction of Mechanical Properties. *Applied Composite Materials*, 16(6):345–364, 2009.
- [70] Aggarwal A, Ramakrishna S, and Ganesh VK. Predicting the Strength of Diamond Braided Composites. *Journal of Composite Materials*, 36(5):625–643, 2002.
- [71] Robitaille F, Long A, Jones I, and Rudd C. Automatically generated geometric descriptions of textile and composite unit cells. *Composites Part A: Applied Science and Manufacturing*, 34(4):303 – 312, 2003.
- [72] Huysmans G, Verpost I, and van Houtte P. A poly-Inclusion Approach for the Elastic Modelling of Knitted Fabric Composites. *Acta Metallurgica Inc.*, 46(9):3003–3013, 1998.
- [73] Verleye B, Lomov S, Long A, Verpoest I, and Roose D. Permeability prediction for the meso-macro coupling in the simulation of the impregnation stage of Resin Transfer Moulding. *Composites Part A: Applied Science and Manufacturing*, 41(1):29 – 35, 2010. Special Issue: Flow Processes in Composite Materials.
- [74] Lomov SV, Verpoest I, Cichosz J, Hahn C, Ivanov DS, and Verleye B. Meso-level textile composites simulations: Open data exchange and scripting. *Journal of Composite Materials*, 2013.
- [75] TexGen. <http://texgen.sourceforge.net>. accessed: 21/02/2014.
- [76] Dassault Systèmes. *Abaqus 6.13 Documentation*, 2013.
- [77] Sherburn M. *Geometric and Mechanical Modelling of Textiles*. PhD thesis, University of Nottingham, 2007.
- [78] Sherburn M, Long A, Jones A, Crookston J, and Brown L. Prediction of textile geometry using an energy minimization approach. *Journal of Industrial Textiles*, 41(4):345–369, 2012.
- [79] Zako M, Uetsuji Y, and Kurashiki T. Finite element analysis of damaged woven fabric composite materials. *Composites Science and Technology*, 63:507 – 516, 2003.
- [80] Hivet G and Boisse P. Consistent 3D geometrical model of fabric elementary cell. Application to a meshing preprocessor for 3D finite element analysis. *Finite Elements in Analysis and Design*, 42(1):25 – 49, 2005.

- [81] Grail G, Hirsekorn M, Wendling A, Hivet G, and Hambli R. Consistent Finite Element mesh generation for meso-scale modeling of textile composites with preformed and compacted reinforcements. *Composites Part A: Applied Science and Manufacturing*, 55(0):143 – 151, 2013.
- [82] Hsu SY and Cheng RB. Modeling geometry and progressive interfacial damage in textile composites. *Journal of Composite Materials*, 47(11):1343–1356, 2013.
- [83] Stig F and Hallström S. Spatial modelling of 3D-woven textiles. *Composite Structures*, 94(5):1495 – 1502, 2012.
- [84] ASTM D3039 (2000). *Standard Test Method for Tensile Properties of Polymer Matrix Composite Materials*. ASTM International, 100 Barr Harbor Drive, PO Box C700, West Conshohocken, PA 19428-2959, United States.
- [85] ASTM D6641 (2009). *Standard Test Method for Compressive Properties of Polymer Matrix Composite Materials Using a Combined Loading Compression (CLC) Test Fixture*. ASTM International, 100 Barr Harbor Drive, PO Box C700, West Conshohocken, PA 19428-2959, United States.
- [86] Masters JE. Strain Gage Selection Criteria for Textile Composite Materials. NASA Contractors Report 198286, National Aeronautics and Space Administration, 1996.
- [87] Masters JE and Portanova MA. Standard Test Methods for Textile Composites. NASA Contractor Report 4751, National Aeronautics and Space Administration, 1996.
- [88] Minguet PJ, Fedro MJ, and Gunther CK. Test Methods for Textile Composites. NASA Contractor Report 4609, National Aeronautics and Space Administration, 1994.
- [89] Naik RA, Ifju PG, and Masters JE. Effect of Fiber Architecture Parameters on Deformation Fields and Elastic Moduli of 2-D Braided Composites. *Journal of Composite Materials*, 28(7):656–681, 1994.
- [90] Smith LV and Swanson SR. Failure of Braided Carbon/Epoxy Composites under Biaxial Compression. *Journal of Composite Materials*, 28(12):1158–1178, 1994.
- [91] Dadkhah M, Flintoff J, Kniveton T, and Cox B. Simple models for triaxially braided composites. *Composites*, 26(8):561 – 577, 1995.
- [92] Minguet PJ and Gunther CK. A Comparison of Graphite/Epoxy Tape Laminates and 2-D Braided Composites Mechanical Properties. NASA Contractor Report 4610, National Aeronautics and Space Administration, 1994.
- [93] Harte AM and Fleck NA. On the mechanics of braided composites in tension. *European Journal of Mechanics - A/Solids*, 19(2):259 – 275, 2000.
- [94] Harte AM and Fleck N. Deformation and failure mechanisms of braided composite tubes in compression and torsion. *Acta Materialia*, 48(6):1259 – 1271, 2000.

- [95] Puck A. *Festigkeitsanalyse von Faser-Matrix-Laminaten (Modelle für die Praxis)*. Hanser, München, Wien, 1996.
- [96] van den Berg S. Braid Property Prediction. In *SAMPE 2010 - Seattle, WA*, 17-20 May 2010.
- [97] Fujita A, Maekawa Z, Hamada H, and Yokoyama A. Mechanical Behavior and Fracture Mechanism in Flat Braided Composites. Part 1: Braided Flat Bar. *Journal of Reinforced Plastics and Composites*, 11(6):600–617, 1992.
- [98] Lomov S, Ivanov D, Truong T, Verpoest I, Baudry F, Bosche KV, and Xie H. Experimental methodology of study of damage initiation and development in textile composites in uniaxial tensile test. *Composites Science and Technology*, 68(12):2340 – 2349, 2008.
- [99] Littell JD, Goldberg RK, Roberts GD, and Binienda WK. Full-Field Strain Methods for Investigating Failure Mechanisms in Triaxial Braided Composites. In *Proceedings of the Earth and Space 2008, 11th International Conference on Engineering, Science, Construction, and Operations in Challenging Environments*, pages 1–12, Long Beach, California, 3–5 March 2008.
- [100] Prodromou AG, Lomov SV, and Verpoest I. The method of cells and the mechanical properties of textile composites. *Composite Structures*, 93(4):1290 – 1299, 2011.
- [101] Gager J, Flatscher T, and Pettermann HE. Elasto-plasto-damage modelling of FRP fabrics - a shell unit cell approach. In *3rd ECCOMAS Thematic Conference on the Mechanical Response of Composites*, Hannover, Germany, 21 - 23 September 2011.
- [102] Ishikawa T and Chou TW. Stiffness and strength behaviour of woven fabric composites. *Journal of Materials Science*, 17(11):3211–3220, 1982.
- [103] Ishikawa T and Chou TW. Elastic Behavior of Woven Hybrid Composites. *Journal of Composite Materials*, 16(1):2–19, 1982.
- [104] Ishikawa T and Chou TW. Nonlinear Behavior of Woven Fabric Composites. *Journal of Composite Materials*, 17(5):399–413, 1983.
- [105] Chou TW and Ishikawa T. One-dimensional micromechanical analysis of woven fabric composites. *AIAA Journal*, 21(12):1714–1721, December 1983.
- [106] Naik N and Shembekar P. Elastic Behavior of Woven Fabric Composites: I–Lamina Analysis. *Journal of Composite Materials*, 26(15):2196–2225, 1992.
- [107] Tarnopol'skii Y, Polyakov V, and Zhigun I. Composite materials reinforced with a system of three straight, mutually orthogonal fibers. *Polymer Mechanics*, 9(5):754–759, 1973.
- [108] Kregers A and Melbardis Y. Determination of the deformability of three-dimensionally reinforced composites by the stiffness averaging method. *Polymer Mechanics*, 14(1):1–5, 1978.

- [109] Kregers A and Teters G. Determination of the elastoplastic properties of spatially reinforced composites by the averaging method. *Mechanics of Composite Materials*, 17(1):25–31, 1981.
- [110] Cox BN and Dadkhah MS. The Macroscopic Elasticity of 3D Woven Composites. *Journal of Composite Materials*, 29(6):785–819, 1995.
- [111] Hallal A, Younes R, and Fardoun F. Review and comparative study of analytical modeling for the elastic properties of textile composites. *Composites Part B: Engineering*, 50(0):22 – 31, 2013.
- [112] Huysmans G, Verpoest I, and Van Houtte P. Eshelby Models Applied to Woven Fabric Composites: A Benchmark Study. Technical report, Department of Metallurgy and Materials Engineering, Katholieke Universiteit Leuven, 2004.
- [113] Aboudi J, Arnold S, and Bednarczyk B. *Micromechanics of Composite Materials: A Generalized Multiscale Analysis Approach*. Elsevier Science, 2012.
- [114] Smith L and Swanson S. Micro-mechanics parameters controlling the strength of braided composites. *Composites Science and Technology*, 54(2):177 – 184, 1995.
- [115] Smith LV and Swanson SR. Failure of Braided Composite Cylinders under Biaxial Tension. *Journal of Composite Materials*, 29(6):766–784, 1995.
- [116] Smith LV and Swanson SR. Strength design with 2-D triaxial braid textile composites. *Composites Science and Technology*, 56(3):359 – 365, 1996.
- [117] Johnson A, Pickett A, and Rozycki P. Computational methods for predicting impact damage in composite structures. *Composites Science and Technology*, 61(15):2183 – 2192, 2001.
- [118] Goyal D, Whitcomb JD, and Tang X. Validation of full 3D and equivalent tape laminate modeling of plasticity induced non-linearity in 2x2 braided composites. *Composites Part A: Applied Science and Manufacturing*, 39(5):747 – 760, 2008.
- [119] Zebdi O, Boukhili R, and Trochu F. An Inverse Approach Based on Laminate Theory to Calculate the Mechanical Properties of Braided Composites. *Journal of Reinforced Plastics and Composites*, 28(23):2911–2930, 2009.
- [120] Xiao X, Kia HG, and Gong XJ. Strength prediction of a triaxially braided composite. *Composites Part A: Applied Science and Manufacturing*, 42(8):1000 – 1006, 2011.
- [121] Beard S and Chang FK. Design of Braided Composites for Energy Absorption. *Journal of Thermoplastic Composite Materials*, 15(1):3–12, 2002.
- [122] Littell J. *The Experimental and Analytical Characterization of the Macromechanical Response for Triaxial Braided Composite Materials*. PhD thesis, The Graduate Faculty of The University of Akron, 2008.



- [123] Lomov SV, Ivanov DS, Verpoest I, Zako M, Kurashiki T, Nakai H, Molimard J, and Vautrin A. Full-field strain measurements for validation of meso-FE analysis of textile composites. *Composites Part A: Applied Science and Manufacturing*, 39(8):1218 – 1231, 2008. Full-field Measurements in Composites Testing and Analysis.
- [124] Jiang WG, Hallett SR, and Wisnom MR. Development of Domain Superposition Technique for the Modelling of Woven Fabric Composites. In Camanho PP, Davila CG, Pinho ST, and Remmers JJC, editors, *Mechanical Response of Composites*, volume 10 of *Computational Methods in Applied Sciences*, pages 281–291. Springer Netherlands, 2008.
- [125] Cox B, Carter W, and Fleck N. A binary model of textile composites-I. Formulation. *Acta Metallurgica et Materialia*, 42(10):3463 – 3479, 1994.
- [126] Blackketter D, Walrath D, and Hansen A. Modeling Damage in a Plain Weave Fabric-Reinforced Composite Material. *Journal of Composites, Technology and Research*, 15(2):136–142, 1993.
- [127] Puck A and Schuermann H. Failure Analysis of FRP Laminates by Means of Physically Based Phenomenological Models. *Composites Science and Technology*, 58(7):1045 – 1067, 1998.
- [128] Kim HJ and Swan CC. Voxel-based meshing and unit-cell analysis of textile composites. *International Journal for Numerical Methods in Engineering*, 56(7):977–1006, 2003.
- [129] Kim HJ and Swan CC. Algorithms for automated meshing and unit cell analysis of periodic composites with hierarchical tri-quadratic tetrahedral elements. *International Journal for Numerical Methods in Engineering*, 58(11):1683–1711, 2003.
- [130] Gager J, Cichosz J, Wolfahrt M, Hinterhölzl R, Pettermann HE, Fleischmann M, and Schubert M. Materialmodellierung von kohlenstofffaserverstärkten Geflecht-laminaten. In *Presentations of the PCCL-Symposium*, Leoben, Austria, 04-05 Oct 2012.
- [131] Xu J, Cox B, McGlockton M, and Carter W. A binary model of textile composites—II. The elastic regime. *Acta Metallurgica et Materialia*, 43(9):3511 – 3524, 1995.
- [132] Yang Q and Cox B. Spatially Averaged Local Strains in Textile Composites Via the Binary Model Formulation. *Journal of Engineering Materials and Technology*, 125(4):418–425, 2003.
- [133] Yang Q and Cox B. Predicting failure in textile composites using the Binary Model with gauge-averaging. *Engineering Fracture Mechanics*, 77(16):3174 – 3189, 2010.
- [134] Cox B and Yang Q. Failure Prediction for Textile Composites via Micromechanics. In *Proceedings of IMECE*, Washington D.C., 15-21 November 2003.

- [135] Yang Q and Cox B. Fracture and Failure Prediction of Textile Composites using Mechanism-Based Models. In *37th International SAMPE Technical Conference*, Seattle, USA, Oct 31 - Nov 3 2005.
- [136] Flores S, Evans AG, Zok FW, Genet M, Cox B, Marshall D, Sudre O, and Yang Q. Treating matrix nonlinearity in the binary model formulation for 3D ceramic composite structures. *Composites Part A: Applied Science and Manufacturing*, 41(2):222 – 229, 2010.
- [137] Blacklock M, Bale H, Begley M, and Cox B. Generating virtual textile composite specimens using statistical data from micro-computed tomography: 1D tow representations for the Binary Model. *Journal of the Mechanics and Physics of Solids*, 60(3):451 – 470, 2012.
- [138] Tabatabaei S, Lomov S, and Verpoest I. Assessment of embedded element technique in meso-FE modelling of fibre reinforced composites. *Composite Structures*, 107(0):436 – 446, 2014.
- [139] Gager J and Pettermann H. Numerical homogenization of textile composites based on shell element discretization. *Composites Science and Technology*, 72(7):806 – 812, 2012.
- [140] Gager J. *Modeling and simulation concepts for Advanced braided composites*. PhD thesis, Technische Universität Wien, 2013.
- [141] Flatscher T. *A constitutive model for the elasto-plasto-damage ply behavior in laminated FRP composites: its development, implementation and application in FEM simulations*. PhD thesis, Technische Universität Wien, 2010.
- [142] Gross D and Seelig T. *Bruchmechanik: Mit einer Einführung in die Mikromechanik*. Springer-Verlag Berlin Heidelberg, 2007.
- [143] Pindera MJ, Khatam H, Drago AS, and Bansal Y. Micromechanics of spatially uniform heterogeneous media: A critical review and emerging approaches. *Composites Part B: Engineering*, 40(5):349 – 378, 2009.
- [144] Pahr D. *Experimental and Numerical Investigations of Perforated Laminates*. PhD thesis, Vienna University of Technology, VDI Verlag GmbH, Düsseldorf, 2003.
- [145] Anthoine A. Derivation of the in-plane elastic characteristics of masonry through homogenization theory. *International Journal of Solids and Structures*, 32(2):137 – 163, 1995.
- [146] Carvelli V and Poggi C. A homogenization procedure for the numerical analysis of woven fabric composites. *Composites Part A: Applied Science and Manufacturing*, 32(10):1425 – 1432, 2001.
- [147] Soden PD, Hinton MJ, and Kaddour AS. Lamina Properties, Lay-Up Configurations and Loading Conditions for a Range of Fibre-Reinforced Composite Laminates. *Composites Science and Technology*, 58:1011–1022, 1998.

- [148] Soden PD, Hinton MJ, and Kaddour AS. A Comparison of the Predictive Capabilities of Current Failure Theories for Composite Laminates. *Composites Science and Technology*, 58:1225–1254, 1998.
- [149] Hinton MJ, Kaddour AS, and Soden PD. A comparison of the predictive capabilities of current failure theories for composite laminates, judged against experimental evidence. *Composites Science and Technology*, 62:1725–1797, 2002.
- [150] Bogetti TA, Hoppel CP, Harik VM, Newill JF, and Burns BP. Predicting the non-linear response and progressive failure of composite laminates. *Composites Science and Technology*, 64(3-4):329 – 342, 2004. Failure criteria in fibre reinforced polymer composites Part C: Additional theories conclusions and recommendations.
- [151] Zinoviev PA, Grigoriev SV, Lebedeva OV, and Tairova LP. The strength of multi-layered composites under a plane-stress state. *Composites Science and Technology*, 58(7):1209 – 1223, 1998.
- [152] Tsai SW and Wu EM. A General Theory of Strength for Anisotropic Materials. *Journal of Composite Materials*, 5(1):58–80, 1971.
- [153] Hashin Z. Failure criteria for unidirectional fiber composites. *Journal of Applied Mechanics*, 47(6):329 – 334, 1980.
- [154] Cuntze R. The predictive capability of failure mode concept-based strength criteria for multi-directional laminates - part B. *Composites Science and Technology*, 64(3-4):487 – 516, 2004. Failure criteria in fibre reinforced polymer composites Part C: Additional theories conclusions and recommendations.
- [155] Kaddour A and Hinton M. Benchmarking of triaxial failure criteria for composite laminates: Comparison between models of Part A of WWFE-II. *Journal of Composite Materials*, 46(19-20):2595–2634, 2012.
- [156] Kaddour A and Hinton M. Maturity of 3D failure criteria for fibre-reinforced composites: Comparison between theories and experiments: Part B of WWFE-II. *Journal of Composite Materials*, 47(6-7):925–966, 2013.
- [157] Kaddour A, Hinton M, Smith P, and Li S. The background to the third world-wide failure exercise. *Journal of Composite Materials*, 47(20-21):2417–2426, 2013.
- [158] Davila CG, Camanho PP, and Rose CA. Failure Criteria for FRP Laminates. *Journal of Composite Materials*, 39(4):323–345, 2005.
- [159] Camanho PP, D’Ávila CG, Pinho ST, Iannucci L, and Robinson P. Prediction of in situ strengths and matrix cracking in composites under transverse tension and in-plane shear. *Composites Part A: Applied Science and Manufacturing*, 37(2):165 – 176, 2006. CompTest 2004.
- [160] Pinho ST, Davila CG, Camanho PP, Iannucci L, and Robinson P. Failure Models and Criteria for FRP Under In-Plane or Three-Dimensional Stress States Including

- Shear Non-Linearity. Technical Memorandum NASA/TM-2005-213530, National Aeronautics and Space Administration, 2005.
- [161] Catalanotti G, Camanho P, and Marques A. Three-dimensional failure criteria for fiber-reinforced laminates. *Composite Structures*, 95(0):63 – 79, 2013.
- [162] Kachanov LM. Time of the rupture process under creep conditions. *Izv. Akad. Nauk. S.S.R. Otd. Tech. Nauk.*, 8:26–31, 1958.
- [163] Lemaitre J. *A Course on Damage Mechanics*. Springer-Verlag, 1992.
- [164] Matzenmiller A, Lubliner J, and Taylor RL. A Constitutive Model for Anisotropic Damage in Fiber-Composites. *Mechanics of Materials*, 20:125–152, 1995.
- [165] Lapczyk I and Hurtado JA. Progressive damage modeling in fiber-reinforced materials. *Composites Part A: Applied Science and Manufacturing*, 38(11):2333 – 2341, 2007.
- [166] Maimi P, Camanho PP, Mayugo JA, and Davila CG. A continuum damage model for composite laminates: Part I - Constitutive model. *Mechanics of Materials*, 39(10):897 – 908, 2007.
- [167] Maimi P, Camanho PP, Mayugo JA, and Davila CG. A continuum damage model for composite laminates: Part II - Computational implementation and validation. *Mechanics of Materials*, 39(10):909 – 919, 2007.
- [168] Vyas G and Pinho S. Computational implementation of a novel constitutive model for multidirectional composites. *Computational Materials Science*, 51(1):217 – 224, 2012.
- [169] Varna J, Joffe R, Akshantala N, and Talreja R. Damage in composite laminates with off-axis plies. *Composites Science and Technology*, 59(14):2139 – 2147, 1999.
- [170] Puck A and Schürmann H. Failure analysis of FRP laminates by means of physically based phenomenological models. *Composites Science and Technology*, 62(12-13):1633 – 1662, 2002.
- [171] Sun C and Yoon K. Elastic-Plastic Analysis of AS4/PEEK Composite Laminate Using a One-Parameter Plasticity Model. *Journal of Composite Materials*, 26(2):293–308, 1992.
- [172] Vyas G, Pinho S, and Robinson P. Constitutive modelling of fibre-reinforced composites with unidirectional plies using a plasticity-based approach. *Composites Science and Technology*, 71(8):1068 – 1074, 2011.
- [173] Vogler M, Rolfes R, and Camanho PP. Modeling the inelastic deformation and fracture of polymer composites - Part I: Plasticity model. *Mechanics of Materials*, 59(0):50 – 64, 2013.

- [174] Camanho P, Bessa M, Catalanotti G, Vogler M, and Rolfes R. Modeling the inelastic deformation and fracture of polymer composites - Part II: Smearred crack model. *Mechanics of Materials*, 59(0):36 – 49, 2013.
- [175] Jones R. *Mechanics of composite materials*. Materials Science and Engineering Series. Taylor & Francis, 1999.
- [176] Datenblatt: Produktprogramm und Eigenschaften für Tenax® HTS Filamentgarn. <http://www.tohotenax-eu.com/>. accessed: 17/02/14.
- [177] HexFlow® RTM 6 - Product Data. <http://www.hexcel.com/>. accessed: 17/02/14.
- [178] VAP - Vacuum Assisted Process. <http://www.vap-info.com>. accessed: 17/02/14.
- [179] STRUERS GmbH. <http://www.struers.de>. accessed: 17/02/14.
- [180] Olympus Stream Motion software. <http://www.olympus-ims.com/en/microscope/stream/>. accessed: 18/02/2014.
- [181] Image J. <http://imagej.nih.gov/ij/>. accessed 15/02/14.
- [182] ASTM D6856 (2003). *Standard Guide for Testing Fabric-Reinforced “Textile” Composite Materials*. ASTM International, 100 Barr Harbor Drive, PO Box C700, West Conshohocken, PA 19428-2959, United States.
- [183] Wegner PM and Adams DF. Verification of the Combined Load Compression (CLC) Test Method. Technical Report DOT/FAA/AR-00/26, U.S. Department of Transportation Federal Aviation Administration, Aug, 2000.
- [184] Huber P. Experimentelle Charakterisierung eines biaxialen CFK-Geflechtes. Semesterarbeit, Institute for Carbon Composites, Technische Universität München, June 2013.
- [185] Sun C and Chung I. An oblique end-tab design for testing off-axis composite specimens. *Composites*, 24(8):619–623, 1993.
- [186] ESAComp 4.4 Material Database:. Toho Tenax HTS 5631 / HTS40.
- [187] Preußner-Messtechnik: F-Series. <http://dms-technik.de/>. accessed: 26/02/14.
- [188] Pan B, Qian K, Xie H, and Asundi A. Two-dimensional digital image correlation for in-plane displacement and strain measurement: a review. *Measurement Science and Technology*, 20(6):062001, 2009.
- [189] Kim HC and Matthews FL. Hysteresis behaviour in CFRP. *Journal of Physics D: Applied Physics*, 6(15):1755, 1973.
- [190] Kotil T, Holmes JW, and Comninou M. Origin of Hysteresis Observed During Fatigue of Ceramic-Matrix Composites. *Journal of the American Ceramic Society*, 73(7):1879–1883, 1990.

- [191] Ladevèze P. Inelastic Strains and Damage. In Talreja R, editor, *Damage Mechanics of Composite Materials*, volume 9. Elsevier Science B.V., 1994.
- [192] Department of Defense. Composite Materials Handbook - Volume 3. Polymer Matrix Composites Materials Usage, Design and Analysis, June 2002.
- [193] Birkefeld K. *Virtuelle Optimierung von Geflecht-Preforms unter Berücksichtigung von Fertigungsaspekten*. PhD thesis, Universität Stuttgart, 2013.
- [194] Wehrkamp-Richter T. Strength Analysis of Biaxial Braided Carbon Composites Under Tension. Diploma thesis, Institute for Carbon Composites, Technische Universität München, Munich, December 2011.
- [195] Wehrkamp-Richter T, Humbs M, Schultheiss D, and Hinterhoelzl R. Damage Characterization of Triaxial Braided Composites Under Tension Using Full-Field Strain Measurement. In *Proceedings of the 19th International Conference of Composite Materials*, Montreal, Canada, July 2013.
- [196] de Verdier MC, Pickett A, Skordos A, and Witzel V. Evaluation of the mechanical and damage behaviour of tufted non crimped fabric composites using full field measurements. *Composites Science and Technology*, 69(2):131 – 138, 2009.
- [197] Quek SC, Waas AM, Shahwan KW, and Agaram V. Analysis of 2D triaxial flat braided textile composites. *International Journal of Mechanical Sciences*, 45(6-7):1077 – 1096, 2003.
- [198] McGlockton M, Cox B, and McMeeking R. A Binary Model of textile composites: III high failure strain and work of fracture in 3D weaves. *Journal of the Mechanics and Physics of Solids*, 51(8):1573 – 1600, 2003.
- [199] Carvalho ND, Pinho S, and Robinson P. Reducing the domain in the mechanical analysis of periodic structures, with application to woven composites. *Composites Science and Technology*, 71(7):969 – 979, 2011.
- [200] Murthy PLN and Chamis CC. Integrated Composite Analyzer (ICAN) - Users and Programmers Manual. NASA Technical Paper 2515, NASA, March 1986.
- [201] Toho Tenax Europe. Internal report, 2001.
- [202] Pinho S, Darvizeh R, Robinson P, Schuecker C, and Camanho P. Material and structural response of polymer-matrix fibre-reinforced composites. *Journal of Composite Materials*, 46(19-20):2313–2341, 2012.
- [203] Shin E and Pae K. Effects of Hydrostatic Pressure on In-Plane Shear Properties of Graphite/Epoxy Composites. *Journal of Composite Materials*, 26(6):828–868, 1992.
- [204] Schubert M. Vergleich eines Resin Transfer Moulding Epoxidharzsystems mit einem Prepregharzsystem. Technical report, Toho Tenax Europe GmbH, Wuppertal, 2009.

- [205] Li S and Wongsto A. Unit cells for micromechanical analyses of particle-reinforced composites. *Mechanics of Materials*, 36(7):543 – 572, 2004.
- [206] Sihh S, Iarve EV, and Roy AK. Three-dimensional stress analysis of textile composites: Part I. Numerical analysis. *International Journal of Solids and Structures*, 41(5-6):1377 – 1393, 2004.
- [207] Sihh S, Iarve EV, and Roy AK. Three-dimensional stress analysis of textile composites. Part II: Asymptotic analysis. *International Journal of Solids and Structures*, 41(5-6):1395 – 1410, 2004.
- [208] Ivanov DS, Lomov SV, Ivanov SG, and Verpoest I. Stress distribution in outer and inner plies of textile laminates and novel boundary conditions for unit cell analysis. *Composites Part A: Applied Science and Manufacturing*, 41(4):571 – 580, 2010.
- [209] Ivanov DS, Ivanov SG, Lomov SV, and Verpoest I. Unit cell modelling of textile laminates with arbitrary inter-ply shifts. *Composites Science and Technology*, 72(1):14 – 20, 2011.
- [210] Littell JD, Binienda WK, Goldberg RK, and Roberts G. Modeling of Failure for Analysis of Triaxial Braided Carbon Fiber Composites. Technical Support Package LEW-18435-1, NASA, 2008.
- [211] Xiao X. A Coupled Damage-plasticity Model for Energy Absorption in Composite. *International Journal of Damage Mechanics*, 19(6):727–751, 2010.
- [212] Körber H. *Mechanical Response of Advanced Composites under High Strain Rates*. PhD thesis, Faculdade de Engenharia da Universidade do Porto Departamento de Engenharia Mecânica, 2010.
- [213] Puck A, Kopp J, and Knops M. Guidelines for the determination of the parameters in Puck’s action plane strength criterion. *Composites Science and Technology*, 62(3):371 – 378, 2002.